600 Jahre Universität Rostock

Traditio et Innovatio

Beyond the spatio-temporal limits of atmospheric radars: Inverse problem techniques and MIMO systems

Dissertation to

obtain the academic degree of Doctor of Engineering (Dr.-Ing)

from the Faculty of Computer Science and Electrical Engineering at the University of Rostock

by

Juan M. E. Urco Cordero

from Jauja, Peru

Reviewers:

Prof. Dr. Tobias Weber, University of Rostock

Prof. Dr. Jorge L. Chau, Institute for Atmospheric Physics

Prof. Dr. Juha Vierinen, The Arctic University of Norway

Date of submission: 15.11.2020

Date of acceptance: 15.02.2021

Date of defense: 16.03.2021

https://doi.org/10.18453/rosdok_id00003356

Abstract

The Earth's upper atmosphere is a highly dynamic region dominated by atmospheric waves and stratified turbulence covering a wide range of spatio-temporal scales. A comprehensive study of the upper atmosphere is challenging since this region is still poorly sampled. The altitude range of the upper atmosphere limits its study since is either inaccessible by in-situ instruments or prohibitively expensive. Remote sensors, such as radars, are the only alternative to observe the upper atmosphere continuously. Nevertheless, current remote sensors cannot provide measurements over the whole range of frequencies and spatial wavelengths associated with atmospheric waves and stratified turbulence due to their limited spatio-temporal resolution and coverage. Most of the previous studies using radar measurements have resolved the spatio-temporal ambiguity associated with the measurements focusing on particular scales and assuming a homogeneous atmosphere within the observed volume. To dramatically improve the understanding of the upper atmosphere and its components at different spatio-temporal scales, an investment in large observational infrastructures is required to obtain 4D observations (space-time) with a sufficient resolution. Unfortunately, the deployment of such systems is still prohibitively expensive.

This work investigates remote sensing techniques based on multiple–input multiple–output (MIMO) and inverse problems to improve the capabilities of current atmospheric radars, namely, improvement of the effective spatial resolution and observational coverage. The former using multiple transmitters and receivers closely separated, and the latter using multiple transmitters and multiple receivers widely separated. MIMO radars are known for their superiority over conventional radar systems because they provide better spatial resolution and coverage due to their higher number of degrees of freedom and their flexible transmit beam pattern. Nevertheless, the application of MIMO might degrade radar systems' performance by reducing the transmitted power per antenna, increasing the computational complexity, and causing cross-interference between the multiple transmitted signals.

This study particularly investigates the design of transmit waveforms and proposes recovery algorithms to retrieve radar parameters like signal amplitude, angle of arrival, and angle of departure from atmospheric MIMO radars. Since the performance of waveform design techniques and recovery algorithms are strictly related to the radar target,

two successful examples of MIMO are described in detail using polar mesospheric summer echoes (PMSE) and specular meteor trail echoes as tracers of the MLT dynamics. These two implementations resulted in measurements of the MLT with unprecedented spatial resolution and coverage. Additionally, numerical simulations are provided for each case to support the experimental results.

The first implementation resulted in PMSE observations with six times higher spatial resolution than the theoretical instrument resolution. These exceptional results have been employed by supplementary studies to identify and characterize atmospheric instabilities of kilometer-scales, which otherwise would be unresolvable by standard techniques. Similarly, the second example presents the largest multi-static meteor radar network deployed in the world, for which the total number of meteor detections per day was $\sim$120k compared to $\sim$10k of commercial meteor radars. Such observations are unique, and the results have also been employed by additional studies to measure the energy spectrum in the mesosphere over a wide range of spatio-temporal scales. These two successful experimental implementations demonstrate the feasibility of MIMO for atmospheric observations and open a new area of exploration in the atmospheric community.

Acknowledgements

First of all, I would like to thank my advisors, Prof. J. L. Chau and Prof. T. Weber, for their excellent guidance during my doctoral studies. Specially to Prof. J. L. Chau who encouraged me to start this journey and have supported me during my stay at the Institute of Atmospheric Physics, Kuehlungsborn. I will deeply miss our conversations and discussions, and even more his advices.

I also want to thank my mother Margot Cordero and my grandmother Gregoria Campos for their love and support for my entire life. Likewise, I would like to give a special thanks to my lovely wife Katerina Garcia for her accompany and love.

I also like to thank my IAP mates. It was truly a great experience working with you. I will miss each and every one of you, as well as the trips we made together. I also want to express my gratitude to Kiara Chau who helped me to sketch some of the nice figures presented in this manuscript.

Last but no least, I would like to thank the Deutsche Forschungsgemeinschaft (DFG, German Research Foundation) for their financial support during my doctoral studies (priority program SPP 1788 (CoSIP)-CH1482/3-1).

Contents

Chapter 1

Introduction

In this chapter

1.1 Motivation

The atmosphere is a highly dynamic region dominated by complex processes such as gravity waves, tides, planetary waves, turbulence, wave-wave linear interactions, non-linear interactions; covering different spatio-temporal scales [WH06]. Observation and characterization of these processes is quite challenging and, most of the time, it requires combined observations by multiple sensors, such as ground-based remote sensors, sounding rockets, and satellite observations [Hin+93; Kat+19; Che+20]. During the

last decades, an increasing interest to characterize the different atmospheric regions together with a huge technological progress have allowed the construction of modern in-situ and remote sensing instruments, and the development of outstanding techniques to observe and measure physical parameters of the atmosphere. However, despite this great progress, there is still an atmospheric region, the mesosphere and lower termosphere (MLT) region, which is still poorly sampled. The altitude of the MLT region, which extends from $50\,\mathrm{km}$ to $200\,\mathrm{km}$, limits its study since it is prohibitively expensive by in-situ instruments such as rockets and it is inaccessible for others such as balloons, aircrafts, drones or in-situ satellites. Only remote sensors, ground-based and satellites, are capable of making continuous measurements of the MLT region.

To fully characterize the MLT and to be able to separate and identify the contribution of its components at different spatio-temporal scales it is required 4D (space-time) measurements with good vertical and horizontal coverage and high spatio-temporal resolution. Recently, such kind of measurements have been proposed to study the MLT using multi-site lidars [Höf18] and multistatic radars [SC15; Vie+16; Ker+19].

Particularly with radars, a great effort has been done to obtain high resolution 4D measurements of the MLT region using high-power large aperture radars [Rap+11; Lat+12a; Sto+13; Som+13] and low-power multi-static meteor radars [SC15; Vie+16]. However, the achieved resolution and space coverage of the measurements have been limited by the radars' size.

In this dissertation, the capability of multiple–input multiple–output (MIMO) radar techniques and inverse problem approaches are analyzed to improve the spatio-temporal resolution and coverage of atmospheric observations, with a particular focus on the MLT region. A MIMO radar is a system employing multiple receivers and multiple transmitters in which each transmit element radiates an independent waveform from each of the multiple transmit antennas. Compared to traditional phased array radars, MIMO provides additional degrees of freedom thanks to the multiple independent transmit-receive links. These additional degrees of freedom lead to an improved angular resolution [BF03], a better antenna beam pattern [LS07], and a larger number of detected targets [Fis+06]. The primary objective of this work is the estimation of target parameters such as range, Doppler, angle of arrival (AOA), and angle of departure (AOD) in MIMO systems, which are required to estimate atmospheric physical parameters such

as wind velocities, momentum fluxes, electron density, electron temperature, and kinetic energy. Moreover, since the main requisite of MIMO systems is the independence of transmit signals, an emphasis is done on the waveform design, which plays a critical role in the MIMO radar performance.

Particularly, this work focus on the estimation of angle of arrival (AOA) and angle of departure (AOD) of atmospheric radar echoes and waveform design for MIMO radars with colocated antennas. Even though MIMO radars have been amply discussed in the past, most of the studies have been done from a theoretical point of view [LS07; XLS06; CV08a], in the context of hard targets [Mas+10; KD10; JLZ12; HL15; Mao+17; Tan+18], or considering punctual targets [GDP12; God+10; GHB09; GHB10; Gom14; Qin+17]. The present thesis analyses existing radar signal processing techniques for traditional atmospheric radars and extends the concept to MIMO radars considering hard and stochastic targets, which are not necessarily punctual. Additionally, this work studies the influence of sparse and limited sampling due to the reduced number of antennas available in a radar system, and thereby, it proposes a set of inverse problem techniques to reduce the undesired effects of distorted radiation patterns and improve the AOA estimation. Furthermore, the performance of the proposed techniques considering Gaussian-shaped targets are evaluated and compared through simulations. Finally, two practical implementations of MIMO are showed to study the mesosphere using distinct tracers: Polar mesospheric summer echoes (PMSE), and specular meteor trails. The results confirm the feasibility and benefits of MIMO for atmospheric applications.

In order to understand the current limitations of radar measurements and the complexity of atmospheric layers, the following sections briefly describe previous atmospheric observations and some of the complex processes we find in the MLT region.

1.2 Earth's atmosphere observations

The Earth's atmosphere is the layer of gases surrounding the planet that contains the air we breathe. These gases are retained around the planet by the Earth's gravity. Indeed, these gases play a critical role in protecting living beings on Earth by absorbing ultraviolet solar radiation, keeping the surface warm, and reducing extreme temperature changes from day to night. The Earth's atmosphere is a large and complex system

which is described in terms of five layers based on their vertical variations of temperature. The troposphere, the stratosphere, the mesosphere, the thermosphere, and the exosphere [UCA15]. Figure 1.1 shows a sketch of the first four layers, as well as some natural phenomena and instruments used to study the different layers.

The troposphere is the lowest layer of the atmosphere, and it has an extension of about $10\,\mathrm{km}$. The air temperature in this region is warmer close to the surface and gets colder as altitude increases. Next is the stratosphere, where absorption of ultraviolet solar radiation by ozone becomes essential, and the temperature starts to increase with altitude. For both layers, airplanes, balloons, and ground-based and satellite instruments can be used regularly to characterize their dynamics.

On top of the stratosphere, we find the mesosphere, which extends from $50\,\mathrm{km}$ to $85\,\mathrm{km}$ altitude. The upper mesosphere, called mesopause, is the coldest part of the Earth's atmosphere and interesting phenomena can be seen in this region, such as meteors, noctilucent clouds (NLC), polar mesospheric winter echoes (PMWE), and polar mesospheric summer echoes (PMSE). This layer is hard to study with in-situ instruments since airplanes and balloons cannot reach these altitudes, and satellites and space shuttles orbit at much higher altitudes. The only way to study the mesosphere is through ground and satellite remote sensors such as radars, lidars, and cameras.

Above the mesosphere is the thermosphere, which extends up to $1000\,\mathrm{km}$. In this region, the absorption of solar extreme ultraviolet (EUV) radiation causes the temperature to increase again. The thermosphere is the layer where auroras occur and satellites orbit. Lastly, we find the uppermost atmosphere's layer, the exosphere, which is not shown in Fig. 1.1. The exosphere separates the Earth's atmosphere from outer space. This region is mainly composed of extremely low densities of hydrogen and helium.

As stated before, this work focuses on the characterization of the MLT through ground-based radar measurements. In the MLT, the transport and exchange of energy occurs through complex processes. The main sources of the energy budget in this region are the sun as solar radiation and the troposphere through upward propagating atmospheric waves. Essentially, the MLT dynamic is dominated by atmospheric gravity wavess (AGWs) and turbulence processes covering different spatio-temporal scales [Vin15; Sto+18; Vie+19]. AGWs are generated in the troposphere by various processes such as flow over orography, wind shear, and convective processes. AGWs play an essential role in transporting

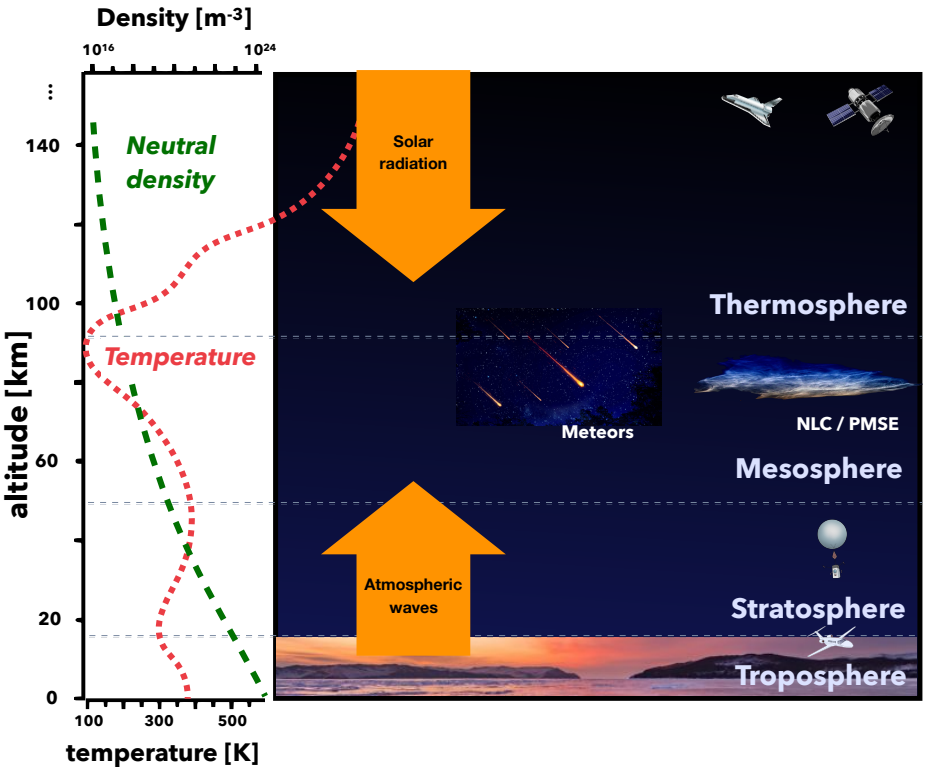

Figure 1.1: Layers of Earth's atmosphere (Exosphere is not shown). Typical neutral temperature and density profiles for daytime solar medium conditions are drawn in red and green, respectively. Sources of the energy budget in the mesosphere are the solar radiation and upward propagating atmospheric waves. Continuous in-situ measurements are available for all the layers except for the mesosphere.

energy and momentum from the troposphere to higher altitudes such as the mesosphere or some times even to the upper thermosphere. As the waves propagate upward, their amplitudes grow due to the vertical decreasing neutral density, becoming significant and unstable at upper heights [Yiğ+09]. At mesospheric altitudes, AGWs amplitude becomes so large that they break and deposit their momentum on the mean flow, which causes the mean zonal wind to change in intensity or even direction [Pla+15].

AGW effects cannot only be observed in the wind, but also in the neutral temperature, the neutral density, and the electron density [Lüb+87; Hoc85]. Multiple in-situ and remote instruments such as airplanes, balloons, rockets, satellites, cameras, lidars, and radars, have been used to characterize the atmospheric dynamics measuring the changes in those atmospheric parameters. Among all of them, only rockets can make high-resolution in-situ measurements of the mesosphere, but they are costly and rare. Another feasible option is to use remote sensors. Next, some studies of the MLT region through radar measurements are presented.

1.3 Radar measurements of the mesosphere and lower thermosphere (MLT) dynamics

In order to fully characterize the complex MLT dynamics it is desired to retrieve 3D resolved structures from remote radar observations for a broad range of spatio-temporal scales [SC15; Cha+19; Vie+19]. These scales are important for understanding the roles of atmospheric tides, gravity waves, and turbulences within the mesosphere [RL14]. Various radars and techniques have been used to measure spatio-temporal features of the mesosphere, such as medium frequency (MF) radars, mesosphere-stratosphere-troposphere (MST) radars, specular meteor radars (SMRs), and incoherent scatter radars (ISRs) in monostatic and multi-static configurations. Unfortunately, in most of cases, radar measurements are local or are limited in spatio-temporal resolution and coverage. Recently, multi-static specular meteor radars have been proposed to obtain 3D radar measurements from the mesosphere with a spatio-temporal resolution of $30\,\mathrm{km}$-$1\,\mathrm{h}$, so-called MMARIA [SC15; Vie+16]. Despite this great advance, the observed scales are not sufficient to characterize km-scales and mesoscale dynamics fully. Figure 1.2 shows a theoretical kinetic energy spectrum at mesospheric altitudes for vertical and horizontal scales,

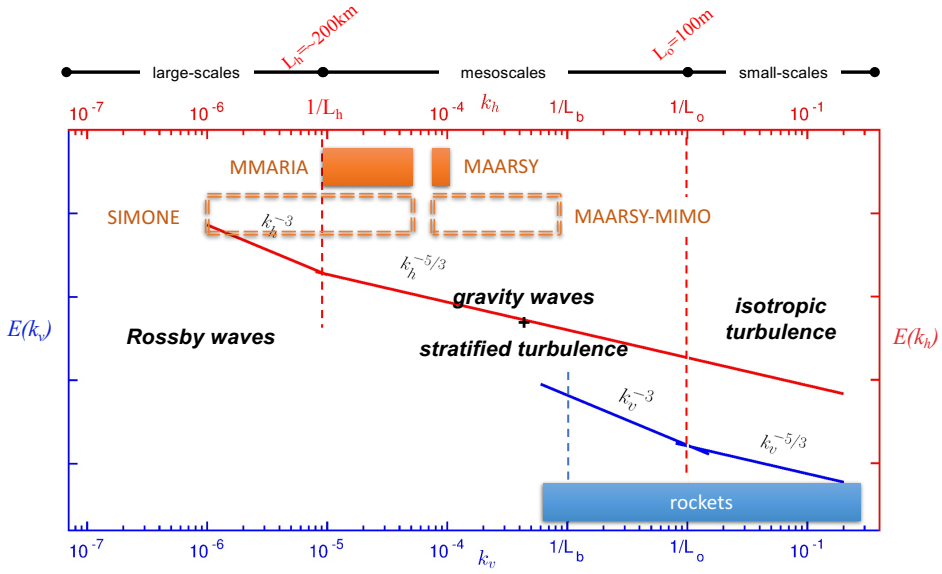

Figure 1.2: Simplified vertical and horizontal kinetic energy spectrum at mesospheric altitudes where regimes dominated by Rossby waves, gravity waves, and Kolmogorov turbulence are ideally well identified [Vie+19]. The X-axis represents the spatial frequency or so called wavenumber. A log-scale is used for representing the Y-axis but no units are shown intentionally. Vertical scales measured by rockets and horizontal scales measured by radars (MAARSY and MMARIA) are indicated with a blue and orange boxes, respectively. Proposed radar techniques based on MIMO (MAARSY-MIMO and SIMONe) to study smaller and larger scales are also indicated with a double dotted box.

where scales covered by standard instruments are indicated. Unquestionably, rockets are by far the best instruments to study the turbulence dynamic at vertical scales in the mesosphere. Unfortunately, they are costly, rare, and not continuous. On the other hand, horizontal scales observed by standard radars like MAARSY [Lat+12b] and MMARIA are restricted to 10 km–45 km and 60 km–300 km, respectively.

1.4 Objective of this work

The primary objective of this work is the improvement of standard radar techniques to observe and measure the MLT region over a wide range of temporal and horizontal scales. Moreover, two practical implementations are presented to measure horizontal

scales between $1\,\mathrm{km}$–$45\,\mathrm{km}$ and $30\,\mathrm{km}$–$1000\,\mathrm{km}$, which are associated to stratified turbulence and AGW dynamics, hereinafter referred to as kilometer-scales and mesoscales.

In radar systems with in-beam capabilities, three factors limit the observation of horizontal waves at multiple scales simultaneously. First of all, the radar antenna aperture, which limits the angular resolution achievable by the system, and hence, determines the smallest resolvable structure. The larger the aperture, the smaller the structure size can be resolved. Secondly, the volume illuminated by the radar beam, which conventionally defines the maximum resolvable spatial wavelength. And finally, the number of antennas which limits the number of distinguishable wave structures within the illuminated volume. The larger the number of structures, the larger the number of receive antennas required to estimate spatial dynamics with the same accuracy. Indeed, observations of horizontal dynamics at the MLT have been accomplished in the past using multi-beam experiments. However, the disadvantage of multi-beam experiments is their reduced time resolution and the poor spatial resolution compared with in-beam experiments.

This study proposes new radar techniques based on multiple–input multiple–output (MIMO) to extend the horizontal spatial scales measurable by a radar system. A MIMO system can be defined as a system with multiple-radiating antennas and multiple-receiving antennas. Since the 1990s, such kind of systems have been widely used in communications to improve the capacity and reliability of communication channels [Tel99; FG98; LT03]. Likewise, MIMO is being employed in the 5G cellular network technology and the IEEE 802.11n WiFi standard due to its excellent performance for interconnecting multiple users at high-speed data transmission.

Particularly in this work, MIMO techniques in two different configurations are used to enlarge virtually the antenna aperture, and to increase the number of transmit-receive links available in a multistatic-radar with emphasis on the investigation of narrowband MIMO radars for the observation of atmospheric targets. Although MIMO radars have been intensely studied in the literature, the existing techniques have been usually proposed and analyzed from a theoretical point of view or for hard targets. The objective of this thesis is to study new MIMO and waveform design techniques, and to develop signal processing algorithms to characterize the mesosphere at different spatio-temporal scales. The proposed techniques will be studied theoretically and experimentally, considering point-like and wide–sense stationary (WSS) targets.

Even though MIMO techniques help to increase the number of virtual antennas and to increase the number of transmit-receive links, we still have to face the signal recovery problem. Since ancient times, scientists have attempted to describe the world through observations, unfortunately, for many cases, direct observations are not possible due to diverse reasons such as limited technology, cost, or physical accessibility. When direct observations are not available, the effects of the parameters of interest might still be measured. For instance, when Newton proposed the concept of the Earth's gravitational field, he did not measure the gravity's acceleration directly, but he timed the falling of a free-fall object, demonstrating that the acceleration of an object in a free fall is independent of its mass. Currently, similar recovery problems when direct measurements are not available can be found in various disciplines such as Seismology, X-rays/Tomography, Optics, Astronomy, and remote sensing in general. In those cases, the problem can be formulated as:

$$\mathbf{y} = \mathbf{G}(\mathbf{x}) + \boldsymbol{\eta}, \tag{1.1}$$

where $\mathbf{x}$ is the parameter of interest or state vector, which cannot be measured directly. $\mathbf{y}$ are the measurable effects or the measurement vector. $\boldsymbol{\eta}$ is the noise associated with the measurements, and $\mathbf{G}$ is the theory that predicts the experimental outcomes $\mathbf{y}$. The problem of finding $\mathbf{x}$ from $\mathbf{G}$ and $\mathbf{y}$ is known as an inverse problem, which is the inverse of the forward problem defined as the problem of finding $\mathbf{y}$ from $\mathbf{G}$ and $\mathbf{x}$. Inverse problems are some of the most important mathematical problems in science because they provide us with parameters which cannot be observed directly. Unlike forward problems, which can be solved by applying (1.1) directly, inverse problems are more complicated and challenging to solve. In most of cases, observations are undersampled and the number of measurements in $\mathbf{y}$ is less than the number of unknowns in $\mathbf{x}$. These problems are known as underdetermined inverse problems. In this thesis, advanced signal recovery algorithms based on inverse problem techniques are used to recover the data of interest appropriately. These algorithms are described along with the thesis for each case individually.

1.5 Thesis structure

The thesis is organized as follows. In Chapter 2, the fundamental radar concepts for range, Doppler, and angle estimation are presented. In Chapter 3, the MIMO signal

model considering atmospheric targets is described. Moreover, various transmission diversity schemes are proposed to mitigate the cross-interference between transmitted signals. Although there are two kinds of MIMO configurations, coherent and non-coherent MIMO, this work focuses only on coherent MIMO. Non-coherent MIMO has been discussed amply in the context of multi-static radars, and it is typically used to increase spatial diversity by observing a target from different view angles. Whereas coherent MIMO is used to increase spatial diversity by observing a target from relatively the same viewing angle. In Chapter 4, the observation and characterization of kilometer-scale dynamics in the MLT region using MIMO radars is described. Moreover, based on the signal model described in Chapter 3, some guidelines to design MIMO antenna arrays are presented. Consecutively, various inversion methods for angle estimation are described, whose performances are evaluated by simulations. At the end of the chapter, experimental results are presented to analyze the real performance of the discussed algorithms. In Chapter 5, a novel meteor radar network based on MIMO with waveform diversity is described in terms of feasibility and performance. More importantly, a novel recovery technique based on compressed sensing is proposed and described to retrieve meteor signal echoes in radar networks, which otherwise are unrecoverable. Simulations are conducted to corroborate the recovery technique and to quantify the estimation error. Experimental results are also shown to corroborate the success of the proposal. Finally, a summary and main conclusions are presented.

Chapter 2

Atmospheric radars

In this chapter

2.1 Introduction

This work proposes advanced radar techniques and novel recovery algorithms to overcome the current limitations of atmospheric radars. To understand what these limitations are and how they can be overcome, the basic concepts of radars, the characteristics of atmospheric targets, and the radar signal processing are discussed in this chapter.

An elementary radar system consists of a radio frequency (RF) signal generator (oscillator), a transmitting antenna, a receiving antenna, and an signal-detecting device (receiver). When a RF signal is feed to the transmitting antenna, the antenna radiates energy in the form of electromagnetic (EM) waves. The EM wave travels through the free space until an object (radar target) intercepts some portion of the energy and re-radiates it in various directions. The receiving antenna collects the portion of energy re-radiated back in the radar direction and transforms it into an electric signal. The receiver detects and quantifies the electric signal whose information is processed to estimate the target's position and relative velocity. The target's position is determined by two parameters: the distance between the radar and the target known as range, and its angular position. Range information is determined by measuring the time taken for the EM wave to travel to the target and back and it can be written as

$$R = ct, \tag{2.1}$$

where R is the two-way range, t is the traveling time to the target and back, and c is the speed of the EM wave, which for free space is equal to the speed of light. In the special case of a monostatic radar in which transmitters and receivers are located at the same location, the distance between radar and target is half the two-way range

$$r = \frac{R}{2}. \tag{2.2}$$

On the other hand, radar target's position can be determined from the angle of arrival (AOA) of the reflected EM wave, which can be obtained by comparing the phase difference between signals received at two spatially separated antennas. Furthermore, if relative motion exists between target and radar, the target's radial velocity can be measured from the Doppler shift in the carrier frequency of the reflected EM wave.

In the following sections, basic concepts like the radar block diagram and radar scattering in the atmosphere are discussed, which will help us to understand the process of transmission and reception of EM waves in the atmosphere. Then, the signal processing to estimate Doppler velocity, range, and angle of arrival (AOA) is described in detail.

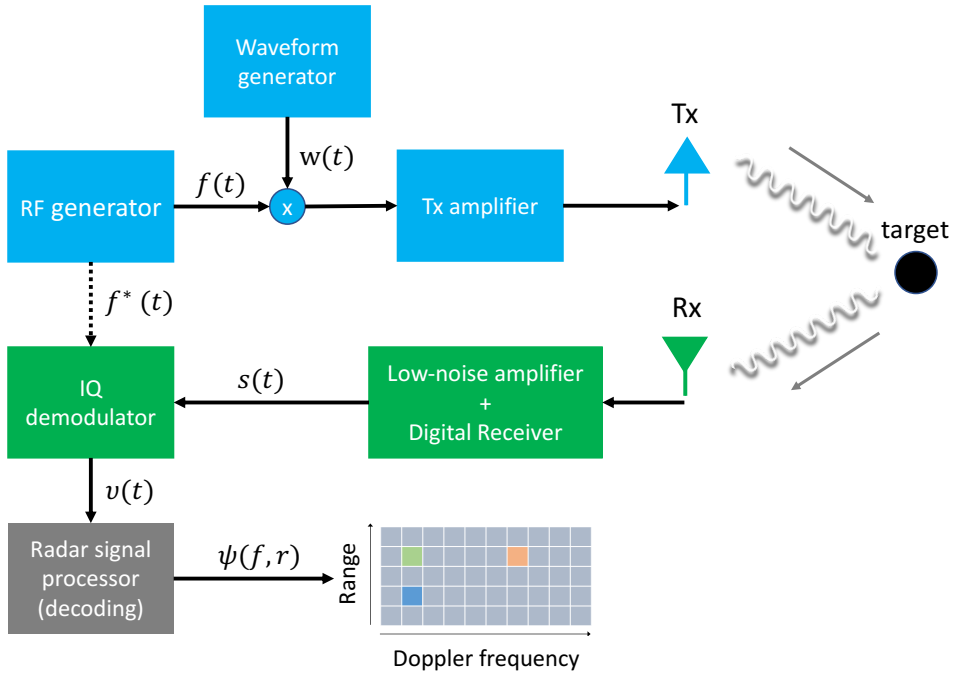

Figure 2.1: Radar block diagram. The black circle represents the radar target.

2.2 Radar block diagram

2.2.1 Radar components

Atmospheric radar systems work similarly as radars used to measure the car speed on a road. The main difference lies in the characteristics of the target. For atmospheric targets, a high transmit power is required and only a selected range of radar wavelengths can be used. Fig. 2.1 shows the main components of an atmospheric pulse radar. These components are classified into four groups: signal transmission, radar scattering, signal reception, and signal processing.

2.2.2 Signal transmission

The transmission starts with the generation of a continuous RF sine-wave, whose frequency determines the radar wavelength λ. Then, the RF signal is modulated by a waveform and radiated by the transmitting antenna. For VHF or UHF radars, the RF generation must be done with an oscillator with tens of mhz of precision.

In the most typical case, a monostatic pulsed radar, the waveform is a single pulse which is periodically repeated every T seconds, where T is so called the inter-pulse period (IPP). The IPP and the waveform bandwidth of a radar determine the range resolution Δr and the radar range r_{max} as

$$\Delta r = \frac{c}{2B}, \tag{2.3}$$

$$r_{max} = \frac{cT}{2}. \tag{2.4}$$

These two parameters are very important because they determine the minimum discernible size and the maximum unambiguous range, respectively. In a radar with a single pulse $B = 1/\tau$, where τ is the pulse-width (PW).

Moreover, the ratio between the PW and the PRI, known as the radar duty cycle, determines the transmit energy. Depending on the atmospheric target, the maximum range and range resolution required can vary between $100\,\mathrm{km}$ to $2000\,\mathrm{km}$ and $50\,\mathrm{m}$ to $1000\,\mathrm{m}$, respectively. To be able to detect such distant objects (targets), high transmit energies are required. High transmit energies can be achieved by using a long duty cycle with the same transmit power but at the expense of a poorer range resolution. In the literature, pulse coded techniques are discussed to increase the radar duty cycle (average transmit energy) but keeping the same range resolution. These techniques are explored with more detail in section 2.3.

Another important component of signal transmission is the transmitting antenna. Detection of small and distant objects requires large antennas with high gains. Typically, this is done building big antenna dishes such as the Arecibo incoherent scatter radar (Arecibo) [Alt98] or the European incoherent scatter scientific association (EISCAT) [FHW83] radar; but also can be done using large antenna arrays such as Jicamarca incoherent scatter radar (Jicamarca) [HCM13], middle atmosphere Alomar radar system (MAARSY) [Lat+12b], Pansy (Pansy) [Luc+06], and middle and up per atmosphere radar (MU) [Sat+14]. This work focuses on the study of antenna arrays and how to improve their performance through new configurations, namely, MIMO techniques, which are explained in chapter 3.

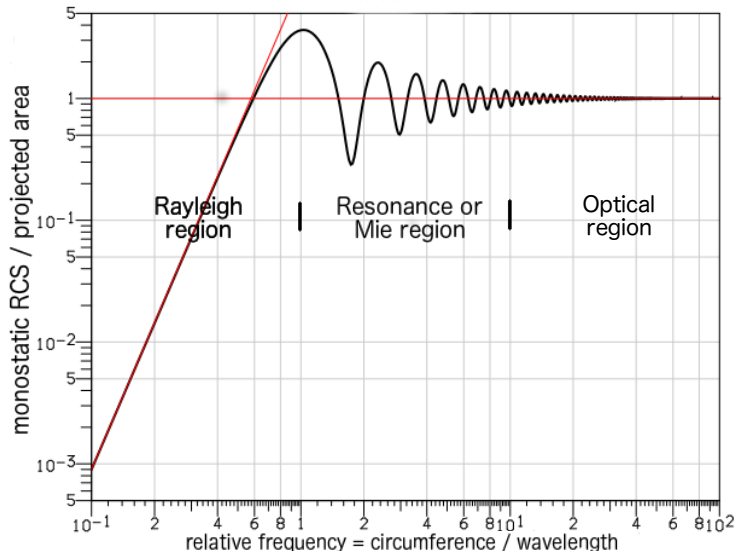

Figure 2.2: Radar cross–section of a perfectly conducting metal sphere as a function of the relative frequency. The x-axis represents the relative frequency, defined as the number of wavelengths in the circumference ($f_{rel} = 2\pi\alpha/\lambda$). The y-axis is the RCS relative to the projected area of the sphere ($\varrho/\pi\alpha^2$). [Adapted from Wikimedia Commons, the free media repository]

2.2.3 Radio wave scattering

When a traveling EM wave encounters a target (particle or molecule) in the atmosphere, some energy thereof is scattered. For that reason, radar targets are also known as scatters. Different from reflection, where a wave is only deflected in one direction, scattering is a phenomenon where radio waves such as light are deviated from a straight trajectory to one or more paths due to a change in the refractive index in the medium through which they travel. Changes in the refractive index are mainly due to the presence of particles, bubbles, droplets, or density fluctuations.

Considering only elastic scattering, where energy transfer is negligible, there are four different types of scattering depending on the relative target's size compared with the wavelength of radiation, as illustrated in Fig. 2.2: (a) Rayleigh, (b) Mie, and (c) non-selective scattering. Furthermore, for atmospheric observations, we have to include (d) Thomson scattering, that is the elastic scattering of electromagnetic radiation by free charged particles.

Firstly, **Rayleigh** scattering occurs when a EM radiation is scattered by a small spherical volume (molecule, particle, or atom) with a variant refractive index where the volume's radius α is much smaller than the wavelength of radiation ($\alpha << \lambda$). The larger the volume compared to the wavelength, the stronger the scattering. Rayleigh scattering is also known as selective scattering since certain particles are more effective at scattering a particular wavelength. Selective scattering by air particles is, for example, responsible for the blue sky we observe since shorter wavelengths (blue color) are stronger scattered than larger wavelengths (red color).

Secondly, **Mie scattering** arises when the target's size is comparable to the wavelength of radiation ($\lambda < \alpha < 10\lambda$). In this case, the scattering intensity slightly varies within the wavelength range. Unlike Rayleigh scattering, where the scattering has the same strength in all directions, Mie scattering is more efficient in the forward direction. Effects of Mie scattering can be observed by the naked eye in our daily life, since it causes the white appearance of cloud droplets. Droplets' sizes are large enough to scatter all visible light wavelengths with the same intensity and causes the white color.

Furthermore, when the target's size is much larger than the wavelength ($\alpha >> \lambda$), the scattering intensity is the same for any wavelength (**non-selective**). The main difference between Mie and non-selective scattering is the scattering intensity. While in the Mie's regime, the scattering intensity can vary from 0.4 to 4 times depending on the wavelength, in the non-selective's regime, the intensity stays constant for any wavelength.

In the case of atmospheric observations, the primary source of scattering are the free charged particles in the atmosphere, namely, free electrons and ions also known as plasma. Rayleigh scattering from charged particles is very weak due to their small sizes (much smaller than atoms or molecules). High radar frequencies would be required to get an appreciable scattering intensity from plasma in the Rayleigh regime. Unfortunately, radio waves with higher frequencies traveling through the atmosphere are more easily attenuated. Thus, they are not used for atmospheric observations.

A different kind of scattering which only applies for charged particles is **Thomson scattering**. It occurs when a EM wave hits a free charged particle, and the particle is accelerated, causing it to oscillate and emit radiation at the same frequency as the incident wave. In the atmosphere, plasma is comprised of electrons and ions. They both can be

used as targets. However, ion's scattering is weaker than electron's scattering because of its mass. Ions are heavier and are more difficult to accelerate. Therefore, electrons are commonly used as targets in the atmosphere [YP68].

Although the Thomson scattering intensity from electrons is higher than from ions, their cross-section is minimal. It is in the order of $6 \times 10^{-29}\,\mathrm{m}^2$. Only very large and high power radars like incoherent scatter radars (ISRs) [FHW83; Alt98; Woo+19] are capable to detect faint scattering from ionospheric plasma. This work uses data from much smaller and lower power radars, whereby Thomson scattering from plasma is not detectable. For low power systems, Thomson scattering from plasma is not detectable and a stronger mechanism which intensify the scattering of free electrons is required.

2.2.3.1 Coherent scattering

In the presence of multiple electrons and depending on how they are organized, the total scattering might be much stronger and easy to detect even by small radar systems. This process is known as coherent scattering and occurs when the reflected waves from multiple scatter interfere constructively, i.e., when all scatters act as one in the medium. Constructive interference enhances the total scattering amplitude and make the scatters visible by low power radar systems.

Typically, organization of free electrons in the atmosphere is randomize and they do not form coherent structures. Only in special cases, electrons are organized coherently. Two known kinds of scattering from coherent structures in the atmosphere are Fresnel and Bragg scattering.

Fresnel scattering takes place when particles, ions, or electrons are organized in a fine horizontal layer in the atmosphere containing sharp vertical gradients of refractivity [GBG81; Kir+10]. Vertical and horizontal extents of these layers are comparable to half the radar wavelength $\lambda/2$ and to the width of the first Fresnel zone $(z\lambda)^{0.5}$, respectively; where z is the altitude. One main feature of Fresnel scattering is that they are highly aspect sensitive, i.e., the scattering is more intense when looking vertically compared with off-vertical beams. The reason is that for off-vertical beams, the interference is not constructive anymore.

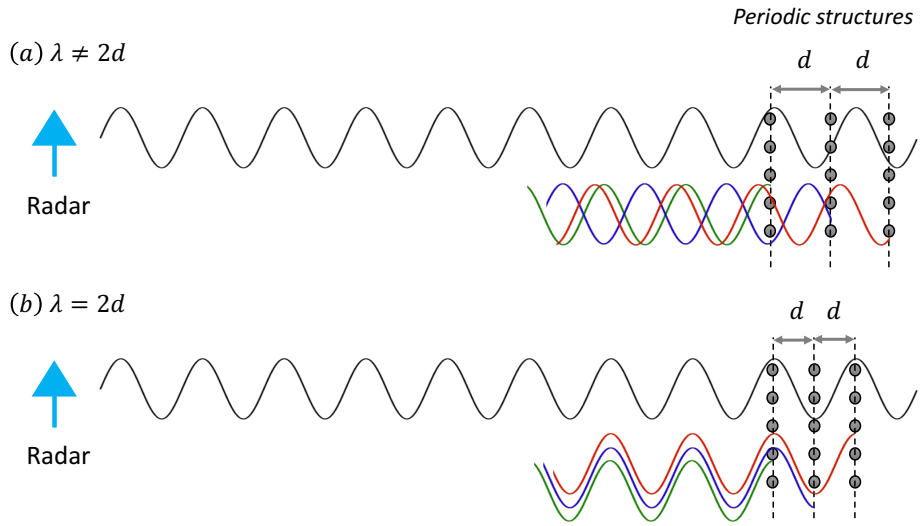

Figure 2.3: Bragg scattering from a periodic structure (a) destructive interference (b) constructive interference, for which the Bragg condition is fulfilled ($\lambda = 2d$).

Bragg scattering results from the constructive reflection of EM waves on periodic structures whose distances are in the order of half the radar wavelength, as illustrated in Fig. 2.3. Bragg scattering maximizes when the distance between structures is exactly half the radar wavelength and it decreases along with any difference between that distance and the radar wavelength. The effect of constructive or destructive interference is intensified by the cumulative reflection in successive structures (layers).

The Bragg's law describes the condition for constructive interference considering the incident angle to be at its strongest when

$$2d \sin\theta = n\lambda, \tag{2.5}$$

where n is a positive integer, d is the distance (separation) between periodic structures, λ is the radar wavelength, and θ is the incident angle of the EM wave respect to the layers.

The Bragg's law described above assumes a perfect crystal structure. Such assumption is not hold in the atmosphere. Instead, the atmosphere can be thought as a layer composed of distinct periodic structures of different distances. For which, the maximum scattering occurs due to the structure with distance equal to half of the radar wavelength ($d = \lambda/2$) for an incident angle of $\theta = 90°$.

Bragg scattering is the main reason why atmospheric radars work at frequency bands from 30 MHz to 600 MHz (radio wavelengths from 10 m to 0.5 m), namely, very high frequency (VHF) and ultra high frequency (UHF) bands. Detectable coherent structures in the atmosphere are mostly organized in meter-scales from 0.1 m to 5 m, which is equivalent to 0.2 m to 10 m radar wavelengths according to Eq. 2.5. Structures smaller than 0.2 m are not detectable since at those wavelengths the transmitted energy is easily attenuated in the atmosphere. On the other hand, radio wavelengths higher than 100 m to 120 m are reflected in the lower mesosphere and do not reach higher altitudes. Radio frequencies that are reflected in the E and F layer are also known as E-layer critical frequency (foE) and F2-layer critical frequency (foF2), respectively. They are typically measured by digisondes and continuous Doppler soundings in a daily basis [KC18].

2.2.3.2 Stochastic nature of atmospheric targets

The primary source of scattering in the atmosphere are the free electrons, which move at fast speeds and random directions. Assuming that the speed and direction of a free electron are measurable, the sampling rate of radar measurements are too slow compared to the electron's speed. Therefore, Doppler and RCS measurements from free electrons are considered as stochastic processes. For stochastic processes, only the statistical parameters matters. One single measurement do not provide any information. Single measurements of Doppler and RCS from free electrons are meaningless since they both depend on the electron's position and velocity at the measuring time. Therefore, multiple realizations are required to estimate the first and second statistical moment (mean and variance) of Doppler and RCS from free electrons.[FL92; FH05]. Even in the case of coherent structures, i.e., an organized cloud of electrons moving at a slow speed, its RCS is still stochastic in nature since the total scattering results from the sum of scattering from single electrons. In the following sections, the measured RCS of coherent structures formed by a cloud of electrons are considered as a stochastic process, whereas, their Doppler is not since most of these clouds move at relatively very slow speeds.

2.2.4 Radar measurements

The ultimate goal of atmospheric science is the understanding of the atmospheric dynamics and all processes within. To study and understand these processes is required to

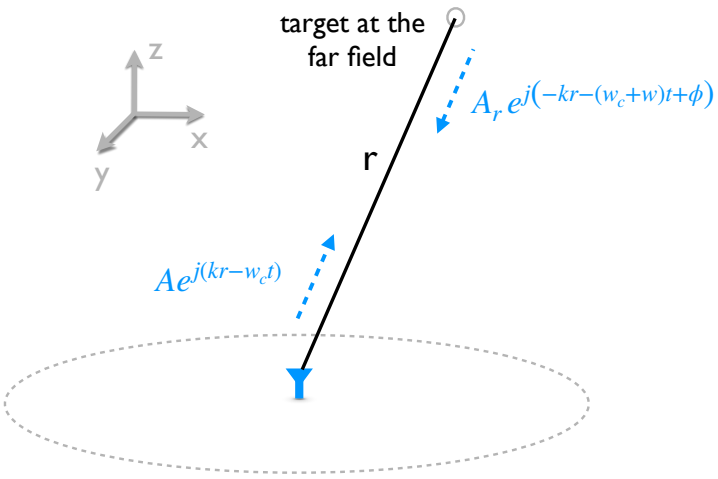

Figure 2.4: Propagating radar wave scattered in a target at the far field.

measure and quantify some atmospheric parameters such as air/electron temperature, air/electron density, air/electron velocity, kinetic energy, and momentum fluxes at different spatial and temporal scales [Hoc83; Hoc85]. Such parameters cannot be measured directly by radars, but instead, they can be inferred from the changes that an electromagnetic wave suffers when are scattered in the atmosphere. Depending on the physical parameter of interest, they can be inferred from changes in amplitude, frequency, or phase of the propagating radar wave.

2.2.4.1 RF signal

The propagation of radio waves is governed by Maxwell's equations. From these equations, one can derive the so-called free-space wave equation and obtain a solution of the form

$$f(t) = A\, e^{j(kr-\omega_c t)}, \tag{2.6}$$

where k is the wave number, r is the travelling distance, and $\omega_c = 2\pi f_c$ is the radar frequency. When a continuous propagating wave is reflected or scattered in a object at range $r = c\,t_r/2$, it suffers changes in amplitude, frequency, or phase that can be de-

noted as

$$s(t) = A_r\, e^{j(-kr-\omega_c(t-t_r)-\omega_r t+\phi_r)} \tag{2.7}$$

$$= A\, e^{-j\omega_c(t-t_r)}\, a_r\, e^{j(-kr-\omega_r t+\phi_r)} \tag{2.8}$$

$$= f(t-t_r)\, \sigma_r(t), \tag{2.9}$$

where $\sigma_r(t) = a_r\, e^{j(-kr-\omega_r t+\phi_r)}$ represents the scattering caused by the presence of a target at range gate r, $f(t-t_r) = A\, e^{-j\omega_c(t-t_r)}$ represents a delayed version of the carrier signal, and s(t) represents the signal at the receiving antenna in a monostatic radar as shown in Fig. 2.4.

There are three parameters in this wave solution that are commonly measured and used to characterize the radar target: (a) The amplitude a_r, which provides information about scattering properties and target's structure. (b) The Doppler frequency ω_r, which allows us to infer the target's velocity, and (c) the phase information ϕ_r, which is used to determine the angle of arrival (position).

Recovery of amplitude, frequency, and phase starts at the receiving antenna, where the EM radiation is transformed into a electric signal. Usually, the radar return is so weak that the signal requires some amplification using low-noise amplifiers, see Fig. 2.1. Then the signal is digitized by the receiver, whose amplitude and phase are proportional to the backscatter coefficient $\sigma_r(t)$.

Equation (2.9) is only valid for continuous wave (CW) radars in the presence of a single target. For a CW radar in the presence of multiple targets at different range gates, the received signal results from the range integral

$$s(t) = \int f(t-t_r)\, \sigma_r(t) \mathrm{d}r. \tag{2.10}$$

Notice that range information cannot be recovered from $s(t)$ since scatters from different ranges σ_r are all combined. Modern radars modulate the carrier signal using a pulse or a waveform $w(t)$ to be able to recover range information from multiple echos. Thus (2.10) becomes

$$s(t) = \int w(t-t_r) f(t-t_r)\, \sigma_r(t)\, \mathrm{d}r + \eta(t), \tag{2.11}$$

where $\mathrm{Re}\{s(t)\}$ is the received signal, and $\eta(t)$ is the receiving noise.

2.2.4.2 Baseband signal

To recover the signal of interest $\sigma_r(t)$ for each range gate from (2.11), we first need to shift the signal $\mathrm{Re}\{s(t)\}$ to baseband, i.e., we need to remove the carrier frequency $f(t)$. This process is known as IQ demodulation and it is done by multiplying the received signal by the conjugate of carrier signal, i.e., by $f^*(t) = e^{j\omega_c t}$

$$v(t) = \mathrm{Re}\{s(t)\} f^*(t). \tag{2.12}$$

This operation results in two components, one of low frequency (baseband) and one of high frequency. After applying a low pass filtering we keep only the low frequency signal which is

$$\begin{aligned} v_{LP}(t) &= \left\{ \int w(t-t_r)\, f(t-t_r)\, \sigma_r(t) \mathrm{d}r + \eta(t) \right\} f^*(t) && (2.13)\\ &= \int w(t-t_r)\, \sigma_r(t)\, f(t-t_r) f^*(t) \mathrm{d}r + \eta(t) f^*(t) && (2.14)\\ &= \int w(t-t_r)\, \sigma_r(t)\, e^{j\omega_c t_r}\, \mathrm{d}r + \tilde{\eta}(t). && (2.15) \end{aligned}$$

The signal in base-band $v_{LP}(t)$ is stored and used for further processing. The new noise term $\tilde{\eta}(t)$ keeps the same statistical characteristics of the measured one, and the term $e^{j\omega_c t_r}$ can be neglected or absorbed into the unknown phase of the scatter σ_r. Therefore, we get

$$v_{LP}(t) = \int w(t-t_r)\, \sigma_r(t)\, \mathrm{d}r + \tilde{\eta}(t). \tag{2.16}$$

The demodulation process, known as in-phase and in-quadrature (IQ) demodulation, is achieved in practice by multiplying the received signal by both a sine and a cosine and then applying a low pass filter to the results. For an adequate demodulation f and f^* must have the same frequency. This is not a problem when the transmitter and receiver are located at the same place since these both signals can be generated from the same source. However, for bistatic or multistatic configurations, the receiver and the transmitter are widely separated and some kind of synchronization between RF generators is required. For VHF and UHF radars, commercial GPS oscillators can be used to synchronize the generation of the carrier signal.

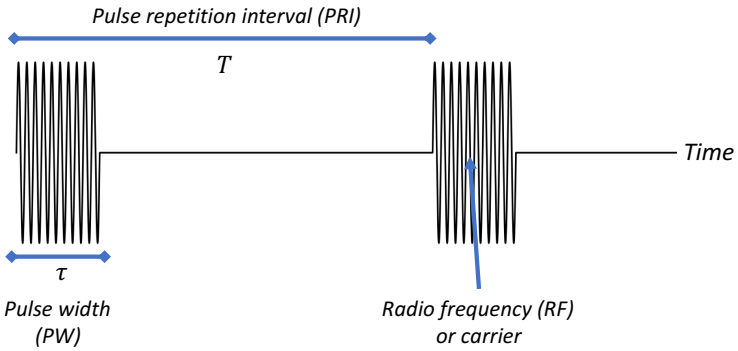

Figure 2.5: Typical radar pulse

2.2.4.3 Matched filter response

To get an estimate $\hat{\sigma_r}$ of the signal of interest σ_r, we still have to get rid of the waveform $w(t)$ from (2.16). Considering that the received signal is passed trough a filter which is matched to the transmitted waveform, the filter output tuned to delay t_r is

$$\hat{\sigma_r}(t_r) = \int_0^T v_{LP}(t)\; w^*(t - t_r)\, \mathrm{d}t \tag{2.17}$$

$$= \int_0^T \int w(t - t_\kappa)\, w^*(t - t_r)\, \sigma_\kappa(t)\, \mathrm{d}\kappa\, \mathrm{d}t + \hat{\eta}(t). \tag{2.18}$$

The output of a matched filter is represented by its range ambiguity function, which describes the interference caused by a target at a given range. The range ambiguity function is expressed as

$$C(t_r, t_\kappa) = \int_0^T w(t - t_\kappa)\, w^*(t - t_r)\mathrm{d}t \tag{2.19}$$

$$= \int_{t_r}^{T+t_r} w\big(t - (t_\kappa - t_r)\big)\, w^*(t)\mathrm{d}t. \tag{2.20}$$

The radar ambiguity function is an essential feature of a radar and it is usually used as a metric for waveform design. Its importance resides in that it determines the range resolution.

In the most simple case, the waveform is a single pulse with pulse width τ and amplitude $|w(t)| = 1$ for $t = [0, \tau]$ and 0 elsewhere, as illustrated in Fig. 2.5. In such cases, the

ambiguity function reduces to

$$C(t_r, t_\kappa) = \begin{cases} \left(1 - \frac{|t_r - t_\kappa|}{\tau}\right), & \text{if } |t_r - t_\kappa| < \tau \\ 0, & \text{elsewhere} \end{cases}. \tag{2.21}$$

Replacing (2.21) in (2.18) and replacing the range integral by a time integral (t_κ instead of κ) we get

$$\hat{\sigma_r}(t_r) = \int_{t_r-\tau}^{t_r+\tau} \left(1 - \frac{|t_r - t_\kappa|}{\tau}\right) \sigma_\kappa(t_\kappa - t_r)\, \mathrm{d}t_\kappa + \hat{\eta}(t_r) \tag{2.22}$$

$$= \int_{-\tau}^{\tau} \left(1 - \frac{|t_\kappa|}{\tau}\right) \sigma_\kappa(t_\kappa)\, \mathrm{d}t_\kappa + \hat{\eta}(t_r). \tag{2.23}$$

The estimate $\hat{\sigma}_r$ is a smooth version of σ_κ, where t_κ is approximately equal to t_r within the interval $[-\tau, \tau]$. This can be seen as the integral of the backscatter coefficients over the neighborhood around the range r.

Although the data can be digitized at a high rate, i.e., small t_r steps, the estimate $\hat{\sigma}_r$ will still be smoothed and limited in resolution by the pulse width τ. Typically, pulse radars are designed to have a sampling time equal to the pulse width ($t_s = \tau$), avoiding unnecessary oversampling. When the range resolution is limited, shorter pulses or pulse compression techniques can be used to overcome this problem.

2.2.5 Digital signal processing

Once the return signal $\sigma(t)_r$ is retrieved, we have to separate the range and Doppler information. Range information is obtained measuring the travel time of the pulse to the target and back, which is referred hereafter as the fast-time domain. On the other hand, when multiple samples over time have been collected from the same range, they can be grouped in a vector to estimate the Doppler frequency. The time separation between samples, in this case, is equal to the PRI and we refer to these samples as samples in the slow-time domain. In this section, we describe how to separate the range and Doppler information.

Let us consider the same pulsed radar as in the previous section, which is shown in Fig. 2.5. Data recording in the fast-time domain starts with the beginning of a radar pulse,

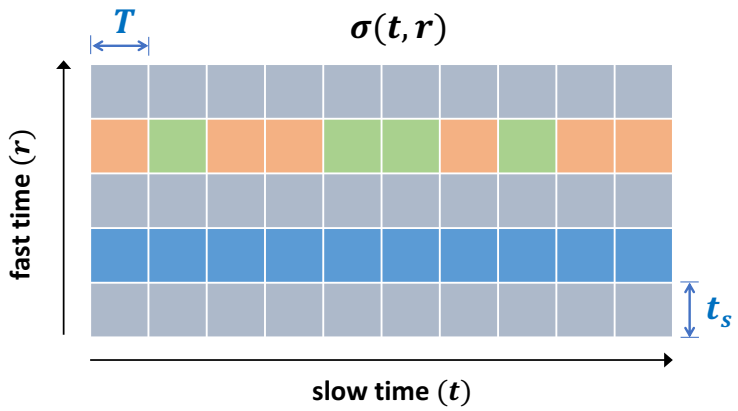

Figure 2.6: Radar samples organized in the fast and slow time domain. Notice that the fast-time and slow-time interval are equal to the receiver's sampling time t_s and the PRI T, respectively. Fast-time samples represent the range bins and t_s represents the range resolution. Three targets are shown, two (orange and green) coexisting at the same range and one (blue) alone.

and it is performed at a sampling rate of $f_s = 1/t_s$. The recording continues until the desired maximum unambiguous range $r_{max} = cT/2$. When the fast-time samples for a given pulse are completed, they are stored in a (column) vector whose elements represent the range bins or range samples. For every new pulse, a new (column) vector is stored and appended to the two-dimensional matrix illustrated in Fig. 2.6. The time between pulses is T, and the sampling frequency in the slow-time domain is $F_s = 1/T$, also called pulse-repetition frequency (PRF).

Using this matrix organization and considering only one target per range bin, like the blue target in Fig. 2.6, the smoothed radar reflectivity $\hat{\sigma}_r(t)$ can be represented in the discrete fast-time t_l and slow-time t_r domain as where $\hat{\sigma}(t_l, t_r)$ represents an element of the matrix shown in Fig. 2.6 with

$$\hat{\sigma}_r(t = l\,T + r\,t_s) = \hat{\sigma}(t_l, t_r) = a_r\; e^{j(-kr - \omega_r t_l + \phi_r)}. \tag{2.24}$$

If enough samples are collected along the slow-time domain the amplitude a_r, Doppler frequency ω_r, and phase ϕ_r can be recovered from (2.24).

When multiple targets coexist in the same range, like the orange and green target shown in Fig. 2.6, the number of Doppler frequencies is higher than one. For such cases, (2.24)

is represented as the superposition of multiples signals with Doppler frequency ω_i as

$$\hat{\sigma}(t_l, t_r) = \sum_i a_{i,r}\ e^{j(-kr-\omega_i t_l+\phi_{i,r})} \tag{2.25}$$

$$= \sum_i \psi(\omega_i, r)\, e^{-j\omega_i t_l}. \tag{2.26}$$

For practical reasons, in the following sections we use σ, t, and r to represent the estimated signal $\hat{\sigma}$, the slow-time domain t_l, the fast-time domain t_r; respectively. Thus, (2.26) becomes

$$\sigma(t, r) = \sum_i \psi(\omega_i, r)\ e^{-j\omega_i t}. \tag{2.27}$$

The signal $\psi(\omega_i, r) = a_{i,r}\ e^{j(-kr+\phi_{i,r})}$ contains information about the amplitude and phase of the reflected signal per frequency bin ω_i and range gate r. Notice that $\sigma(t, r)$ and $\psi(\omega, r)$ form a Fourier transform pair and Doppler information might be recovered applying the inverse Fourier transform to the signal $\sigma(t, r)$. In the following section, signal processing techniques are described to recover range, Doppler, and angle information from radar measurements.

2.3 Range estimation

In section 2.2.4.3 a simple technique to recover range information of radars transmitting a single pulse was described. In this section, the concept is extended to a more general waveform.

Ideally, we would like to detect very distant radar targets with a high range resolution. To reach distant targets, a pulsed radar requires to radiate a high energy E, where $E = \tau P_t$, τ is the pulse width, and P_t is the transmit power. Likewise, to achieve a high range resolution, the pulse bandwidth also must be high, where $\Delta r = c/(2B_\tau)$, B_τ is the bandwidth, and c is the speed of light. In a radar transmitting a single pulse they both depend on the pulse width and therefore, the transmitted energy and the range resolution are inversely proportional to each other. To attain a high E and a small Δr, pulse radars should be able to generate a high transmit peak power in a short of time, i.e., high peak powers P_t and short pulse width τ. Although this can be achieved with current technologies, it

is expensive and difficult to do in practice. To overcome this problem, long pulses with high bandwidths are employed instead of short single pulses. When long pulses with high bandwidths are used, the information is later recovered employing pulse compression techniques.

2.3.1 Pulse compression

Pulse compression is a technique used to attain a high transmitting energies enlarging the pulse width but without losing range resolution. In order to radiate more energy with the same peak power, the pulse width must be longer. For single pulse radars, the longer the pulse, the smaller its bandwidth and hence a poorer range resolution. To keep the same range resolution as the one obtained with a short pulses, the bandwidth of the long pulse must be enlarged. The process of increasing the bandwidth of a pulse is known as modulation. Modulation of a pulse can be done in amplitude, frequency, or phase and they can be used indistinctly for most of the cases.

Pulse compression techniques are eployed to recover the radar signal echos from modulated transmitted signal. To understand this concept recall the discrete version of (2.16), where the measured complex signal v is equal to the convolution of the envelope w and the target backscatter coefficient σ

$$v(t,\kappa) = \sum_{i=0}^{n-1} w(\kappa - r_i)\,\sigma(t,r_i) + \tilde{\eta}(t,\kappa). \tag{2.28}$$

Note that the envelope value depends on only the range index since it is a periodic function with period T. In the most simple case, a radar with a single pulse, the envelope is a rectangular pulse of width τ. However, in practice, the envelope can take any shape such as Gaussian, triangular, rectangular, or even a random shape. Changes of w in amplitude are known as amplitude modulation, which has been used in communications for a long time. For atmospheric radars, amplitude modulation is not recommended for two main reasons. Firstly, amplifiers are not totally linear it the whole range. Non-linearities might introduce errors in the process which are difficult to identify and correct. Secondly, the objective of pulse compression techniques is to maximize the transmitted energy. So it is better to keep the envelope's amplitude at its maximum and do not play with it.

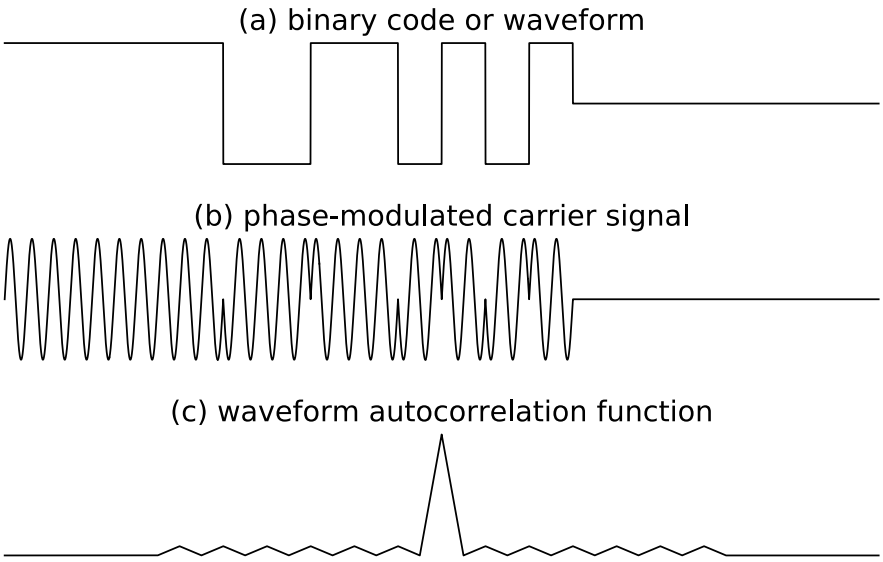

Figure 2.7: Pulse coded signal (a) waveform or code, (b) phase-modulated RF signal, and (c) autocorrelation function of the waveform

Others modulation techniques that are extensively used in communication and radars are frequency and phase modulation. Due to the nature of radar targets, the usable frequency bandwidth is limited and frequency modulation is not commonly employed. The limited spectrum can be better used employing phase modulation. This work primarily focuses on pulse compression by phase modulation, also known as spread-spectrum. Spread-spectrum is done by dividing a pulse of length L in N time slots of duration L/N, where the phase of the envelope at each slot can take any value between $-\pi$ to π. By doing this, the pulse bandwidth increases N times, from $B_L = 1/L$ to $\tilde{B}_L = N/L$. Likewise, the range resolution increases by N. To maximize the pulse energy, the amplitude of the envelope is kept at its maximum $|w(r) = 1|$ when the radar is transmitting and 0 elsewhere.

Waveform with rectangular shapes are quite used in many applications, although they are undesirable since their Fourier harmonics might affect other systems at nearby frequencies. Typically, rectangular pulses are Gaussian filtered to mitigate the harmonics and minimize undesired effects. Despite these considerations, we describe the envelope as a rectangular pulse divided into sub-pulses since they are more simple to describe mathematically. An example is illustrated in Fig. 2.7(a). In this case, the envelope can take only a binary phase coding, 0 and π.

2.3.1.1 Signal decoding

If the envelope, also known as the waveform, is more complex than a single pulse, an additional step is needed to get an estimate $\hat{\sigma}(t,r)$ of $\sigma(t,r)$ from (2.28). The process of recovering $\hat{\sigma}(t,r)$ is also known as decoding. One of the most known and simple decoding techniques is the matched filter estimator (MFE) defined as the cross-correlation between the transmitted waveform and the received signal

$$\hat{\sigma}(t,r) = \sum_{j=0}^{n-1} \upsilon(t,\kappa_j) w^*(\kappa_j - r) \tag{2.29}$$

$$= \sum_{j=0}^{n-1}\sum_{i=0}^{n-1} w(\kappa_j - \kappa_i)\, \sigma(t,\kappa_i)\, w^*(\kappa_j - r) + \hat{\eta}(t,r) \tag{2.30}$$

$$= \sum_{i=0}^{n-1} C(r,\kappa_i)\, \sigma(t,\kappa_i) + \hat{\eta}(t,r), \tag{2.31}$$

where $C(r,\kappa_i) = \sum_{j=0}^{n-1} w(\kappa_j - \kappa_i)\, w^*(\kappa_j - r)$ is the range ambiguity function. If the waveform $w(r)$ has ideal auto-correlation properties such that the range ambiguity function is equal to the Dirac delta function δ, then (2.31) reduces to

$$\hat{\sigma}(t,r) = \sum_{i=0}^{n-1} \delta(\kappa_i - r)\sigma(t,\kappa_i) + \hat{\eta}(t,r) \tag{2.32}$$

$$= \sigma(t,r) + \hat{\eta}(t,r), \tag{2.33}$$

where the estimate $\hat{\sigma}(t,r)$ is a good estimate of $\sigma(t,r)$. The resolution got with (2.33) is the same as the one got with a short pulse but with the advantage of a higher transmitted energy. The problem lies in that there are no waveforms with such a perfect range ambiguity function.

In the literature, some waveforms with good auto-correlation properties are proposed, such as Frank codes, Costas codes, Pseudo-random codes, and Barker codes. Figure 2.7(a) and (c) show an example of a Barker code and its autocorrelation function, respectively; where each symbol represents a different phase of the carrier signal. The auto-correlation function of Barker codes looks like a triangular function with some sidelobes, which different from the desired Dirac delta function.

In general, the goodness of the range ambiguity function is limited by two factors, (a) the number of waveform symbols and (b) the number of time slots N. The symbols are the

possible values a waveform can take in a time slot. In the case of Barker codes, the available symbols are $+1$ and -1. Previous studies have proved that the larger the number of symbols available, the better the range ambiguity function [LK81, e.g.]. Nevertheless, systems with many symbols are more difficult to implement. Therefore, most of the applications prefer to use binary codes to keep a simple system.

Furthermore, for codes with good properties, the longer the waveform, the closer the auto-correlation to the Dirac delta function is. To obtain a long waveform, we require to increase the number of code bits, which can me done (a) reducing the time duration of the code bit, or (b) increasing the total wavform length. The duration of the time slot is limited by the effective sampling time, and it might be difficult to change it in real systems. On the other hand, when there is no limitation on the waveform length, it can be increased up to it maximum, i.e., a continuous wave radar.

2.3.2 Phase-coded continuous wave radar

Unlike pulsed radar systems, continuous wave (CW) radar systems transmit EM radiation at all times, maximizing the amount of radiated energy. Conventional CW radar cannot measure range because there is no basis for the measurement of the time delay since the energy is transmitted continuously. However, when a CW radar is modulated as done in pulse compression, estimation of range information is possible using similar processing techniques such as matched filter estimator (MFE).

CW signals can be modulated in amplitude, frequency, or phase. Nevertheless, radar returns from atmospheric targets are weak and highly dependent on the carrier frequency. Typical radars do not use amplitude and frequency modulations since amplitude modulation requires to vary the amplitude of the transmitted signals, which is not desired if we want to maximize the radiated energy, i.e., to use the maximum amplitude available. and frequency bands are limited to a few MHz.

Although the application of frequency-modulated continuous wave (FMCW) is not feasible and recommended for atmospheric applications since it requires a high bandwidth,

and its maximum unambiguous range is small compared to what is required for atmospheric observations [Poo85; Sto92; MHL07], variations of frequency modulation techniques using a couple of different frequencies have been applied before in pulsed radars to improve the range resolution of atmospheric radars [PYC99; Che+16]. These techniques are also known as frequency domain interferometry (FDI) or range imaging (RIM). Application of FDI is possible because it transmits two or more pulses whose frequencies are separated less than a few MHz in order to ensure they sense the same target. A variant of frequency domain interferometry (FDI) can be applied in CW radars, however, it requires hardware with multi-frequency capability. Here we describe only CW radars modulated in phase due to their simplicity.

Phase-modulated CW systems, also called phase-coded CW systems, are a generic version of pulse compression, where the waveform $w(t)$ can take any value. Recall (2.28), where the measured signal at a given receiver results from the convolution of the waveform and the backscatter coefficient

$$v(t,\kappa) = \sum_{i=0}^{n-1} w(\kappa - \kappa_i)\, \sigma(t,\kappa_i) + \tilde{\eta}(t,\kappa). \tag{2.34}$$

For radars with a single pulse, most of the values of $w(r)$ are zero and simple techniques like MFE are suitable since the resulting ambiguity function has few and small sidelobes. Moreover, the presence of several targets at different ranges does not affect the performance of the system. However, for long pulses or continuous waves, the presence of multiple targets might enhanced the sidelobes of adjacent ranges. For those cases, the MFE technique is not efficient to recover radar returns since MFE maximizes the signal-to-noise ratio (SNR) but also the sidelobes. Thus, a more efficient approach is required to decode CW radar returns where range sidelobes are minimized.

Let's rewrite (2.34) for a given time delay t in matrix form

$$\boldsymbol{v} = \mathbf{W}\, \boldsymbol{\sigma} + \tilde{\boldsymbol{\eta}}, \tag{2.35}$$

where $\boldsymbol{\sigma} \in \mathbb{C}^R$ is the unknown vector which comprises the back-scattered reflectivity for all the range gates, $\boldsymbol{v} \in \mathbb{C}^L$ is the vector measurement, L is the waveform length which must be larger than the number of range gates, i.e., $L \geq R$, and $\mathbf{W} \in \mathbb{C}^{LxR}$ is a

circulant matrix specified by the waveform $w(r)$.

$$\mathbf{W} = \begin{bmatrix} w_0 & w_{L-1} & w_{L-2} & \dots & w_{L-R+1} \\ w_1 & w_0 & w_{L-1} & \dots & w_{L-R+2} \\ w_2 & w_1 & w_0 & \dots & w_{L-R+3} \\ \vdots & \vdots & \vdots & \ddots & \vdots \\ w_{L-1} & w_{L-2} & w_{L-3} & \dots & w_{L-R} \end{bmatrix}. \tag{2.36}$$

There are a couple of ways to solve (2.35). We can use the MFE used in pulsed radars which in matrix form is expressed as

$$\hat{\boldsymbol{\sigma}} = \mathbf{W}^H \mathbf{W}\, \boldsymbol{\sigma} + \tilde{\boldsymbol{\eta}}. \tag{2.37}$$

The problem of MFE is that its solution might contain a lot of artifacts since $\mathbf{W}^H\mathbf{W} \neq \mathbf{I}$. Another alternative applied to CW meteor radars was proposed by Vierinen et.al. [Vie+16] based on least squares estimation (LSE), which is expressed as

$$\hat{\boldsymbol{\sigma}} = \mathbf{W}^H \mathbf{W}\, \boldsymbol{\sigma} + \tilde{\boldsymbol{\eta}}, \tag{2.38}$$

with

$$\mathbf{W}^H = (\mathbf{W}^H\mathbf{W})^{-1}\mathbf{W}^H. \tag{2.39}$$

The advantage of LSE compared to MFE is that range sidelobes are cancelled. Nevertheless, the noise floor is enhanced. By using LSE, we expect to loose the weak radar echoes which might be confused with the noise because of the reduced SNR. Depending on the characteristic of the target, modern algorithms can be used to recover the signal of interest and to even recover the very weak echoes. Some of them are based on compressed sensing as described in Chapter 5.

2.3.2.1 Waveform design

Coding techniques used for pulsed radars are employed in CW radars as well, such as Frank codes, Costas codes, Pseudo-random codes, and Gold codes. The selection of one of them when only one transmitter is used is not a problem. However, it becomes a problem when the number of transmitters is high given that it is difficult to guarantee low cross-correlation between multiple codes.

Vierinen et.al. [Vie+16] describe a simple waveform design based on pseudo-random sequences. As known, pseudo-random sequences have good auto-correlation and cross-correlation properties. The basic idea is to generate a pseudo-random binary code sequence of length L, where each bit represents a different phase. To improve the range ambiguity function of the codes, we can select a random code i with a specific length which minimizes the mutual coherence property

$$\mu = \arg\min_{i} |\mathbf{W_i}^H \mathbf{W_i} - \mathbf{I}|. \tag{2.40}$$

This equation selects the waveform with the smallest sidelobes (off-diagonal elements). When the mutual coherence is normalized, it is bounded by [Wel74]

$$1 \geq \mu \geq \sqrt{\frac{L-R}{R(L-1)}}. \tag{2.41}$$

The lower bound, in particular, is useful for grading the designed waveform. The search of $\mathbf{W_i}$ can be done by brute force or can be adjusted based on target and clutter statistics [Fri07]. More complex codes, as poly-phase codes, have better cross-correlation properties. However, systems using binary codes are much simpler to manufacture, operate, and maintain.

2.3.2.2 Advantages

The main advantage of CW radars is that they operate at low transmit power since the energy is radiated continuously. Low power transmitters are cheaper to manufacture and simpler to operate. Moreover, for long waveforms, CW radars compared to pulsed radars have the advantage that range and Doppler aliasing can be selected after performing the measurements, i.e., in the post-processing stage. Furthermore, CW radars using orthogonal codes allow to operate multiple geographically separated transmitters operating at the same frequency.

2.3.2.3 Disadvantages

On the negative side, CW radars require the transmitting antenna and the receiving antenna to be separated. CW radars cannot use the same antenna for both transmission

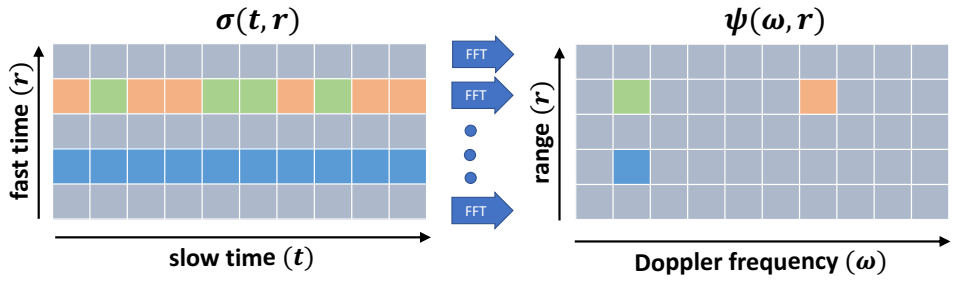

Figure 2.8: Doppler processing by taking the DFT of the slow-time data from a range bin. Targets coexisting at the same range (green and orange) can be separated perfectly in the Doppler domain [adapted from Christos Ilioudis, University of Strathclyde].

and reception as pulsed radar does. The problem lies in that the transmitting antenna is continuously radiating a signal, saturating the receiving system, and thus, reducing the receiver's dynamic range. Depending on the power, the transmitting and receiving antenna must be separated by a significant distance.

Signal processing of CW radar measurements require more computational power than pulsed radars'. Depending on the desired Nyquist frequency, dedicated hardware might be required to decode the radar data. Nevertheless, for typical Nyquist frequencies (a few kHz) a standard PC is more than enough.

2.4 Doppler estimation

The Doppler effect is a phenomenon observed when a radio wave is reflected by a moving target. The motion of the target causes a (Doppler) frequency shift in the reflected wave. Doppler shift has been used to estimate the velocity of moving targets since the 1940s [Mal47; Bar49; Ber57]. In the presence of a moving target with a radial velocity of v_r, the shift frequency f_d due to the Doppler phenomenon in a monostatic radar is

$$f_d = \frac{2\,\mathrm{v}_r}{c} f_c, \tag{2.42}$$

where f_c is the carrier frequency and c the speed of light. Positive Doppler shifts ($f_d > 0$) indicate that the target is moving towards the radar, whereas negative Doppler ($f_d <$

0) away from it. We have to clarify that v_r is the relative velocity of the target in the direction to the radar, i.e., v_r is only a projection of the true target velocity $\mathbf{v}$ into the radial direction. If θ is the angle between the incident wave and the vector $\mathbf{v}$, then

$$f_d = \frac{2\,|\mathbf{v}|\cos\theta}{c} f_c. \tag{2.43}$$

This equation tells us that to estimate the 3D vector-velocity $\mathbf{v}$, we need at least three radar Doppler measurements from three different viewing angles. Such kind of measurements are not possible using only a monostatic radar. Since the estimation of the vector velocity is essential for the understanding of the atmospheric dynamics, new multistatic radars have been proposed recently to measure the 3D vector $\mathbf{v}$ unambiguously in the MLT. We show an example of this in chapter 5.

Knowing that the velocity of a target and its Doppler frequency are directly related, we can focus on the recovery of the target's Doppler frequency and then transform it to velocity. An easy way to estimate the Doppler frequency from (2.27) is to apply the 1D inverse discrete Fourier transform (IDFT) to the signal $\sigma(t, r)$.

$$\psi(w, r) = \sum_{i}^{n-1} \sigma(t_i, r)\; e^{jwt_i}, \tag{2.44}$$

where each value of $\psi(\omega, r)$ represents the magnitude and phase of one element of the Doppler-range map from Fig. 2.8. Notice that the IDFT is applied only to the slow-time domain t. The range of frequencies and the frequency resolution are determined by the sampling time (T) and the selected number of samples n in the slow-time. For a given T and n, the resulting frequency resolution $\Delta\omega$, and the maximum frequency ω_{max} are determine by

$$\Delta\omega = \frac{2\pi}{nT}, \tag{2.45}$$

$$\omega_{\text{max}} = \frac{2\pi}{2T}, \text{ and} \tag{2.46}$$

$$\omega = \Big[-\frac{n}{2}\Delta\omega, ..., \frac{n-1}{2}\Delta\omega\Big]. \tag{2.47}$$

The larger the number of samples in the slow-time domain n, the closer the frequency ω to the real target's frequency. The value of n is determined by the radar setup and depends on the characteristics of the target. Mainly, n is limited by the duration of the target within the illuminated beam and by the target's correlation time. Typical correlation times in the atmosphere go from hundred of ms to few seconds.

Another parameter to consider is the maximum frequency ω_{max}. When the target's frequency is smaller than ω_{max}, it can be estimated without ambiguity. For that reason, ω_{max} is also known as the maximum unambiguous Doppler frequency or Nyquist frequency. To increase the Nyquist frequency, T can be reduced. However, this will also reduce the maximum unambiguous range $r_{max} = cT/2$. The selection of T is a compromise between the desired maximum unambiguous range r_{max} and the maximum unambiguous frequency ω_{max}, and must be carefully selected since

$$\omega_{\text{max}} = \frac{\pi c}{2r_{max}}. \tag{2.48}$$

2.5 Angle of arrival estimation

Until this point, we have briefly described how to estimate the target's cross-section, range information, and Doppler frequency from radar measurements. As explained above, these parameters can be inferred from measurements with only one single antenna. However, when the target's location is desired, it must be inferred from not just one, but several antennas spatially separated, which is known as antenna array. In fact, the target's location is determined by two factors: the range and angle of arrival. Whereas range information is estimated by measuring the time a wave travels to the target and back, angle of arrival is estimated exploiting the interference between waves transmitted or received at different spatially separated antennas. Constructive or destructive interference cause that the radiated energy can be focused in the desired direction or reduced in other directions. We discuss two radar techniques in the following sections which use the wave interference principle to estimate angle of arrival.

2.5.1 Phased array antennas and digital beamforming

Typically, single antennas have a wide antenna beam pattern since they radiate energy in multiple directions. However, when a set of antennas is connected to the same feeding system, the EM wave radiation can be focused in a single direction. This is known as beam steering, and it is done by employing multiple antennas spatially separated where each of them transmit a EM wave with a different phase shift depending on the desired

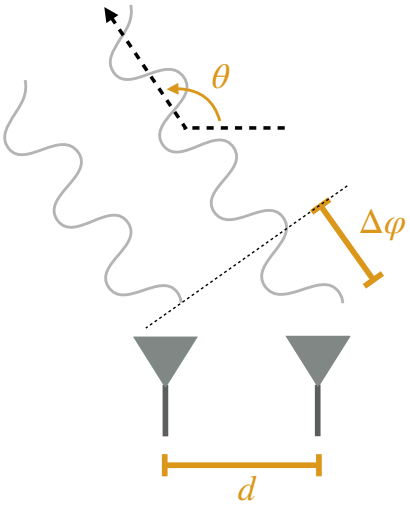

Figure 2.9: Phased antenna array. Constructive interference of two (or more) radiating sources focus the energy in the direction θ. Notice that the direction θ depends on the separation of the antennas d and the phase difference $\Delta\phi$

direction. The principle of a phased array is based on the wave interference effect as illustrated in Fig. 2.9. A phase-dependent superposition of two or several waves amplify or cancel each other in a given direction. In-phase signals amplify each other, and counter-phase signals cancel each other out. So if two radiated signals have the same phase at a given position a superposition is achieved, and the resulting signal is amplified in that direction and attenuated in other directions.

The phase shift for every antenna element can be regulated electronically, and thus, the direction of radiation. Theoretically, the resulting gain in any direction should be constant. However, in practice, the effectiveness of an antenna array is maximized in the direction perpendicular to the antenna field, while extreme tilting degrades the antenna performance due to antenna coupling.

The relative phase shift required to steer the beam in a desired direction θ is determined by the distance d between the antenna element and the reference point:

$$\Delta\varphi = \frac{2\pi}{\lambda} d \cos\theta. \tag{2.49}$$

There are two kind of phased arrays: (a) the passive phased array, and (b) the active electronically scanned array. In a passive phased array, all the antennas are connected to

a single transmitter or receiver, where the phase shift of each antenna element cannot be changed. Even though there are still some radars such as Jicamarca [Woo+19] that use passive arrays, they are not the most common nowadays. On the other hand, in active phased arrays, each antenna element has a phase-regulating module, which creates the phase-shifting required to steer the antenna beam electronically. Active arrays are a more advanced phased-array technology which has become most common nowadays. In this second category we can find modern radars such MAARSY [Lat+12b] or even fully digitized radio receivers such KAIRA [McK+15].

In order to achieve very narrow antenna beam patterns with small side lobes, radars require many antennas. For example, the Jicamarca radar [Woo+19] requires more than 19000 dipoles to form an antenna beam with half-power beam width (HPBW) of 1°. Similarly, the MAARSY radar [Lat+12b] with 433 Yagi antennas is able to form a beam with HPBW of 3.6°. Not all the radars have such an amount of antennas. When only a few antennas are available and assuming a small number of targets, techniques such as digital beamforming or radar imaging can be employed to improve the angular resolution or to reduce the sidelobe's gain.

The process of steering the antenna beam is also called beamforming. Beamforming can be applied either on transmission or reception. Phased arrays on transmission are capable of steering the transmitted energy toward the desired direction by radiating delayed versions of a single waveform. On reception, the receiving beam can also be steered in a given direction to maximize the received signal-to-noise ratio (SNR). Beam steering or beamforming can be done in two ways (a) analog beamforming, via the use of phase shifters in the transmitting or receiving side, or (b) digital beamforming, via adaptive processing of previously recorded data at each receiving antenna element. On reception, signals at each receiving antenna are stored independently for further signal processing. However, on transmission radar returns associated to different transmitting antennas can not be decoupled on the receiving side since all the transmitting antennas radiated the same signal.

Compared to analog beamforming, DBF has the advantage that digital data streams can be combined to steer the beam in many directions at once [KV96; VB88]. This is done by combining the receiving signals with appropriate phase shifts in a way that signals coming from a particular direction experience constructive interference while other directions destructive. The phase shifts are modified accordingly in software to cover all

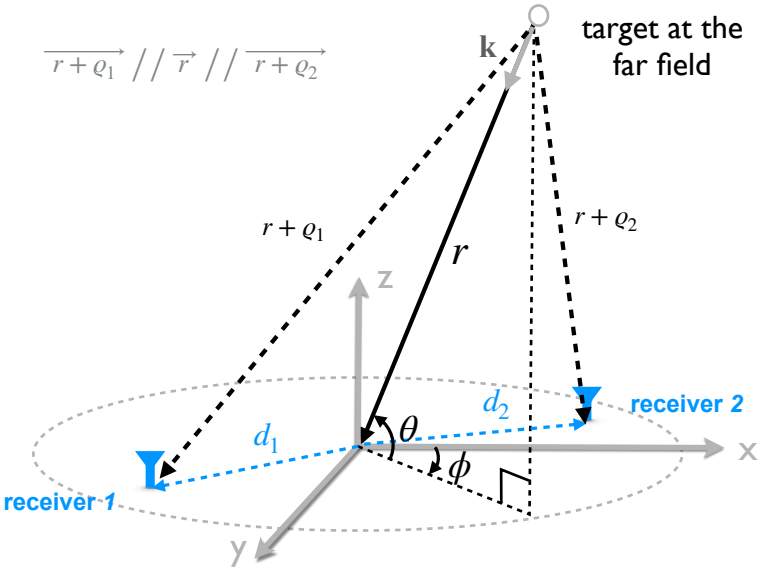

Figure 2.10: Antenna array. Signals at receive antennas are stored and processed digitally. Notice that for a target at the far field $\overrightarrow{r+\varrho_1}$, $\overrightarrow{r}$, and $\overrightarrow{r+\varrho_2}$ can be considered parallel vectors.

the directions. Moreover, advanced algorithms allow to process the digital data adaptively to minimize the sidelobe's gain [Jef09].

To be able to separate angle information with DBF, let us first consider the radar system shown in Fig. 2.10 and rewrite (2.24) considering radar echos from targets at the far-field coming from multiple directions.

$$\sigma(\mathbf{d},t,r) = \sum_i a_{i,r}\, e^{j\left(k_i(r+\varrho)-\omega_{i,r}t+\phi_{i,r}\right)}, \tag{2.50}$$

where $\mathbf{k}_i = 2\pi/\lambda[\cos\theta_i\cos\phi_i,\ \cos\theta_i\sin\phi_i,\ \sin\theta_i]$ is the wave vector or beam direction, $k_i = |\mathbf{k}_i|$ is the wave number, ϱ is the difference in magnitude between the range measured from the center of the array and the range from the location of the receiving antenna, and $k\varrho = \mathbf{kd}$ is the phase offset of a target at far field which depends on the wave vector and the antenna's position. Notice that ϱ is too small compared to the range resolution and it is neglected in the range bin. However, it is large enough to add a phase offset $k\varrho$. Replacing all the terms in (2.50) and considering $k_i r$ a constant phase shift

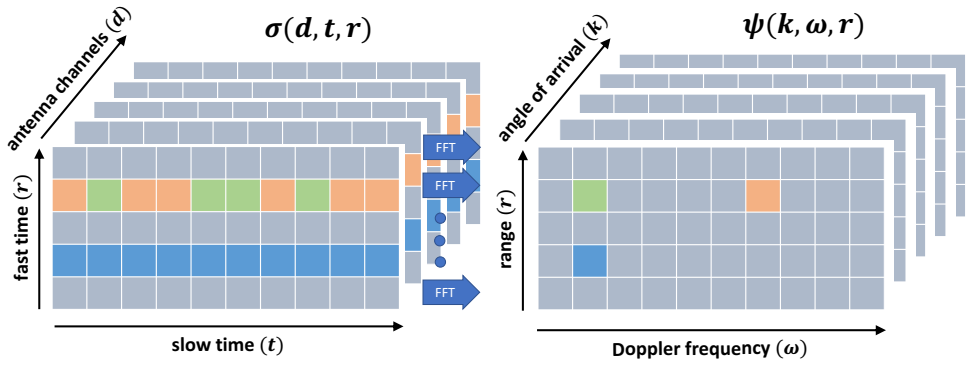

Figure 2.11: Doppler and direction estimation by taking the 2D-DFT of the slow-time and antenna (spatial) samples, respectively.

absorbed by $\phi_{i,r}$, we get

$$\sigma(\mathbf{d}, t, r) = \sum_i a_{i,r}\, e^{j\left(\mathbf{k}_i\mathbf{d} - \omega_{i,r}t + \phi_{i,r}\right)} \tag{2.51}$$

$$= \sum_i \psi(\mathbf{k}_i, t, r)\, e^{j\mathbf{k}_i\mathbf{d}}, \tag{2.52}$$

where $\psi(\mathbf{k}_i, t, r) = a_{i,r}\, e^{j(-\omega_{i,r}t + \phi_{i,r})}$ represents the radar return from direction $\mathbf{k}_i$ and range bin r. Notice that, for uniform arrays, $\sigma(\mathbf{d}, t, r)$ and $\psi(\mathbf{k}, t, r)$ also form a Fourier transform pair.

Similar to the Doppler case, when multiple antennas spatially separated are available, we can apply the discrete Fourier transform (DFT) to separate the radar return for each direction $\mathbf{k}$:

$$\psi(\mathbf{k}, t, r) = \sum_i \sigma(\omega_i, t, r)\, e^{-j\mathbf{k}\mathbf{d}_i}. \tag{2.53}$$

Equation (2.53) is known as digital beamforming (DBF) which is obtained by applying the DFT. DBF is also known as the sum of delayed versions of the received signals $\sigma(\mathbf{d}_i, t, r)$.

Considering an arbitrary weight, the backscatter coefficient can be obtained from

$$\psi(\mathbf{k}, t, r) = \sum_i \sigma(\mathbf{d}_i, t, r)\, h(\mathbf{k}\mathbf{d}_i), \tag{2.54}$$

where h are the weights. Note that when $h(\mathbf{kd}_i) = e^{-j\mathbf{kd}_i}$ (2.54) is equivalent to (2.53). When only few antennas are available, the angular resolution is heavily limited. In such situations, adaptive algorithms can be applied to find a more suitable weight, such as Capon [Pal+98], that improves the angular resolution and reduces the sidelobes selecting $h(\mathbf{kd})$ adaptively.

In fact, the angular resolution and the maximum unambiguous angle are limited by the number of antennas and the separation between them. In a uniform linear antenna array, with $\mathbf{k} = 2\pi/\lambda[\theta_x, \theta_y, \theta_z]$, and $\mathbf{d}_i = [d_{x_i}, d_{y_i}, d_{z_i}]$; the angular resolution and the maximum unambiguous angle in the x, y, and z direction are determined by

$$\Delta\theta_x = \frac{\lambda}{d_{x_{\text{max}}}}, \tag{2.55}$$

$$\theta_{x_{\text{max}}} = \frac{\lambda}{2d_{x_{\text{min}}}}, \text{ and} \tag{2.56}$$

$$\theta_x = \Big[-\frac{n}{2}\Delta\theta_x, ..., \frac{n-1}{2}\Delta\theta_x\Big]. \tag{2.57}$$

For antennas separated by $d_{x_{\text{min}}} = \lambda/2$, the maximum unambiguous $\theta_{x_{\text{max}}}$ is 1.0, i.e., no ambiguity. Unfortunately, such small separations are not feasible in practice due to antenna couplings. Separations of more than 0.7λ are recommended to avoid antenna couplings.

Furthermore, the 2D Fourier transform can be applied to both the antenna samples and the slow-time domain to recover angle and Doppler information, respectively. Figure 2.11 shows the resulting matrix after applying the 2D-DFT. The resulting 3D matrix contains amplitude and phase information for each range gate, Doppler, and angle of arrival.

$$\Psi(\mathbf{k}, \omega, r) = \sum_i \sum_l \sigma(\mathbf{d}_i, t_l, r)\; e^{-j(\mathbf{kd}_i - \omega t_l)} \tag{2.58}$$

$$= a_{k,\omega,r}\; e^{j\phi_{k,\omega,r}}. \tag{2.59}$$

DBF is nothing more than a weighted sum of the measured signals, where the weights are $e^{-j\mathbf{kd}_i}$.

Scattering from atmospheric targets can be considered volume-filling at a particular spatio-temporal scale, i.e., a volume that presents the same statistical characteristics in space and time. Moreover, when the scattering comes from a volume filled of electrons

the RCS presents fluctuations. These fluctuations are faster than the sampling time. For those cases, the instantaneous RCS amplitude and phase from (2.59) are meaningless and the signal ψ is better modeled as a stochastic process with mean 0 and variance b, i.e., $a_{k,w,r} \sim \mathcal{N}(0, b)$. The variance b is the important parameter and it can be estimated from the expected value of the measurements by $\langle \psi^2 \rangle = b$. The algorithm to obtain b directly from radar measurements is known as radar imaging.

2.5.2 Radar imaging

Radar imaging is a technique that extracts the angular distribution of volume targets through the analysis of correlation functions. The cross-correlation of signals at two antennas spatially separated $\Delta\mathbf{d}$ is expressed as

$$\rho(\Delta\mathbf{d}, t, r) = \Big\langle \sigma(\mathbf{d}, t, r),\ \sigma^*(\mathbf{d} + \Delta\mathbf{d}, t, r) \Big\rangle, \tag{2.60}$$

where $\langle . \rangle$ stands for expected value, and $\rho(\mathbf{k}\,\Delta\mathbf{d})$ is known as the visibility function. As seen in the previous section, the complex baseband signal σ can be expressed as $\sigma(\mathbf{d}, t, r) = \psi(\mathbf{k}, t, r)\ e^{j\mathbf{kd}}$, where ψ includes the backscatter coefficient amplitude and phase, and $\mathbf{kd}$ is the phase offset due to the direction of arrival of the radar return. Replacing in (2.60), we get

$$\rho(\Delta\mathbf{d}, t, r) = \Big\langle \sum_i \psi(\mathbf{k}_i, t, r)\ e^{j\mathbf{k}_i\mathbf{d}} \sum_l \psi^*(\mathbf{k}_l, t, r)\ e^{-j\mathbf{k}_l(\mathbf{d}+\Delta\mathbf{d})} \Big\rangle. \tag{2.61}$$

Most of the atmospheric targets are stochastic in nature. Considering that $\psi(\mathbf{k}_i, t, r)$ and $\psi(\mathbf{k}_l, t, r)$ are stochastic processes and that these targets are separated by a considerable distance such that they are spatially uncorrelated, we get

$$\langle \psi(\mathbf{k}_i, t, r)\psi(\mathbf{k}_l, t, r) \rangle = 0, \qquad \text{for } k_i \neq k_l. \tag{2.62}$$

Using the above equation (2.61) can be simplified to

$$\rho(\Delta\mathbf{d}, t, r) = \Big\langle \sum_i \psi^2(\mathbf{k}_i, t, r)\ e^{-j\mathbf{k}_i\Delta\mathbf{d}} \Big\rangle \tag{2.63}$$

$$= \sum_i \Big\langle \psi^2(\mathbf{k}_i, t, r) \Big\rangle\ e^{-j\mathbf{k}_i\Delta\mathbf{d}} \tag{2.64}$$

$$= \sum_i b(\mathbf{k}_i, t, r)\ e^{-j\mathbf{k}_i\Delta\mathbf{d}}. \tag{2.65}$$

$b(\mathbf{k}_i, t, r) = \langle \psi^2(\mathbf{k}_i, t, r) \rangle$ is also known as the Brightness function. Since the visibility and the brightness form a Fourier transform pair for uniform antenna arrays, we can recover the brightness applying the inverse Fourier transform to the visibility.

$$b(\mathbf{k}, t, r) = \sum_i \rho(\Delta \mathbf{d}_i, t, r) e^{j\mathbf{k}\Delta\mathbf{d}_i}. \tag{2.66}$$

As in DBF, angular resolution and maximum unambiguous angle are determined by the number of antennas and distance between them, see (2.57). To improve the angular resolution or when no uniform arrays are available, inversion methods such as the discrete Fourier transform (DFT) [Woo97], Capon [Pal+98], MaxEnt [HC06], and CS [HM13] can be applied to recover b from ρ.

2.5.2.1 Inversion methods

The radar imaging problem is to estimate the brightness b from the visibility measurements ρ. For each range gate and time sample (2.65) can be expressed in matrix form as

$$\boldsymbol{\rho} = \boldsymbol{\Phi}\, \mathbf{b}, \tag{2.67}$$

where $\boldsymbol{\rho} \in \mathbb{C}^M$ is a column vector comprising the V measured visibility samples, $\mathbf{b} \in \mathbb{R}^B$ is a column vector representing the discretized brightness, and $\Phi \in \mathbb{C}^{VxB}$ is a matrix operator resulting from the phase shifts $\Phi_{ij} = e^{-jk_i \Delta d_j}$. The value B are the number of unknows in the equation and it defines the image resolution. This value should be chosen so that the grid size is smaller than expected features of the image. Notice that the total number of visibility measurements in (2.67) is $2V$ (complex) for which not necessarily all of them are non-redundant.

2.5.2.1.1 Direct inversion Originally Kudeki and Sürücü [KS91] proposed a direct inversion of (2.67) using the inverse Fourier transform.

$$\mathbf{b} = \boldsymbol{\Phi}^H \boldsymbol{\rho}. \tag{2.68}$$

Nevertheless, most of the atmospheric radars have a limited number of digital receivers, and hence a limited number of digitized signals at different antennas. Independently

of the number of antennas available, the usable number of antennas is limited by the number of receivers. Thereby $\boldsymbol{\rho}$ is only known for certain Δd, which implies that $B > 2V$, i.e., the problem is underdetermined. Implicit in the inverse Fourier transform is the assumption that the values of the unmeasured antenna separations are zero, which limits the achievable resolution.

2.5.2.1.2 Capon's method An adaptive technique proposed by Palmer [Pal+98] to solve (2.67) is the Capon's method [Cap69]. Capon's can be seen as an extension of the beam steering approach. It chooses the antenna weights adaptively at each angle in order to minimize sidelobe interference.

$$\mathbf{b} = \left(\boldsymbol{\Phi}^H \mathbf{V}^{-1}\right)^{-1}. \tag{2.69}$$

In this case, the visibility $\mathbf{V}$ must be in matrix form where an element of the visibility is $V_{ij}(t,r) = \langle \sigma(d_i,t,r), \sigma^*(d_j,t,r) \rangle$, for $i = 1,...,p$ and $j = 1,...,p$; where p is the number of receiving antennas.

2.5.2.1.3 Maximum Entropy When the problem in (2.67) is underdetermined, there are infinite possible image solutions $\mathbf{b}$ which agree with the data $\boldsymbol{\rho}$. Of all possibilities, maximum entropy (MaxEnt) chooses the solution with the maximum entropy or minimal amount of information [Hys96]. The MaxEnt solution is believed to be the most likely brightness distribution and consistent with the available measurements and their statistical uncertainties. The entropy for a given range gate and time sample is expressed as

$$s(\mathbf{b}) = \sum_i b_i \ln(b_i/F), \text{and} \tag{2.70}$$

$$F = \sum_i b_i. \tag{2.71}$$

The MaxEnt solution $\hat{\mathbf{b}}$ is the one that maximizes the entropy and minimizes the square error.

$$\begin{aligned} &\hat{\mathbf{b}} = \arg\max_{\mathbf{b}} s(\mathbf{b}), \\ &\text{subject to } \|\boldsymbol{\rho} - \boldsymbol{\Phi}\mathbf{b}\|_2^2 < \epsilon^2, \end{aligned} \tag{2.72}$$

where ϵ^2 is the expected noise variance. As Hysell and Chau suggested [HC06], the error covariance matrix arising from correlated visibilities can be considered to optimize the radar imaging problem. Moreover, the resulting non-linear problem (2.72) can be solved numerically using a hybrid method [Pow70].

2.5.2.1.4 Compressed sensing Traditionally, the Shannon-Nyquist sampling theorem holds that the exact recovery of an arbitrary signal is possible if the signal is sampled at twice its bandwidth. However, for simple signals that do not fully occupy the spectrum, only a few measurements are required for exact recovery. Compressed sensing (CS) formalizes this idea stating that exact signal recovery of any arbitrary signal is possible with fewer measurements than Nyquist requires if the signal is expressed in some known basis where the signal is sparse.

Natural images are not sparse in their original domain. Nevertheless, several authors have shown that they are sparse in the Fourier and wavelet domain [TM02; Sté09; YH17; HM13]. To improve the sparsity of complicated images, other authors proposed the use of curvelets [Smi+13], bandelets [LM05], and adaptive dictionaries [Pey10]. The generalization of any sparsity basis can be expressed as

$$\mathbf{b} = \mathbf{\Psi}\mathbf{s}, \text{ and} \tag{2.73}$$

$$\boldsymbol{\rho} = \mathbf{\Phi}\mathbf{\Psi}\mathbf{s}, \tag{2.74}$$

where $\mathbf{\Psi} \in \mathbb{C}^{BxB}$ is the matrix that defines the sparsity basis of $\mathbf{b}$, and $\mathbf{s}$ is a sparse vector resulting from the transformation of $\mathbf{b}$ into the $\mathbf{\Psi}$ domain.

Despite the fact that (2.74) is still underdetermined, CS claims that the signal $\mathbf{s}$ can be recovered even from a very limited number of measurements if two conditions are fulfilled (a) the signal is K-sparse, meaning that the number of non-zero values is less than K, with $K < 2V$; and (b) the sensing matrix $\mathbf{H} = \mathbf{\Phi}\mathbf{\Psi}$ satisfies the restricted isometry property (RIP) [CT05], which requires that any K columns of $\mathbf{H}$ are orthogonal. Even though this may seem impossible, numerous authors have proven the robustness and efficacy of CS even when the signal is approximately sparse and noisy [CT05; CRT06a; CRT06b; DW14; SL15]. For a noisy data, the CS solution is expressed as

$$\begin{aligned} \hat{\mathbf{s}} &= \arg\min_{s} \|\mathbf{s}\|_0, \\ \text{subject to } &\|\boldsymbol{\rho} - \mathbf{\Phi}\mathbf{\Psi}\mathbf{s}\|_2^2 < \epsilon^2, \end{aligned} \tag{2.75}$$

where $\|\mathbf{s}\|_0$ is the "L0-norm" of $\mathbf{s}$, i.e., the number of non-zero elements in $\mathbf{s}$. This equation recovers the most compressed version of $\mathbf{s}$ that agrees with the measurements. Unfortunately, the "L0-norm" is computationally intractable for most of the problems.

If the RIP condition is satisfied, Candès [CRT06b] and Donoho [Don06b] demonstrated that the "L0-norm" minimization problem is equivalent to the "L1-norm" problem.

$$\begin{aligned} \hat{\mathbf{s}} &= \arg\min_{s} \|\mathbf{s}\|_1, \\ \text{subject to } &\|\boldsymbol{\rho} - \boldsymbol{\Phi}\boldsymbol{\Psi}\mathbf{s}\|_2^2 < \epsilon^2, \end{aligned} \tag{2.76}$$

The "L1-norm" minimization is more attractive computationally and it can be solved by linear programming [CT05]. The "L1-norm" problem is also known as basis pursuit. Once $\hat{\mathbf{s}}$ is recovered, we can use then (2.73) to get $\mathbf{b}$.

Of all the methods described here, MaxEnt and CS give the best results. However, their running time is much worse than Capon or Fourier. At least 20 times slower for small antenna arrays (8 antennas) [HM13]. For large arrays (several antennas), this difference increases exponentially. Harding and Milla [HM13] have shown that the performance of CS and MaxEnt applied to radar imaging are quite similar in quality and computational complexity. So, in this text, we use any of them indistinctly to solve the radar imaging problem.

2.5.2.2 Normalized visibility

Equation (2.60) assumes we have noiseless measurements σ. Nevertheless, we have access only to noisy measurements and sometimes no calibrated signals $\hat{\sigma}$

$$\hat{\sigma}(\mathbf{d}, t, r) = a_1 \, \sigma(\mathbf{d}, t, r) + \eta_1, \tag{2.77}$$

$$\hat{\sigma}(\mathbf{d} + \Delta\mathbf{d}, t, r) = a_2 \, \sigma(\mathbf{d} + \Delta\mathbf{d}, t, r) + \eta_2, \tag{2.78}$$

where $a_1^2 = \left\langle \hat{\sigma}^2(\mathbf{d}, t, r) \right\rangle$ and $a_2^2 = \left\langle \hat{\sigma}^2(\mathbf{d} + \Delta\mathbf{d}, t, r) \right\rangle$ represent the receiving gains which might be uncalibrated. Using this definition and assuming uncorrelated noises with variance η_1^2 and η_2^2, the cross-correlation function is expressed as

$$\left\langle \hat{\sigma}(\mathbf{d}, t, r), \; \hat{\sigma}^*(\mathbf{d} + \Delta\mathbf{d}, t, r) \right\rangle = \sum_i a_1 \, a_2 \, b(\mathbf{k}_i, t, r) \, e^{-j\mathbf{k}_i \Delta\mathbf{d}}, \tag{2.79}$$

which redefines the visibility function as

$$\rho(\Delta\mathbf{d},t,r) = \frac{\left\langle \hat{\sigma}(\mathbf{d},t,r),\ \hat{\sigma}^*(\mathbf{d}+\Delta\mathbf{d},t,r)\right\rangle}{a_1\ a_2} \tag{2.80}$$

$$= \frac{\left\langle \hat{\sigma}(\mathbf{d},t,r),\ \hat{\sigma}^*(\mathbf{d}+\Delta\mathbf{d},t,r)\right\rangle}{\sqrt{\left(\left\langle \hat{\sigma}^2(\mathbf{d},t,r)\right\rangle - \eta_1^2\right)\left(\left\langle \hat{\sigma}^2(\mathbf{d}+\Delta\mathbf{d},t,r)\right\rangle - \eta_2^2\right)}} \tag{2.81}$$

$$= \sum_i b(\mathbf{k}_i,t,r)\ e^{-j\mathbf{k}_i\Delta\mathbf{d}}. \tag{2.82}$$

Real experiments described later in this work use the normalized visibility function, (2.81), to estimate the brightness function. Hereafter, we refer to visibility as the normalized visibility.

2.5.2.3 Uncertainties

One source of uncertainties which was not included in (2.81) is the error associated with estimating the cross-correlation $\left\langle \psi^2(\mathbf{k},t,r)\right\rangle$. It is known that the error at estimating the variance of a random number ψ using ensemble averaging depends on the number of ensembles. Ensemble average can be expressed as

$$\left\langle \tilde{\psi}^2\right\rangle = \frac{1}{n}\sum_{t=0}^{n-1}\psi_t^2 \tag{2.83}$$

$$= b+\epsilon, \tag{2.84}$$

where $\epsilon = b/\sqrt{n}$ is the deviation from the expectation because of the finite number of samples involved [Dek+05; HC06]. One way to reduce the error ϵ is to increase the number of ensembles. Nevertheless, this number cannot be too high because it is limited by dynamic nature of the imaged target. The maximum number of ensembles depends on how long a target remains at the same angular position. Hysell and Chau [HC06] improved the of the MaxEnt algorithm by taking into account the uncertainties caused by the finite number of ensembles. Such uncertainties are known also as the covariance error.

In the next chapter, we discuss radar techniques to increase the spatial resolution of atmospheric measurements. In such cases, the time integration must be even shorter.

Otherwise, the resulting image might be blurred since the time a target stays at the same finer pixel is shorter. This is an essential point to consider in high angular resolution imaging.

Chapter 3

Coherent MIMO radar techniques

In this chapter

3.1 What is MIMO?

Multiple–input multiple–output (MIMO) systems can be defined as systems with multiple radiating antennas and multiple receive antennas. Since the 1990s, such kind of systems have been widely used in communications to improve the capacity [Tel99; FG98], and reliability [LT03] of communication channels. Currently, MIMO is being employed

in the 5G cellular network technology and the IEEE 802.11n WiFi standard due to its excellent performance when interconnecting multiple users at high-speed data transmission.

In the case of radars, colocated multiple radiating and multiple receive antennas have been used in the past to focus the transmitted energy and to steer the beam in the desired direction [Wid+67], which is known as phased arrays. Phased arrays on transmission are capable of steering the transmitted energy toward the desired direction by radiating delayed versions of a single waveform. At the receiving side, the receiving beam can be steered in a given direction to maximize the signal-to-noise ratio (SNR) using the same principle. Phased arrays are widely employed on transmission and reception for atmospheric observations as well. The first published Doppler radar wind measurements using multi-beam configurations (phased arrays) in the troposphere were reported by Browning [BSW73], in the equatorial mesosphere by Woodman [Woo72], and to measure vector winds employing multi-beam configurations by Reid [Rei87].

The key difference between MIMO and phased arrays is that MIMO radars radiate independent/orthogonal waveforms through multiple spatially separated transmit antennas. By transmitting orthogonal signals, transmit signals scattered at a radar target can be received and decoupled on the receiving side. Compared to phased arrays, MIMO provides additional degrees of freedom because of the multiple independent transmit-receive links. What allows is, for example, the application of digital beamforming on reception as well as on transmission. Additional degrees of freedom might lead to an improved angular resolution [BF03], a better antenna beam pattern [LS07], or a larger number of targets a radar can detect [Fis+06]. Figure 3.1 shows two radars configurations (a) a conventional radar system employing one transmitting antenna and multiple receiving antennas (SIMO) vs. (b) a system employing multiple transmitting and multiple receiving antennas (MIMO). Notice that in case of SIMO or MIMO the antenna symbol might represent a single antenna or an antenna array transmitting/receiving a single waveform.

There are two kinds of MIMO configurations, depending on the relative separation of the transmitting and receiving antennas. First, when the transmit/receive antennas are closely separated such that the wave vectors for all the transmit-receive links are approximately the same, the reflected signals for two different links are correlated in magnitude

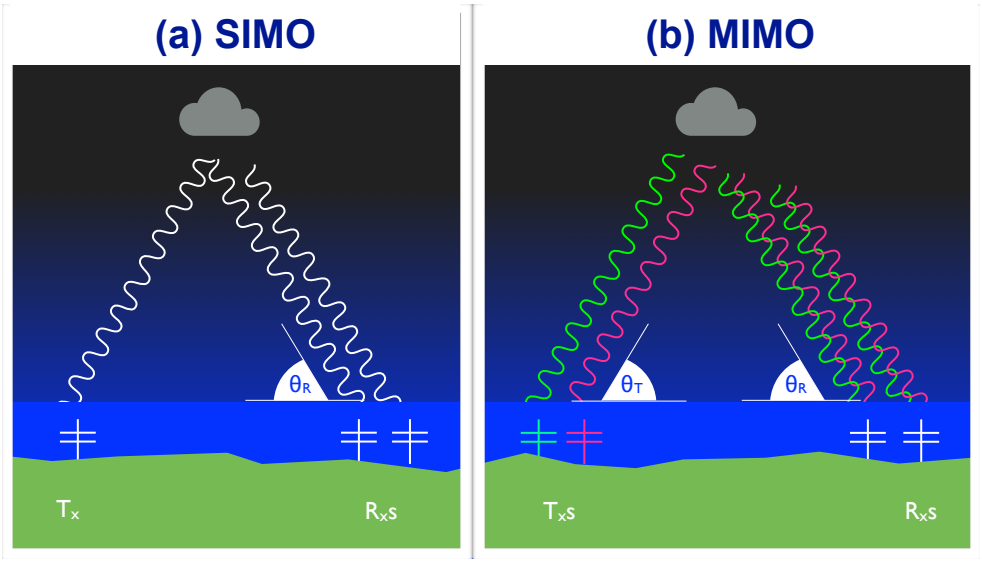

Figure 3.1: A bi-static radar system (a) in a SIMO configuration, and (b) in a MIMO configuration. Unlike SIMO, MIMO illuminates the target employing independent/orthogonal signals, which are indicated in red and green.

and phase. This correlation results because the different transmit-receive links observe the same radar cross–section (RCS). For that reason, radars using closely separated antennas are known as coherent or collocated MIMO radars [LS07]. To keep some correlation between the reflected signals for the different links, the antenna separation must be a few tens of wavelengths. Coherent MIMO can be considered an advanced version of phased antenna arrays given that by combining all the independent transmit-receive links, a larger virtual antenna can be formed [Wan12]. Figure 3.1(b) is an example of a coherent MIMO configuration, even though the transmit and receive station are widely separated, all the transmit-receive links have the same wave vector.

On the other hand, when the transmit and receive antennas are widely separated, so that the target's RCS can no longer be considered the same for all the transmit-receive paths, the return signal for two different transmit-receive paths are decorrelated. These kind of radars are referred to as non-coherent or statistical MIMO [Fis+06; Leh+07]. Non-coherent MIMO has been discussed extensively in the radar community in the context of multistatic radar systems [Che18], which are used to measure unambiguous vector drifts and to exploit spatial diversity of random fluctuations of the target's reflectivity.

MIMO techniques are applied to a broad range of applications thanks to the improved capability in the number of links, resolution, target parameter identification, and beam

pattern. Examples include communications [Tel99], ground penetrating radars [JLZ12], through-the-wall imaging radar applications for urban remote sensing [Mas+10], maritime navigation [Hua+11], and medical applications such as breast cancer detection [FB08]. This chapter describes conceptual and mathematically the application of coherent MIMO radars for the observation of atmospheric targets, which are mostly stochastic in nature.

In this chapter, we consider only MIMO radars with colocated antennas (coherent MIMO), and all subsequent mentions of MIMO refer to this type only.

3.2 Why is MIMO required?

Radars are widely used to measure reflectivity, position, and Doppler velocity of distant objects in many fields. In atmospheric science, radar measurements are employed to infer physical parameters such as wind velocities, ion and electron temperatures, electron density, electric fields, and kinetic energy [Hoc83; Hoc85; HTJ97; HFV01; Sul15; Li+16]. In most cases, they were done assuming homogeneous and quasi-stationary volume filling targets within the illuminated beam because of the limited spatio-temporal resolution of radar measurements. Temporal resolution in radars is restricted by the PRI, range resolution is by the transmit waveform bandwidth, and horizontal spatial resolution is by the radar antenna size. Previous studies have focused on improving the temporal and range resolution of radars. This study focus on improving the horizontal spatial resolution.

Over time, remote sensing techniques have evolved, and now they are capable of differentiating echoes coming from different directions with good precision. This capability is achieved via spatial diversity on reception and employing radar imaging algorithms [Wid+67; Tal+16; Mor+13]. Angle estimation is beneficial, for example, to determine mesospheric 3D wind fields from specular meteor measurements [SC15], where knowledge of meteors' location is extremely important. Although significant improvement was done during the last four decades, several atmospheric radars still have a limited horizontal spatial resolution. In order to improve the spatial resolution of a radar, we require to construct larger antenna arrays. Figure 3.2 shows the relationship between the angular resolution and the antenna size, where the resolution is inversely proportional to the antenna aperture. In order to properly sample a spatial structure or wave,

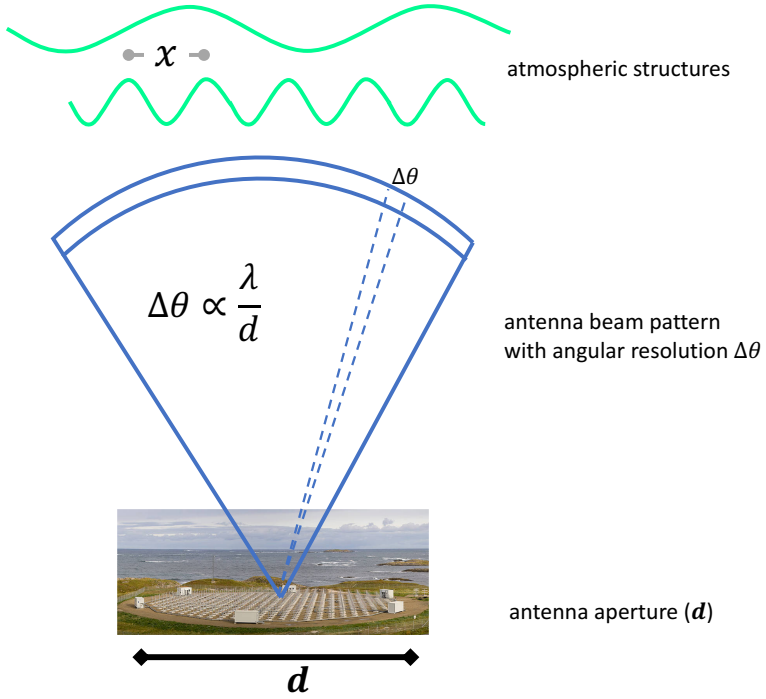

Figure 3.2: Angular resolution of a radar ($\Delta\theta$) and its dependency on the antenna size (d) and the radar wavelength (λ)

the Nyquist condition must be satisfied, i.e., the spatial wave must be sampled at half of its size. For a wave of size x located at an altitude h, we get

$$x \geq 2\ h \sin\left(\Delta\theta\right) \tag{3.1}$$

where "$h \sin(\Delta\theta)$" is the spatial resolution at altitude h.

Even though very large radar antennas have been constructed to observe atmospheric targets, their angular resolution is still limited to a few kilometers. Table 3.1 shows the spatial resolution of state of the art atmospheric radars. Not surprisingly, the achievable horizontal spatial resolution with some of the biggest atmospheric radars in the world is only a few kilometers at $85\ \mathrm{km}$ of altitude. To observe km-scale structures, even much larger antennas are required.

In this chapter, we describe multiple–input multiple–output (MIMO) systems that make use of diversity on transmission and reception to virtually increase the antenna size and the number of antenna, allowing the observation of km-scales structures with current

Radar system	**Antenna size (d)**	**Angular resolution ($\Delta\theta$)**	**Spatial resolution at $85\,\mathrm{km}$**	**Observable horizontal scales (x)**
MAARSY	$90\,\mathrm{m}$	$3.6°$	$5.3\,\mathrm{km}$	$\geq 10.6\,\mathrm{km}$
Jicamarca	$300\,\mathrm{m}$	$1.0°$	$1.5\,\mathrm{km}$	$\geq 3.0\,\mathrm{km}$
EISCAT VHF	$32\,\mathrm{m}$	$1.2°$	$1.8\,\mathrm{km}$	$\geq 3.6\,\mathrm{km}$
EISCAT 3D	$80\,\mathrm{m}$	$0.97°$	$1.45\,\mathrm{km}$	$\geq 2.9\,\mathrm{km}$

Table 3.1: Angular and spatial resolution of some of the biggest atmospheric radars in the world

radars systems already installed. Furthermore, we investigate the main requirements for the design and construction of future atmospheric radars.

As it was mentioned before, that the first condition a MIMO radar must fulfill is the transmission of orthogonal signals from each antenna. Furthermore, MIMO also requires that the transmitted signals are still orthogonal between after they are scattered back from the target. This means that the transmitted signals must be orthogonal even after the time delay and the Doppler shift caused by the target, which in the most simple case depends on the target's range and velocity. In a more comprehensive scenario, it will depend on the target's extension and the Doppler bandwidth.

Let's imagine a scenario where two independent signals are transmitted by two antennas spatially separated, where the signal frequencies are separated by $1\,\mathrm{Mhz}$. Considering ideal band-limited signals, these two signals are independent from each other. If they are used to illuminate a hard target with a narrow Doppler, for example a specular meteor with a Doppler frequency less than $100\,\mathrm{Hz}$, the scattered signals will still be independent of each other. However, if these two transmit signals are used to illuminate a volume filling target with multiple scatters where each of them has its own Doppler frequency higher than $500\,\mathrm{kHz}$, i.e., an overspread target, the signals might not be orthogonal anymore once they are scattered back. When designing a MIMO system, we have to take into account not only the transmit signals but also the target's features.

3.3 Transmit diversity in MIMO radars

MIMO radar is a system which employs multiple transmitting antennas and multiple receiving antennas to improve the performance compared to conventional radars. The

use of multiple antennas at the receiver or transmit side is also known as spatial diversity. To achieve spatial diversity on transmission, a MIMO radar requires to transmit independent signals by each antenna. This is also known as transmit diversity. Transmit diversity is done by transmitting signals at a different time, with different frequencies, with different phases, or with different polarizations. Although time, frequency, and phase-coded diversity are based on the same principle (varying the properties of a periodic waveform) and they might achieve the same performance, their implementation and hardware requirements are quite different. Transmit diversities have extensively been discussed in the context of MIMO radars [Fis+06; Leh+07, e.g.] and in the field of communications [Wee93; WSG94; NTW99, e.g.]. Common diversities used in MIMO communication channels are frequency [Wee93, e.g.] and phase coded [BP00, e.g.] due to their performance and easiness to implement.

Unlike communication channels, atmospheric targets exhibit particular features as described in Chapter 2, which make them highly dependent on the radar frequency and polarization. Therefore, application of frequency and polarization diversity are not suitable for atmospheric MIMO radars and other transmit diversities are required to obtain independent signals.

In practice, fully independent signals on transmission are not viable. Depending on the transmit diversity used and the target's features, such as its extension and Doppler bandwidth, radar returns from different transmitters might be partially correlated. Therefore, decoupling of return signals might be more complicated. Moreover, the larger the number of transmitters, the more difficult the signal decoupling would be.

In this section, we describe three transmit diversity alternatives, considering the target's extension and bandwidth. Table 3.2 summarizes the advantages and disadvantages of the transmit diversities. The most simple transmit diversity is described first, time diversity, which can be implemented with commercial radars. Then, the advantages of waveform diversity compared to time diversity is described. Finally, a more suitable transmit diversity is presented, which requires a more advanced hardware and software.

3.3.1 Time diversity

One of the most simple ways of ensuring independent signals is implementing time diversity in a pulsed radar system. Time diversity is no more than transmitting the same

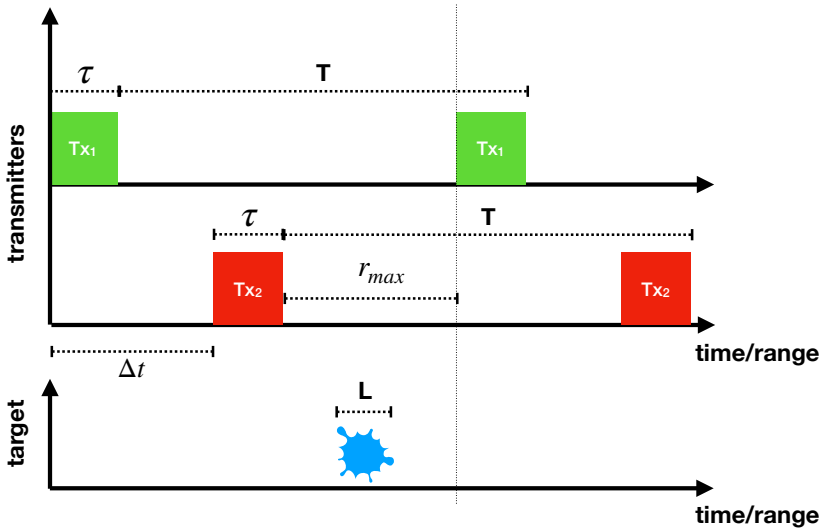

Figure 3.3: Time diagram of a pulsed MIMO radar with two transmitters using time diversity. Notice that the time difference between transmitters Δt depends on the radar pulse width τ and the target's extension L.

Transmit diversity	**Advantages**	**Disadvantages**
Time	-easy to implement -no additional signal processing	-poor time resolution -range ambiguity -less average Tx power
Waveform	-one single operating frequency -scalable	-requires specialized software -coupling between transmit signals might be problematic
Optimal	-one single operating frequency -scalable	-requires specialized hardware and software -coupling between transmit signals is minimized

Table 3.2: Advantages and disadvantages of transmit diversities

waveform from each transmit antenna but just delayed by some time Δt. To avoid overlapping between radar returns from two different transmissions, the minimum time separation between transmissions Δt is a function of the pulse width τ and the expected target thickness or target's extension L, see Fig. 3.3:

$$\Delta t = \tau + L. \tag{3.2}$$

Because of the additional delay between transmitters the pulse-repetition interval (PRI) of each transmitter has to be extended to

$$T = \Delta t + 2\, r_{max}/c, \tag{3.3}$$

where T is the radar PRI, r_{max} is the desired maximum unambiguous range, and c is the speed of light. Notice that if there is no delay between transmitters, the PRI is equal to the maximum unambiguous range $r_{max} = c\,T/2$, as shown in Chapter 2.3.

Equation (3.2) and 3.3 are only valid if no additional targets are expected at other ranges. Usually multiple targets are expected within the range r_{max}, which might cause interference between radar returns from different transmitters. In such cases, to avoid interference, r_{max} must be considered as the target's extension, thereby (3.2) and (3.3) become:

$$\Delta t = \tau + 2\, r_{max}/c, \text{and} \tag{3.4}$$

$$T = \Delta t + 2\, r_{max}/c, \tag{3.5}$$

resulting in $T = \tau + 4\, r_{max}/c$. It means that the new radar PRI must be larger than

four times the maximum unambiguous range to avoid interference and to ensure independent receive signals. Usually, it is only two times larger. When M transmitters are employed, (3.4) and (3.5) become:

$$\Delta t = \tau + 2\,(M-1)\,r_{max}/c, \text{and,} \tag{3.6}$$

$$T = \tau + 2\,M\,r_{max}/c. \tag{3.7}$$

Not surprisingly, we notice that the larger the number of transmitters, the longer the required radar PRI; which means a poorer time resolution and a reduced transmit energy. The application of time diversity must be restricted to targets with high signal-to-noise ratio, small range extension L, and long correlation times.

Few atmospheric targets satisfy the three conditions mentioned above. Nevertheless, some practical experiments were performed in this study to validate the MIMO concept with time diversity using two different targets: (a) equatorial electrojet [Urc+18], and (b) polar mesospheric summer echoess [Urc+19a]. One of the main advantages of time diversity is that it does not require special hardware nor additional data processing. The radar processing technique described in Chapter 2 is sufficient to process signals acquired with a MIMO radar using time diversity.

3.3.1.1 Bandwidth and power reduction

As described in (2.47), the maximum unambiguous Doppler frequency w_{max} is limited by the PRI. In a MIMO radar with M transmitters using time diversity the maximum unambiguous Doppler frequency is given by

$$w_{max} = \frac{\pi}{T} \tag{3.8}$$

$$= \frac{\pi}{\tau + 2\,M\,r_{max}/c} \tag{3.9}$$

$$\approx \frac{c\pi}{2\,M\,r_{max}}. \tag{3.10}$$

This equations indicates that the Doppler bandwidth in a MIMO radar with M transmitters is M times smaller compared to the bandwidth of a radar with a single transmitter. Notice that τ is negligible compared to $2\,M\,r_{max}/c$.

A similar analysis can be done for the average transmit energy in one second

$$E_{avg} = \frac{\tau}{T} P_t \ (1s), \tag{3.11}$$

$$= \frac{\tau}{\tau + 2\,M\,r_{max}/c} P_t, \tag{3.12}$$

$$\approx \frac{c\,\tau}{2\,M\,r_{max}} P_t, \tag{3.13}$$

where P_t is the peak transmit power. Under these conditions, the average transmit energy decreases in the same proportion as the number of transmitters M increases. Pulsed radars using time diversity are restricted to applications for which radar targets are concentrated within a small range. Thus keeping a short delay between transmitters and a small loss in energy and bandwidth. In order to use shorter delays, time diversity can be combined with waveform diversity, thereby the correlation between radar returns might be reduced even if there is an overlap in time between returns.

3.3.2 Waveform diversity

Although waveform diversity can be implemented using linear frequency modulation (FM) techniques and phase-coded waveforms, only phase-coded waveforms are used in this thesis due to the reasons described above. Phase-coded waveforms are a good alternative to build radar networks with transmitters operating at the same frequency as described in [Vie+16]. Although, continuous-wave radars have some disadvantages as described in Chapter 2.3.2, they can be combined with phase-coded waveforms to generate quasi-orthogonal waveforms and to allow the deployment of large radar networks without much effort.

Waveform diversity can also be applied to pulsed radars, which can be seen as a special case of a phase coded continuous-wave radar. The difference lies in the fact that most of the code bits are zero in amplitude. Shorter codes present higher correlations between them. Therefore, the application of only waveform diversity is not recommended in pulsed radars.

For long pulses, various codes with good correlation properties exist such as Gold codes [Gol67], Walsh-Hadamard codes [Har72], polyphase codes [Fra06; Chu72], and pseudo-random binary codes [MS76]. The choice of one of them depends basically on the hardware capabilities. The more complex the codes, the lower the correlation between them.

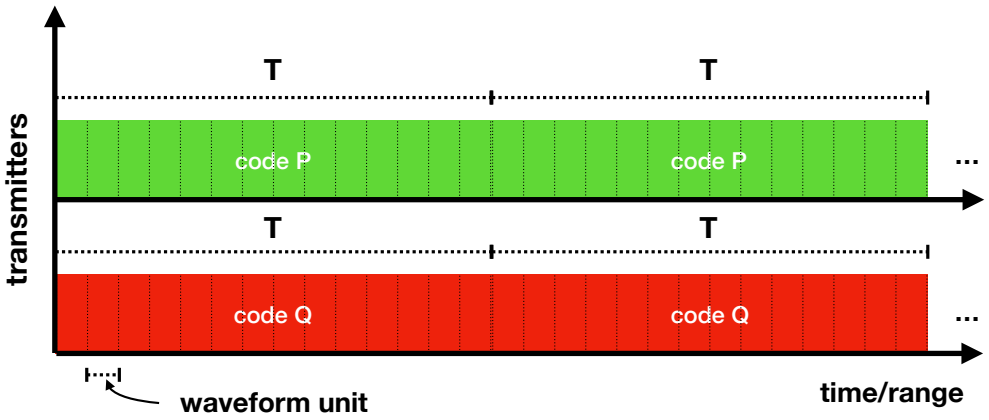

Figure 3.4: Time diagram of a continuous wave MIMO radar with two transmitters using waveform diversity.

Figure 3.4 shows a time diagram of two antennas transmitting concurrently but with different code sequences. Once the code sequences are selected (including code length and baud), it is possible to recover the signal for each transmit-receive link using an inverse problem approach. Since specialized signal processing is required for the MIMO case, we first need to understand the signal model in a MIMO radar which is described in section 3.6.

In this section, we focus on the analysis of the auto and cross-correlation properties of two codes P and Q. The codes will be based on pseudo-random binary sequences since they are easier to implement with current radar systems. The pseudo-random binary sequence can be generated using any random number generator to produce L random binary values, where L is the waveform length. Then, we convert the random numbers to phases, from 0 to $0°$ and from 1 to $180°$.

The auto-correlation of a code, also known as the ambiguity function, was defined in section 2.3.1.1. Similarly, the cross-correlation of two waveforms P and Q can be written as

$$\mathbf{C}(r_i, r_j) = \sum_{k=1}^{n} w_P(r_k - r_i) w_Q^*(r_k - r_j). \tag{3.14}$$

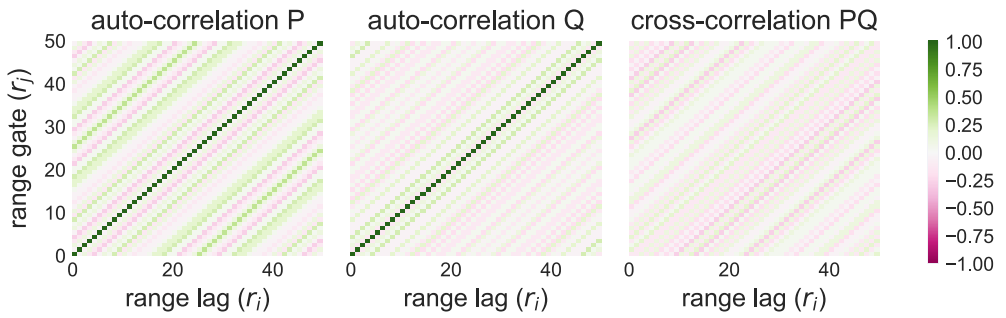

Figure 3.5: Auto and cross-correlation functions of two waveforms P and Q of length 50. Notice that the correlation values are normalized to the code length. The mean cross-correlation value is 0.12 (side-lobe gain).

This equation indicates how strong is the sidelobe caused by the interaction of two waveforms at a given range gate r_i due to a target at range r_j. In case of the auto-correlation, maximum correlation is expected for $r_i = r_j$. Figure 3.5 shows the normalized auto and cross-correlation functions for two pseudo-random binary codes P and Q of length 50. As expected, the auto-correlation for $r_i = r_j$ is 1, which can be considered as the main-lobe. In average the correlation values for sidelobes ($r_i \neq r_j$) is 0.12, indicating that the peak-to-sidelobe ratio (PSLR) is ≈ 10.

In order to improve the PSLR, the code length can be extended. Figure 3.6 shows how the mean cross-correlation of two pseudo-random waveforms varies as a function of the waveform length. For each waveform length, the simulation was repeated 20 times with different codes to mitigate statistical fluctuations. These results corroborates that the cross-correlation between waveforms decreases with their length. Surprisingly, waveform's lengths larger than $200\,\text{bits}$ don't improve the orthogonality between pseudo-random codes significantly. Such results must be considered when designing a MIMO system or a MIMO experiment.

3.3.3 Suboptimal diversity

An optimal transmit diversity is the one that combines the advantages of all the transmit diversities and minimize their disadvantages. Theoretically, an optimal diversity provides the highest number of fully independent transmitted signals using the same radio

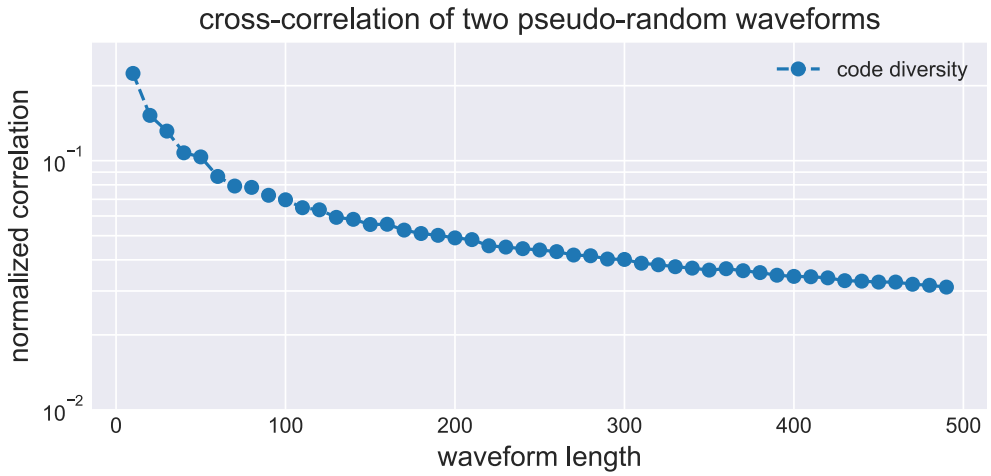

Figure 3.6: Mean cross-correlation of two pseudo-random binary codes P and Q as a function of their length. Fully orthogonal codes should have zero cross-correlation. Notice that after a length of 200 bits the improvement is less than $1x10^{-2}$ per 100 bits.

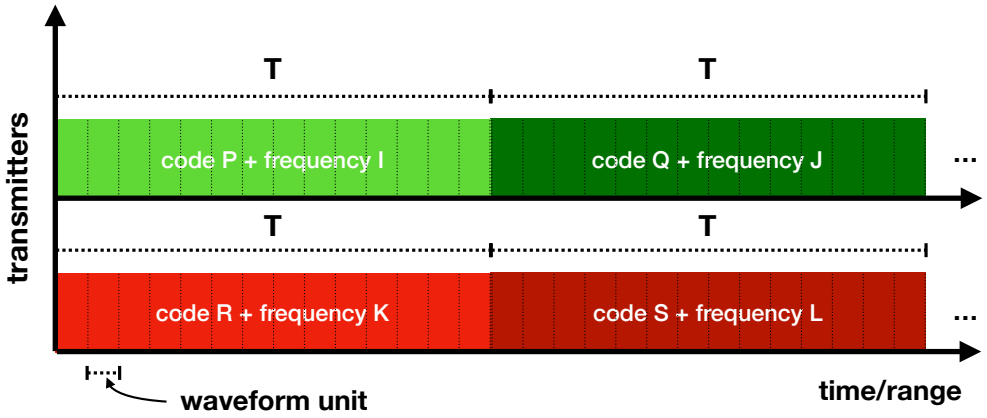

Figure 3.7: Time diagram of a continuous wave MIMO radar using optimal diversity.

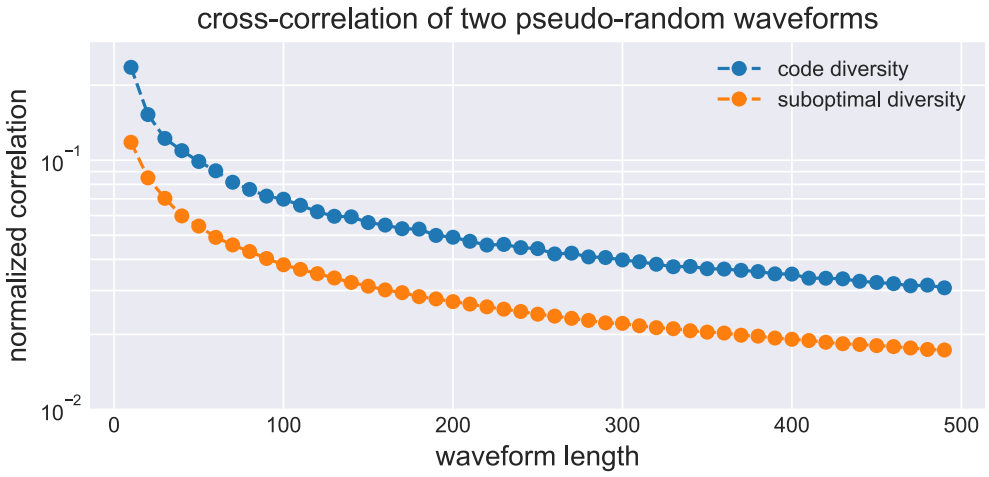

Figure 3.8: Comparison of the cross-correlation of two waveforms P and Q using code and optimal diversity (code+frequency).

spectrum and achieving the same time resolution (Doppler bandwidth). However, a system with such capability might be too complex to implement. In this section, a suboptimal diversity that combines phase-coded and frequency diversity is proposed, which might be implemented with small hardware modifications.

Combination of frequency and code diversity has already been employed to improve the performance of communication MIMO channels, namely, OFDM and coding [BP00, e.g.]. This suboptimal diversity can be seen as a way to increase the number of code bits of a waveform, and thus the orthogonality between waveforms. Although, the same result might be achieved by increasing the waveforms' length directly, it would require to increase the effective sampling rate on transmission and reception (data throughput), which is limited by the capability of current computers since currently most of the radar signal processing is done in software.

Figure 3.7 shows a time diagram where phase-coded and frequency diversity are combined to obtain a lower correlation between the transmitted waveforms in a MIMO radar with two transmit antennas. Polarization diversity might also be included but most of atmospheric targets are highly dependent on polarization, and therefore, it is excluded from this example. In the figure, a code bit represents a change both in phase and frequency. Corresponding phase and frequency for each bit can be generated using pseudo-random sequences as described before.

When frequency diversity is employed alone, the working frequencies of two different transmit antennas must be separated by at least the target's bandwidth in order to guarantee independent radar returns. For atmospheric targets, it could be a few Mhz. For most of the atmospheric targets, such frequency separation causes that the observed targets are not the same. Nevertheless, when both frequency and code diversity are employed, the large frequency separation is not required. Changes in frequency can be limited to a few tens of kHz, ensuring that the same target is being observed but, at the same time, incorporating additional diversity. Figure 3.8 shows the performance of this combined diversity using two symbols for phase modulation and four symbols for frequency modulation. This kind of combined diversity is suggested for most of the applications, but it would require some changes of current atmospheric radar systems.

3.4 MIMO virtual array

Coherent MIMO radar is a technique that employs multiple transmit and multiple receive antennas closely separated to obtain radar images with higher angular (spatial) resolution compared to conventional SIMO radars. As explained in Section 2.5.2, angular resolution and image quality depend on the radar antenna aperture and the number of receive antennas, respectively. With coherent MIMO, the angular resolution and image quality both can be improved. While coherent MIMO does not provide spatial diversity as non-coherent MIMO, it can improve angular (spatial) resolution by combining the information from all the transmit-receive paths. This results from the fact that all the transmit-receive links observe the same radar cross–section (RCS). In a coherent MIMO radar, the return signal from each transmit-receive path is correlated and the combination of them results in a larger virtual array. Similarly to how digital beamforming exploits spatial degrees of freedom on reception, coherent MIMO exploits both degrees of freedom on transmission and reception, which can be seen as a combination of a transmit and a receive phased array.

The advantage of MIMO radars over traditional phased arrays can be explained by the virtual array [Li+08]. A virtual array, for a system with a transmit array of P antennas transmitting independent waveforms and a receive array of M antennas, consists of PM virtual antennas. In the literature, the virtual array is also known as the co-array [HK90].

However, in this work, we refer to it as the virtual array since it is the term most used. Depending on the location of the transmit and receive antennas, not necessarily all of the antennas of the virtual array are unique. Nevertheless, the additional degrees of freedom provided by the transmission of independent waveforms improve the performance of a radar system significantly.

To have an idea of how MIMO helps to increase the number of virtual receivers and to enlarge the antenna aperture, figure 3.9 shows a MIMO layout with two transmit and three receive antennas. Where the resulting receive array can be explained as a combination of a receive array having three antennas to the right of TX_1 and another receive array having three antennas to the left of TX_2, resulting in six virtual receive antennas in total. We see that the number of virtual receive antennas has increased by 2 times compared with the original number of receivers. In general, the number of the resulting number of virtual receive antennas in a MIMO system is equal to the number of transmit antennas times the number of receive antennas, which means that the number of virtual antennas grows multiplicatively with the number of transmit-antennas. Due to its great impact adding one antenna at one side (Tx or Rx), affects the resulting array multiplicatively. But not only that, but we also see that the resulting antenna aperture is larger compared to the original aperture. In the example shown it is three times larger.

Similar to what is done in phased array antennas, many adaptive array processing techniques, including digital beamforming, Capon, maximum entropy, and compressed sensing, can be applied for direction estimation when using coherent MIMO. In the following section, the narrowband signal model for a MIMO radar considering a target at the far-field is described. Moreover, we describe the signal model in terms of an equivalent virtual array and the signal processing to estimate range and angle information.

3.5 Far-field signal model of pulsed MIMO radars

Lets use the monostatic pulsed radar system shown in Fig. 3.10, with multiple receiving antennas and multiple radiating antennas where each of antenna transmits a pulse at a different time instant. Considering a MIMO system using time diversity that is perfectly

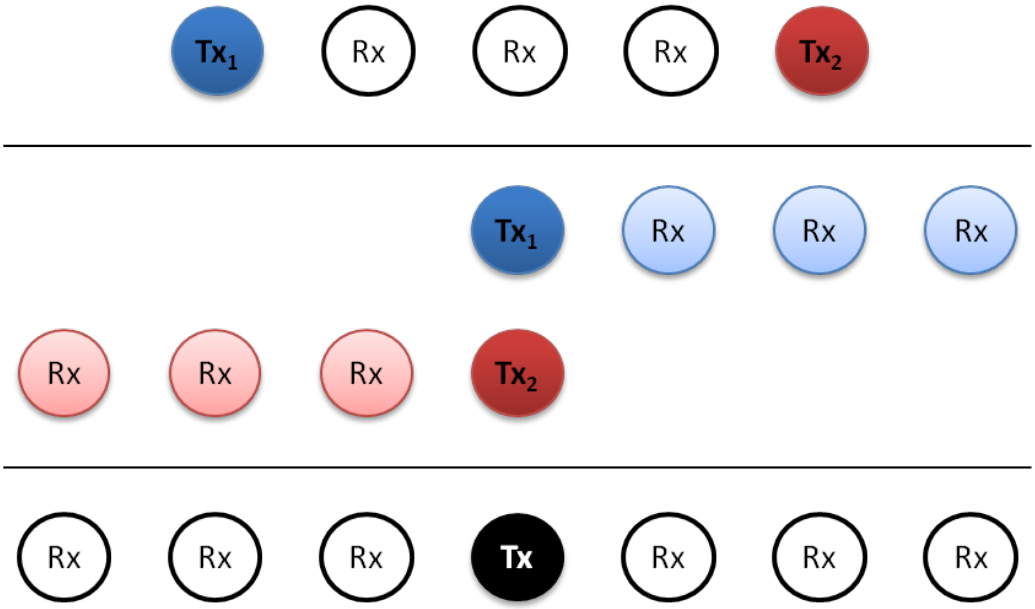

Figure 3.9: A MIMO radar (top) and its resulting virtual array (bottom). The first row shows the MIMO radar with two Tx and three Rx antennas. The second and third row show the layout considering only one Tx. The fourth row shows the equivalent array which is a combination of the two independent layouts.

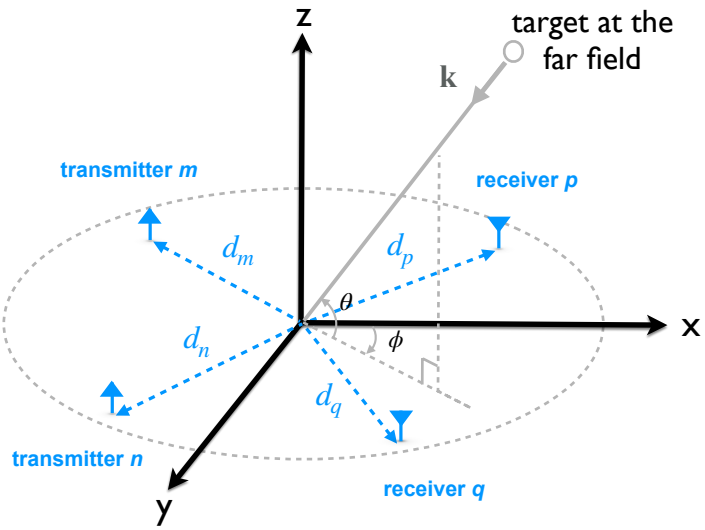

Figure 3.10: A coherent MIMO radar with two transmit antennas and two receive antennas closely separated.

synchronized and calibrated in phase and time, the signal seen by the receive antenna m due to the transmitter antenna p can be denoted as

$$v(\mathbf{d}_m, t + \Delta t_p, r) = \sum_i a_{i,r}\, e^{j\,(-2\pi f_{i,r}(t+\Delta t_p)+\phi_{i,r}+\mathbf{k}_i\,\mathbf{d}_p+\mathbf{k}_i\,\mathbf{d}_m)} + \eta(\mathbf{d}_m), \quad (3.15)$$

where $\mathbf{d}_p \in \mathbb{R}^3$, and $\mathbf{d}_m \in \mathbb{R}^3$ are the vector distances of the transmit antenna p and receive antenna m, respectively, $a_{i,r}$, $f_{i,r}$, and $\phi_{i,r}$ are backscatter coefficient amplitude, Doppler frequency, and phase offset of the target at a given range gate r and direction $\mathbf{k}_i$, Δt_p is the time separation between the transmission of the first transmitter and the transmitter p, and $\mathbf{k}_i = (2\pi/\lambda)\,[\cos\theta_i \cos\phi_i,\ \cos\theta_i \sin\phi_i,\ \sin\theta_i]$ is the wave vector which is a function of the azimuth and elevation angle ϕ_i and θ_i. The summation is over a range of angles which is limited by the illuminated area.

We start with a pulsed MIMO radar using time diversity since the signal model is much simpler and the signals can easily be decoupled for each transmit-receive link using the time information. As a result we get

$$v(\mathbf{d}_m, \mathbf{d}_p, t, r) = \sum_i a_{i,r}\, e^{j\,(-2\pi f_{i,r}(t+\Delta t_p)+\phi_{i,r}+\mathbf{k}_i\,\mathbf{d}_p+\mathbf{k}_i\,\mathbf{d}_m)} + \eta(\mathbf{d}_m), \quad (3.16)$$

where $v(\mathbf{d}_m, \mathbf{d}_p, t, r) \in \mathbb{C}$ is the measured baseband signal seen by the virtual receiver mp for a given time t and range gate r.

Since the aim of this chapter is to describe the radar signal model mathematically to find the equivalent virtual array, and to see how this virtual array helps to improve the angular resolution of a radar system, (3.15) is simplified as follows:

$$v(\mathbf{d}_m, \mathbf{d}_p, t, r) = \sum_i \sigma(\mathbf{k}_i, t, r)\, e^{j\,\mathbf{k}_i\,(\mathbf{d}_p+\mathbf{d}_m)}\, e^{j f_{i,r}\Delta t_p} + \eta(\mathbf{d}_m), \quad (3.17)$$

where $\sigma(\mathbf{k}_i, t, r) = a_{i,r}\, e^{j\,(-2\pi f_{i,r} t+\phi_{i,r})}$ is the backscatter coefficient amplitude and phase for a given range gate r and direction of arrival $\mathbf{k}_i$. Note that this equation is quite similar to the phased array equation described in section 2.5.1 (2.52). However, there are two big differences: First, the phase offset due to Doppler and time separation between transmissions ($f_{i,r}\Delta t_p$), which must be corrected before any kind of analysis. For the purposes of this section we consider that this phase offset is calibrated and equal to 0. Secondly, the signal $v(\mathbf{d}_m, \mathbf{d}_p, t, r)$ does not only depend on the position of the receiver $\mathbf{d}_m$ but it also depends on the position of the transmitter $\mathbf{d}_p$. In the literature,

$\upsilon(\mathbf{d}_m, \mathbf{d}_p)$ is better known as the "virtual" receiver mp, whose virtual location is given by $\mathbf{d}_{mp} = \mathbf{d}_p + \mathbf{d}_m$.

Depending on the selection of the transmitters' and receivers' positions, a larger virtual array might be created consisting of P M virtual antennas, where P is the number of transmitters and M is the number of receivers. Recall that the angular resolution depends directly on the radar aperture. The larger the array, the higher the angular resolution. Figure 3.11 shows a MIMO configuration with a vertical transmitting array with seven antennas and a horizontal receiving array with seven antennas. Notably, the resulting virtual array with 49 unique antennas is a perfect and uniform 2D-array, which offers us much higher degrees of freedom in the spatial domain compared to the Tx or Rx array. It improves not only the angular resolution (in the diagonal direction) [BF03], but it also increases the capacity of the system to identify targets in 3D.

The selection of the Tx and Rx array, i.e., the MIMO antenna array design problem, is not a trivial task. If the location of the Tx and Rx antennas can be selected arbitrarily, diverse design techniques can be used to select the best antenna locations. Some examples of antenna array design are based on hexagonal arrays [DRV15] or polynomial factorization [WSC13]. On the other hand, if the antenna array is already installed and the problem is the selection of the best subset, genetic algorithms might be useful to find the best Tx and Rx array combination [Hau94]. The MIMO antenna array design problem is out of the scope of this thesis since it highly depends on the scenario. Despite the small but important difference between the MIMO and the phased array equation, the same processing techniques explained in Chapter 2 can be used to recover the range, frequency, and direction of arrival information from virtual phased arrays.

Until this point, the signal model was described for MIMO radar using time diversity. As described before, time diversity is restricted to systems with a very low number of transmitters. To extend the MIMO concept to systems with a high number of transmitting antennas, we have to combine the concept of MIMO and waveform diversity. In (3.17), σ includes implicitly the transmitted waveform $w(r)$; which for a pulsed radar transmitting a single pulse is represented ideally by a Dirac delta function $w(r - r_0) = \delta(r_0)$. In the next section, we describe the signal model when the waveform is distinct from the Dirac delta function. It could be a pulsed radar using pulse compression techniques or a CW radar using waveform diversity. Hereafter, pulse coded radars are considered a special case of CW radars using waveform diversity (phase-coded).

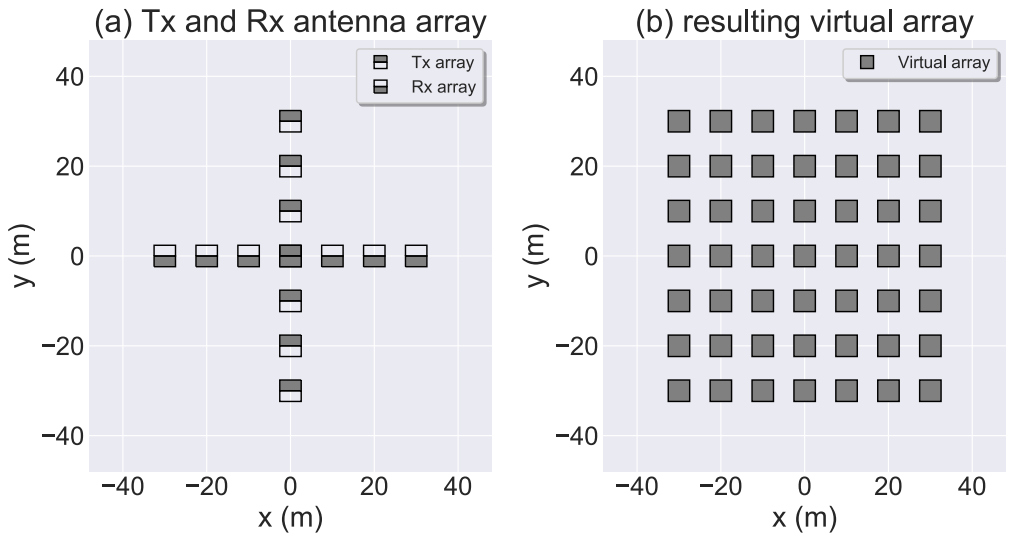

Figure 3.11: (a) A MIMO antenna array with 7 Tx antennas and 7 Rx antennas, (b) The resulting MIMO virtual antenna array consisting of 49 antennas.

3.6 Far-field signal model of CW-MIMO radars

MIMO systems can also be implemented with continuous wave (CW) radars where the carrier wave might be modulated in amplitude, phase, or frequency. In the literature, the modulating envelope is commonly known as the waveform. As seen in section 2.3.2, for a CW radar employing one transmitter with an arbitrary waveform $w(r)$, (3.17) becomes

$$y(\mathbf{d}_m, t, l) = \sum_r \sum_i w(l-r)\ \sigma(\mathbf{k}_i, t, r)\ e^{-j\,\mathbf{k}_i(\mathbf{d}_p+\mathbf{d}_m)} + \eta(\mathbf{d}_m, t, l), \qquad (3.18)$$

where $y(\mathbf{d}_m, t, l)$ is the measured complex baseband signal seen by the receiver that does not distinguish which transmitter originated the return signal, and l is the apparent range. The model is described using only one transmitter and then it will be extended the to a model with many transmitters. Although it is not possible to recognize which transmitter originated the radar return, the phase shift $(\mathbf{k}_i\mathbf{d}_p)$ due to the position of the transmitter still influences the measured signal.

Unlike pulsed radars, where v from (3.17) represents a measured value corresponding to one range r only. In CW-radars, y results from the convolution between the transmitted

waveform and all the scatters along the range R. To estimate σ from the measurements y, (3.18) can be inverted directly. However, for real applications this is computationally expensive due to the high dimensionality of σ. In order to reduce the computational complexity and to apply the same forthcoming processing techniques to both the pulsed radar and the CW-radar data, the CW-radar signal measurements y can be expressed as a function of an equivalent pulsed radar measurements υ from (3.17) as follows

$$y(\mathbf{d}_m, t, l) = \sum_r w(l-r)\ \upsilon(\mathbf{d}_m, \mathbf{d}_p, t, r) + \eta(\mathbf{d}_m, t, l). \tag{3.19}$$

To solve this equation, we divide the problem in two parts (a) First, retrieval of the unknown parameter $\upsilon(\mathbf{d}_m, \mathbf{d}_p, t, r)$ (decoding) for all the range gates r and one transmit-receive link at a time, and then (b) recovery of the angle information $\sigma(\mathbf{k}, t, r)$ for one range at a time using (3.17).

3.6.1 Signal recovery

In order to recover the signal y from (3.19), the equation can be simplified expressing it in matrix form and solving the problem for a given receiver m and a delay t at a time. Considering noisy measurements we get

$$\mathbf{y}_m = \mathbf{\Phi}\boldsymbol{\upsilon}_{mp} + \boldsymbol{\eta}_m, \tag{3.20}$$

where $\mathbf{y}_m \in \mathbb{C}^L$ is the measurement vector, $\boldsymbol{\upsilon}_{mp} \in \mathbb{C}^R$ is the unknown parameter vector for all the range bins, $\boldsymbol{\eta}_m \sim N(0, \mathbf{\Sigma}_m)$ is the receiver noise, and $\mathbf{\Phi} \in \mathbb{C}^{LxR}$ is the sensing matrix, which is a circulant matrix defined by the transmit waveform vector $\mathbf{w} \in \mathbb{C}^L$, where $L \geq R$ is the waveform length, and R is the number of range gates. With the consideration mentioned above, the sensing matrix is given by

$$\mathbf{\Phi} = \begin{bmatrix} w_0 & w_{L-1} & w_{L-2} & \dots & w_{L-R+1} \\ w_1 & w_0 & w_{L-1} & \dots & w_{L-R+2} \\ w_2 & w_1 & w_0 & \dots & w_{L-R+3} \\ \vdots & \vdots & \vdots & \ddots & \vdots \\ w_{L-1} & w_{L-2} & w_{L-3} & \dots & w_{L-R} \end{bmatrix}. \tag{3.21}$$

Equation (3.20) is valid for radars using pulse compression techniques as well as for CW radars using waveform diversity. The difference lies in that, for pulse radars most of the w_i terms are zero.

Note that all previous equations consider only one transmit waveform. When multiple antennas are transmitting at the same frequency but with different waveforms (MIMO using waveform diversity) the cross-interference between waveforms might degrade the performance of the system. In such systems, with several transmit antennas using waveform diversity, (3.20) becomes

$$\mathbf{y}_m = \sum_{p=1}^{P} \mathbf{\Phi}_p \boldsymbol{\upsilon}_{mp} + \boldsymbol{\eta}_m, \tag{3.22}$$

where $\mathbf{\Phi}_p \in \mathbb{C}^{LxR}$ is the sensing matrix due to the transmit waveform $\mathbf{w}_p$, and P is the number of antennas transmitting different waveforms. Equation (3.22) can be written as

$$\mathbf{y}_m = \mathbf{\Phi}\mathbf{x}_m + \boldsymbol{\eta}_m, \tag{3.23}$$

$$\text{with} \quad \mathbf{x}_m = \begin{bmatrix} \boldsymbol{\upsilon}_{m1}^T & \boldsymbol{\upsilon}_{m2}^T & \dots & \boldsymbol{\upsilon}_{mP}^T \end{bmatrix}^T, \tag{3.24}$$

$$\text{and} \quad \mathbf{\Phi} = \begin{bmatrix} \mathbf{H}_1 & \mathbf{H}_2 & \dots & \mathbf{H}_P \end{bmatrix}, \tag{3.25}$$

where $\mathbf{y}_m \in \mathbb{C}^L$, $\mathbf{x}_m \in \mathbb{C}^N$, $\mathbf{\Phi} \in \mathbb{C}^{LxN}$, and $N = PR$ is total number of unknowns equal to the number of transmitters times the number of range gates.

It is known that the matrix $\mathbf{\Phi}$ defines the range and Doppler resolution of the MIMO system [SFR08; CV08b], which can be characterized by the ambiguity function as in (3.14) or in matrix form as

$$\mathbf{C} = \mathbf{\Phi}^H \mathbf{\Phi}, \tag{3.26}$$

where $\mathbf{C}$ is equivalent to the ambiguity function. Ideally, the matrix $\mathbf{C}$ should be equal to the identity matrix. However, this is not the case in real applications with multiple transmitters. Many studies on waveform design [Fri07; Li+08; CHM09; GDP12; SBL14] focus on finding the best $\mathbf{\Phi}$ based on the orthogonality between codes. Others proposed special algorithms to reduce the cross-correlation between codes and avoid undesired effects [Kay09; SZW10; Fri11].

The retrieval problem reduces to find an inverse of the matrix $\mathbf{\Phi}$ such that

$$\hat{\mathbf{x}}_m = \mathbf{\Phi}^{-1}\mathbf{y}_m. \tag{3.27}$$

In the literature, several techniques exist to find an approximate inverse when the problem is overdetermined ($L > N$), such as the pseudo-inverse matrix [Gre59; Ste77], the matched filter estimator (MFE) [Tur60], the least squares estimation (LSE) [Ste77; Bjö96], the minimum mean squares error estimator (MMSE) [Tri+12; Tag+17], the maximum a posteriori estimator (MAP) [BD19], and when there are errors in both sides of the equation the total least squares estimator (TLSE) [Van+07; VV91].

In this work, we use the approach described in section 3.3.2 to select waveforms with reduced cross-talk. Because of the trade-off between performance and speed, we recommend the weighted least squares estimator [Vie+16] to recover the backscatter signals in overdetermined linear problems

$$\mathbf{\Phi}^{-1} \approx (\mathbf{\Phi}^H \mathbf{\Sigma} \mathbf{\Phi})^{-1} \mathbf{\Phi}^H \mathbf{\Sigma}, \tag{3.28}$$

where Σ is the inverse of the covariance matrix error. If the covariance is not known, it can be replaced by the identity matrix.

When the problem is underdetermined ($L < N$), the addition of extra constrains is necessary to find a unique solution. Some very well known algorithms are the regularized least squares estimation (RLSE) [AF14], the truncated singular value decomposition (tSVD) [Han87], the least absolute shrinkage and selection operator (LASSO) [Tib96; PC08], the Tikhonov regularization [Tik+95; EL97], and least angle regression (LARS) [Efr+04]. In section 2.3.1.1, we described some of them applied to arbitrary v_{mp} signals. For particular cases, when the signal v_{mp} satisfies certain properties, advanced algorithms like CS can be applied to obtain a cleaner solution. One of these special cases are explained in Chapter 5.

Once all the $\boldsymbol{v}_{mp}$ signals are recovered, they can be combined to estimate the angle of arrival (AOA). The next subsection describes the signal analysis to estimate AOA in a MIMO radar.

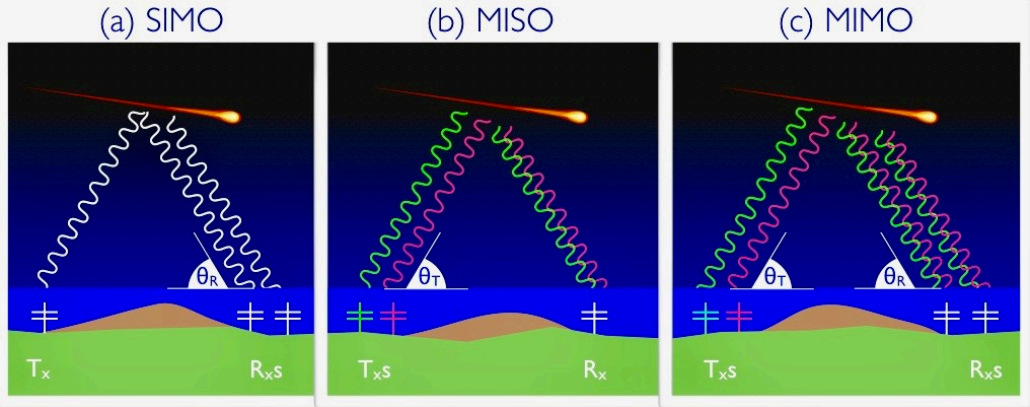

Figure 3.12: Bistatic radar configurations to estimate target's location (a) SIMO to estimate AOA, (b) MISO to estimate AOD, and (c) MIMO to estimate both AOA and AOD at the same time. See text for more details.

3.7 Estimation of direction of arrival and departure in MIMO radars

Angle of arrival (AOA) estimation of narrowband targets located at the far-field employing antenna arrays is a topic that has been highly discussed in the past decades [VB88; New+10; Mor+13]. AOA and angle of departure (AOD) estimation can be done combining signals at multiple receive antennas or signals coming from multiple transmit antennas, respectively. Let us consider the monostatic MIMO radar system illustrated in Fig. 3.10, with a pair of transmit antennas p and q and a pair of receive antennas m and n closely separated at positions $\mathbf{d}_p$, $\mathbf{d}_q$, $\mathbf{d}_m$, and $\mathbf{d}_n$, respectively. The transmit signals are independent, and the return signals for each transmit-receive link are decoupled as described in the previous section. Therefore, a larger virtual receive array can be formed by combining all the transmit-receive signals.

Since the information for each range bin r is independent, we make the analysis for one range bin only. Moreover, considering a maximum of one target with the same Doppler bin and at the same wave vector, the signal model can be treated as a superposition of independent narrow band signals in the frequency domain. The signal model is given by

$$\upsilon(\mathbf{d}_m, \mathbf{d}_p, f, r) = \sum_{i=1} \sigma(\mathbf{k}_i, f, r)\; e^{-j\mathbf{k}_i(\mathbf{d}_m+\mathbf{d}_p)}, \tag{3.29}$$

In this section, we are interested in the target's reflectivity $\sigma(\mathbf{k}_i, f, r)$ as a function of the wave vector $\mathbf{k}_i$. The radar return σ can be estimated from the measurements υ by

applying digital beamforming (2.68). Nevertheless, as explained in Chapter 2, most of the atmospheric targets are stochastic in nature. This means that only the statistical properties of the target can be determined, namely, the expected value and its variance. The expected value of the angular scattered power distribution is given by $b(\mathbf{k}, r) = \langle \sigma^2(\mathbf{k}, f, r) \rangle$, and it is also known as the brightness function.

As described in Chapter 2, we can use the spatial cross-correlation ρ between radar returns from two different transmit-receive paths to estimate the brightness. The spatial correlation is given by

$$\rho(\Delta\mathbf{d}_{pq}, \Delta\mathbf{d}_{mn}, f, r) = \Big\langle \upsilon(\mathbf{d}_m, \mathbf{d}_p, f, r)\ \upsilon^*(\mathbf{d}_q, \mathbf{d}_n, f, r) \Big\rangle, \tag{3.30}$$

where $\Delta\mathbf{d}_{mn} = \mathbf{d}_m - \mathbf{d}_n$ is the spatial separation between receivers, and $\Delta\mathbf{d}_{pq} = \mathbf{d}_p - \mathbf{d}_q$ is the spatial separation between transmitters. Likewise, $()^*$ represents the conjugate, and $\langle . \rangle$ stands for the expectation along time. Replacing (3.29) in (3.30) we get

$$\begin{aligned} &\rho(\Delta\mathbf{d}_{pq}, \Delta\mathbf{d}_{mn}, f, r) \\ &\quad = \Big\langle \sum_{i=1} \sigma(\mathbf{k}_i, f, r)\, e^{j\mathbf{k}_i(\mathbf{d}_m + \mathbf{d}_p)} \sum_{l=1} \sigma(\mathbf{k}_l, f, r)\, e^{-j\mathbf{k}_l(\mathbf{d}_n + \mathbf{d}_q)} \Big\rangle. \end{aligned} \tag{3.31}$$

Considering that signals coming from different directions are distant and uncorrelated, their expected cross-correlation is zero. The cross-correlation is different than zero only when $\mathbf{k}_i = \mathbf{k}_l$. Replacing in (3.32):

$$\rho(\Delta\mathbf{d}_{pq}, \Delta\mathbf{d}_{mn}, f, r) = \sum_{i=1} \Big\langle \sigma(\mathbf{k}_i, f, r)\, \sigma(\mathbf{k}_i, f, r) \Big\rangle e^{-j\mathbf{k}_i(\Delta\mathbf{d}_{pq} + \Delta\mathbf{d}_{mn})} \tag{3.32}$$

$$= \sum_{i=1} b(\mathbf{k}_i, r)\, e^{j\mathbf{k}_i(\boldsymbol{\Delta}\mathbf{d}_{pq} + \boldsymbol{\Delta}\mathbf{d}_{mn})}. \tag{3.33}$$

Equation (3.33) presents two caveats (a) implementation imperfections such as the difference in amplifiers' gain, cables' attenuation, and filters' gain are not taken into account, and (b) phase shift caused by time difference between transmitters is not considered. Phase offset calibration is described with more details in the next subsection. To compensate the gain's difference between two different transmit-receive links, the spatial correlation can be normalized using the signal power $|\upsilon_{mp}|^2$ and noise variance η^2. As

such the spatial cros-correlation is obtained by

$$\rho(\Delta\mathbf{d}_{pq}, \Delta\mathbf{d}_{mn}, f, r) = \frac{\langle \upsilon_{mp}\, \upsilon_{nq}^{*} \rangle}{\sqrt{\langle |\upsilon_{mp}|^2 - \eta_1^2 \rangle \langle |\upsilon_{nq}|^2 - \eta_2^2 \rangle}}, \tag{3.34}$$

$$= \sum_i b(\mathbf{k}_i, r)\, e^{j\mathbf{k}_i(\Delta\mathbf{d}_{pq} + \Delta\mathbf{d}_{mn})}. \tag{3.35}$$

Equation (3.35) is a generalized form of the radar imaging equation shown in (2.65), which considers only one transmit antenna. Similarly, radar imaging can be applied to systems consisting of only one receiver but with a transmit antenna array, i.e., a multiple–input single–output (MISO) configuration. In such case (3.35) reduces to

$$\rho(\Delta\mathbf{d}_{pq}, \Delta\mathbf{d}_{mn} = 0, f, r) = \sum_i b(\mathbf{k}_i, r)\, e^{j\mathbf{k}_i\, \Delta\mathbf{d}_{pq}}, \tag{3.36}$$

indicating that the position of a single target can also be estimated using only one receive antenna and a transmit array.

Figure 3.12 shows a comparison of three bistatic radar configurations to determine a meteor trail's location. The three configurations are considered as a coherent MIMO since all the transmit-receive paths have the same Bragg-vector. For a bistatic radar, (3.35) can be rewritten considering the incident k_T and the scattered k_R wavevector

$$\rho(\Delta\mathbf{d}_{pq}, \Delta\mathbf{d}_{mn}, f, r) = \sum_i b(i, r)\, e^{j\mathbf{k}_{T_i}\Delta\mathbf{d}_{pq} + j\mathbf{k}_{R_i}\Delta\mathbf{d}_{mn}}. \tag{3.37}$$

Performances of single-input multiple-output (SIMO) radars and multiple–input single–output (MISO) radars are expected to be the same since the number of antennas in the array are the same. However, MIMO configurations' performance exceeds the two previous configurations because of the resulting larger number of independent measurements and the improved observing geometry [Urc+18], i.e., the target can be tracked from two different view angles avoiding problems related to low elevation angles. Errors associated to low elevation angles are generally caused by antenna coupling. Other possible source of errors in a MIMO radars and ways to optimize a MIMO configuration are discussed in the following subsections.

3.7.1 Relative compensation of phase offsets

In (3.29) no instrumental phase calibration was considered. Phase offsets might be associated to the receivers, the transmitters, and the time difference between transmissions. Usually phase offsets are caused by differences in cable length, amplifiers, or filters, which can be affected by the air temperature. Even though they can be compensated at the beginning of an experiment, the phases might change with time. Considering all the instrumental phase offsets (3.29) becomes

$$\upsilon_{mp}(f,r) = \sum_{i=1} \sigma(\mathbf{k}_i, f, r)\, e^{j(-2\pi f \Delta t_p + \mathbf{k}_i(\mathbf{d}_m+\mathbf{d}_p)+\phi_m+\phi_p)}, \tag{3.38}$$

where ϕ_m is the instrumental phase offset of receiver m, and ϕ_p is the instrumental phase offset of transmitter p.

There are many ways to calibrate a MIMO system. However, the results presented in this work have been done using the following recipe:

1. Calibrate the instrumental phase difference $\Delta\phi_{mn}$ between receivers.
2. Calibrate the phase offset $(2\pi f \Delta t_p)$ due to the time difference between transmissions and Doppler shift.
3. Calibrate the instrumental phase difference $\Delta\phi_{pq}$ between transmitters.

First, phase calibration of a receiving array is a very well known topic and it is not described in this thesis. For example, Chau, et.al. [Cha+08] propose diverse approaches for absolute and relative calibration using radio stars, meteor echoes, radio beacons, and self-calibration approaches.

Secondly, to compensate the phase offset due to the time difference between transmitters, the data analysis has to be done in the frequency domain. Let us consider two transmitters p and q transmitting at time t and time $t + \Delta t_{pq}$, and only one receiving antenna m. For a given Doppler the signals at the virtual receivers are proportional to

$$\upsilon_{mp}(f,r) \propto e^{-j2\pi f t}, \tag{3.39}$$

$$\upsilon_{mq}(f,r) \propto e^{-j2\pi f (t+\Delta t_{pq})}, \text{ and} \tag{3.40}$$

$$\langle \upsilon_{mp}(f,r)\ \upsilon^*_{mq}(f,r) \rangle \propto e^{j2\pi f \Delta t_{pq}}. \tag{3.41}$$

To calibrate the system, it would be enough to multiply the signal υ_{mq} with the complex exponential $e^{2\pi f \Delta t_{pq}}$ for each Doppler frequency f.

Finally, one of the most tricky parts is to compensate the phase offsets of the transmit array. Similar to what is done to calibrate a receiving array, we can use a point-like target with a known position such as an airplane, a meteor head, or a drone where the phases at each transmit antenna are also known and they can be compensated. As in receive phase arrays, once the phases are calibrated, they might change over time. In order to keep the phases calibrated relatively, the phase offsets might be measured over time and be corrected online.

When no drones or airplanes are available, relative phase calibration of a transmit array can be done by taking advantage of the redundant virtual receivers generated for two different transmit antennas. Two virtual receivers located in the same virtual position, must have the same offset, i.e., they must have a phase difference equal to zero. Let us consider that υ_{mp} and υ_{nq} are two virtual receivers located at the same virtual position where phase offsets due to the receive array and the transmit time difference have already been calibrated. Then

$$\upsilon_{mp}(f,r) \propto e^{-j\phi_p}, \tag{3.42}$$

$$\upsilon_{nq}(f.r) \propto e^{-j\phi_q}, \tag{3.43}$$

$$\langle \upsilon_{mp}(f,r)\ \upsilon^*_{nq}(f,r) \rangle \propto e^{-j(\phi_p - \phi_q)}. \tag{3.44}$$

We know that the phase offset $\Delta\phi_{pq} = (\phi_p - \phi_q)$ must be zero since υ_{mp} and υ_{nq} are located at the same virtual position. When the phases are not calibrated, the measured phase difference $\Delta\tilde{\phi}_{pq}$ is different from zero. Taking one transmitter as a reference, i.e., $\phi_p = 0$, we can calibrate the other transmitter using

$$\phi_q = \phi_p + \Delta\tilde{\phi}_{pq}, \tag{3.45}$$

$$\phi_q = \Delta\tilde{\phi}_{pq}. \tag{3.46}$$

3.7.2 Angular resolution

In the previous chapter, we stated that the angular resolution is defined by the number of antennas and the maximum separation between them. Depending on the MIMO configuration, these parameters might change. Here we analyze the implications of selecting one or another configuration. The analysis is done in 1D but is easily expandable to 3D.

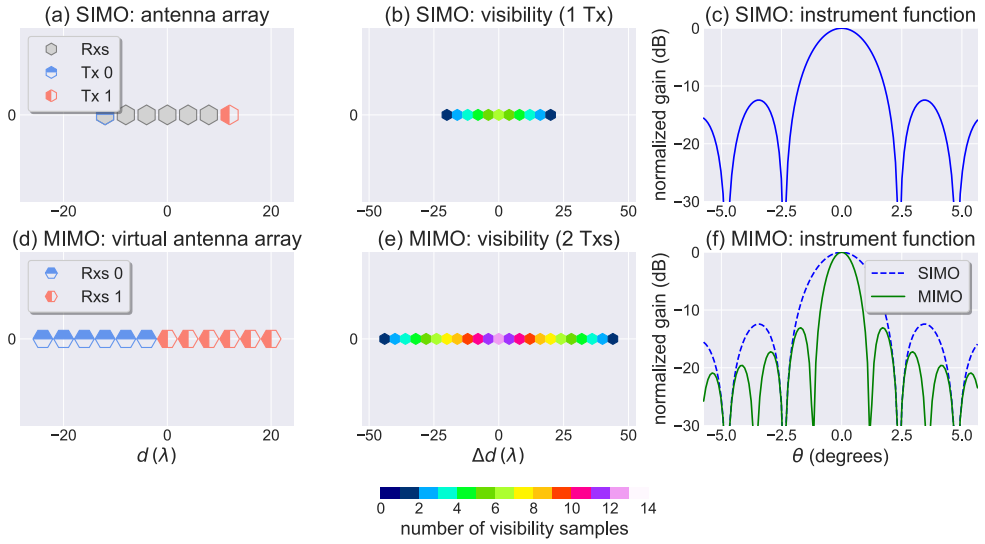

Figure 3.13: Angular resolution comparison between SIMO and MIMO. (a) Transmit and receive array (b) Visibility samples considering only one transmitter and the receive array, i.e., SIMO. (c) Point spread function the corresponding visibility. (d) Resulting virtual array by using MIMO. (e) Visibility samples corresponding to the virtual array, i.e., MIMO. (f) Point spread function for MIMO.

Let us consider the uniform linear array shown in Fig. 3.13(a), consisting of a transmit array with two antennas and a receive array with six antennas. The spatial points at which the visibility $\rho(\Delta\mathbf{d}_{pq}, \Delta\mathbf{d}_{mn}, ...)$ is sampled are known as baselines. The resulting baselines for MIMO can be expressed as $\Delta\mathbf{d} = \Delta\mathbf{d}_{pq} + \Delta\mathbf{d}_{mn}$. For SIMO $\Delta\mathbf{d}_{pq} = 0$ and hence $\Delta\mathbf{d} = \Delta\mathbf{d}_{mn}$ holds. Fig. 3.13(b) shows the baselines for the SIMO configuration in which only one transmitter is considered. Note that many baselines are located at the same position since the receive array is uniform and a combination of different antennas result in the same baseline. Baselines located in the same position are known as redundant baselines. The number of redundant baselines are color coded in Fig. 3.14(b) and (e).

To evaluate the performance of antenna arrays, the point spread function or instrument function is commonly used as a metric. The point spread function of an array is obtained by inverting (3.35) for all the vectors k assuming the presence of only one punctual target at k_0, i.e., $(\mathbf{k}_i, r) = 0$ for $i \neq 0$. Under that condition the visibility reduces to

$$\rho_0(\Delta\mathbf{d}, f, r) = b(\mathbf{k}_0, r)\, e^{j\mathbf{k}_0(\Delta\mathbf{d})}. \tag{3.47}$$

The point spread function $\hat{b}$ is obtained by applying the inverse Fourier transform to the visibility, which can be written as

$$\hat{b}(\mathbf{k}, r) = \sum_i \rho_0(\Delta\mathbf{d}_i, f, r)\, e^{-j\mathbf{k}(\Delta\mathbf{d}_i)}. \tag{3.48}$$

Replacing (3.47) in (3.48), we get

$$\hat{b}(\mathbf{k}, r) = \sum_i b(\mathbf{k}_0, r)\, e^{j\mathbf{k}_0(\Delta\mathbf{d}_i)}\, e^{-j\mathbf{k}(\Delta\mathbf{d}_i)}, \tag{3.49}$$

where

$$C(\mathbf{k}) = \sum_i e^{j\mathbf{k}_0(\Delta\mathbf{d})}\, e^{-j\mathbf{k}(\Delta\mathbf{d}_i)} \tag{3.50}$$

$$= \sum_i e^{-j(\mathbf{k}-\mathbf{k}_0)(\Delta\mathbf{d}_i)} \tag{3.51}$$

is known as the angular ambiguity function. It characterizes the angular resolution achieved by an antenna array. Plainly, the ambiguity function does not depend on the selected $\mathbf{k}_0$. An ideal antenna array has an angular ambiguity function equal to the Dirac delta function. However, this is not possible in practice. Conventional arrays have a limited number of visibility samples and hence a finite angular resolution. Fig. 3.13(c) shows the resulting angular ambiguity function or point spread function for the SIMO array considering $\mathbf{k}_0 = 0$. Clearly, the result is not close to a Dirac delta function. It contains a main lobe with a half-power beam width (HPBW) of 2° and sidelobes of $-14\,\mathrm{dB}$.

For uniform linear arrays with $\mathbf{k} = \frac{2\pi}{\lambda}\sin(\theta)$, the angular resolution $\Delta\theta$ and the maximum unambiguous angle θ_{max} are given by

$$\sin(\Delta\theta) = \frac{\lambda}{(\Delta d_{\text{max}})}, \text{ and} \tag{3.52}$$

$$\sin(\theta_{\text{max}}) = \frac{\lambda}{2(\Delta d_{\text{min}})}. \tag{3.53}$$

In our example, the MIMO array can be expressed as a (virtual) uniform array containing twelve antennas. Figures 3.13(d), (e), and (f) show the resulting virtual array, visibility, and instrument function for the MIMO configuration, respectively. Notably, the angular resolution achieved by our MIMO configuration is two times better than the SIMO's. This is explained by the maximum baseline (Δd_{max}) for the MIMO case, which is two times larger than the SIMO's maximum baseline. Notice that, even though the sidelobes have

been modified the peak sidelobe is still $\approx -14\,\mathrm{dB}$

3.7.3 Redundant baselines

In most of the practical applications, the number of redundant baselines by applying MIMO might be very high since current atmospheric radars were not designed for such kind of applications, and they are not optimized for MIMO configurations. Moreover, the distribution of the redundant baselines might be irregular over the sampling domain. This section investigates the effects of redundant visibility samples and their implications in the angular resolution.

To understand the impact of redundant visibility samples, we analyze the instrument function of two arbitrary antenna arrays, where the first one has no redundant visibility samples, and the second one does. Figure 3.14 illustrates the two arbitrary arrays, their visibilities, and their resulting instrument functions. According to the conventional definition of the achievable angular resolution of an antenna array described in (3.53), these two arbitrary radars should have the same angular resolution since the maximum baseline for both of them are the same. However, if we analyze the resulting instrument function for both cases, we notice that they don't have the same angular resolution. Surprisingly, the angular resolution or half-power beam width (HPBW) of the second array, which contains a higher number of antennas, is not better than the first one. Its main lobe is slightly wider, which intuitively is not expected. Nevertheless, if we observe the resulting sidelobes, the second array has sidelobe peaks reduced by at least $8\,\mathrm{dB}$.

These results can be explained by the angular ambiguity function considering only unique (non-redundant) baselines tapered by the number of repetitions.

$$C(\mathbf{k}) = \sum_{u} h(\Delta\mathbf{d}_u)\, e^{j(\mathbf{k}_0-\mathbf{k})(\Delta\mathbf{d}_u)}, \tag{3.54}$$

where $h(\Delta\mathbf{d}_u)$ is the weight or number of repetitions of a given baseline, and the summation is done over the unique baselines $\Delta\mathbf{d}_u$.

In our example, the weight function has a triangular shape, and the resulting instrument function is a convolution of the first array's instrument function and the triangular function. Therefore, the main lobe is widened, but the sidelobes are reduced. Depending on

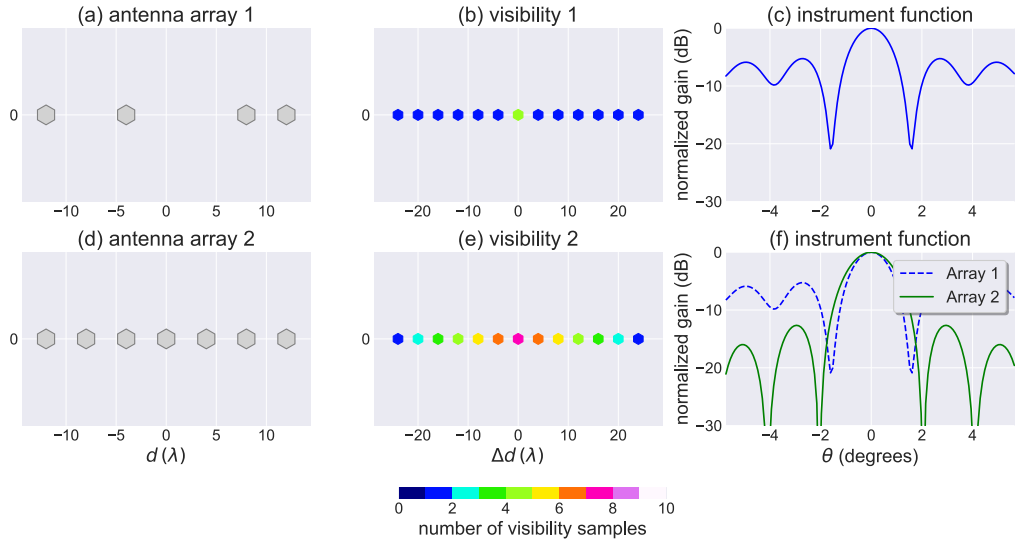

Figure 3.14: Same as Fig. 3.13 but for two arbitrary arrays. The first row shows the antenna array, the resulting visibility, and the instrument function of an array which contains non-redundant visibility samples. The second row shows an array with the same visibility samples but in which some of them are redundant.

the selection of the transmit and receive array, and hence the weight function, the sidelobes of the resulting virtual array might be reduced or enhanced. Diverse design techniques can be used to select the best antenna configuration, such as the one based on hexagonal arrays [DRV15] or polynomial factorization [WSC13]. If the antenna array is already installed and the problem is the selection of the best subset, genetic algorithms might be useful to find the best Tx and Rx array combination [Hau94].

3.7.4 Signal processing

When multiple targets coexist within the illuminated volume, it is desired to identify their position and their Doppler frequency as well. If (3.35) is analyzed in the time domain, we will only get the angular distribution of the scattered power. In order to estimate both Doppler information and AOA, the spatial cross-correlation is expressed in the frequency domain as in (3.35).

The difference between the spatial cross-correlation in the time domainand in the frequency domain lies in that the latter estimates B for each Doppler frequency f. This

means that the brightness can be separated in its different frequency components, similar to how a camera does when it takes a picture in color. The disadvantage is that the total number of time samples required to estimate the expected value $\hat{\rho}$ decreases in the same proportion as the number of selected frequency points. If the number of time samples is too few, the uncertainty in $\hat{\rho}$ might be problematic. This problem was described in section 2.5.2.

Since the analysis could be done in the time or the frequency domain, the domain and the time difference between transmitters Δt_{pq} is omitted intentionally hereafter. In the radio astronomy community, the visibility $\rho(\Delta\mathbf{d}_{mn}, \Delta\mathbf{d}_{pq})$ for a given range gate and frequency bin is also called the visibility sample at $(\Delta\mathbf{d}_{mn} + \Delta\mathbf{d}_{pq})$ and can be written in matrix form as

$$\boldsymbol{\rho} = \boldsymbol{\Phi}\mathbf{b} + \boldsymbol{\varepsilon}, \tag{3.55}$$

where $\boldsymbol{\rho} \in \mathbb{C}^V$ is a column vector comprising all the visibility samples, $\mathbf{b} \in \mathbb{R}^K$ is the brightness in vector form (flattened), $\boldsymbol{\Phi} \in \mathbb{C}^{VxK}$ is the Fourier matrix, and $\boldsymbol{\varepsilon} \sim N_{\mathbb{C}}(0, \Sigma)$ is the statistical uncertainty associated with estimating the cross-correlation with finite integration times. The number of visibility samples $V = PM(PM+1)/2$ represents the total number of virtual receiving pairs and it is a function of the number of transmitters P and the number of receivers M. Likewise, K is the number of wave number directions or (image) pixels.

To simplify the notation we use $\Delta\mathbf{d}_j = \Delta\mathbf{d}_{mn} + \Delta\mathbf{d}_{pq}$ for $j = 1, 2..., V$ to indicate all resulting (virtual) antenna separations, where V is the number of possible combinations between m, n, p, and q. Using this notation the Fourier matrix for a MIMO system is written as

$$\boldsymbol{\Phi} = \begin{bmatrix} e^{\mathbf{k}_1(\Delta\mathbf{d}_1)} & e^{\mathbf{k}_2(\Delta\mathbf{d}_1)} & \dots & e^{\mathbf{k}_K(\Delta\mathbf{d}_1)} \\ e^{\mathbf{k}_1(\Delta\mathbf{d}_2)} & e^{\mathbf{k}_2(\Delta\mathbf{d}_2)} & \dots & e^{\mathbf{k}_K(\Delta\mathbf{d}_2)} \\ \vdots & \vdots & \ddots & \vdots \\ e^{\mathbf{k}_1(\Delta\mathbf{d}_V)} & e^{\mathbf{k}_2(\Delta\mathbf{d}_V)} & \dots & e^{\mathbf{k}_K(\Delta\mathbf{d}_V)} \end{bmatrix} \tag{3.56}$$

The selection of the brightness grid $\mathbf{k}_i$ for $i = 1, 2..., K$, and the number of pixels K might be arbitrary. However, it should follow certain rules as in the Fourier transform. Firstly the angular resolution $\Delta k = \mathbf{k}_{i+1} - \mathbf{k}_i$ should be defined according to the maximum separation of two antennas $\Delta k = 1.0/\max(\mathbf{d}_j)$, similar to how the frequency resolution is defined by the total observation time in a Fourier transform $\Delta f = 1.0/T_{max}$.

Secondly, the number of pixels N should be less than the number of visibility samples M. When this is not the case, the problem becomes ill-posed, and inverse problem techniques are required to try to find a solution.

For most applications, MIMO helps to increase the number of independent measurements and to make the problem less underdetermined. However, it is necessary to add a regularizer to solve (3.55) if the problem is still underdetermined. So the problem reduces to find an estimate $\hat{v}$, which minimizes the following equation:

$$\hat{\mathbf{b}} = \arg\min_{\mathbf{b}} \{f(\mathbf{b}) + \lambda g(\mathbf{b})\}, \tag{3.57}$$

where $f(\mathbf{b})$ is the cost function, $g(\mathbf{b})$ is the regularizer, and λ is the Lagrange multiplier or the trade-off between the cost function and the regularizer. In most of the cases the L2-norm is selected as the cost function, i.e., $f(\mathbf{b}) = \|\boldsymbol{\rho} - \Phi\mathbf{b}\|_2^2$. The selection of the regularizer depends on the problem and so does the algorithm to solve the problem. Some of the most important inverse problems techniques are described in Chapter 2.5.2 for phased arrays and can be applied for the MIMO virtual array indistinctly.

Chapter 4

Resolving kilometer-scale dynamics in the mesosphere

In this chapter

4.1 Introduction

The dynamics in the mesosphere and lower termosphere (MLT) region are mainly dominated by atmospheric gravity wavess (AGWs), atmospheric tides, non-migrating tidal modes, and turbulent processes, whose effects can be observed by in-situ instruments, ground based remote sensors, and satellites. There are plenty of studies of the MLT region using observations from ground-based sensors such as meteor radars [Hoc05], MF radars [Hof+10; Pla+15], airglow imagers [Hec03], lidars [HL07; RGL08], and cameras

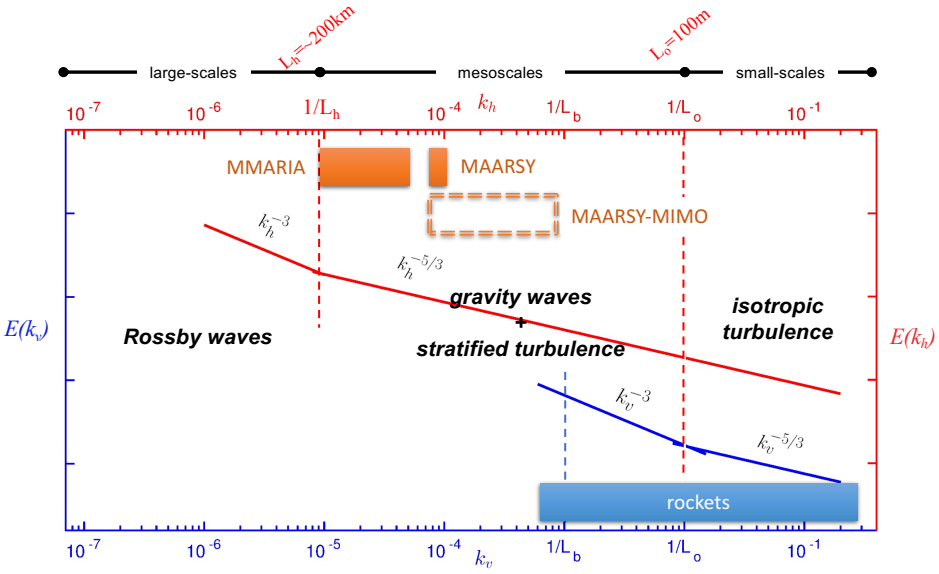

Figure 4.1: Simplified vertical and horizontal kinetic energy spectrum at mesospheric altitudes where regimes dominated by Rossby waves, gravity waves, and Kolmogorov turbulence are well identified. Similar to [Vie+19]. Vertical scales observed by rockets and horizontal scales resolved by the MAARSY and MMARIA radars are indicated with a blue and orange box, respectively. Horizontal scales resolved by the proposed radar technique based on MIMO (MAARSY-MIMO and SIMONe) are also shown.

[Pau+11; Dem+14], as well as satellites [Ern04; Ern+11] and numerical modelling. Although these observations have helped to understand the importance of AGWs in the MLT region, AGWs effects on the background flow and on the global circulation, and the mesosphere-ionosphere coupling [Vin15], none of them provided unambiguous spectral information of small and medium scale dynamics, which is important to understand turbulence processes and mesospheric instabilities in the MLT.

Turbulence processes and mesospheric instabilities generated by wave breaking, turbulence dissipation, and turbulence mixing, play an important role in the energy budget in the MLT, since they transport heat and momentum from and to other atmospheric altitudes [SV01]. To be able to quantify the contribution of each of these processes, 4D observations (space-time) at their different scales are required. Figure 4.1 shows an ideal kinetic energy spectrum of very well identified regimes (AGWs, Kolmogorov turbulence, and isotropic turbulence) and their scales in the horizontal and vertical direction. Note that scales of isotropic turbulence are in the order of tens of meters, whereby they are only measurable by in-situ sensors with very good resolution such as sounding rockets.

antenna aperture	angular resolution	spatial resolution	horizontal scales
90 m	3.6°	5.6 km	11.2 km
450 m	0.72°	1.12 km	2.2 km
900 m	0.36°	0.56 km	1.1 km

Table 4.1: Antenna aperture required to measure horizontal scales at 80km altitude

On the other hand, horizontal scales of Kolmogorov turbulence and AGWs are observable from kilometer-scales up to hundreds of kilometers.

In order to characterize Kolmogorov turbulence, mesospheric instabilities, and AGWs in the MLT, 4D measurements at small, medium and large-scales in the vertical and horizontal direction are desired. Spatial resolution in the vertical direction achieved by radars is about 150 m, which is within the desired range. However, the vertical coverage is still a challenging problem. In the horizontal direction, the problem lies in both coverage and resolution. Stober and Chau [SC15] recently proposed the use of meteor radar networks to measure 4D wind fields within a region of 300 km with a horizontal resolution of about 25 km. Thus, being able to resolve medium-scale dynamics in the order of 50 km to 150 km in the horizontal direction. Unfortunately, the network proposed by Stober and Chau is not scalable and its deployment in large areas is prohibitively costly. Chapter 5 describe a novel and scalable meteor radar network based on MIMO to overcome this problem.

On the other hand, small and kilometer scale dynamics have barely measured by remote sensors. Most of available measurements have been done by sounding rockets, which are also rare and costly. This chapter focuses on the capability of MAARSY combined with MIMO to measure medium-scales dynamics from 1 km to 30 km in the MLT, hereafter referred as kilometer-scale dynamics. Typical 4D radar observations with MAARSY have a horizontal resolution limited to a 5.4 km at 80 km altitude and a temporal resolution of a few minutes. Thereby, resolvable horizontal scales with MAARSY in a standard configuration are limited to 10 km to 30 km.

Measurements of kilometer-scale dynamics have not been previously obtained with radars due to the limited size of existing systems. As shown in Fig. 4.2, the angular resolution and hence the resolvable horizontal scales are limited by the antenna aperture. The larger the aperture, the smaller the resolvable horizontal scales. Table 4.1 shows the antenna aperture required to resolve horizontal scales at mesospheric altitudes ($\sim$80 km) with a

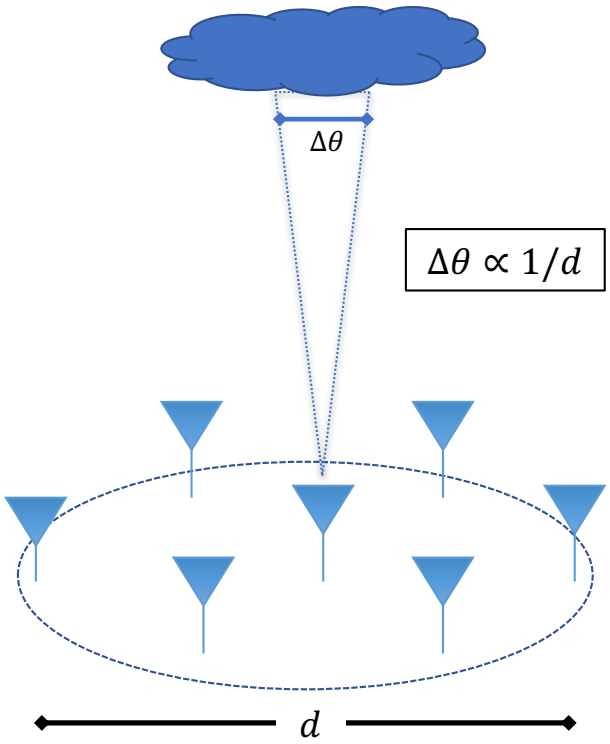

Figure 4.2: Maximum achievable angular resolution by an antenna array. Notice that the angular resolution $\Delta\theta$ is limited by the antenna aperture d.

radar operating at $50\,\mathrm{MHz}$. As the Nyquist theorem states, the sampling frequency must be at least two times the desired signal frequency. Thus, to characterize horizontal structures of $11.2\,\mathrm{km}$ or more in the spatial domain, at least a spatial resolution of $5.6\,\mathrm{km}$ is required. Likewise, to resolve kilometer-scale structures ($1.1\,\mathrm{km}$), a spatial resolution of $0.56\,\mathrm{km}$ is required, which is equivalent to having an antenna aperture of $900\,\mathrm{m}$. Unfortunately, such big antennas are not feasible in practice. Even the largest radars in the world, such as a Jicamarca and Arecibo, have an antenna aperture limited to few hundreds meters ($\leq$300 m) [HCM13; Alt98].

In the following sections, a radar approach based on coherent MIMO and radar imaging is described that allows PMSE observations with unprecedented angular resolution (0.6°) [Urc+18]. The technique combines the concept of MIMO to virtually enlarge the antenna size of MAARSY and radar imaging to obtain 4D measurements of kilometer-scale structures at mesospheric altitudes. The resulting resolution is evaluated by simulations and imaging specular meteor echoes. Furthermore, the advantage of the new technique

is evaluated with two events of 3D PMSE structures showing: (a) a Kelvin—Helmholtz instability (KHI) event drifting with the background wind with a horizontal wavelength of $8\,\mathrm{km}$ to $10\,\mathrm{km}$ and a period of $4\,\mathrm{min}$ to $7\,\mathrm{min}$, and (b) a possible gravity wave structure drifting against the background wind with a horizontal wavelength of $12\,\mathrm{km}$ to $16\,\mathrm{km}$ and a period of $15\,\mathrm{min}$ to $20\,\mathrm{min}$.

4.2 High resolution spatio-temporal measurements of the MLT dynamics

It is known that mesosphere and lower termosphere (MLT) dynamics (background wind flows) are not measurable directly by VHF radars. To track the background, some kind of tracer is required to make it detectable by radars. Typically, meteor trails [RLE53; Hoc05; Wil09], polar mesospheric winter echoes (PMWE) [LS15], and polar mesospheric summer echoes (PMSE) [JH03; Sto+13; GSC19] are used as natural tracers of the MLT dynamics over the polar regions. Particularly, PMSE is known to be a suitable tool to monitor the thermal and dynamic structure of the MLT region [RL04]. In this chapter, we use the middle atmosphere Alomar radar system (MAARSY) radar to perform 4D measurements of the MLT using PMSE as tracers.

Various authors have used MAARSY to study PMSE and its dynamics in 4D [Sto+12; Sto+13; SC16]. In the best case, the resolution achieved by MAARSY was limited to a couple of minutes in time, $150\,\mathrm{m}$ in altitude, and $\sim 5\,\mathrm{km}$ in the horizontal direction at mesospheric altitudes. The low resolution in the horizontal direction achieved by previous studies using MAARSY, and other modern radars, did not allow to characterize the kilometer-scales dynamics present in PMSE.

Here, MIMO and radar imaging techniques are implemented to improve the angular (spatial) resolution of MAARSY to be able to characterize kilometer-scale dynamics of the MLT in 4D (space-time). As described in the previous section, MIMO can be implemented employing time or waveform diversity. Although the performance of waveform diversity in MIMO is remarkably better than time diversity, its implementation would require infinitely long pulses to guarantee totally independence between transmitted

waveforms. This is not feasible in practice. However, long waveforms with good correlation properties can be generated using CW radars.

Unfortunately, monostatic radars like MAARSY do not posses CW capability and the use of only waveform diversity might result in highly correlated transmitted waveforms. Therefore, MIMO with time diversity is the most adequate diversity to measure PMSE dynamics with MAARSY. Since the application of MIMO with time diversity is not free, some restrictions during its application must be considered such as power loss, and a large sampling time. In particular, the feasibility of MIMO to observe any kind of phenomena will be restricted by its scattering intensity and its correlation time (spectral width). In the next section, we describe the nature of PMSE and why MIMO with time diversity is suitable to measure these kind of echoes.

4.2.1 Polar mesospheric summer echoes as tracers of the MLT dynamics

It is very well known that polar mesospheric summer echoes (PMSE) are very strong radar echoes produced by the presence of ice particles, turbulence, and free electrons in the mesopause at polar regions [Rap03]. Although the first observations of PMSE go back to the 1970s, the scattering mechanism of these echoes were in discussion for long time [HRC86; Zec+01]. Nowadays, we know that PMSE is caused by irregularities in the radar refractive index which satisfy the Bragg condition [RL04]. The Bragg condition states that for efficient scattering, the electron density irregularities must reveal structures at the half radar wavelength, which for VHF radars ($50\,\mathrm{MHz}$) it is $\sim 3\,\mathrm{m}$.

Previous studies of PMSE investigated the physical processes leading to formation of these irregularities [Rap03; RL04] in the mesopause. Under normal conditions, plasma irregularities at spatial scales significantly smaller than the inner scale of the turbulent velocity field (meter-scales) should not last, and hence should not be detectable by radars. To allow these plasma irregularities survive for much longer times, their electron diffusivity should somehow be reduced significantly. It is very well known that the electron diffusivity is reduced significantly in the presence of heavy charged ice aerosol particles, which in combination with neutral air turbulence, lead to the creation of plasma irregularities at meter-scales that last for very long lifetime ($10\,\mathrm{min}$-few hours), and therefore, are detectable by VHF radars [RLB03]. Surprisingly, the conditions for ice formation in

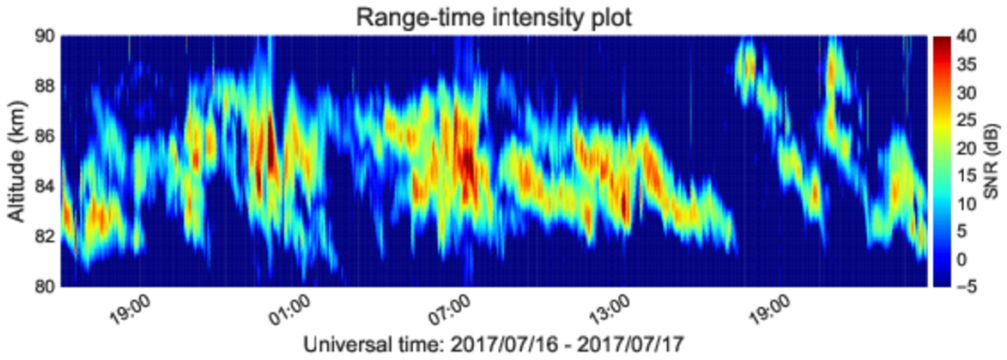

Figure 4.3: Range time intensity (RTI) plot of PMSE observed with the MAARSY vertical beam.

the mesopause are satisfied only in summer due to the gravity wave disturbances which cool the atmosphere above the summer pole [Lüb99]. This explains why PMSE can be observed only during summer.

PMSE has been used as a tracer of the complex atmospheric dynamics for long time. Physical parameters such as neutral winds [DLH96; Hol+97; Sto+13; GSC19] and turbulence parameters [BR84; HF95] have been obtained from PMSE radar observations assuming horizontal homogeneity at scales of tens of kilometers. However, Sommer and Chau [SC16] have recently shown that PMSE is not homogeneous horizontally, and instead it is composed of localized isotropic scatters. Moreover, their results suggest the existence of small-scale structures in PMSE, which might be resolved using high-resolution observations in 4D space-time.

Figure 4.3 shows typical radar measurements of PMSE made by MAARSY using a vertical beam, in which only $1/7$th of the available power and $1/7$th of the antenna array were employed. Clearly, PMSE structures are highly dynamic in time, altitude, and power. We can even observe some wave-like structures in the range time intensity (RTI) plot. Although, a small portion of the antenna and the transmit power were used in this example, the SNR is still very high. Sometimes, it reaches up to $45\,\mathrm{dB}$.

To implement MIMO with time diversity at MAARSY, the antenna array and the transmitting power is splitted into P sub-arrays. Thereby, the sensitivity of our MIMO system will be reduced compared to its counterpart SIMO by P. For example, in a MIMO configuration with seven transmit sub-arrays, both the antenna gain and the transmit power

are divided by seven. Thus, the total power loss on transmission will be $-17\,\mathrm{dB}$, which indicates that some of the weak PMSE echos will be lost. Looking at the radar reflectivity distribution of PMSE from Fig. 1 in [LB17], we notice that around $20\,\%$ of the weakest PMSE echoes would be lost only by the reduction on the transmitting side. In addition, we also have to consider the losses of MIMO on the receiving side, and the losses caused by the reduced sampling time. Next, let us describe the MAARSY radar, the radar parameters to observe PMSE, and the MIMO experiment to understand how these parameters affect the PMSE observations.

4.2.2 The MAARSY radar

The middle atmosphere Alomar radar system (MAARSY) is a monostatic radar system located in Andoya, Norway ($69.30°$ N, $16.04°$ E), with an active phased antenna array operating at $53.5\,\mathrm{MHz}$ and at a maximum peak power of $800\,\mathrm{kW}$. The array consists of 433 Yagi antennas arranged in a nearly circular grid of approximately $90\,\mathrm{m}$ of aperture as shown in Fig. 4.4. The core array is arranged in 55 symmetric "hexagons" containing 7 antennas each. In addition, 7 adjacent hexagonal antenna structures can be grouped into an "anemone", which can act as one to transmit or receive antennas.

The main characteristics of each Yagi antenna are a bandwidth of $5\,\mathrm{MHz}$ and a directive gain of $6.88\,\mathrm{dBi}$. When the full array is used to point to the zenith, the beam has a directive gain of $33.5\,\mathrm{dBi}$, a half power beam width of $3.6°$, and a maximum sidelobe suppression of $17\,\mathrm{dB}$ with respect to the main lobe. Similarly, the beam width for a "hexagon" and an "anemone" are $30°$ and $11°$, respectively. Refer to [Lat+12b] for more details.

One of the main advantages of the MAARSY radar is that each Yagi element is connected to its own transceiver module, allowing the modulation of the transmit/receive signal in phase and amplitude independently at each element. Using this capability, the beam can be steered in any desired direction up to $30°$ off zenith, with a minimum beam width of $3.6°$ [Lat+12b]. This arrangement provides a great flexibility allowing different modes of operation such as beam swinging, simultaneous multi-beam, and in-beam imaging. It is important to notice that MAARSY is the only VHF high-power large-aperture radar in northern polar region capable of radar imaging.

Figure 4.4: Sketch of the MAARSY antenna array. The core array consists of 55 identical hexagons from $A01$ to $F11$ containing 7 Yagi antennas each. A group of 7 adjacent hexagons can form an anemone as indicated by the colored areas, which can act as one antenna to transmit or receive. [Courtesy: Ralph Latteck].

Unlike the multi-beam experiments, radar imaging allows to retrieve 3D images at once, avoiding the interleaving from beam to beam and hence increasing the achievable sampling time. The disadvantage comes with the limited number of receivers. MAARSY possesses only 16 signal processing units and hence only signals from 16 selected antennas or group of antennas can be stored. These 16 signals can be selected either from "hexagons" or "anemones".

A simple radar-imaging experiment to image PMSE was conducted using MAARSY to compare MIMO to SIMO. Since a fair comparison between the two implementations is not possible because of the difference in transmitting power, antenna gain, and sampling time, firstly, results from a numerical simulation considering equivalent conditions is presented and discussed and, next, experimental results are discussed highlighting differences caused by both MIMO and SIMO implementations.

4.2.3 SIMO configuration

To image PMSE, a radar imaging experiment was conducted similar to Sommer and Chau's [SC16] using 15 "hexagons" on reception and 1 "anemone" on transmission. Figure 4.5(a) shows the selected transmitting and receiving array. Although three transmitting antennas are shown, only one was used for the SIMO case. Fig. 4.5(b) shows the resulting visibility considering only one of the transmitters and the fifteen receivers, i.e., the visibility for SIMO.

In the SIMO implementation, the receiving setup was optimized employing genetic algorithms [Hau94], and using as cost function the minimum number of gaps in the visibility (more uniform) and the minimum number of redundant baselines. Genetic algorithms are a class of algorithms designed to optimize a large search and to find near-optimal solutions by mimicking evolution and natural selection. The resulting number of unique baselines in our implementation is 163 compared to 145 of the Sommmer and Chau's implementation. The larger number of unique visibilities in our implementation results in a more uniform point spread function with smaller sidelobes. Fig. 4.5(c) show the resulting point spread function of our SIMO configuration. Notice that the shortest baseline of this configuration is $10.6\,\mathrm{m}$, and the longest $73.3\,\mathrm{m}$. Moreover, the resulting HPBW is about $3.6°$.

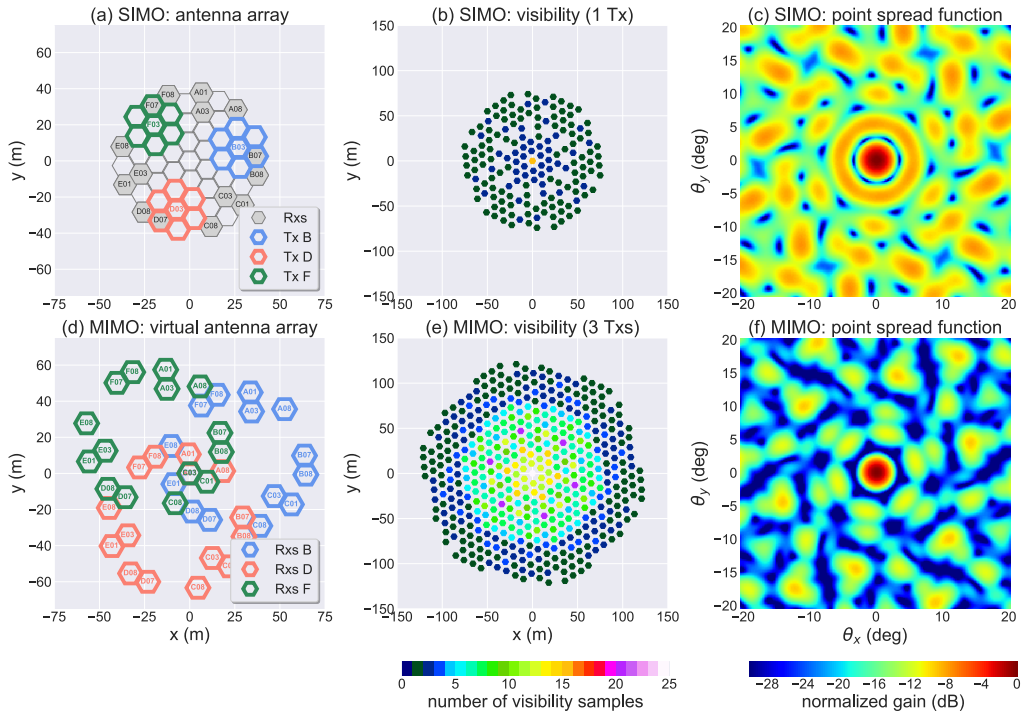

Figure 4.5: MAARSY antenna configuration for SIMO (a, b, c) and MIMO (d, e, f). (a) The receiving array consisting of fifteen hexagons is shown in grey and the transmitting array consisting of three anemones is colored. (b) Visibility samples for SIMO in which the redundant baselines are color-coded. (c) Resulting point spread function of SIMO. (d) Resulting virtual array by using MIMO. (e) Visibility samples for MIMO. (f) Point spread function of MIMO. The point spread function was calculated using both the non-redundant and redundant visibilities.

4.2.4 MIMO configuration

As described above, MIMO with time diversity was chosen to improve the performance of the radar imaging experiment. Employing the same receiving antenna layout used in the SIMO implementation, the transmitting antenna array was splitted in three sub-arrays. The transmitting sub-arrays can only be selected from the available locations at MAARSY as shown in Fig. 4.4, which can be either an "hexagon" or an "anemone". The criteria of selection of one or another is based on the trade-off between antenna gain and flexibility to form a larger virtual array. For example, if hexagons ($A01$ and $C01$) compared to anemones (A and C) are used as transmitting antennas, the longest baseline of the resulting virtual array might be 1.4 times larger. However, the antenna gain of a hexagon ($15.33\,\mathrm{dBi}$) is $8\,\mathrm{dB}$ less compared to the anemone gain ($23.78\,\mathrm{dBi}$). This difference affects significantly the detection of PMSE, particularly, of the weakest echoes. Therefore, anemones are picked as transmit units.

All available anemones might be employed as transmitters. However, when time diversity is used, the transmit power is reduced linearly by the selected number of transmitters. Moreover, after a given point, addition of new anemones does not improve the visibility function. It only increases the number of redundant baselines. Since the number of possible selections is reduced and the array is symmetric, the optimal solution can be found straight away.

Fig. 4.5(a) and (d) show the selected anemones used as transmitters and the resulting virtual array, respectively. Fig. 4.5(e) shows the visibility of the virtual MIMO array. Note that the longest baseline for MIMO is $121\,\mathrm{m}$ compared to $73.3\,\mathrm{m}$ for SIMO. The improvement of MIMO can be better observed in the point spread function shown in Fig. 4.5(f). Not only the HPBW improved by 1.65 , but also the sidelobes are largely reduced.

The MIMO array was carefully selected to have three redundant virtual receivers located at the origin, see Fig. 4.5(d). These three redundant virtual receivers are used for transmitter phase calibration purposes as described in the previous chapter. To corroborate the advantage of MIMO vs. SIMO, simulations results are presented in the following section.

4.3 Simulations

A simple radar imaging experiment is simulated in this section to compare the performance of SIMO and MIMO under identical conditions of transmit power, antenna gain, and sampling time. For the sake of simplicity, the simulation is carried out in 2D only, one range gate and one frequency bin. Equation (3.29) is used as a forward model since it is valid for uniform and non-uniform arrays. The forward model can be written for a given range gate and frequency bin in matrix form as

$$\mathbf{v} = \mathbf{\Sigma}\boldsymbol{\psi} + \boldsymbol{\eta}, \tag{4.1}$$

where $\mathbf{v} \in \mathbb{C}^N$ is a column vector comprising the measured complex signals for all the transmit-receive links, $N = P\,M$ is the number of virtual receivers equal to the number of transmitters P times the number of receivers M, $\boldsymbol{\psi} \in \mathbb{R}^K$ is the complex valued image in vector form (flattened), $\mathbf{\Sigma} \in \mathbb{C}^{NxK}$ is the Fourier kernel matrix, and $\boldsymbol{\eta} \sim N_{\mathbb{C}}(0, \Sigma)$ is the receiving noise. Although the image is in 2D, here $\boldsymbol{\psi}$ is represented as a column vector with a total number of K pixels.

Similar to the model used by Yu et.al. [YPH00], the signal $\psi \sim N(0, \sigma^2)$ from (4.1) represents a Gaussian random process with mean 0 and variance σ^2. In those cases, the expected variance of $\boldsymbol{\psi}$ can be estimated from the spatial cross-correlation of the measured signals $\mathbf{b}$ using (3.55).

$$\boldsymbol{\rho} = \mathbf{\Phi}\mathbf{b} + \boldsymbol{\varepsilon}, \tag{4.2}$$

where $\boldsymbol{\rho} \in \mathbb{C}^V$ is a column vector comprising all the visibility samples (cross-correlated measured values), $\mathbf{b} \in \mathbb{R}^K$ is the brightness in vector form (flattened), $\mathbf{\Phi} = \Sigma^H\Sigma \in \mathbb{C}^{VxK}$ is the kernel matrix, and $\boldsymbol{\varepsilon} \sim N_{\mathbb{C}}(0, \Sigma)$ is the statistical uncertainty associated with estimating the cross-correlation with finite integration times. Since the white noise for different channels ($\boldsymbol{\eta}_i$, $\boldsymbol{\eta}_j$) are uncorrelated, its effect is only considered for auto-correlated samples, which is subtracted at calculating the normalized visibility. The number of visibility samples $V = PM(PM+1)/2$ represents the total number of virtual baselines for MIMO.

Following Harding and Milla's work [HM13], a high-resolution 2D grid (K=640x640) is used to simulate the signal measurements, and a coarser grid (K=128x128) is employed

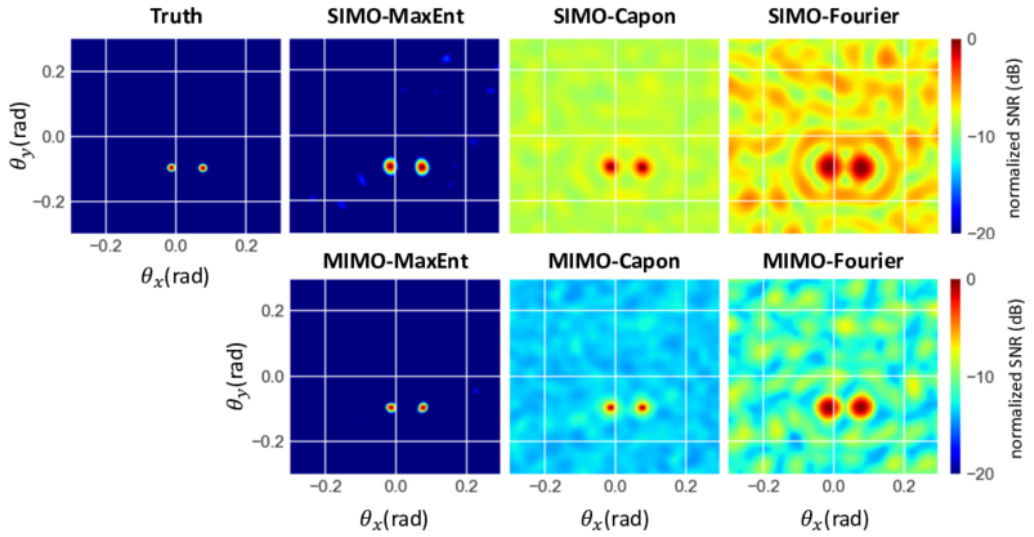

Figure 4.6: Results of simulated radar data employing three inversion methods for SIMO and MIMO configurations.

for the inverting algorithms. This is done to ensure that the model captures the image features even if the recovering algorithm cannot recover them. The error term η is modeled as a Gaussian white noise and the number of integration times used is 200, which gives us a statistical error of $7.07\,\%$ using the definition from (2.84). The true image $\mathbf{b}$ is considered to be formed by the superposition of multiple Gaussians or blobs. To investigate the performance of SIMO and MIMO, we analyze the results by reconstructing an image composed of two narrow blobs with three different algorithms.

4.3.1 Filter response

Let us consider an image composed of two narrow blobs of $0.6°$ width each as the truth. To simulate a near-real scenario a Gaussian noise with variance η^2 is added to the image and the measured signal at one receiving antenna is obtained from (4.1). The visibility (expected value) is estimated from the received signal using 200 realizations. Then, the problem in (4.2) is inverted by using one of the three algorithms described in Chapter 2.5.2: the inverse Fourier transform, Capon's method [Pal+98], and the maximum entropy (MaxEnt) method [HC06]. Results for the three methods using SIMO and MIMO configurations are shown in Fig. 4.6. Since Capon's method does not produce meaningful absolute values, the results have been normalized for a better comparison.

Visually the MIMO results outperforms their counterpart SIMOs in all the cases. Previous studies [YPH00; HM13] have already shown the superiority of MaxEnt over the other two methods. The interest of this section is to show the improvement of the image reconstruction when the imaging methods are combined with MIMO. Qualitatively, Fig. 4.6 suggests that the solution closest to the Truth is the one using MIMO and the MaxEnt method. Meanwhile, Fourier combined with SIMO produces the worst reconstruction with many artifacts. The following section quantifies the estimation error and the performance of each algorithm when combined with MIMO.

4.3.2 Error analysis

Quantifying the image quality is a hard problem when comparing different algorithms. Typical metrics such as the mean squared error assume unbiased absolute values and offsets, which is not the case for Capon's method. Following the work done by Harding and Milla [HM13], the normalized correlation is used as metric to quantify the similarity between our results and the Truth. The correlation is defined as

$$\text{corr} = \frac{\mathbf{b}_{\text{est}}^T \mathbf{b}}{\|\mathbf{b}_{\text{est}}\|_2 \|\mathbf{b}\|_2} \tag{4.3}$$

where $\mathbf{b}_{\text{est}}$ and $\mathbf{b}$ are the estimated and true values with means subtracted. This can be seen as the normalized squared error.

To investigate the performance of our MIMO configuration, the simulation presented above is repeated many times with values of the SNR from $-20\,\text{dB}$ to $30\,\text{dB}$. For each value of the SNR, the simulation is carried out 50 times in which the blobs are localized randomly in order to mitigate statistical fluctuations. The average over the 50 realizations is shown in Fig. 4.7.

Evaluating the imaging methods, the Fourier results are poor and they barely reproduce the true image. The main reason of their low correlations are the strong sidelobes, which are confused as real echoes. On the other hand, Capon's method reduces the sidelobes considerably that for high SNR echoes the sidelobes are almost indistinguishable from the noise. Finally, the MaxEnt method results outperform all the previous methods.

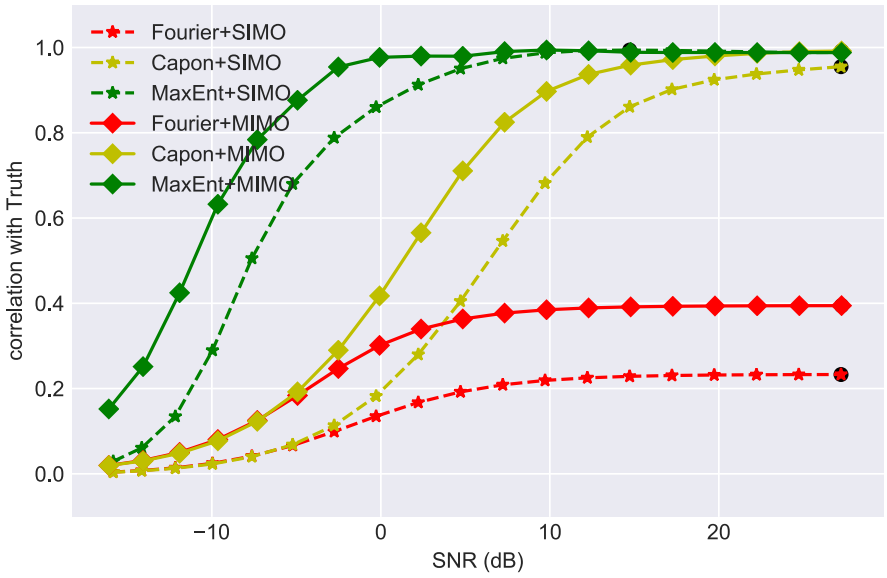

Figure 4.7: Comparison of inversion methods as a function of the SNR for the SIMO and MIMO configuration. The metric selected is the correlation with Truth.

Evaluating the transmitting antenna configuration, the MIMO results are better than their counterpart SIMO by $\sim 60\,\%$ for low SNR signals. Considering the results for MaxEnt only, the improvement can be observed within the range $-15\,\mathrm{dB}$ to $0\,\mathrm{dB}$. The $60\,\%$ improvement is expected since the antenna aperture was enlarged by $65\,\%$ by using MIMO.

Nevertheless, compared to the improvement achieved by using more efficient algorithms the improvement due to MIMO is not significant. Note the improvement from Capon to MaxEnt at $0\,\mathrm{dB}$, it is larger than $100\,\%$. Does it imply that an more efficient inversion technique is more important than a larger antenna array?

For simple images like the one composed by two narrow blobs, the SIMO antenna array and the resulting visibility are sufficient to get a good estimate. The addition of more visibility samples (larger aperture) by using MIMO does not affect the result as significantly as it does the application of a good inversion method because the unknown signal is already oversampled.

For more complex images, one might expect a different result. To evaluate both configurations in the presence of more complex structures, a simulation run was performed

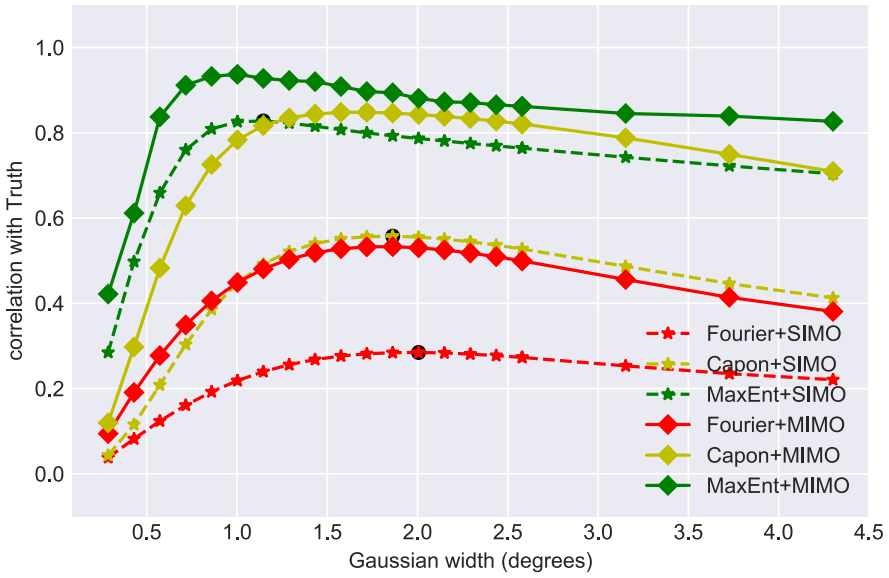

Figure 4.8: Same as Fig. 4.7 but with an image composed of multiple blobs. In this case, the performance is evaluated as a function of the blob width.

consisting of an image with fifteen blobs and resulting SNR of 0 dB. The simulation was repeated multiple times with Gaussian widths from $0.2°$ to $4.5°$. The results are shown in Fig. 4.8.

Looking at the results, we observe that the improvement from SIMO to MIMO is as good as the one achieved by using a more efficient algorithm, i.e., from Fourier to Capon or from Capon to MaxEnt. For example, see the performance gain from Fourier-SIMO to Capon-SIMO vs. Fourier-SIMO to Fourier-MIMO. These results do not tell us that the performance of MIMO has increased but that the performance of the inversion techniques have been reduced due to the more complex structures. These results corroborate the necessity of more antennas to image more complex images.

Another important feature of the correlation shown in Fig. 4.8 is the resulting correlation as a function of the blob width. The performance of the six techniques is poor at extremes width values, for very narrow and very wide structures. However, when the blob width coincides with the technique's resolution, the correlation maximizes. The point of maximum correlation is indicated with a black dot in Fig. 4.8, and it gives us an idea of the resolution achieved by each technique.

Even though the reconstruction results seem very promising, we have to consider the running time of each algorithm. For Fourier and Capon's the running time were below a couple of seconds per inversion, whereas, for the MaxEnt method it was about $20\,\mathrm{s}$ for SIMO and about $30\,\mathrm{min}$ for MIMO. The larger running time for MaxEnt and MIMO was expected since the complexity of the MaxEnt method depends exponentially on the number of visibility samples.

4.4 Experimental implementation

The techniques described above are applied to actual data using the MAARSY radar. An experiment was conducted on July 16, 2017 during PMSE conditions using the same antenna configuration as in the simulation. The transmit diversity employed was time diversity, which was implemented by interleaving the transmitters every $2\,\mathrm{ms}$. Indeed, five anemones were used on transmission but only three of them are considered for signal processing corresponding to the same anemones used in the simulations. The radar pulse was phase coded using a binary Complementary-16 code [Gol61; SG96; MCK96, e.g.]. The decoded data was stored using two coherent integrations and the resulting pulse-repetition interval (PRI) was $10\,\mathrm{ms}$ for each transmitter. Visibility estimation was done in the frequency domain applying four extra coherent integrations to the complex signals for each transmit-receive link, FFT with sixteen points, and 128 incoherent integrations to obtain an estimate (average) of the visibility. The complete list of radar parameters are summarized in Table 4.4.

Although the experiment was performed using five anemones B, C, D, E, and F on transmission, only three of them were processed. For the SIMO case, the anemone B was considered as transmitter, whereas, for the MIMO case, anemones B, D, and F were used as it was in the simulation. Notice that the effective time difference between transmitters for the selected anemones is $4\,\mathrm{ms}$. As mentioned in section 3.7.1, this time difference adds an additional phase offset to the system and needs to be calibrated.

4.4.1 Phase offset compensation

Before data inversion, instrumental phase offsets associated to the receivers and transmitters, as well as the phase offset due to the interleaving between transmitters were

Radar parameters	**SIMO**	**MIMO**
frequency	53.5MHz	53.5MHz
pulse coding	Complementary 16	Complementary 16
effective PRF (after decoding)	100Hz	100Hz
range resolution	450m	450m
number of coherent integrations	4	4
effective PRF (after integration)	25Hz	25Hz
number of FFT points	16	16
number of incoherent integrations	128	128
equivalent integration time	81.92s	81.92s
equivalent integration time	81.92s	81.92s
number of transmitters (beams)	1	5 (3 processed)
transmit diversity	-	Time
Tx interleaving	-	2ms

Table 4.2: Radar parameters used for PMSE observations

corrected using the procedure described in section 3.7.1. Specifically, absolute phase calibration of the receivers was done using the radio star Cassiopeia-A, similar to Chau et.al. [Cha+14]. For the MIMO configuration, phase offsets due to the time difference between transmitters and Doppler shift ($\Delta\phi = 2\pi f_d \tau$) were corrected directly since the Doppler frequency f_d and the time difference between transmitters τ are known, similar to [Urc+18].

On the other hand, a relative phase calibration of the transmitters was performed using the three redundant virtual receivers located at the origin which were shown in Fig. 4.5(d). Each of these redundant virtual receivers belongs to a different transmitter, and since they three are located at the same virtual position, the difference in phase between their signals must be zero. Assuming a phase offset of zero for transmitter B, the other two were corrected.

4.4.2 Integration time: uncertainties and blurring

The main source of uncertainties in the imaging problem is the one associated with the limited number of time samples to estimate the visibility. As we have seen in section 2.5.2, the estimate $\tilde{\rho}$ is proportional to

$$\tilde{\rho} = \rho + \rho/\sqrt{n}, \tag{4.4}$$

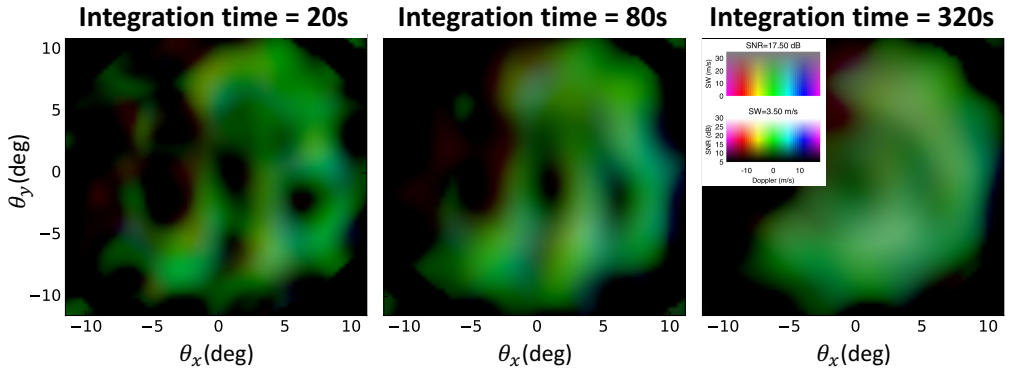

Figure 4.9: 2D PMSE images for a range of $85.95\,\mathrm{km}$, where intensity, Doppler, and spectral width are represented as lightness, hue, and saturation, respectively. Red, green, and blue colors represent negative, zero, and positive Doppler, respectively. Data inversion was done using Capon's method with integration times of (a) $20\,\mathrm{s}$ (b) $80\,\mathrm{s}$ and (c) $320\,\mathrm{s}$.

where ρ is the true value, n is the number of time samples (integrations) used to estimate $\tilde{\rho}$, and $\varepsilon = \rho/\sqrt{n}$ is the error associated with estimating the visibility with finite integration times [Dek+05; HC06].

For a large number of integrations (> 1000), we expect a negligible error. However, in real applications, the number of integrations is restricted by the dynamic nature of atmospheric targets. Structures in the atmosphere drift as they are imaged. Drifting structures limit the angular resolution achieved by any method since the resulting image might be blurred.

To avoid image smearing, short integration times should be used. However, the uncertainties might grow significantly causing artifacts in the resulting image. Figure 4.9 shows the results inverting PMSE data with Capon's method for three different integration times. For an integration time of $20\,\mathrm{s}$, the image exhibits some artifacts which fluctuate in intensity and position over time (only one frame is shown here). For $80\,\mathrm{s}$ of integration, the image is smoother and most of the artifacts are gone, although the structures are slightly wider than the first case. Finally, the result for $320\,\mathrm{s}$ of integration time is completely smeared.

Given the relatively long temporal correlation of PMSE (a few minutes), long integration times are required even if the data is sampled at high rates. Based on the results presented in Fig. 4.9, we decided to use an integration time of $80\,\mathrm{s}$, which is equivalent to

128 incoherent integrations. The associated uncertainty to this number is 8.83 %, which is a bit high.

To deal with drifting structures and limited integration times, we will in future explore tracking techniques such as Kalman Filter when an approximate state model is known [Kal60; Sal01], or the Expectation-Maximization algorithm [Moo96; MBL11] to estimate additionally the state model.

4.5 Experimental results

4.5.1 Comparison of SIMO and MIMO

The results of using Capon and MaxEnt on actual PMSE data for SIMO and MIMO are shown in Fig. 4.10. The inversion was performed for every frequency bin and the results stacked to form the image. Similarly to what we got in the simulations, MIMO-MaxEnt outperforms all the other methods. Capon has a poor performance compared to its counterpart MaxEnt for both configurations, SIMO and MIMO. The same kind of results were observed in the simulations for complex structures. The reason is that Capon tries to reduce the sidelobes adaptively, steering them to echo-free zones. Unfortunately, for the event shown, the illuminated volume is filled with PMSE (no echo-free zones), thus the performance of Capon is poor.

Furthermore, we observe that the improvement from SIMO-MaxEnt to MIMO-MaxEnt is much better than from SIMO-Capon to MIMO-Capon. The improvement in angular resolution of MIMO-Capon with respect to SIMO-Capon is about 60 % due to the larger virtual antenna array. However, for MaxEnt the improvement from SIMO to MIMO is much larger. In the case of MaxEnt, the better resolution results from the larger virtual antenna array plus the use of statistical uncertainties as described by Hysell and Chau [HC06]. These results suggest that MaxEnt takes better advantage of the addition of more visibility samples.

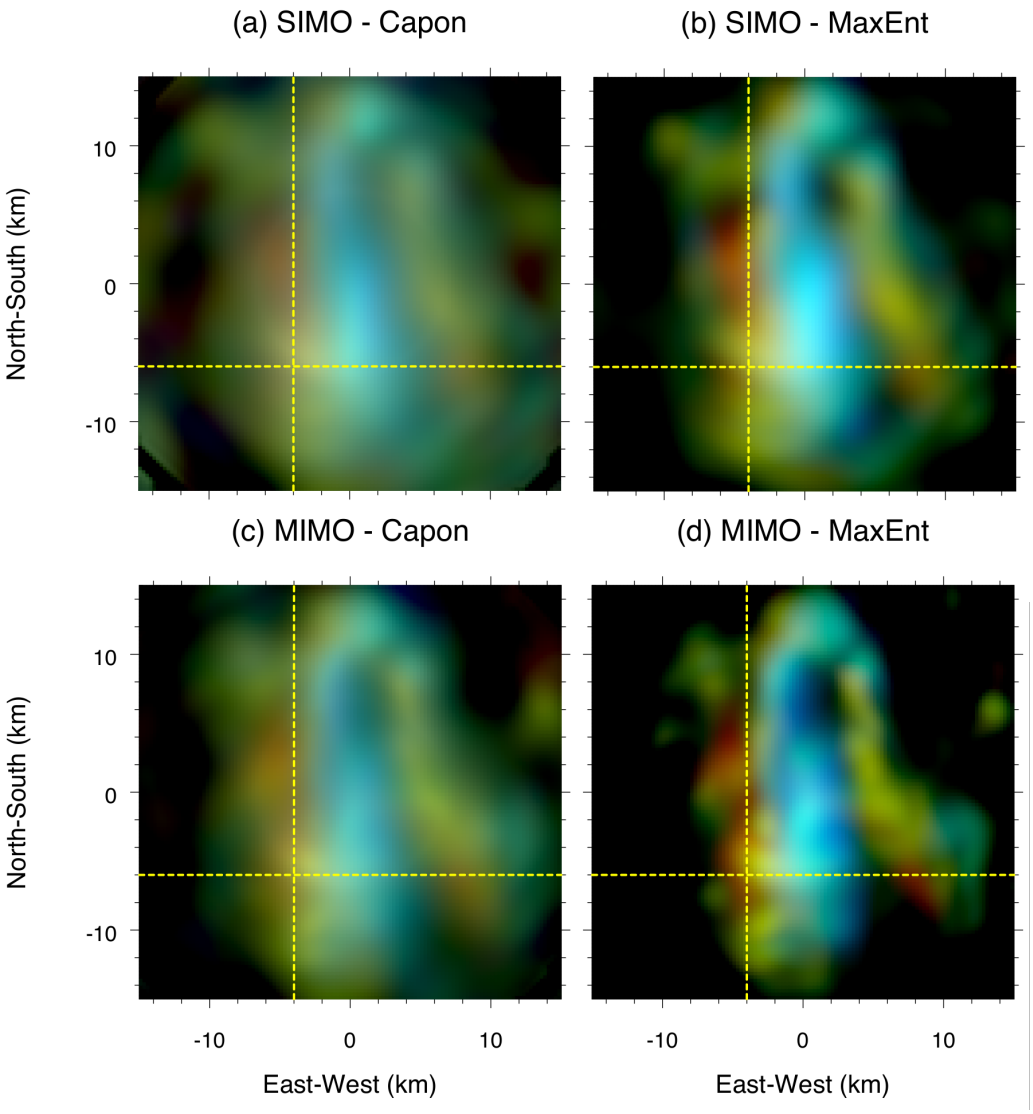

Figure 4.10: 2D PMSE images similar to Fig. 4.9 but for different inversion techniques (Capon, MaxEnt) and configurations (SIMO and MIMO).

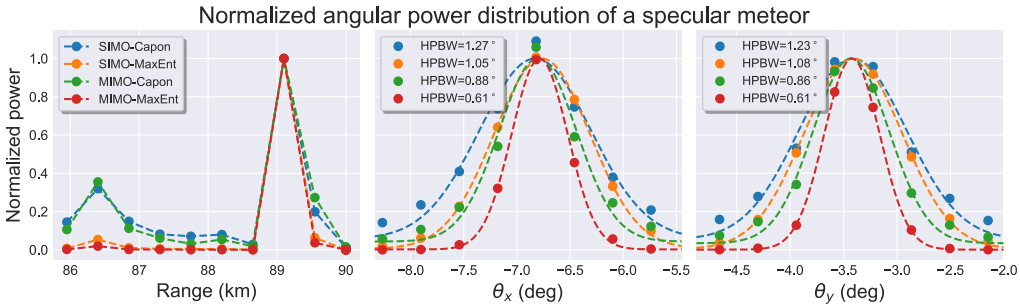

Figure 4.11: Normalized angular power distribution of a specular meteor echo as a function of (a) range, (b) East-West direction (θ_x), and North-South direction (θ_y). The results are shown for the four implementations: SIMO-Capon (blue), SIMO-MaxEnt (orange), MIMO-Capon (green), and MIMO-MaxEnt (red). The half-power beam width (HPBW) associated with each technique is indicated for the x and y direction.

4.5.2 Achieved resolution

Quantifying the image quality and angular resolution achieved when no reference is available is a really hard task. Qualitatively, the MIMO-MaxEnt results have the best resolution. However, the true image is unknown, and no precise evaluation is possible. To quantify the performance of any technique, we require to image a known target and then evaluate its discrepancy with its estimate.

Fortunately, our observations include echoes from specular meteor trails. One example of these bright and punctual echoes can be observed in Fig. 4.10 at $(10.5, -12.5)$. Specular meteors have been studied for decades, and their scattering is very well known. Specular meteor echoes can be considered to be a point target in range and angle. Although the trail is long along its trajectory, its angular response is narrow since its scattering mechanism is explained by Fresnel scattering. Meanwhile, in the transverse direction, the trail extension is very narrow and so its angular response. Specular meteor reflections are considered to be a mirror-like reflection, and thus they should be observed as a punctual object and can be used to quantify the image quality.

Figure 4.11 shows the results of imaging a specular meteor by the four techniques described above. For a better visualization of the differences, cuts in range and angle are plotted. Similar to our simulations, the power was normalized since Capon's does not produce meaningful absolute values.

Technique	**Angular resolution**	**Spatial resolution at** $85\,\mathrm{km}$	**Equivalent antenna aperture**	**Improvement factor**
MAARSY	$3.60°$	$5.33\,\mathrm{km}$	$76\,\mathrm{m}$	-
SIMO - Capon	$1.27°$	$1.88\,\mathrm{km}$	$216\,\mathrm{m}$	2.83
MIMO - Capon	$0.88°$	$1.30\,\mathrm{km}$	$312\,\mathrm{m}$	4.09
SIMO - MaxEnt	$1.05°$	$1.55\,\mathrm{km}$	$261\,\mathrm{m}$	3.42
MIMO - MaxEnt	$0.61°$	$0.90\,\mathrm{km}$	$450\,\mathrm{m}$	5.90

Table 4.3: Performance of imaging techniques

In an ideal case, no differences are expected in range for the four techniques. However, we notice a small peak at $\sim 86.5\,\mathrm{km}$ for Capon but not for MaxEnt, either in a SIMO or MIMO configuration. This peak is possibly associated with sidelobes of strong echoes located at other angles in the same range. As mentioned before, Capon's performance is reduced considerably in the presence of volume-filling targets as in this case. On the other hand, MaxEnt deals better with sidelobes for both configurations and the artifact is suppressed significantly.

To quantify the angular resolution achieved in the x and the y direction, the brightness samples were fitted to a Gaussian function. The resulting standard deviation of the Gaussian, equivalent to the half-power beam width (HPBW), is indicated in the figure for each technique. Notice that, among the four techniques, the two using MIMO have better resolution. The lower resolution of SIMO is due to the meteor echo is surrounded by PMSE. PMSE is a volume filling target composed of multiple scatters. As seen in the simulations, the larger the number of scatters the lower the algorithm's performance. These results suggest that for cases where the number of scatters is large or for complex structures, MIMO is a good alternative.

Table 4.3 summarizes the results obtained by imaging a specular meteor. In addition to the angular resolution achieved by each technique, a improvement factor is included using as a reference the theoretical angular resolution of the full MAARSY array. As expected, the improvement from SIMO and MIMO is about $50\,\%$. Surprisingly, the angular resolution achieved by using MIMO-MaxEnt is $0.6°$, which is approximately six times better than the nominal MAARSY angular resolution. The spatial resolution at $85\,\mathrm{km}$ associated with $0.6°$ of angular resolution is $0.9\,\mathrm{km}$. The following section shows the PMSE structures identified with this resolution.

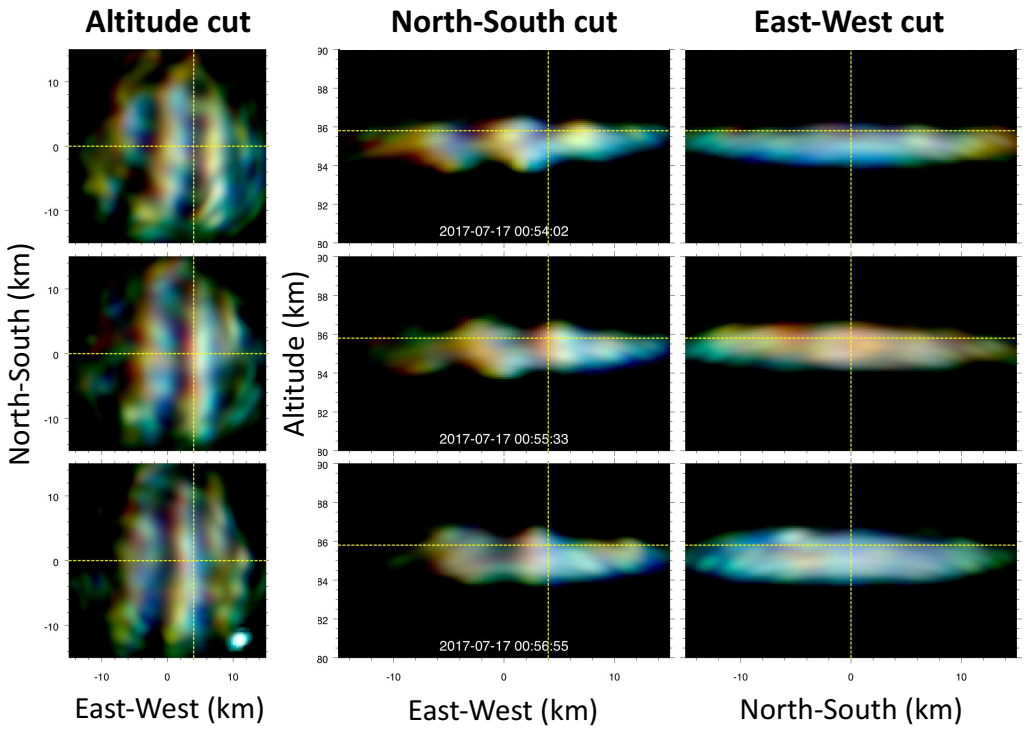

Figure 4.12: 3D PMSE kilometer-scale structures observed at MAARSY corresponding to MIMO-MaxEnt. Altitude, North-South, and East-West cuts are shown for three time frames, one per row. The yellow dashed lines indicate the plane of the sliced images.

4.5.3 Observation of km-scales structures in PMSE

The unprecedented resolution achieved at MAARSY by combining MIMO and MaxEnt allows us to observe kilometer-scales structures in PMSE, which have never been observed before by other radars. Since brightness estimation is done in polar coordinates (θ_x, θ_y, r), a cubic spline interpolation was applied to convert it to Cartesian coordinates (x, y, z), assuming the center of the antenna as the origin $(x = 0, y = 0, z = 0)$. Note that x, y, and z represent the East-West, North-South, and altitude direction, respectively, where positive values correspond to East and North. A cut of the 3D image in altitude, East-West, and North-South direction are shown in Fig. 4.12 for three consecutive time frames.

The altitude cuts at $85.8\,\mathrm{km}$ show a wave-like structure with elongated meridionally oriented wavefronts drifting from east to west. From the EW and NS cut, we see that the structure has a limited extension in altitude about $2\,\mathrm{km}$. The blue and red color (positive

and negative Doppler) in the NS cut indicate that this structure might be composed of eddies. Similar structures at larger scales have been observed by airglow imagers, which are known to be associated with gravity wave breaking [Hec03; Hec+07].

Radar imaging provides 4D radar measurements that allow to study the evolution of these complex structures in time. Figure 4.13 shows the time evolution of the selected event in altitude, NS, and EW direction. Background winds estimated from specular meteor radars (SMRs) and from PMSE Doppler measurements are represented as arrows in the plot, in which their slope (distance/meters) depict the wind magnitude. SMR mean winds were obtained combining meteor detections from Andenes and Tromso in Norway and following the technique described in [HFV01; Hal+05; Cha+17]. Mean winds from PMSE measurements were obtained using the same procedure described in [Urc+19a].

As expected, PMSE is composed of structures at multiple scales. Some of them spatially uniform like the one around 00:20 UTC, and others more dynamic like the wave-like structure seen around 00:56 UTC with a wavelength of about $8\,\mathrm{km}$. In the EW direction, this wavy structure is drifting at the same pace as the background mean wind, in direction and magnitude. In the NS direction, the elongated structures are apparently also drifting with the background but it is difficult to confirm it since the illuminated volume is spatially limited.

Surprisingly, we found other events were kilometer-scale PMSE structures were not drifting with the background. These events are of great interest since they might be associated to small-scale gravity waves, which are known to have their own velocity and direction independent of the background wind. One example of this kind of structures is shown in Fig. 4.14. Compared to the first case, this structure has an altitude extent of $\sim 3\,\mathrm{km}$, between $82\,\mathrm{km}$ to $85\,\mathrm{km}$. Moreover, in the EW direction, the wavefronts are propagating in the opposite direction to the background zonal wind. Whereas the background is going from east to west, the wavefronts are propagating from west to east. The approximate distance between wavefronts in the EW direction, i.e., the wavelength, is $\sim 12\,\mathrm{km}$. Since its relatively small wavelength, this structure might be classified as an atmospheric instability. Nevertheless, its opposite direction of propagation suggests that it might be a propagating gravity wave. Further analysis of the two events is required to classify them properly and to realize the physical mechanism behind them. Those investigations are out of the scope of the present work. However, a complete analysis of a KHI event from data resulting from this work has recently been published by Chau et.al [Cha+20].

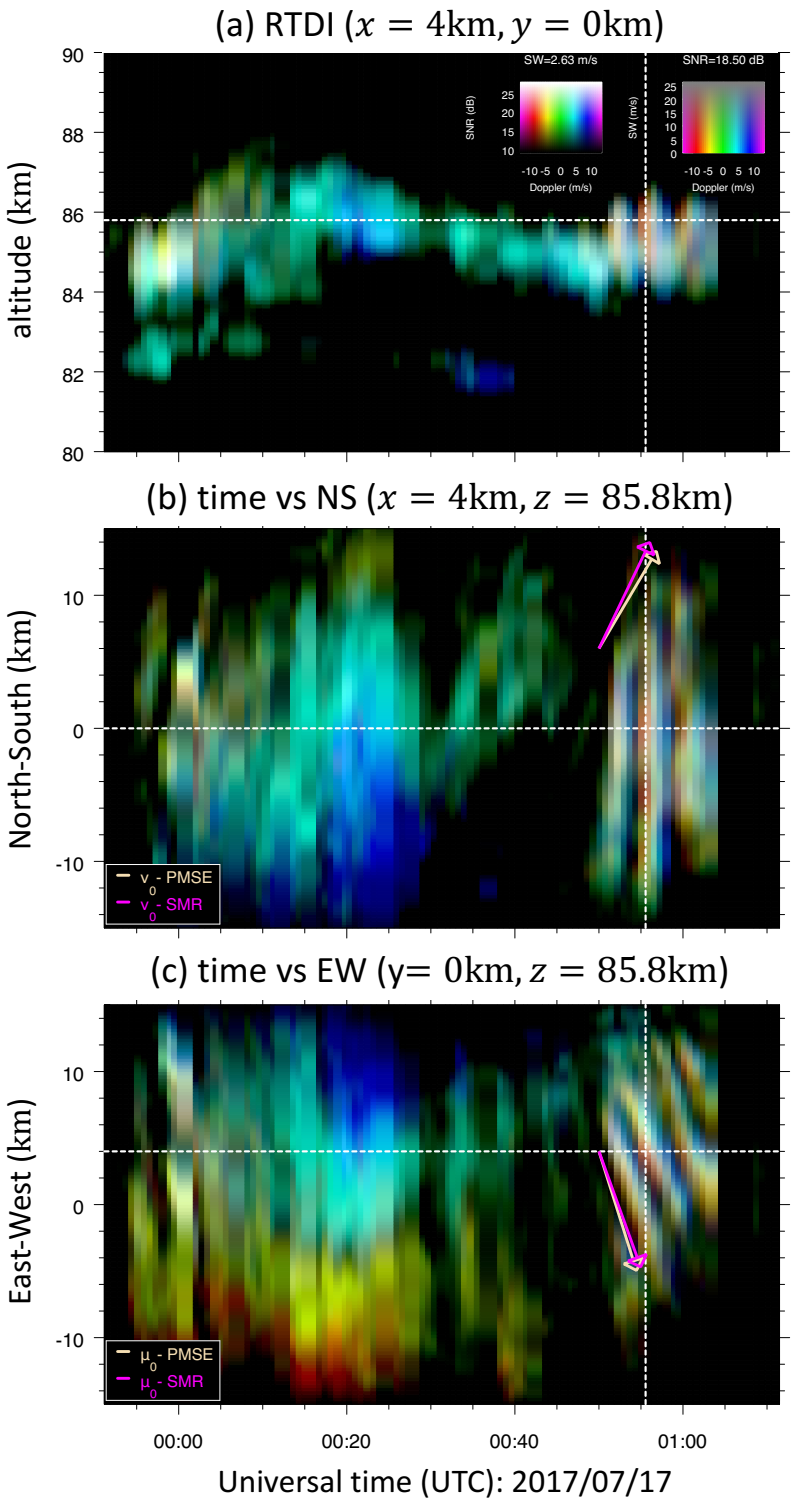

Figure 4.13: Time evolution of PMSE structures as a function of (a) altitude (RTDI), (b) NS location, and (c) EW location for the same event shown in Fig. 4.12. Zonal (μ_0) and meridional (υ_0) mean wind values estimated from specular meteor radars (SMRs) and PMSE are represented by arrows. The dashed horizontal lines indicate the planes of altitude, NS, and EW cuts shown in the previous figure. Similarly, the dashed vertical line indicate the time.

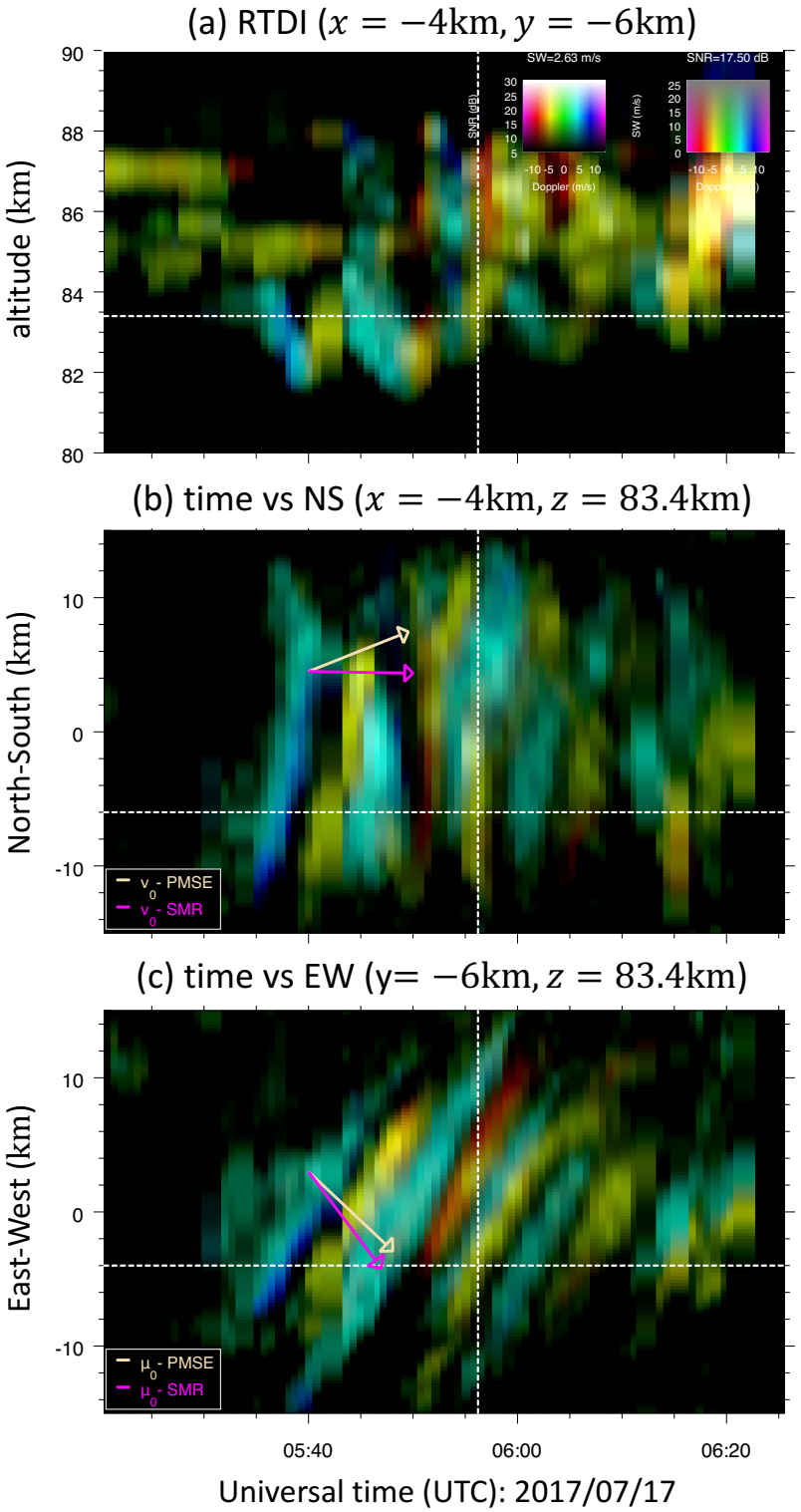

Figure 4.14: Same as Fig. 4.13 but for a PMSE structure propagatig against the background wind.

Chapter 5

On mesoscale spatio-temporal dynamics

In this chapter

5.1 Introduction

In the previous chapter, MIMO and radar imaging techniques were combined to observe kilometer-scale dynamics using PMSEs as tracers. Specifically, a large aperture radar with a high spatial resolution was employed to illuminate relatively small volumes. On the other hand, when the objective is to measure mesoscale dynamics, large aperture antennas are not efficient because of their limited illuminated volume. Instead nearly

isotropic antennas or multi-stations are required to observe large volumes and the dynamics within. Quasi isotropic antennas or single antennas posses low antenna gains and echoes such as PMSEs are usually not detectable by these systems. For mesoscale dynamics, stronger tracers and all-sky radars are needed [HFV01].

Another good tracer of the MLT dynamics are specular meteor trail echoes. When a meteor enters the Earth's atmosphere it heats up and ablates leaving an ionized plasma trail along its trajectory. Meteor trails survive in the mesosphere hundred of miliseconds and during their lifetime they drift with the neutral wind. When the radar line-of-sight is approximately perpendicular to the trail, the scattered signal is strong and low-power radars are able to detect these echoes. This perpendicular point is also known as specular point. Specular meteor radars (SMRs) are small and low power systems capable of measuring the backscattered signal from meteor trails. SMR systems only measure a projection of the trail velocity (radial velocity). By using several of these radial velocity measurements from distinct view angles, the background wind can be estimated. Since the 1950s, SMRs have been used to characterize the atmospheric dynamics in the MLT region [MVP50; RLE53].

Typically, mean wind estimation requires several meteor detections within a specific volume and time, and moreover assumes horizontal homogeneity [HFV01; HRC04]. The reliability of wind estimates depends highly on the number of detected meteors per volume and on the meteor location accuracy. Indeed, there are many thousands of meteors entering the Earth's atmosphere per minute. Nevertheless, only a few of them satisfy the specular condition and can be detected by a given SMR. A reduced number of detections limits the quality of the estimation and the resolvable scales.

Recently, Stober and Chau, and Vierinen et al. [SC15; Vie+16] proposed the use of multi-static meteor radars (radar networks) to increase the number of meteor detections and thus to improve the time, altitude, and horizontal resolution of wind estimates. Specifically, they have shown that a significant increase in meteor detections admits to relax the horizontal homogeneity assumption allowing to derive horizontal wind fields (3D winds). The first multi-static radar network proposed by Stober and Chau, and Chau et al. [SC15; Cha+17] uses spatial and frequency diversity. It consists of multiple transmitters (Tx stations) and multiple receivers (Rx stations) widely separated from each other, in which the Rx stations possess interferometric capabilities for angle of arrival

(AOA) estimation. Its main advantage lies in that it can be implemented with commercial radars working at different frequencies, keeping the data analysis the same. Nevertheless, the complexity comes by requiring a broad bandwidth as the number of Txs increases, complicating also the receiving side. Later, [Vie+16] proposed a radar network with multiple transmitting and multiple receiving stations, for which waveform diversity was used to separate the contribution of Tx stations. In this kind of network, each Tx station transmits a different pseudorandom code sequence but at the same frequency, i.e., uses spread-spectrum. This allows to interconnect a receiver to all the Tx stations.

In the MIMO community, these kinds of radars are also known as non-coherent MIMO radars [HBC08]. They are named non-coherent since the scattered echoes at one receiving station coming from two distinct transmitting stations are not correlated. Even if two distinct transmit-receive links observe the same target, their scattered signals will be uncorrelated since the observed radar cross–section (RCS) will be different (from a different view angle). Non-coherent MIMO radars have been widely discussed in the context of multistatic radars, where the transmit and receive antennas are widely separated from each other. The main difference between conventional multi-static and MIMO systems lies in the use of multiple transmit antennas radiating independent signals for MIMO, which increases significantly the number of independent transmit-receive links and the number of measurements compared to multistatic radars using only one transmitter.

In this chapter, the limitations of existing radar networks are investigated and a novel and scalable radar network is proposed based on the combination of non-coherent and coherent MIMO with waveform diversity. The proposed approach significantly simplifies the deployment of radar networks, increase the number of meteor detections, and improve the quality of meteor measurements. Thus, improving the quality and resolution of wind estimates. The network is based on multiple transmitting stations combined with multiple receiving stations widely separated, i.e., using non-coherent MIMO; in which each station has multiple transmit/receive antennas closely separated, i.e., using coherent MIMO. In our proposal, the non-coherent MIMO approach helps to increase the number of meteor detections due to the high number of independent transmit-receive links. Whereas the coherent MIMO approach allows to add interferometric capability to both the Tx and Rx side, improving the meteors' location estimation. Moreover, MIMO with waveform diversity permits every station to work at the same frequency and to reuse the spectrum, allowing interoperability between all the stations. To avoid any

kind of confusion, hereafter we refer to non-coherent MIMO as multi-static radars and to coherent MIMO as simply MIMO.

Even though the great advantage of multi-static radars combined with MIMO using waveform diversity, multiple Txs transmitting different waveforms at the same frequency might degrade the performance of the system since the transmitted waveforms are not totally independent. The larger the number of transmitters, the higher the resulting cross-interference between all the Txs. In order to minimize the cross-interference between Tx stations, we require a proper recovery algorithm to decouple the return signal due to each transmit antenna.

Different approaches have been proposed in the past to recover signals in interference environments. For example, the linear least squares estimation (LSE) has been used in MIMO communications systems for its simplicity and tolerable performance. Its main limitation is that it is only applicable to overdetermined problems. Some studies using LSE to recover signals in MIMO systems with more Rxs than Txs can be found in [Wan+07; AF14]. On the other hand, Vierinen et.al [Vie+16] proposed the use of the maximum likelihood estimator (MLE) for multistatic SMR networks with more Txs than Rxs. In this case, MLE was used to find the same solution as the weighted least squares estimator (WLSE). As it was stated before, LSE is only applicable for overdetermined problems. In [Vie+16], they introduced a trick and solved the problem for one Tx at a time to make the problem overdetermined, considering the contribution from other Txs as noise. Since the transmitted waveforms are not totally independent, this works in networks with a small number of transmitters or if the echoes from other transmitters are weak. Otherwise, the noise floor might increase considerably, reducing the number of meteor detections. Other approaches have been proposed to overcome the underdetermination problem, such as the minimum mean squares error estimator (MMSE) [RGV09] but at the price of increasing the computational complexity and requiring prior knowledge of the noise variance.

In addition to the mulstistatic SMR network based on MIMO, a novel algorithm is proposed to recover specular meteor signals from radar measurements in interference enviroments. The proposed approach is based on compressed sensing, which adds a sparsity constraint to our problem to find the best solution. Compared to conventional methods like matched filter [Tur60] or LSE [AF14], our approach is capable of recovering weak signals in the presence of strong ones.

In the following sections, the specular meteor radar system is briefly described, and the advantages and disadvantages of preceding multi-static SMRs configurations. Then the proposed network based on MIMO and the signal recovery algorithm based on compressed sensing are fully described. Finally, the advantage of the proposed system is validated through simulations and experimental results.

5.2 Existing specular meteor radars to measure MLT winds

5.2.1 Specular meteor radar

Meteors entering the atmosphere heat and vaporise forming a trail of ionised gas along their trajectories. As long as they survive, meteor trails are carried along by the neutral atmospheric wind. By the aid of radars, meteors' trail velocities and positions can be determined. Meteors' trail velocities can be estimated from measurements of one single receiving antenna. However, measuring meteor's locations require radars having interferometric capabilities. Typically, interferometry is implemented in a system with a single transmit antenna and multiple receive antennas, i.e., a single-input multiple-output (SIMO) radar. By comparing the phase delays between receive signals the angle of arrival (AOA) can be estimated. Figure 5.1 shows a typical specular meteor radar with one transmitting element and a receiving array with interferometric capability. To optimize the meteor radar measurements, standard meteor radar systems use the well known Jones antenna configuration [JWH98]. This configuration allows to determine both the meteor's Doppler velocity f and the angle of arrival $\mathbf{k} = 2\pi/\lambda[\theta_x, \theta_y, \theta_z]$ with good accuracy.

In a meteor radar, the measured Doppler velocity is a projection of the background wind $\mathbf{u} = [u, v, w]$ on the radial direction $\mathbf{k}$. For a meteor trail measurement i, we get

$$\mathbf{u} \cdot \mathbf{k}_i = -2\pi f_i. \tag{5.1}$$

By combining several meteor trail measurements and assuming an homogeneous wind within a volume and time window deductions of the magnitude and direction of the atmospheric mean wind can be made at the altitude at which the meteor was observed

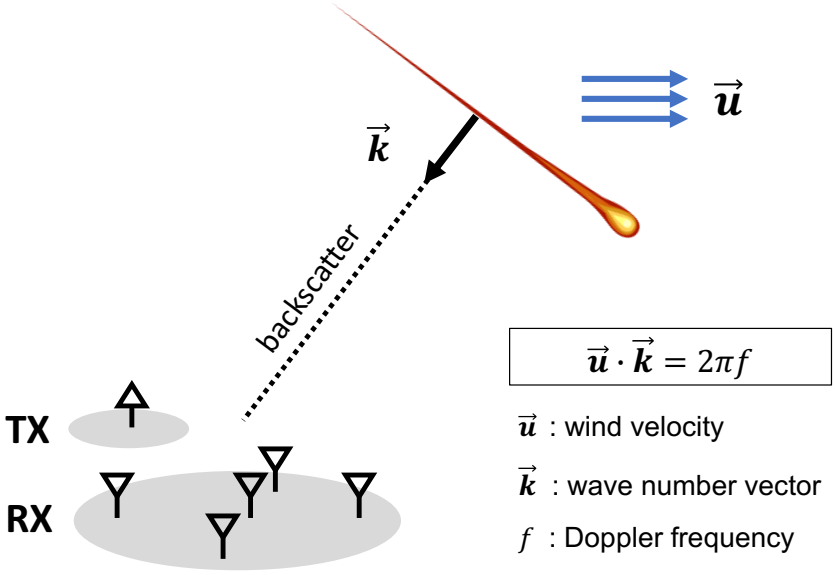

Figure 5.1: Specular meteor radar system with interferometric capability to measure radial velocity f and angle of arrival $\mathbf{k}$ of a meteor trail. Note that the radial velocity is a projection of the background wind on the radar line-of-sight.

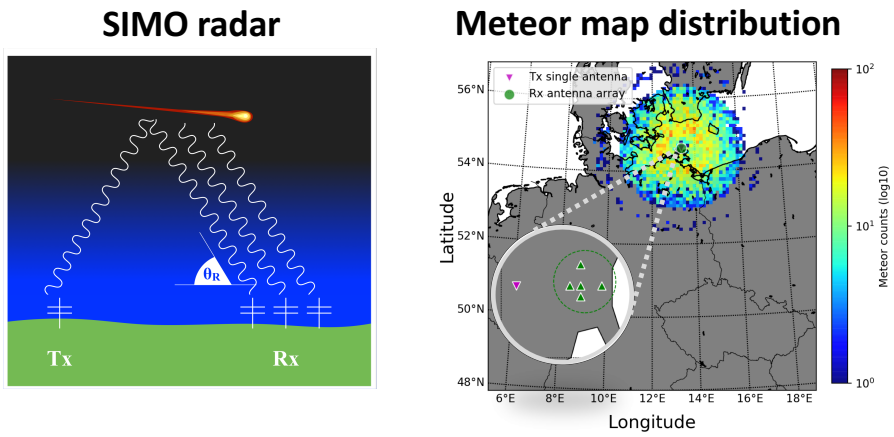

Figure 5.2: Meteor detections. (a) Bi-static meteor radar system, and (b) distribution of total meteor detections for one day.

[HFV01]. Typically, the least squares estimation (LSE) is used to obtain a wind estimate. The LSE is an algorithm that minimizes the discrepancy between the measurements and the unknown value

$$\tilde{\mathbf{u}} = \arg\min_{\mathbf{u}} \sum_{i} (\mathbf{u} \cdot \mathbf{k}_i + 2\pi f_i), \tag{5.2}$$

where i stands for the meteor index in a specified volume and time window, and $\tilde{\mathbf{u}}$ is the estimated wind. The quality of the estimate depends on the number of meteors per volume and time. Figure 5.2 shows the distribution of total number of meteor detections for one day in a volume of $250\,\mathrm{km}$ x $250\,\mathrm{km}$ x $10\,\mathrm{km}$. For a bistatic system installed in northern Germany the total number of detections was $\sim 10\,\mathrm{k}$ in $24\,\mathrm{h}$, where meteors with low elevation angles ($\theta_z < 60°$) are not considered due to their high associated error provoked by antenna coupling. To obtain an accurate wind estimate, a minimum of ten meteor measurements in a volume of $250\,\mathrm{km}$ x $250\,\mathrm{km}$ x $1\,\mathrm{km}$ and a time window of $1\,\mathrm{h}$ are typically used. Other important considerations for wind estimations such as outliers removal or a zero vertical wind assumption are recommended by Hocking et.al. [HFV01] and are typically used in standard systems.

A graphical example of estimates of zonal u and meridional v wind obtained with a radar installed in northern Germany are shown in Fig. 5.3. Patterns of global-scale oscillations known as atmospheric tides are visible in the figure, which have been extensively studied for several authors with different instruments [HT97; CL69; Kop+15]. Since their large extension and long periods, tides are easily studied with low resolution systems. However, AGWs and turbulence processes require systems with high spatio-temporal resolution.

Standard meteor observations are limited to the study of large-scale dynamics owing to their low resolution in time and space. Wind estimates from monostatic SMR are not able to resolve mesoscale or small-scale dynamics. A higher number of meteor detections per space and time bin is required to increase the spatio-temporal resolution for mesoscale studies. This can be achieved by using multitatic SMR networks.

5.2.2 Multistatic specular meteor radars based on SIMO

In order to increase the number of meteor detections, Stober and Chau [SC15] proposed the addition of receiving stations with interferometric capability to existing SMRs. Figure 5.4 (left) shows a sketch of a radar network operating at a given frequency consisting

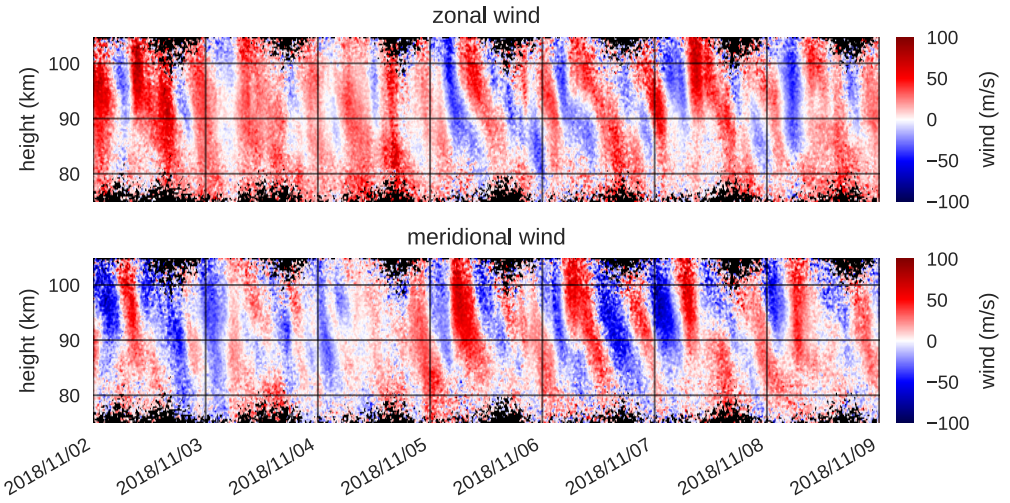

Figure 5.3: High resolution zonal u and meridional v winds obtained with a multi-static system installed in northern Germany.

of one Tx station and two Rx stations, in which each Rx station has interferometric capability. Stober and Chau have shown that the addition of a new Rx station increases the number of usable meteor detections by $\sim 70\,\%$. The $30\,\%$ loss is mainly caused by the larger Tx-Rx distance and the low elevation angles of some detected meteors. To extend the horizontal coverage, new radar systems operating at different frequencies can be added as shown in Fig. 5.4 (right).

Since between $5\,\mathrm{meteordetections}$ to $10\,\mathrm{meteordetections}$ are required to estimate the mean wind in a volume, the increase in the number of detections lead to a better spatio-temporal resolution and altitude coverage. If the number of detections is significantly high the horizontal homogeneity assumption can be relaxed (smaller volumes) and the 3D wind field can be estimated. Details of 3D wind field retrieval can be found in [SC15; Cha+17]. Essentially, since the number of meteor detections is high, the same minimization problem as in (5.2) is solved but for smaller volumes. In addition, some smoothnes constraints can be added for neighboring volumes.

Although Stober and Chau [SC15] implemented two radar networks operating at frequencies separated almost $4\,\mathrm{MHz}$, the separation required is only a few hundred kHz since the meteor's bandwidth is less than $100\,\mathrm{kHz}$. Note that each link can be classified as a (coherent) SIMO radar since it is composed by one transmit element and multiple receiving elements, and the total number of links is directly proportional to the number

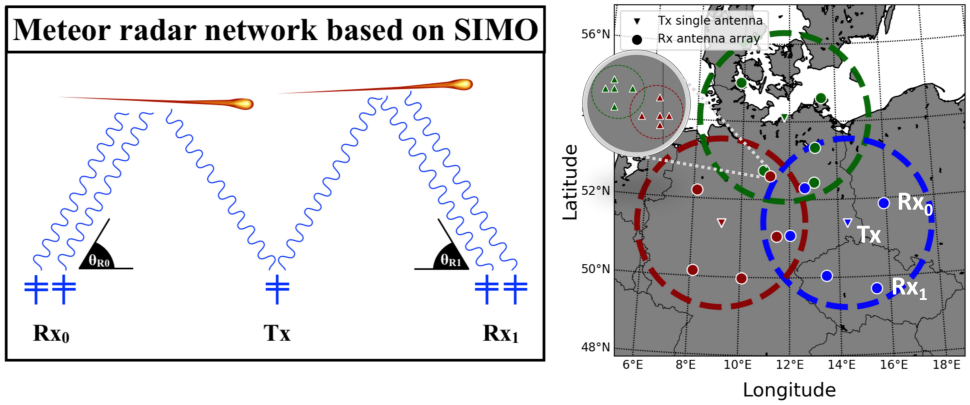

Figure 5.4: Left: Addition of Rx stations to an existing Tx allows to increase the number of meteor detections (Radar network based on SIMO). Right: Addition of radar networks operating at different frequencies allows to increase the horizontal coverage of meteor measurements. Red, green, and blue colors indicate that the stations are working at a specified frequency.

of Rx stations. Hereafter, we refer to this kind of networks as a radar network based on a SIMO configuration employing frequency diversity and spatial diversity.

Implementation of radar networks using frequency diversity is relatively simple since it can be implemented with commercial meteor radar systems, such as the meteor system SkiYMET [HFV01] or ATRA [HRC04]. Frequency diversity is the simplest way of ensuring orthogonality if the frequency separation between two transmitters is larger than the range bandwidth required ($\sim$100 kHz). Nevertheless, it requires much more resources than any other transmit diversity. First, a broader radio spectrum is required, which is one of the most limited resources. Second, additional receivers are required for each new transmitter since antennas and digital receivers are usually narrowband, and they cannot listen to multiple frequencies at the same time. Each new network is completely isolated from the others, and existing resources like Rx antennas and digital receivers cannot be reused.

Figure 5.4(right) shows an example of a network consisting of three transmitter stations and fifteen receiver stations. Even though the high number of Txs and Rxs, the number of resulting links is limited to fifteen. Moreover, some Rx stations have to be duplicated at the same location, one for each operating frequency. To increase the number of resulting links using the same amount of resources, among other advantages, Vierinen et.

al. [Vie+16] proposed a radar network based on SIMO working at the same frequency but in which each transmitter radiates an independent waveform, i.e., a radar network using waveform diversity and spatial diversity. In the next section, a radar network using waveform diversity based on (coherent) MISO and MIMO was implemented to increase the number of resulting transmit-receive links and the accuracy of meteor detections.

5.3 Multistatic specular meteor radars based on MIMO

Winds are estimated by combining several meteor radial velocity measurements with their corresponding location. Radial velocities can be estimated from one single receiving antenna. However, measuring meteor's locations require interferometric capabilities. Interferometry can be applied to a radar link employing multiple receive or multiple transmit antennas closely separated. In the case of a system with a single transmit antenna and multiple receive antennas, i.e., a single-input multiple-output (SIMO) radar, we can only estimate the target's angle of arrival (AOA), see Fig. 5.5(a). On the other hand, if a system with a single receive antenna and multiple transmit antennas transmitting independent signals is employed, i.e., a multiple–input single–output (MISO) radar, we can estimate the target's angle of departure (AOD), see Fig. 5.5(b). When a multiple–input multiple–output (MIMO) radar is used, both AOA and AOD can be estimated jointly to improve the accuracy of the target's location, see Fig. 5.5(c). The reason of the better accuracy by MIMO is that when the position estimation is done only from one side (Tx or Rx), the measurement error associated to low elevation angles is considerably larger. Instead, when the meteor is observed from both sides only one of them will suffer of this effect augmenting the accuracy of position estimation.

Former studies only proposed networks based on SIMO configurations since estimation of AOD is not possible with standard methods. In this section, a radar network based on (coherent or co-located) MISO and MIMO configurations using waveform diversity is proposed. The AOA and AOD can be obtained solving (3.37). Figure 5.6(left) shows a Tx station with two antenna elements and two Rx stations with one antenna element each. On the Tx side, each element transmits a different waveform but at the same frequency. On reception, the reflected signals from each Tx are decoupled (decoded) and they are processed to estimate the AOD. Note that in this case, a Tx station plus a Rx station form

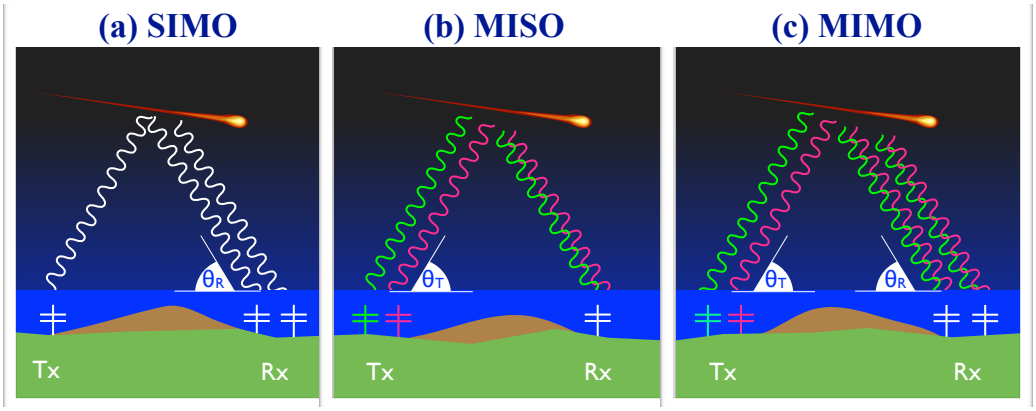

Figure 5.5: A bistatic Tx-Rx link based on (a) SIMO, (b) MISO, and (c) MIMO. SIMO and MISO allows estimation of AOA and AOD, respectively; whilst MIMO allows estimation of both AOA and AOD, which results in a higher location accuracy. A MISO or MIMO system make use of multiple transmitters radiating independent signals (in frequency, waveform, time or polarization), which are represented in red and green.

a (coherent) MISO link. Figure 5.6(right) shows three networks composed of three Tx stations and twelve Rx stations, which results in 36 independent Tx-Rx links, three times higher compared to the network using frequency diversity.

Waveform diversity allow us to use one frequency for all the Tx and Rx stations, making the network scalable and increasing the effective number of links compared to networks using frequency diversity. Thus, increasing the number of detected meteors. As explained by Vierienen et.al. [Vie+16], compared to radar networks using frequency diversity in which the number of detected meteors is $\eta N_0 N_{rx}$, networks using waveform diversity allows to increase the number of detections to $\eta N_0 N_{rx} N_{tx}$. Where N_0 is the typical number of meteors detected by a monostatic system, N_{rx} is the number of receivers, N_{tx} is the number of transmitters, and $\eta \approx 0.3{-}0.8$ is an efficiency factor, which depends on the distance between transmitter and receiver. The larger the distance, the smaller the efficiency.

The number of detections in a radar network using waveform diversity is N_{tx} times larger than a typical radar network with only one transmitting station. This difference lies in the fact that in a radar network using waveform diversity all Tx and Rx stations are interconnected. On the other hand, (coherent) MISO and MIMO allow us to add interferometric capability to the Tx side. Particularly, MISO permits to move the complexity in power, number of antennas, and space required only to the Tx side. For networks based

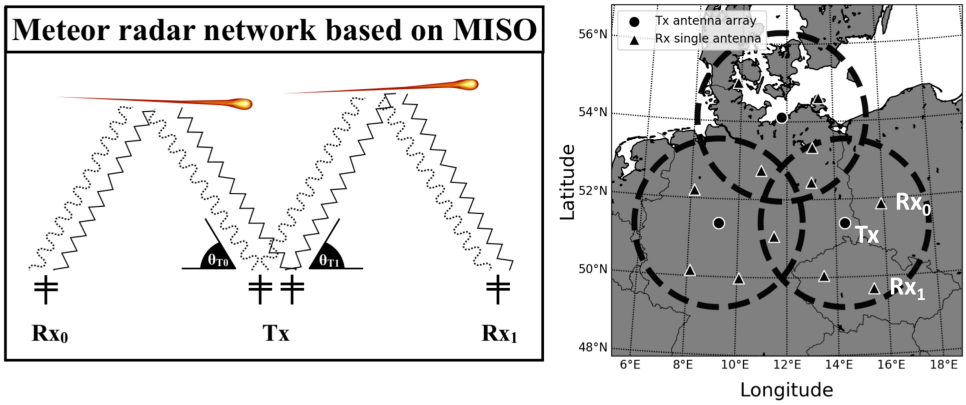

Figure 5.6: Similar to (5.4). Left: A multistatic SMR network using waveform diversity. The Tx antennas radiate independent waveforms at the same frequency. Scattered signals are decoupled on the receiving side. Right: Addition of Txs and Rxs operating at the same frequency allows to increase the horizontal coverage and the number of meteor detections.

on MISO, the Rx stations can be composed of a single antenna, which makes its installation suitable in small places such as gardens, schools, and on houses' roofs. This small but important difference allows the installation of these systems at great scale (with many Rx stations).

To make a quick comparison, the number of antennas required to build the networks based on SIMO and MISO shown in Figs. 5.4(right) and 5.6(right), respectively, are 75 compared with 12 for the Rx stations, and 3 compared with 15 for the Tx stations. Thus, the resulting number of antennas required are 78 compared to 27 for SIMO and MISO, respectively. Not only the number of antennas used is less for MISO but, more importantly, the effective number of Tx-Rx links is three times higher.

Furthermore, by using MIMO links rather than MISO, the meteor's position can be estimated from both the Tx and Rx side, augmenting the accuracy of location estimation. MIMO does not only increase the accuracy of estimations, it also increases the SNR of detected meteors due to a higher antenna gain in both transmission and reception. Nevertheless, installation complexity of MIMO links are similar to SIMO s.

A summary of radar networks using four different implementations is shown in Table 5.1: (a) The one based on SIMO using frequency diversity proposed by Stober and Chau

configuration	**SIMO**	**SIMO**	**MISO**	**MIMO**
diversity	**frequency and spatial diversity**	**waveform and spatial diversity**	**waveform and spatial diversity**	**waveform and spatial diversity**
antennas per Tx	1	1	5	5
antennas per Rx	5	5	1	5
Tx array gain	+0 dB	+0 dB	+6.98 dB	+6.98 dB
Rx array gain	+6.98 dB	+6.98 dB	+0 dB	+6.98 dB
space per Tx	5 m x 5 m	5 m x 5 m	30 m x 30 m	30 m x 30 m
space per Rx	30 m x 30 m	30 m x 30 m	5 m x 5 m	30 m x 30 m
scalable	No	Yes	Yes	Yes
example:				
Tx stations	3	3	3	3
Rx stations	12	12	12	12
total Tx antennas	3	3	15	15
total Rx antennas	60	60	12	60
total antennas	63	63	27	75
independent Tx-Rx links	12	36	36	36
pulse type	coded pulsed	coded CW	coded CW	coded CW
code type	Barker	Pseudorandom	Pseudorandom	Pseudorandom
Tx power (average)	660 W	400 W	2 KW	2 KW
number of detected meteors	cN_0N_{RX}	$cN_0N_{RX}N_{TX}$	$cN_0N_{RX}N_{TX}$	$cN_0N_{RX}N_{TX}$
efficiency factor (c)	0.7	0.7	1.0	1.1
reference	[SC15]	[Vie+16]	[Cha+20; Urc+19b]	[Cha+20; Urc+19b]

Table 5.1: Performance of implementations

[SC15], (b) the one based on SIMO using waveform diversity proposed by Vierinen et.al. [Vie+16], and the two based on (c) MISO and (d) MIMO described in this work, which have been recently published in [Cha+20] and [Urc+19b]. Notably, compared to the other implementations, the MISO configuration obtains the largest number of meteor detections per antenna. It only uses 27 antennas in total. The efficiency factor was estimated from the experimental results published in [Cha+20] (Table 2: Total counts). The simplicity and performance of radar networks based on MISO allowed us to deploy these systems in Germany, Argentina, and Peru to study the MLT dynamics with high spatio-temporal resolution at different geographic conditions. Some results are presented in the Section 5.5.

An adverse effect of using MISO or MIMO with waveform diversity is the augmented

cross-interference between transmitted signals since the waveforms are not totally independent. The total cross-interference in the system grows as the number of transmitters does. In our example, the number of Tx antennas is fifteen, which results in fifteen different waveforms. Standard decoding techniques don't decouple and retrieve the Tx-Rx signals successfully. To deal with the cross-interference in such environments, an advanced signal processing approach based on compressed sensing is proposed. Metrics used to select the proper recovery method are (a) its computational complexity, and (b) its accuracy to recover weak signals.

5.3.1 Traditional signal recovery algorithms

The signal recovery problem in a MIMO radar using waveform diversity was described in Section 3.6, which is written as

$$\mathbf{y}_m = \mathbf{\Phi}\mathbf{x}_m + \boldsymbol{\eta}_m, \tag{5.3}$$

$$\text{with} \quad \mathbf{x}_m = \begin{bmatrix} \mathbf{v}_{1m}^T & \mathbf{v}_{2m}^T & \dots & \mathbf{v}_{Pm}^T \end{bmatrix}^T, \tag{5.4}$$

$$\text{and} \quad \mathbf{\Phi} = \begin{bmatrix} \mathbf{H}_1 & \mathbf{H}_2 & \dots & \mathbf{H}_P \end{bmatrix}, \tag{5.5}$$

where $\mathbf{y}_m \in \mathbb{C}^L$ is a column vector comprising all measured complex signals at receiving m, L is the waveform length, $\mathbf{v}_{pm} \in \mathbb{C}^R$ is a column vector comprising the scattering amplitudes for all range bins for the Tx-Rx link pm, $p = [1, 2, ..., P]$ is the transmitter index, $\mathbf{\Phi} \in \mathbb{C}^{LxN}$ is the sensing matrix, $N = PR$ is total number of unknowns equal to the number of transmitters P times the number of range gates R, and $\mathbf{H}_p$ is the matrix defined by the transmitted waveform p. Note that, the location of the transmitter (closely or widely separated) does not matter in this equation.

The recovery problem reduces to retrieve the backscattered coefficients for each Tx-Rx link, i.e., retrieve the column vector $\mathbf{x}_m$. The ideal solution would be to find the inverse of the matrix $\mathbf{\Phi}$ such that

$$\hat{\mathbf{x}}_m = \mathbf{\Phi}^{-1}\mathbf{y}_m. \tag{5.6}$$

Since $\mathbf{\Phi}$ is not full-rank ($L < N$), its inverse does not exist. Instead, we require to use approximations or prior information in form of constrains to solve the problem.

5.3.1.1 Matched filter estimator

One the most straightforward and fastest algorithms to decode radar data is the matched filter estimator (MFE) [Tur60]. As its name states, MFE is a filter which is matched to the transmitted signal, and therefore, maximizes the SNR. The MFE can be written as

$$\hat{\mathbf{x}}_m^{\text{MFE}} = \mathbf{\Phi}^H \mathbf{y}_m, \tag{5.7}$$

where $(\,)^H$ is the Hermitian transpose operator and $\hat{\mathbf{x}}_m^{\text{MFE}}$ is an estimation of $\mathbf{x}_m$. MFE is known to be an optimal filter since it maximizes the SNR; whereby its application is recommended for detection of weak signals. When MFE is applied to MIMO radars, it maximizes the SNR but also it enhances the sidelobes and the cross-interference between waveforms. Moreover, sidelobes' amplitude get stronger as the SNR and number of targets increase. In a MIMO system with a high number of Tx-Rx links, the application of MFE results in a highly contaminated solution with several artifacts. Therefore, application of MFE is not recommended in MIMO systems with several transmitters. To reduce the artifacts (cross-interference), different approaches are required.

5.3.1.2 Least squares estimator

In a system of equations where the matrix $\mathbf{\Phi}$ is of full column rank ($L \geq N$), there is no vector $\mathbf{x}_m$ which satisfies all the noisy observations. One criteria to solve the problem is to select the solution which minimizes the residual $\mathbf{r} = \|\mathbf{y}_m - \mathbf{\Phi}\mathbf{x}_m\|^2$. This technique is known as the least squares estimation (LSE) and it can be applied to recover $\mathbf{x}_m$ from (5.5). LSE is known for minimizing the discrepancy between the measurements and the unknown vector. The LSE problem can be written as

$$\hat{\mathbf{x}}_m^{\text{LSE}} = \underset{\mathbf{x}_m}{\arg\min} \, \|\mathbf{y}_m - \mathbf{\Phi}\mathbf{x}_m\|_2^2, \tag{5.8}$$

where $\|.\|_2$ represents the Euclidean norm. In a well-posed problem ($L \geq N$), LSE gives a unique solution in which the cross-interference and sidelobes are reduced. The LSE solution to (5.8) is given by

$$\hat{\mathbf{x}}_m^{\text{LSE}} = \mathbf{\Phi}^+ \mathbf{y}_m, \tag{5.9}$$

where $\mathbf{\Phi}^+ = (\mathbf{\Phi}^H\mathbf{\Phi})^{-1}\mathbf{\Phi}^H$ is the Moore-Penrose pseudoinverse.

In an ill-posed problem, like the one for our MIMO system, $\mathbf{\Phi}$ is not of full column rank ($L \leq N$) and there may be infinitely many LSE solutions of $\mathbf{x}_m$ which fit $\mathbf{y}_m$. For those cases, additional constraints are required to make the solution unique. Vierinen et al. [Vie+16] got results similar to the LSE using the maximum likelihood estimator.

5.3.1.3 Truncated SVD

A method known to regularize an ill-posed least squares problem is the truncated singular value decomposition (tSVD). The basic idea behind tSVD is to convert the ill-posed problem shown in (5.5) to a well-posed problem, in which the solution will be unique and less sensitive to perturbations [Han87].

The definition of singular value decomposition (SVD) is

$$\mathbf{\Phi} = \mathbf{U}\mathbf{S}\mathbf{V}^T, \tag{5.10}$$

$$\mathbf{S} = \mathrm{diag}(\delta_1, \delta_2, ..., \delta_N) \tag{5.11}$$

where δ_i is the i-th singular value of the matrix $\mathbf{\Phi}$. In tSVD, the matrix $\mathbf{\Phi}$ is approximated with another one of lower rank, which ignores the smallest singular values of $\mathbf{\Phi}$. The matrix $\mathbf{\Phi}_k$ used in the tSVD is defined as the rank-k matrix.

$$\mathbf{\Phi}_k = \mathbf{U}\mathbf{S}_k\mathbf{V}^T, \tag{5.12}$$

$$\mathbf{S}_k = \mathrm{diag}(\delta_1, ..., \delta_k, 0, ..., 0), \tag{5.13}$$

where $k \leq N$, and S_k is equal to S with the smallest $N - k$ singular values replaced by zero. In our problem, k is equal to $\min(L, N)$. Using this definition, the approximate inverse of the matrix $\mathbf{\Phi}$ would be

$$\mathbf{\Phi}^+ = \mathbf{V}\mathbf{S}^+\mathbf{U}^T, \tag{5.14}$$

$$\mathbf{S}^+ = \mathrm{diag}\{\tau_i\},\ \tau_i = \begin{cases} 1/\delta_i & \text{if } i \leq k \\ 0 & \text{if } i > k \end{cases}. \tag{5.15}$$

The main idea of tSVD is to truncate the small singular values, and thus to truncate the condition number of $\mathbf{\Phi}$ (δ_1/δ_k), which might introduce high errors to the solution. Using tSVD, we will obtain a unique solution in which the interference is reduced, even if the

problem is ill-posed. In other disciplines, the tSVD is also known as the minimum-norm least squares solution, since the tSVD picks the least squares solution with the smallest energy $\|\mathbf{x}_m\|^2$. Such minimization helps to reduce the cross-interference between waveforms in a MIMO system. Nevertheless, it also minimizes the energy of the weak echos, which might be hidden in the noise.

5.3.1.4 Regularized least squares estimator

To find a balance between the maximum-norm (matched filter estimator) and the minimum-norm (truncated singular value decomposition), an additional regularization term can be added to the minimization problem

$$\hat{\mathbf{x}}_m^{\text{RLSE}} = \arg\min_{\mathbf{x}_m} \|\mathbf{y}_m - \mathbf{\Phi}\mathbf{x}_m\|_2^2 + \lambda||\mathbf{x}_m||_2^2, \tag{5.16}$$

where $\lambda > 0$ is the regularizer, which represents the trade-off between the minimization of the residual and the total energy in $\mathbf{x}_m$. The analytical solution to (5.16) can be written as

$$\hat{\mathbf{x}}_m^{\text{RLSE}} = (\mathbf{\Phi}^H\mathbf{\Phi} + \lambda I)^{-1}\mathbf{\Phi}^H\mathbf{y}_m. \tag{5.17}$$

Equation (5.17) is known as the regularized least squares estimation (RLSE) or Ridge regression [HK70]. Notice that, when $\lambda = 0$, the RLSE solution is the same as the ordinary LSE, in which the total energy in $\mathbf{x}_m$ is minimized. On the other hand, when λ tends to infinite, RLSE has a similar solution as the MFE, in which the total energy in $\mathbf{x}_m$ is maximized. The selection of λ is crucial to have a good balance between both minimizers in (5.16). Typically, the best λ is found by cross-validation algorithms [Jam+09; TT09]. This additional step might result in a high demand in computational power, and not always the selected λ is the best.

Similar results to RLSE can be found using the minimum mean squares error estimator (MMSE), for which $\lambda = \frac{1}{\text{SNR}}$ [Kay93]. Nevertheless, neither RLSE nor MMSE reduces the cross-interference significantly if the matrix $\mathbf{\Phi}$ is ill-conditioned. In the field of MIMO communications, successive interference cancellation (SIC) approaches have been employed to improve the performance of linear detectors like MFE or MMSE [Wol+98; WWL03; RGV09]. SIC approaches are quite similar to the CLEAN algorithm used in radio astronomy [Hög74], in which stars and planets are considered to be point objects that are found

through successive point source cancellation. The application of CLEAN for punctual and sparse objects can be considered the most basic implementation of the orthogonal matching pursuit (OMP) algorithm [CW11], which is used in compressed sensing to solve sparse problems.

5.3.2 Signal recovery based on compressed sensing

Compressed sensing (CS), also known as sparse recovery [Don06a; CRT06a] was previously described in Section 2.5.2.1. Compared to the Nyquist theorem, which claims that an arbitrary signal must be sampled at twice its bandwidth for exact recovery, CS states that a signal can be recovered even from a very limited number of measurements under two conditions: (a) the signal is K-sparse in some domain, i.e., the number of non-zero values in the unknown vector is less than K; and (b) the sensing matrix satisfies the restricted isometry property (RIP) [CT05], which requires that any K columns of $\mathbf{\Phi}$ are approximately orthogonal.

In case of a specular meteor MIMO radars using waveform diversity, both the K-sparsity and RIP condition are satisfied. Firstly, specular meteor echoes can be considered to be sparse point targets. Although, the meteor trail is long along its trajectory, its angular response is narrow since its scattering mechanism is explained by Fresnel scattering. In the direction transverse to the trail, its extension is narrow and so its angular response. Consequently, specular meteor reflections can be considered as punctual objects in range and angle. Moreover, since the specular condition is satisfied only for few meteors, the number of detections is very low, so they are sparse. Although specular meteors are sparse in range and angle, only sparsity in range is exploited to avoid inversion of large matrices.

Secondly, by selecting proper waveforms, as described in Section 3.6, the matrix $\mathbf{\Phi}$ can satisfy the RIP condition. Further details to improve the waveform design in specular meteor MIMO radars are described later. For now, it is assumed that the matrix $\mathbf{\Phi}$ satisfies the RIP condition.

Under the two conditions described above, CS aims to recover the sparsest solution by adding a constraint to (5.5)

$$\hat{\mathbf{x}}_m^{\text{CS}} = \arg\min_{\mathbf{x}_m} ||\mathbf{y}_m - \mathbf{\Phi}\mathbf{x}_m||_2^2, \quad \text{subject to } ||\mathbf{x}_m||_0 < K, \tag{5.18}$$

where $||\mathbf{x}_m||_0$ is the l_0-norm, which counts the number of non-zero values in the vector $\mathbf{x}_m$. Equation (5.18) recovers the solution $\hat{\mathbf{x}}_m^{\text{CS}}$ with the smallest possible number of non-zeros which fits with the data $\mathbf{y}_m$.

Although the l_0-norm minimization problem seems to be an easy problem, recovery of the unknown vector requires an exhaustive search over all subsets of columns of $\mathbf{\Phi}$, resulting in C_K^N possible support sets. Thereby, the l_0-norm problem is computationally intractable. To find an approximate solution, studies by Donoho and Candes [Don06b; CRT06b] have shown that the l_0-norm problem can be relaxed and reformulated to a more computationally graceful problem, the l_1-norm. The l_1-norm is also known as basis pursuit (BP) [CDS98], and it is the most prompted approach to solve (5.18) because of its reduced complexity $O(N^3)$ compared to the l_0-norm $O(C_K^N)$ [Cre+19; Che15]. Since l_1-problem is a convex optimization problem, it can be solved via interior point methods such as gradient-based algorithms. Even though fast algorithms have been introduced to solve the BP problem and to reduce its complexity to $O(L^2 N^{\frac{3}{2}})$ [WEV13], this is still not applicable when facing real-time analysis for large data like in the specular meteor MIMO radar case.

Numerous researchers have been working in developing more efficient algorithms for sparse signal estimation. Among all of them, greedy algorithms are the most practical and fastest to solve (5.18). Greedy algorithms are iterative algorithms which make a locally optimal selection at each iteration with the intent to find the global optimum at the end of the algorithm [Tro04; Bi+16]. A good example of these algorithms is the orthogonal matching pursuit (OMP) algorithm [TG07; CW11] and its variations such as GOMP [WKS12], ROMP [NV09], StOMP [Don+12], and CoSaMP [NT09]. Although OMP requires more measurements ($K \log(N)$, [TG07]) than BP ($K \log(N/K)$, [Don06a]) to achieve the same accuracy, the low computational cost of OMP makes it feasible for real-time applications. In this work, a variation of StOMP is proposed to recover SMR MIMO data.

5.3.2.1 Stagewise orthogonal matching pursuit

Stagewise orthogonal matching pursuit (StOMP) is a greedy method for finding the sparsest solution of underdetermined systems of linear equations [Don+12]. Compared to earlier methods like BP and OMP, StOMP is significantly faster on large-scale problems. Since StOMP is based on OMP, first the OMP algorithm is described. OMP is an iterative greedy algorithm which starts identifying the column of $\mathbf{\Phi}$ (scaled) which maximizes the correlation with the measurements. Then the index of this column is added to a list of selected columns. Next, the contribution of the selected (scaled) columns are subtracted from the measurements generating a measurement residual for the next iteration. The steps above are repeated s times until the residual is minimum. In OMP, the number of iterations s must be known in advance, i.e., it requires prior knowledge of the sparsity.

Even though OMP has a low complexity $O(2NLs + 3Ls^2)$ [WKS12], some studies have made some modifications to improve its computational efficiency and recovery performance. For example, Wang et.al. [WKS12] describes the generalized orthogonal matching pursuit (GOMP) method, where more than one indices are identified at each iteration. In this way, GOMP decreases the number of required iterations and reduces the algorithm complexity to $O(2NLs)$, with s being the number of iterations. Similarly, Donoho et.al. [Don+12] proposed StOMP, where multiple indices higher than a threshold are selected at each iteration and the number of iterations has not to be known in advanced. Unlike GOMP, StOMP uses a residual threshold ϵ as a stooping condition. StOMP steps are summarized in Table 5.2.

In StOMP, the selection of the SNR threshold n and the stopping condition ϵ are directly related, and they both depend on the orthogonality of the sensing matrix $\mathbf{\Phi}$ and the sparsity K of $\mathbf{x}_m$. The better the orthogonality and sparsity, the lower n and ϵ. A small value of n allows to select more columns per iteration and reduces the number of total iterations. However, as a consequence, the number of false detections (bad selections) might increase. This effect is caused by the use of MFE in the first step of StOMP. As explained above, the use of MFE enhances the sidelobes which might be confused as real echoes by StOMP. Typically, n is a high value and few columns are selected per iteration in StOMP, which increases the processing time.

Input	measurements at receiver m, $\mathbf{y}_m \in \mathbb{C}^L$ sensing matrix $\mathbf{\Phi} \in \mathbb{C}^{LxN}$ threshold $n \in \mathbb{R}$ stopping condition $\epsilon \in \mathbb{R}$
Initialize	iteration count $s = 0$ residual vector $\boldsymbol{\rho} = \mathbf{y}_m$ support $\Omega_0 = \emptyset$
Iteration	**While** ($\epsilon < \frac{1}{L}\|\boldsymbol{\rho}\|_2^2$) **Identify** a subset $\mathbf{\Phi_r}$ (indices) of $\mathbf{\Phi}$ which satisfies $R = \{r : \|\hat{\mathbf{x}}(r)\|^2 > n\,\sigma^2\}$, where $\hat{\mathbf{x}} = \mathbf{\Phi}^H \boldsymbol{\rho}$, and σ^2 is the variance of $\hat{\mathbf{x}}$ (noise floor). Merge the new subset with the previous support $\Omega_s = \Omega_{s-1} \bigcup R$. Compute a better approximation of $\mathbf{x}$ supported by Ω_s $\hat{\mathbf{x}} = (\Phi_{\Omega_s}^H \Phi_{\Omega_s}^H)^{-1} \Phi_{\Omega_s}^H \mathbf{y}_m$. **Subtract** the contribution of the selected columns and **update** the residual for the next iteration $\mathbf{r} = \mathbf{y}_m - \Phi_{\Omega_s}^H \hat{\mathbf{x}}$, s = s+1.
Output	the estimated signal at receiver m, $\hat{\mathbf{x}}_m = \hat{\mathbf{x}}$

Table 5.2: **StOMP algorithm**

5.3.2.2 Fast stagewise orthogonal matching pursuit

To reduce the number of iterations and to increase the performance of StOMP, A modification employing the tSVD in the first iteration instead of MFE is proposed. Unlike MFE, tSVD allows us to identify correctly the highest non-zero values in the first iteration (strongest echoes, SNR $> 15\,\mathrm{dB}$), which finally introduce the highest errors. Once the strongest echoes are identified, and their contributions have been subtracted from the measurements, MFE is employed to enhance the smaller non-zero values (medium echoes, SNR $> 6\,\mathrm{dB}$), making them detectable. The modified StOMP, which is shown in Table 5.3, allows to find the sparsest solution using only two iterations, one for the strong and the other for the medium echoes. Thereby it is named as fast stagewise orthogonal matching pursuit (FaStOMP).

Input	measurements at receiver m, $\mathbf{y}_m \in \mathbb{C}^L$ sensing matrix $\mathbf{\Phi} \in \mathbb{C}^{LxN}$ threshold $n \in \mathbb{R}$ stopping condition $\epsilon \in \mathbb{R}$
Initialize	iteration count $s = 0$ residual vector $\boldsymbol{\rho} = \mathbf{y}_m$ support $\Omega_0 = \emptyset$
Iteration	**While** ($s < 2$) **Identify** a subset $\mathbf{\Phi_r}$ (indices) of $\mathbf{\Phi}$ which satisfies $R = \{r : \lvert\hat{\mathbf{x}}(r)\rvert^2 > n\,\sigma^2\}$, where $\hat{\mathbf{x}} = \begin{cases} \mathbf{\Phi}^{+}\boldsymbol{\rho} \text{ for } s = 0 \\ \mathbf{\Phi}^{H}\boldsymbol{\rho} \text{ for } s > 0 \end{cases}$, and σ^2 is the variance of $\hat{\mathbf{x}}$ (noise floor). Merge the new subset with the previous support $\Omega_s = \Omega_{s-1} \bigcup R$. Compute a better approximation of $\mathbf{x}$ supported by Ω_s $\hat{\mathbf{x}} = (\Phi_{\Omega_s}^H \Phi_{\Omega_s}^H)^{-1} \Phi_{\Omega_s}^H \mathbf{y}_m$. **Subtract** the contribution of the selected columns and **update** the residual for the next iteration $\mathbf{r} = \mathbf{y}_m - \Phi_{\Omega_s}^H \hat{\mathbf{x}}$, s = s+1.
Output	the estimated signal at receiver m, $\hat{\mathbf{x}}_m = \hat{\mathbf{x}}$

Table 5.3: **FaStOMP algorithm**

In practice, FaStOMP is good at recovering strong and medium echoes, and to reduce the interference between waveforms. Nevertheless, we noticed that the smallest non-zero values (weak echoes, SNR ≈ 0) were not recovered even using FaStOMP. This occurs since the SNR of these echoes are comparable to the noise and their distinction from it is highly complicated. To make them detectable we require either to increase their SNR or to improve their detectability. To do so, a technique similar to the Joint and Block Sparsity is used [EKB10; Xua+17]. Essentially, a third iteration is added to FaStOMP in which the SNR of the smallest echoes are improved. In the third iteration, the contribution of strong and medium echoes have been already subtracted from the measurements and only weak echoes remain on the residual. To increase the SNR, the estimated values can be coherently integrated along time since meteor echoes last for at least a few

ms (T samples) in the same range. For which the identification step can be replaced by $|\hat{\mathbf{x}}_{joint}(r,t)|^2 > n\,\sigma^2$, with

$$\hat{\mathbf{x}}_{joint}(r,t) = \frac{1}{T}\sum_{t_0=-T/2}^{T/2} \hat{\mathbf{x}}(r, t+t_0). \tag{5.19}$$

Furthermore, the identification step in FaStOMP can be further improved when coherent MIMO is employed. For coherent MIMO configurations, radar echoes coming from different transmitters will be located at the same range bin and the signal can be incoherently integrated along the Tx-Rx channels, improving the detectability of the weak echoes

$$|\hat{\mathbf{v}}_{mp}(r,t)|^2 = |\hat{\mathbf{v}}(r,t)|^2 = \frac{1}{MP}\sum_{m=1}^{M}\sum_{p=1}^{P}|\hat{\mathbf{v}}_{mp}(r,t)|^2. \tag{5.20}$$

For such cases, the identification step can be replaced by $|\hat{\mathbf{v}}(r)|^2 > n\,\sigma^2$.

Figure 5.7 summarizes the steps of the StOMP algorithm. Notice that, although the SNR threshold is $6\,\mathrm{dB}$ for the three cases (a) strong, (b) medium, and (c) weak echoes, the power of selected echoes at each iteration are not. For the first iteration, only indices of strong echoes are selected since the estimated noise level is relatively high due to the strong sidelobes. In the second iteration, given that the strong echoes have been removed, we expect small sidelobes which are comparable to the noise level, so only indices for which the SNR is higher than $6\,\mathrm{dB}$ are selected. In the last iteration, the noise level is reduced by integrating the signal incoherently, which allows to select the indices of weak echoes with SNRs lower than $6\,\mathrm{dB}$. The threshold of $6\,\mathrm{dB}$ was selected since it represents $4\,\mathrm{standarddeviations}$, i.e., a confidence level of selecting non-noise indices of $99.9\,\%$.

Hereafter, when we refer StOMP or FaStOMP, they both include the third stage with coherent and incoherent integrations. In which the SNR threshold is $n = \frac{6}{\sqrt{MP}}$.

5.3.3 Sensing matrix design

Exact recovery of a K-sparse vector $\mathbf{x}_m$ requires the sensing matrix $\mathbf{\Phi}$ to fulfill certain conditions. Such conditions can be expressed as restricted isometry property (RIP) in

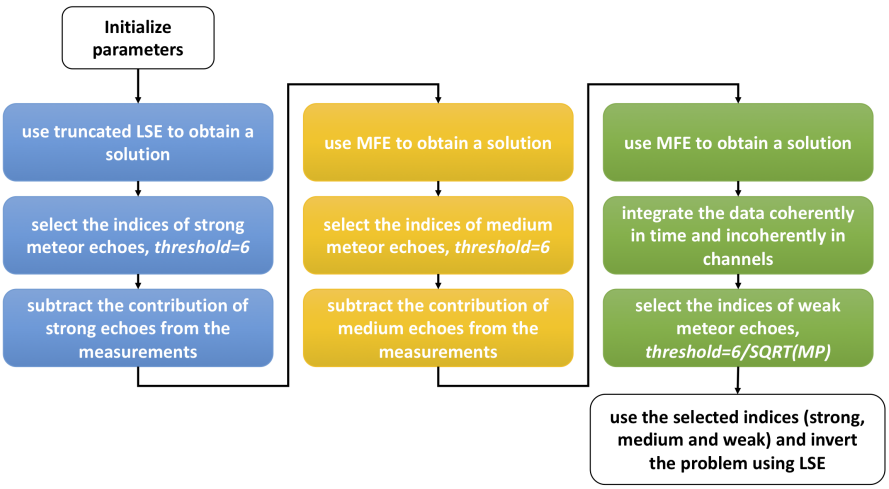

Figure 5.7: Flow chart summarizing the StOMP algorithm used to recover specular meteor echoes in a radar network with multiple transmitters (MIMO radars). The red, yellow, green boxes represent the identification and estimation of strong, medium, and weak meteor echoes, respectively.

[CT05], as uniform uncertainty principle (UPP) in [CT06], as exact recovery condition (ERC) [Tro04], or as mutual incoherence condition (MIC) in [DH06]. In practice, only MIC and ERC are feasible in real problems.

To optimize the sensing matrix design, the mutual incoherence condition is defined as a metric

$$\mu_{\max}(\mathbf{\Phi}) = \max_{p \neq q} |\mathbf{\Phi}_p^H \mathbf{\Phi}_q|, \tag{5.21}$$

where $\mathbf{\Phi}_p$ is the p-th column of $\mathbf{\Phi}$ and $\mu_{\max}$ represents the largest off-diagonal element of the gram matrix $\mathbf{G} = \mathbf{\Phi}^H \mathbf{\Phi}$. In some sense, MIC measures how independent the columns in $\mathbf{\Phi}$ are. When $\mu_{\max}$ is zero, the columns $\mathbf{\Phi}$ are fully independent. Tropp [Tro04] proved that the maximum sparsity of a system $K_{\max}$ is bounded by its MIC value

$$K_{\max} < \frac{1}{2}\left(1 + \frac{1}{\mu_{\max}}\right). \tag{5.22}$$

This equation indicates that the system of equations shown in (5.5) with a given MIC, can be solved by compressed sensing only if the number of non-zero values in $\mathbf{x}_m$ is less than $K_{\max}$. Other authors suggested an averaged mutual coherence μ_{avg} instead of $\mu_{\max}$. The average value is more adequate in our problem since the distribution of the non-zero

values are equally probable along $\mathbf{x}_m$. Thus, the sensing matrix design problem reduces to finding a matrix $\mathbf{\Phi}$ which minimizes the mutual coherence $\mu_{\text{avg}}(\mathbf{\Phi})$. As described in section 3.6, the matrix $\mathbf{\Phi}$ is a function of the transmitted waveforms. To optimize $\mathbf{\Phi}$, we have to select a proper set of waveforms $\mathbf{w}_p$ which minimize $\mu_{\text{avg}}(\mathbf{\Phi})$.

Similar to [Vie+16], pseudorandom binary phase-coded sequences are employed as waveforms. Although they are not fully independent, they maximize the transmit energy, are easy to be generated, and have good orthogonality properties [BM16]. Other authors have also suggested the use of other quasi-orthogonal codes such as the Gold and Frank codes [Gol67; Fra06], however, they are not used here since pseudo-random sequences are more flexible. In our case, the transmitted signal (waveform) is divided in L bauds where each of them has a constant amplitude equal to 1 ($|\mathbf{w}_p| = 1$), and a binary phase (0 or π). The phase values for each baud are selected randomly from a given seed number as described in Section 3.3.2. To optimize the sensing matrix design $\mathbf{\Phi}$, a set of seeds which minimizes $\mu_{\text{avg}}(\mathbf{\Phi})$ are selected.

When multiple closely separated transmitters are employed, i.e., coherent MISO or MIMO, the sensing matrix can be further optimized. As mentioned above, MIC measures how large the off-diagonal elements of the gram matrix $\mathbf{G}$ are, which can be seen as a measure of how strong the cross-interference between two columns of $\mathbf{\Phi}$ is. As shown in (2.36), a column of $\mathbf{\Phi}$ represents a shifted version $\mathbf{w}_p(\tau)$ of the waveform $\mathbf{w}_p$. Particularly, we are interested in minimizing the cross-interference of every possible combination of the columns $(\mathbf{w}_p(\tau_1), \mathbf{w}_{p'}(\tau_2))$ for $p \neq p'$ since each combination is equally probable. In case of MISO or MIMO, a target which is detected at a given range bin by one Tx channel, i.e., $|\mathbf{v}_{m1}(\tau)| \neq 0$, it is always detected at the same range bin by the other Tx channels, i.e., $|\mathbf{v}_{mp}(\tau)| \neq 0$ for $p = [2, ..., P]$. Therefore, the probability of having cross-interference due to the combination $(\mathbf{w}_p(\tau), \mathbf{w}_{p'}(\tau))$ is $100\,\%$, for which the artifacts created by this combination must be further minimized.

Since the average interference between waveforms along lag τ is the same as the one along lag 0, see Fig. 3.5, the problem reduces to minimize the amplitude of $\mu_{pp'} = w_p^H w_{p'}$. For the experiments and simulations presented in this work, the average coherence μ_{avg} and the coherence at zero lag between waveforms $\mu_{pp'}$ are used as metrics to select the set of waveforms.

$$\text{seeds} = \underset{\mathbf{\Phi}(\text{seeds})}{\arg\min} \{|\mu_{\text{avg}}(\mathbf{\Phi}) - \mu_0| + |\mu_{pp'}(\mathbf{\Phi}) - \mu_1|\}, \tag{5.23}$$

where μ_0 and μ_1 are the desired coherence values and are selected based on the maximum number of non-zero values $K_{\max}$ expected in $\mathbf{x}_m$, and $\mathbf{\Phi}$ is function of the waveforms which depend on the selected seeds. Considering a coherent MIMO radar with five transmit elements and five meteor echoes per unit time in average, $K_{\max} = 25$, and using (5.22) $\mu_{\text{avg}} = 2e^{-2}$. Since we desire to reduce the cross-interference between waveforms at zero lag even more, the mutual coherence $\mu_{pp'} = 2e^{-3}$ is selected to be one order of magnitude lower. Once the two parameters are defined, an iterative search is used to find the proper seeds which satisfy the given conditions.

5.4 Montecarlo simulations

Preliminary results of the proposed algorithm based on compressed sensing (CS) applied to a multi-static meteor radar system installed in northern Germany have recently been published by Chau et.al. [Cha+18]. Since CS is fundamentally based on probabilities and boundary conditions, it is challenging to prove its success only based on experimental results. Consequently, some simulations are performed to support the proposed approach and to delimitate it before exploring the experimental results.

The simulated system, similar to the MIMO link used in [Cha+18], consists of one Tx station with five transmitting antennas and one receiving station with five receiving antennas. In the simulations, each transmitting antenna radiates a different waveform. The waveforms are optimally selected using the conditions described in section 5.3.3. For which, an iterative search, which satisfies (5.23), was implemented in Python to find the most adequate seeds. The sequence of pseudo-random binary numbers were produced using the numpy.random library. The seeds that produce quasi independent waveforms were the sequences with seeds $[1, 97, 173, 1885, 8928]$.

To evaluate the advantage of our recovery algorithm, it was compared with two of the most common approaches like MFE and tSVD. The forward model simulated is the one described in (5.5), which was simulated under three different scenarios (a) variable SNR (b) variable sparsity (number of meteors) and (c) variable waveform length. In all three cases, the noise variance σ_n^2 was equal to 1 and the signal power of the simulated meteors σ_s^2 was relative to the noise (SNR$= \sigma_s^2/\sigma_n^2$). Since the simulated system was a coherent

MIMO system, the meteor range gates were randomly selected, however, they were kept at the same range bin for all the Rx and Tx channels, i.e., $|\mathbf{v}_{mp}(r)| = |\mathbf{v}_{mp'}(r)|$ for $p, p' = [1, .., P]$.

In our simulations, once the ground truth $\mathbf{x}_m$ was defined, $\mathbf{y}_m$ was obtained by (5.5) and adding a Gaussian noise. Using MFE, tSVD, and FaStOMP, we get estimates $\hat{\mathbf{x}}_m$ from the measurements $\mathbf{y}_m$. In all the cases, the sparsity K (unknown in real systems) defined as the number of simulated meteors times the number of transmitters was only used to corroborate the success of the recovery algorithm.

To compare the performance of the three algorithms, a relative error was chosen as a metric and it is defined as

$$\Delta e = \sum_{k=1}^{K} \frac{|\mathbf{x}_m(k) - \hat{\mathbf{x}}_m(k)|^2}{|\mathbf{x}_m(k)|^2}, \tag{5.24}$$

where $\mathbf{x}_m(k)$ is the k-th non-zero value of $\mathbf{x}_m$. The typical mean-square-error is not used since the three algorithms MFE, tSVD, and StOMP try to minimize it and the resulting (error) value is almost the same for any case. Instead, a weighted error is used since the primary objective is the total error independent of the signal amplitude. To avoid statistical fluctuations, the simulation was repeated for each case 200 times (realizations) and the error associated with them was averaged out.

Figures 5.8, 5.9, and 5.10 show the performance of the recovery algorithms under the three selected scenarios: (a) variable SNR, (b) variable sparsity, and (c) variable waveform length, respectively. Since the relative error defined in (5.24) does not consider errors coming from the zero elements (possible artifacts), the number of false-detections is included in the plots, i.e., the number of elements in $\hat{\mathbf{x}}_m$ which should have been zero but were not due to the algorithm being used. In our definition, false-detections are those values for which the power is higher than the noise level by a given amount. Being conservative a threshold of $4\sigma^2$ is selected, for which σ^2 is the noise variance estimated from $\hat{\mathbf{x}}_m$. It is important to notice that the artifacts or sidelobes also affect the noise level estiamtion.

In our simulations, the StOMP algorithm does not include the coherent integration step described in (5.19) since only one time sample is simulated. However, it includes the incoherent integration step shown in (5.20). The number of incoherent integrations selected for all the simulations were five.

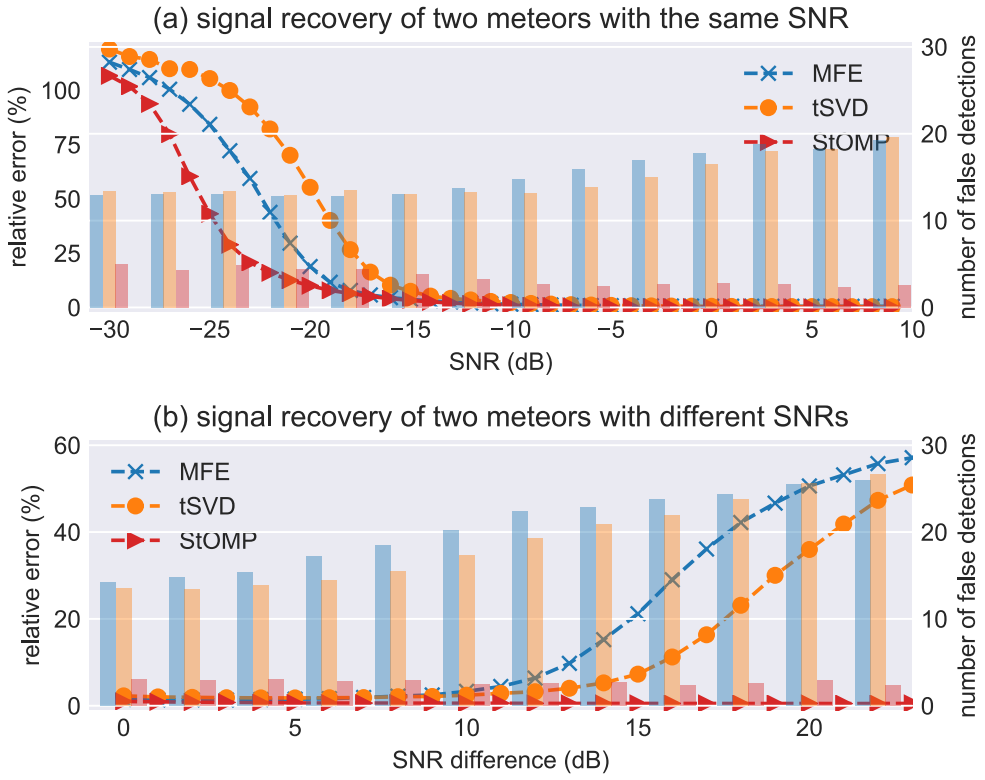

Figure 5.8: Performance comparison of recovery techniques as a function of SNR. Every simulation run contains two meteor targets with (a) both having the same SNR and (b) having a SNR difference indicated in the plot, with the weakest one fixed to $-10\,\mathrm{dB}$. The colored bars indicate the average number of false detections for each technique. During the simulation M, N, and K were set to 1000, 2000, and 10 respectively.

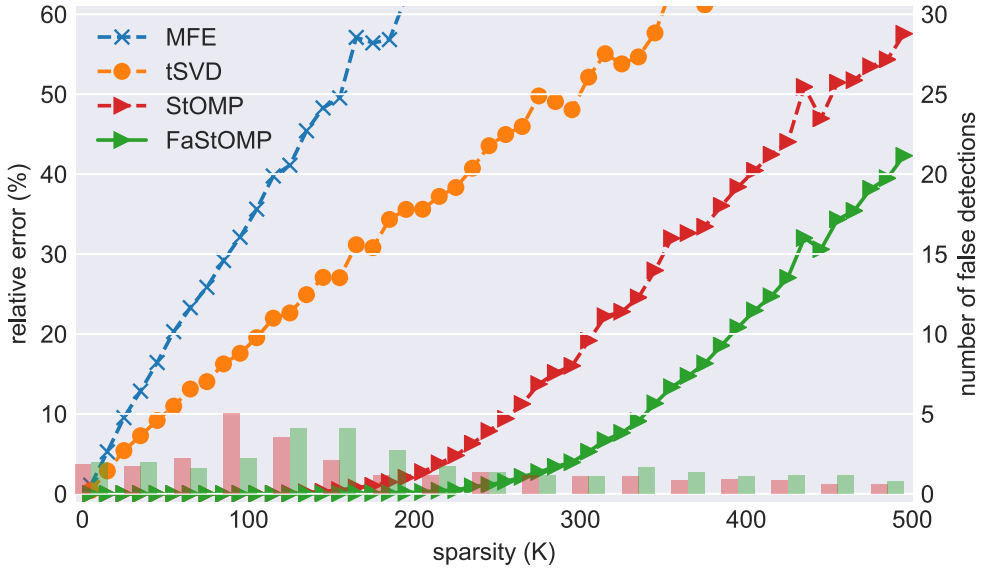

Figure 5.9: Same as Fig. 5.8. Recovery performance as a function of sparsity. In every simulation run, the SNR and the range bin of simulated meteors were randomly assigned. Only colored bars for StOMP and FaStOMP are included. M, N, and SNR_{max} were set to 1000, 2000, and 25, respectively.

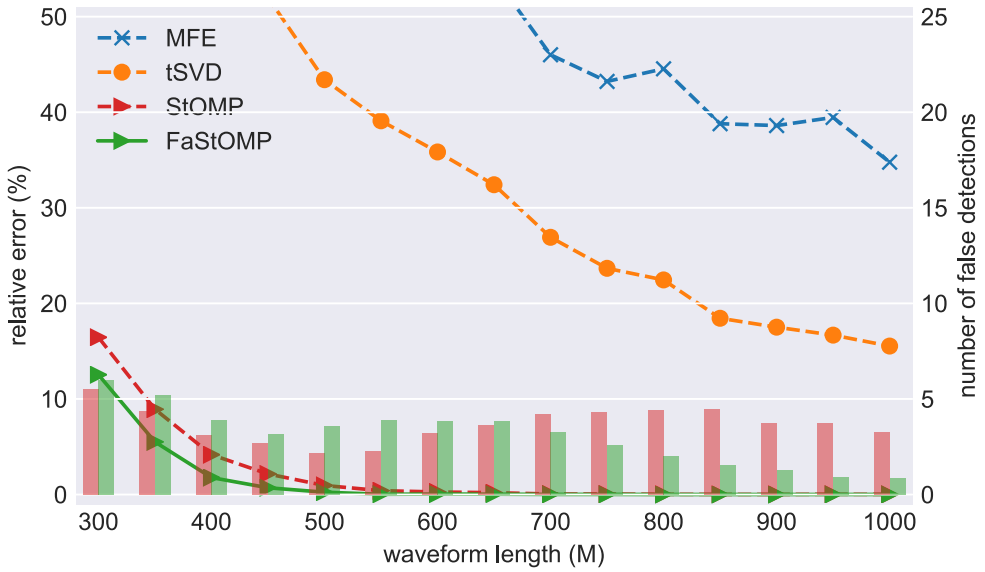

Figure 5.10: Same as Fig. 5.9. Recovery performance as a function of the waveform length. N, K, and SNR_{max} were set to 1500, 100, and 25, respectively.

Figure 5.8 shows the results for MFE, tSVD, StOMP as a function of SNR. For this simulation, only two meteor echoes are considered, i.e., $K = 10$, a waveform length of $L = 1000$, and a number of range bins of $R = 300$. Figure 5.8(a) shows the results in the presence of two meteor echoes with the same SNR, whereas, Fig. 5.8(b) shows the results for the same meteors but having a SNR difference. For the first case, clearly most of the algorithms have a good performance for SNRs higher than $-15\,\mathrm{dB}$. Nevertheless, for MFE and tSVD, the number of false echoes increases as the meteors' SNR do. This effect is highly related to the sidelobes' amplitude. In case of StOMP, the performance improves as the SNR increases. The reason is that as higher the SNR, the easier it is to identify, and thus easier to remove the sidelobes.

Surprisingly, StOMP's results in Fig. 5.8(a) are lower than MFE's even for low SNRs values. MFE is known for being a linear filter which maximize the SNR. The question is why StOMP is better than MFE even for weak echoes. The reason is the ability of the StOMP implementation to reduce the noise variance and to improve the detectability after integrating the signal incoherently. When no integration is used in StOMP, its performance is similar to MFE. FaStOMP was not included in this case since its performance under these conditions is similar to StOMP.

In the second case shown in Fig. 5.8(b), in which the two meteors have different SNRs. One of them was fixed to $-10\,\mathrm{dB}$ and the other one fluctuated between $-10\,\mathrm{dB}$ to $30\,\mathrm{dB}$. As expected, as soon as the SNR difference is higher than $10\,\mathrm{dB}$, the tSVD has a better performance than MFE, almost $20\,\%$ better. This indicates that tSVD reduces the interference due to strong signals better. In case of StOMP, the error is negligible for this simple scenario.

The previous simulation was a simple case and it was selected to highlight the differences between the recovery algorithms. In the following simulation, with radar parameters similar to the first one, the performance of the algorithms are evaluated in a more complicated scenario, namely, a system with many meteor detections. In the recovery problem, the number of meteors detections is equivalent to the sparsity or number of non-zero values in the vector $\mathbf{x}_m$. The question here is what the maximum sparsity K for which exact recovery is guaranteed is. According to (5.22), the theoretical maximum sparsity $K_{\max}$ is 26 for the selected seeds considering a waveform length of 1000, which is not so accurate.

The performance of the algorithms as a function of sparsity are shown in Fig. 5.9. For this simulation, the index of the non-zero values (range bins) and the SNR of them were randomly selected. The SNR range was similar to the previous case, from $-10\,\mathrm{dB}$ to $30\,\mathrm{dB}$. Observing the results, clearly, the performance of MFE and tSVD decrease quickly with increasing K. Not only the error but also the number of false detections increases. The number of false detections were not included for MFE and tSVD because they were extremely high (> 50).

On the other hand, the results of the algorithms based on compressed sensing (CS) prove that they work successfully even when the sparsity is about 250. When the sparsity is less than 150, there is no difference between StOMP and FaStOMP. Considering a maximum error of $5\,\%$ as acceptable, the maximum sparsities for StOMP and FaStOMP are 255 and 340, respectively, which compared to the number of measurements (waveform length) is one third ($340 \approx 1000/3$). This means that the number of measurements has to be at least three times the number of non-zero values (unknowns).

Another important point of these results is the improvement from StOMP to FaStOMP. It shows that using tSVD instead of MFE in the first iteration helps to choose correctly the highest non-zero values and remove their effects from the measurements. The number of false echoes for StOMP and FaStOMP are below 5, which indicates they are working properly under the conditions descrideb here.

A similar analysis was implemented to determine the minimum waveform length required for exact recovery. In this simulation, a maximum number of meteors equal to 20 is considered, i.e., $K = 100$, and a maximum number of ranges equal to $R = 300$. Figure 5.10 shows the results of this simulation. Considering the same relative error of $5\,\%$, the waveform lengths required to recover up to 20 meteor echoes in a MIMO radar with five transmmiting antennas are 395 and 350 for StOMP and FaStOMP, respectively, corroborating our previous finding that the waveform length L should be at least three times larger than the sparsity K. In a SMR network with five transmitting antennas, a waveform length of 300 might be used since, under normal conditions, less than 20 meteors per time unit are expected.

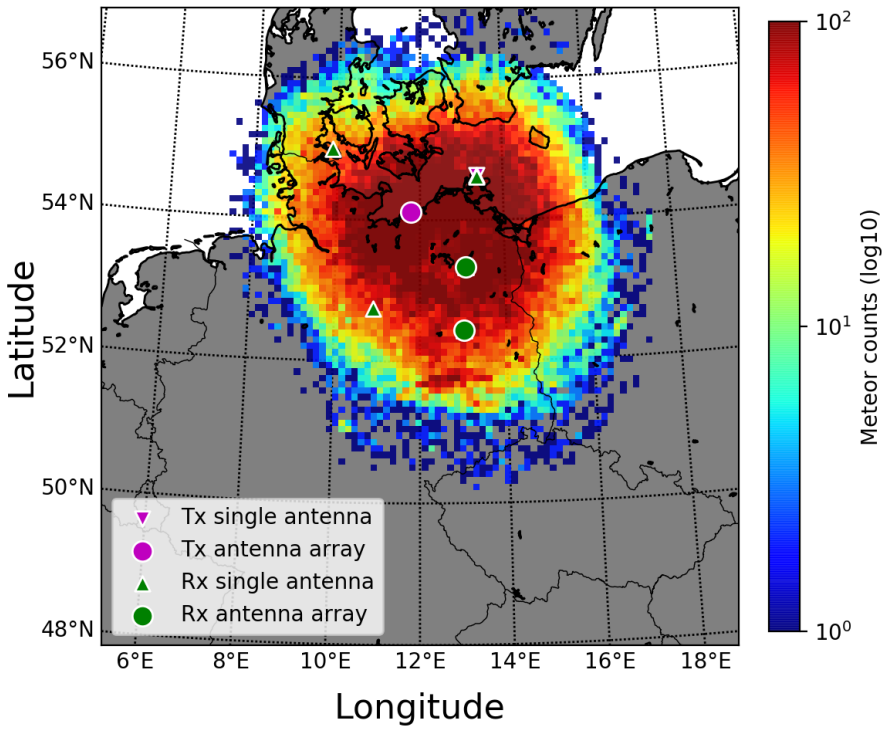

Figure 5.11: Meteor map distribution of specular meteor detections during 1 d of observation by a radar network deployed in northern Germany. The magenta marks represent the location of transmitting stations and the green marks the location of receiving stations. Circles indicate an antenna arrays (interferometry capabilities), whereas triangles indicate single antennas.

5.5 Experimental results

Having shown the success of the proposed system and recovery algorithm, a multi-static radar network was deployed in 2018 in northern Germany. The radar network based on MIMO using waveform diversity, consisted of two Tx stations and five Rx stations operating at 32.5 MHz as shown in Fig. 5.11. The first Tx station is a pulsed radar located in Juliusruh, Germany ($54.6°E, 13.3°N$) and it is indicated with a magenta triangle in the figure. More details of this radar system can be found in [SC15]. The second Tx station is a CW transmitter, it consisted of five transmit antennas located in Kühlungsborn, Germany ($54.11°E, 11.76°N$) and it is indicated with a magenta circle in the figure. Each transmit antenna radiated a continuous waveform with 400 W of power. The waveform length and the number of range gates used were 1000 and 350, respectively. This network is the same as the one used by Chau et.al. [Cha+20]. Only two receiving stations, which are indicated with a green circle had interferometric capability.

Figure 5.12 shows the range time intensity (RTI) plot for one of the MIMO links (Kühlungsborn-Neustrelitz) after applying (a) MFE, (b) tSVD, and (c) FaStOMP using coherent and incoherent integration. In this case, the number of coherent (along time samples) and incoherent (along Tx and Rx channels) integrations were 16 and 25, respectively. Since FaStOMP only recovers non-zero values, the noise level was estimated from the residual and added to the data synthetically. By looking at the MFE results, we observe its success to recover weak echoes. However, it fails in the presence of strong airplanes or meteor echoes. As mentioned before, MFE enhances the sidelobes and cross-interference between transmit waveforms, which does not allow to distinguish between real echoes and artifacts. On the other hand, the tSVD reduces the cross-interference for the strong echoes but as a consequence, the weak echoes are missing. Moreover, in case of very strong echoes, we can still see some sidelobes. This is due that the sensing matrix is ill-conditioned. Finally, FaStOMP recovers properly strong and weak echoes, and more importantly the sidelobes are strongly reduced.

The StOMP method described above assumes the presence of sparse specular meteor detections (non-zero values). However, distinct atmospheric targets like non-specular meteors, E-region irregularities, airplanes, and ground clutter are generally included in the radar data. For those cases, the non-zero values might be not restricted to one range

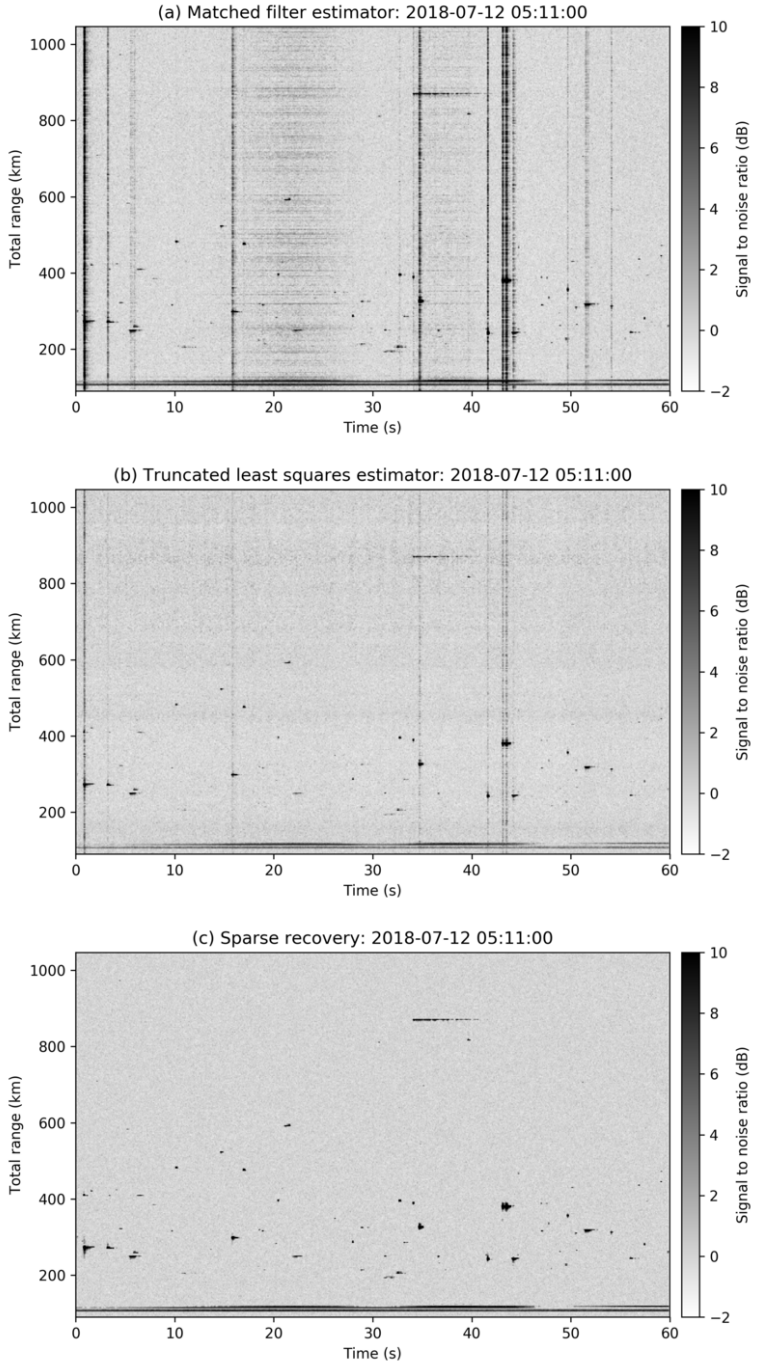

Figure 5.12: Comparison of recovery techniques with data acquired in a meteor radar network deployed in northern Germany. (a) matched filter estimator (MFE) (b) truncated singular value decomposition (tSVD) (c) fast stagewise orthogonal matching pursuit (FaStOMP)

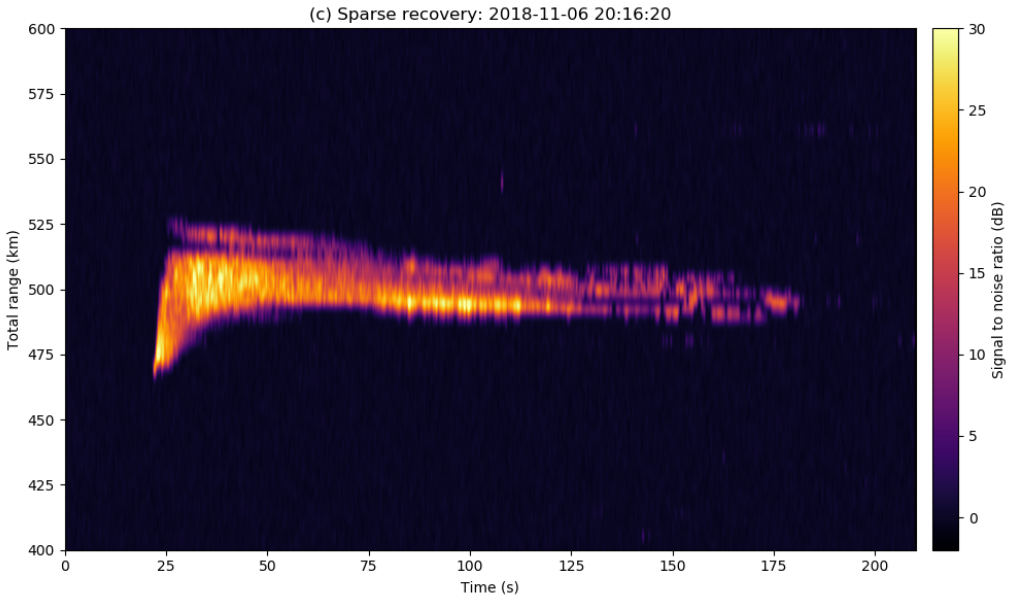

Figure 5.13: A fireball spread along several ranges recovered by StOMP.

only, and instead, they might be spread in several ranges. As the simulations show, even in those cases, the StOMP algorithm should work properly as long as the number of non-zero values is less than one-third of the number of measurements. Figure 5.13 shows an example of a fireball detected by the proposed algorithm where the target is spread along 50 ranges. A transform domain, where these non-point-targets are more sparse, might be added to the recovery problem to further improve the recovery of these type of echoes. However, it is not the focus of this work.

The resulting number of meteor detections compared to a standard SMR was at least seven times larger. As mentioned at the beginning of this work, the primary objective is to help in understanding the atmospheric dynamics in the MLT region. Although estimation of atmospheric parameters are out of the scope of this thesis, it is important to mention the benefits and advantages of this large set of meteor detections regarding its capability to determine atmospheric parameters unambiguously in time and space.

5.5.1 3D wind field

Thanks to the increased number of meteor detections, one can relax the assumption of horizontal homogenity and estimate the wind field for smaller volumes as was explained

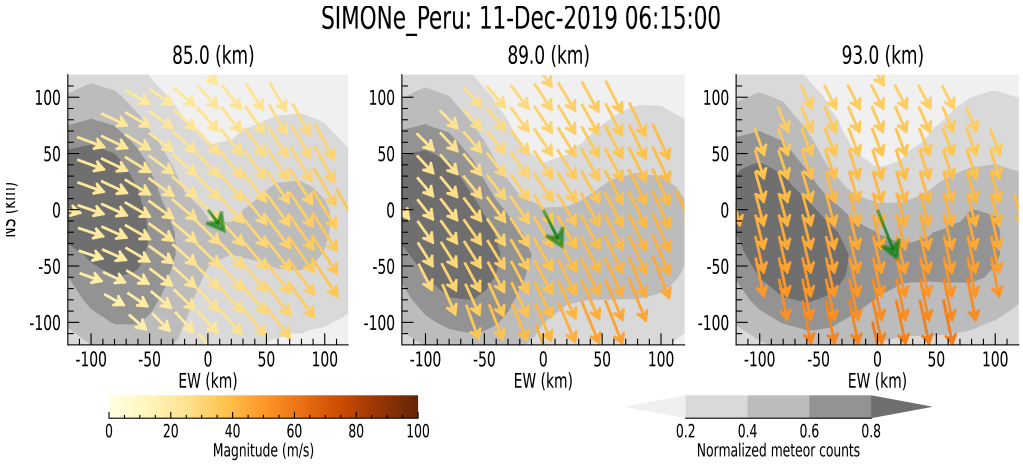

Figure 5.14: Wind field estimates on December 11th, 2019 for selected heights (left) $85\,\mathrm{km}$, (mid), $89\,\mathrm{km}$, and (right) $93\,\mathrm{km}$. The normalized meteor counts are indicated as contours. The mean horizontal wind is indicated with a green arrow [Courtesy: Jorge Chau].

by Stober and Chau [SC15]. An example of the wind field obtained with a radar network system installed in Peru named spread–spectrum interferometer meteor system observing network (SIMONe) is shown in Fig. 5.14. The data retrieval is an extension of the algorithm described by Harding et.al. [HMM15]. Essentially, since the number of meteor detections is high, the same minimization problem of (5.2) is solved but for smaller volumes. In addition, some smoothness constraints are added for neighboring volumes.

5.5.2 Second order statistics

Another important advantage of having a large number of detections is the capability to estimate the three-dimensional mesospheric wind field correlation function from specular meteor trail echoes. As described by Vierinen et.al. [Vie+19], each meteor echo provides a measurement of a one-dimensional projection of the wind velocity vector at a randomly sampled point in space and time. Using pairs of such measurements the correlation function of the wind with different spatial and temporal lags can be estimated. For example, having the correlation function at different time lags allows us to estimate the power spectrum using the Wiener-Khinchin theorem [Wie30], which can be used to retrieve the kinetic energy spectrum.

Figure 5.15 shows the estimated temporal autocorrelation functions for the horizontal wind components using the technique described in [Vie+19] for 6 days of data. The left

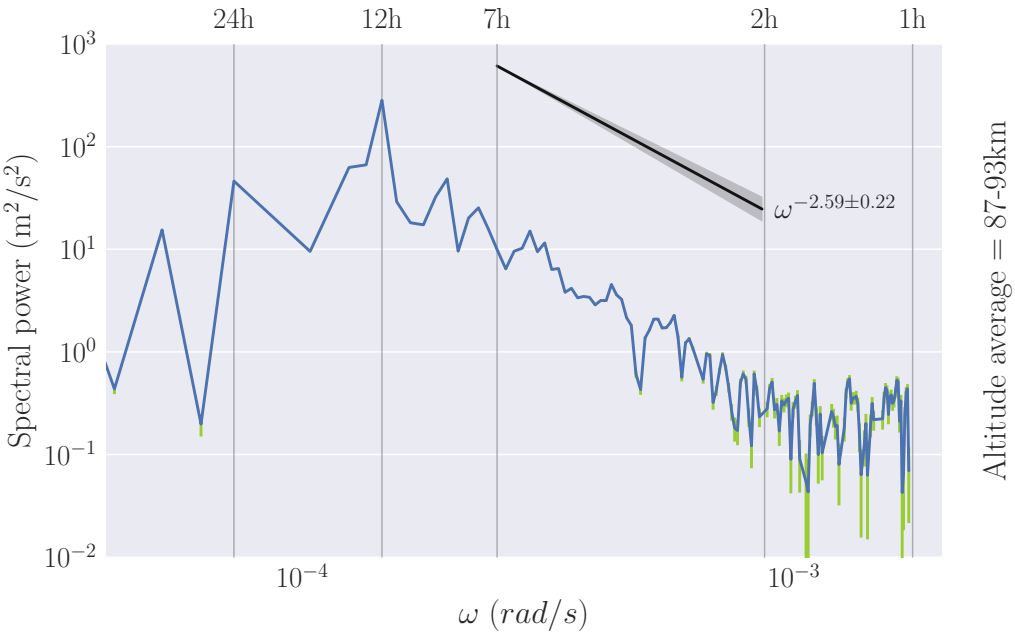

Figure 5.15: Power spectral density derived from the full autocorrelation function of radial meteor measurements. No windowing or zero padding is used to calculate the spectra. [Courtesy: Harikrishna Charuvil].

plot shows the 100-km horizontal scale autocorrelation function. The right plot shows the spectrum calculated from the autocorrelation using the Wiener-Khinchin theorem. Clearly, we can see the 12-h and 24-h tide, and the energy cascade from large scales to small scales.

Another example of the capability and advantage of the proposed network can be found in the easiness to install this system in other places to study the MLT at different geographic regions, such the systems installed in Peru and Argentina.

5.6 Conclusions

This chapter introduces a new radar network based on MIMO systems using waveform diversity to increase considerably the number of meteor detections with a few Tx and Rx stations and thus to allow the estimation of spatio-temporal physical parameters such the wind field in 4D and the kinetic spectrum at different temporal and spatial scales.

Since in MIMO systems using waveform diversity, the transmitters interfere each other, and conventional approaches like MFE or tSVD do not decouple well the signals coming from different transmitters. This chapter proposes a recovery algorithm based on compressed sensing (CS) to overcome the undetermination of the problem. The proposed approach takes advantage of the sparse nature of the meteor echoes to regularize the problem by choosing the sparsest solution which matches the measurements.

The algorithm selected to find the sparsest solution was a variation of the stagewise orthogonal matching pursuit (StOMP) given its high performance and simplicity. stagewise orthogonal matching pursuit (StOMP) is highly recommended than its counterpart basis pursuit (BP) due to its reduced complexity. Although it is known that StOMP requires a larger number of measurements than BP to recover a signal with the same accuracy, its computational cost makes it much more attractive for real-time applications.

Including the truncated tSVD to StOMP, i.e., FaStOMP, the meteor signal was recovered from the radar measurements using only three iterations. One each for the strong, medium, and weak echoes. Since the weak echoes were not distinguishable from the noise, coherent integration in time was applied to improve the SNR in the last iteration. Moreover, for coherent MIMO configurations, further improvements were achieved integrating the weak echoes incoherently along the Tx and Rx channels.

The reduced complexity of the proposed sparse recovery approach makes it applicable even for large data sets. To have a rough idea of the computational time, the implementation was tested in two different scenarios: (a) a MIMO link consisting of 5 Tx channels and 1 Rx channel, and (b) a MIMO link consisting of 5 Tx channels and 5 Rx channels, i.e., 25 channels in total. For the first case, a Core i5 PC with 8GB of RAM was used to process the MIMO radar data, for which the processing time was around 2 s for 60 s of data. In the second case, a Core i7 PC with 16GB of RAM was used, getting 12 s to process 60 s of data. In both cases, the radar data was acquired continuously at a sample rate of 100kHz and the algorithm was implemented in Python using Intel's optimized version of numpy and scipy libraries [Int]. Even though the new python libraries allow us to use more than one core, our implementation made use only of one core at a time.

Additionally, the CS approach can help to reduce or compress the meteor radar data. Since FaStOMP only recovers echoes above a threshold, most of the data contains zeros

and can be compressed using conventional compression filters. In this application, the HDF5 file format with gzip compression was used to save the decoded data. By doing this, the hard drive space required for decoded data was reduced almost 60 times compared to data obtained applying conventional algorithms. Furthermore, standard meteor analysis involves decoding and meteor detection. However, by employing CS, the two steps was joined in one.

Another future task is to consider the waveform errors in the problem. Along with this work, an ideal transmitted waveform was assumed, which is not the case in the real world. The synthesized signal passes through limited bandwidth filters, amplifiers, and antennas before being irradiated, which introduces imperfections to the transmitted signal. Our model, i.e., the matrix $\mathbf{\Phi}$ in (5.5), does not consider these imperfections. It could be problematic in the presence of high SNR echoes given that the waveform imperfections might introduce high errors in the solution, creating false echoes or artifacts. In our simulations, see Fig. 5.12, this was not observed given that the waveform imperfections were not taken into account. However, this problem was observed in a quasi-monostatic link where the transmitter and the receiver station were only 5km apart, observing a strong ground clutter with an SNR of 60dB, for which the sidelobes (due to waveform imperfections) were not removed completely even using CS. In the future, errors in the matrix Φ can be considered in the equation and the total least squares estimator algorithm [GL80] can be applied instead of the ordinary tSVD in our FaStOMP implementation.

Chapter 6

Summary and conclusions

A comprehensive understanding of the processes in the atmosphere at their different spatio-temporal scales would require global and continuous observations at high spatio-temporal resolution. Measurements at mesosphere and lower termosphere (MLT) altitudes are hard to obtain routinely because current instruments and remote sensing techniques only provide scarce or local observations. An important investment in observational infrastructure could dramatically improve the understanding of the complex MLT dynamics. However, such deployment is prohibitively costly.

This work proposes the use of MIMO techniques to improve the capability of current atmospheric radars, with a special focus on observations of the MLT region. To show the advantage of MIMO systems over conventional techniques, Chapter 2 describes basic concepts regarding atmospheric radars and their limitations, such as the signal model, the scattering mechanisms, and state-of-the-art algorithms to estimate radar parameters. One of the main limitations of existing atmospheric radar systems is their limited spatial resolution in the horizontal direction, which restricts the characterization of small-scale and mesoscale dynamics. The spatial resolution in a radar is limited by the antenna size. To increase the spatial resolution, a larger antenna is required.

Chapter 3 introduces the MIMO technique, which is used to improve the performance of atmospheric radars, namely, the spatial resolution and observational coverage. MIMO

employs multiple transmitting antennas to illuminate the same target and multiple receiving antennas to get independent measurements. In the case of existing radars, MIMO is done by dividing the available transmitting antenna array into sub-arrays and splitting the total transmitting power among the subarrays. Depending on the transmit diversity used, MIMO might cause either a reduction in the transmitted power (time diversity) or a cross-interference between transmitted signals (waveform diversity). The calculations show that time diversity can only be applied to observe strong radar targets with long correlation times. Whereas, waveform diversity is recommended to be used in modern systems with capability to generate multiple transmit waveforms. A waveform design technique based on pseudo-random codes is proposed to reduce the cross-interference between transmitted signals due to its performance and scalability (independent of the number of transmitters). In general, waveform diversity should be used over time diversity, but it requires modern hardware and bi-static configurations.

Chapter 4 shows results of the first MIMO implementation to image PMSE in 4D using the MAARSY radar. The transmit diversity employed was time diversity since PMSE are very strong radar echoes with relatively long correlation times. This configuration lowered the time resolution and the transmitted power per antenna but it allowed to improve the radar image's spatial resolution and accuracy by a factor of 2. Additionally, the MaxEnt algorithm was employed to improve the image resolution even more. The combination of MIMO and MaxEnt resulted in PMSE measurements with an unprecedented angular resolution, six times better than the nominal MAARSY angular resolution, i.e., $0.6°$. Such results allowed for the first time to resolve km-scale structures from PMSE observations [Cha+20].

Another important factor that limits the spatial resolution is associated to the dynamic nature of the structures being imaged. Drifting structures limit the spatial resolution achieved by any method. To deal with drifting structures, I am exploring tracking techniques based on Kalman Filter and the Expectation-Maximization algorithm. The results will be published in an additional manuscript.

Characterization of winds in the MLT region over a wide range of spatial scales is crucial to understand the complex dynamics in the atmosphere. Typically, specular meteor radars consisting of one transmitting antenna and five receiving antennas in an interferometric configuration are used for this purpose. Chapter 5 describes a novel technology

for detecting meteor trail echoes using both multiple transmitters and multiple receivers (MIMO) in an interferometric configuration. Compared to conventional meteor radar networks, the advantage of this novel MIMO network is the significantly higher number of Tx-Rx links, which results in more accurate and larger meteor detections per day. For the first time, a unique dataset consisting in more than 120k meteor detections in a day were collected using this multistatic MIMO meteor radar. Compared to the 10k meteor detections obtained with standard specular meteor radars, the 120k detections allowed to resolve the MLT dynamics over a wide range of spatial scales, $50\,\mathrm{km}$ to $500\,\mathrm{km}$ [Vie+19]. Although the larger number of transmitting stations operating at the same frequency in the multistatic MIMO meteor radar increases the total number of Tx-Rx links, and thus, the number of meteor detections, they interfere each other degrading the signal to interference ratio. An advanced algorithm based on compressed sensing was proposed to get rid of the cross-interference between transmitted signals and to decouple the reflected signals originated at different transmitters properly.

A multistatic meteor radar employing MIMO can be seen as the global position system (GPS) satellite system where a number of transmitting stations can be deployed across to a region, country, or continent. And the receiving systems can be added later according to the needs. The success of the GPS network lies in that the receivers are cheap and easy to install. Currently, there are thousands of GPS receivers on the ground and on low-orbiting satellites.

Similarly, the main advantage of the proposed multistatic MISO meteor network is that this system is scalable. We could start deploying in a continental region a few transmitting stations consisting of five antennas each and a few receiving stations consisting of one antenna each. Later, more receiving stations can be added increasing the number of measurements multiplicatively. With an efficient, cheap, and simple receiving system, the network might be extended over the whole continent. It was proved that the required receiving antenna for this system could be installed in small places like gardens, roofs, courtyards, etc., without affecting the environment. We now require to develop a cheap receiving system. The transmitting and receiving stations might be seen as a mimic of the GPS satellites transmitters and the ground based receivers of a GPS system, respectively, with a similar impact regarding observations of the atmosphere.

A natural next step of this work is the deployment of the proposed multistatic radar system to study the MLT in regional or continental scales. Although this is an ambitious

plan and it is out of the scope of this thesis, the MIT Haystack observatory has recently got a proposal accepted to build a distributed MIMO meteor radar network based on the results of this work in the US [National Science Foundation, award number 1933005].

Chapter 7

Zusammenfassung und Fazit

Ein umfassendes Verständnis der Prozesse in der Atmosphäre auf ihren verschiedenen räumlich-zeitlichen Skalen würde globale und kontinuierliche Beobachtungen erfordern. Es ist schwierig, regelmäßig Messwerte zur oberen Atmosphäre zu erlangen, da die aktuell verfügbaren Fernerkundungstechniken wenige oder nur lokale Beobachtungen liefern. Eine Investition in die Beobachtungsinfrastruktur, die das Verständnis der komplexen Dynamik der MLT-Region drastisch verbessern könnte, ist zwar wichtig, jedoch äußerst kostspielig.

In dieser Ausarbeitung wird der Vorschlag gemacht, anhand von MIMO-Techniken die Fähigkeit von Atmosphärenradargeräten zu verbessern, die MLT-Region zu erkunden. Um den Vorteil von MIMO-Systemen gegenüber konventionellen Radargeräten aufzuzeigen, beginnt Kapitel 2 mit einer Beschreibung der wesentlichen Konzepte, auf deren Basis Atmosphärenradargeräte arbeiten, und der damit einhergehenden Einschränkungen. Da wären zum Beispiel das Signalmodel, die Streuungsmechanismen und speziell entwickelte Algorithmen zur Schätzung der Radarparameter. Die größte Einschränkung konventioneller Radargeräte ist ihre begrenzte räumliche Auflösung, bedingt durch die Größe der Antenne. Um die räumliche Auflösung zu erhöhen, müssten wir größere Antennen herstellen. Kapital 3 stellt die MIMO-Technik vor, die genutzt wird, um die Leistung von Atmosphärenradargeräten zu verbessern, indem sie räumliche Auflösung und

Reichweite erhöht. MIMO verwendet mehrere Sendeantennen zur Ausleuchtung desselben Ziels und mehrere Empfangsantennen zum Empfangen voneinander unabhängiger Messwerte. Bei den existierenden Radargeräten wird MIMO eingesetzt, indem die zur Verfügung stehende Sendeantennengruppe in Untergruppen eingeteilt wird und die gesamte Übertragungsenergie zwischen diesen Untergruppen aufgeteilt wird. In Abhängigkeit von der verwendeten Sendediversität kann MIMO entweder eine Reduzierung der übertragenen Energie (Zeitdiversität) oder eine Kreuzinterferenz zwischen den übertragenen Signalen (Schwingungsverlaufsdiversität) verursachen. Berechnungen zeigen, dass Zeitdiversität nur zur Beobachtung von starken Radarzielen mit langen Korrelationszeiten verwendet werden kann. Schwingungsverlaufsdiversität hingegen empfiehlt sich in modernen Systemen mit der Fähigkeit, bei der Übertragung mehrere verschiedene Schwingungsverläufe zu generieren. Eine Schwingungsverlaufsgestaltungstechnik auf der Basis von Pseudozufallscodes soll aufgrund ihrer Leistungsfähigkeit und Skalierbarkeit die Kreuzinterferenzen zwischen den übertragenen Signalen (unabhängig von der Zahl der Überträger) reduzieren. Grundsätzlich ist eine Nutzung der Schwingungsverlaufsdiversität der Nutzung von Zeitdiversität vorzuziehen. Dabei sind jedoch mehr moderne Hardware und bistatische Konfigurationen notwendig. Kapitel 4 zeigt die Ergebnisse des ersten Einsatzes von MIMO zur bildlichen Darstellung von PMSE in 3D unter Nutzung des MAARSY-Radars. Die dort verwendete Sendediversität war Zeitdiversität, da PMSE sehr starke Radarechos mit relativ langen Korrelationszeiten sind. Diese Konfiguration reduzierte die zeitliche Auflösung und die pro Antenne übertragene Energie, ließ jedoch eine Verbesserung der räumlichen Auflösung des Radarbilds und der Genauigkeit um den Faktor 2 zu. Zudem wurde der MaxEnt-Algorithmus verwendet, um die Bildauflösung weiter zu verbessern. Die Kombination von MIMO und MaxEnt resultierte in PMSE-Messergebnissen mit beispielloser Winkelauflösung, sechsmal besser als die Nominalwinkelauflösung des MAARSY-Radars. Durch diese Ergebnisse konnten zum ersten Mal Strukturen in Kilometerdimensionen aus PMSE-Beobachtungen aufgelöst werden. Die Charakterisierung der Winde in der MLT-Region über eine große Spanne räumlicher Skalen ist entscheidend für das Verständnis der komplexen Dynamik der Atmosphäre. Typischerweise werden zu diesem Zweck spiegelnde Meteorradare verwendet, die aus einer Sendeantenne und fünf Empfangsantennen in einer interferometrischen Konfiguration bestehen. Kapitel 5 beschreibt eine neuartige Technologie zum Detektieren von Meteorschweif-Echos, die sowohl mehrere Sendeantennen als auch mehrere Empfangsantennen in interferometrischer Konfiguration verwendet. Der Vorteil dieser Konfiguration im Vergleich zu konventionellen Meteorradar-Netzwerken ist die deutlich höhere Zahl von Tx-Rx-Verbindungen mit dem Ergebnis genauerer und höherer Meteordetektionen pro Tag. Unter Nutzung dieses multistatischen MIMO-

Meteorradars wurde erstmalig ein einzigartiger Datensatz von Messergebnissen aus mehr als 120.000 Meteordetektionen pro Tag gesammelt. Verglichen mit den 10.000 Meteordetektionen, die man mit standardmäßigen Spiegelmeteorradargeräten erhält, ließen diese 120.000 Detektionen die Auflösung der Energiespektren auf eine große Bandbreite räumlicher Maßstabsebenen zu. Obwohl die Vielzahl der Sendestationen bei MIMO die Gesamtzahl der Tx-Rx-Verbindungen erhöht, wird die Signal-Interferenz-Ratio vermindert. Es wird ein fortgeschrittener Algorithmus auf der Basis komprimierter Erfassung präsentiert, der die reflektierten Signale, die von unterschiedlichen Sendern stammen, entkoppelt und so die Kreuzinterferenzen zwischen den übertragenen Signalen deutlich reduziert. Ein multistatischer Meteorradar unter Anwendung von MIMO kann als ein GPS-Satellitensystem betrachtet werden, bei dem mehrere Sendestationen über eine Region, ein Land oder einen Kontinent hinweg stationiert werden können. Die Empfängersysteme können später nach Bedarf hinzugefügt werden. Der Erfolg des GPS-Netzwerkes liegt darin, dass die Empfänger billig und leicht zu installieren sind. Derzeitig gibt es Tausende GPS-Empfänger auf dem Boden oder auf tieffliegenden Satelliten. Das ist auch der Hauptvorteil des vorgeschlagenen Meteor-MISO-Systems, das aus fünf Sendeantennen und nur einer Empfängerantenne besteht. Es wurde nachgewiesen, dass die Empfangsantenne kleinräumig in Gärten, auf Dächern, in Innenhöfen usw. installiert werden kann, ohne die Umgebung zu beeinträchtigen. Ein folgerichtiger nächster Schritt dieser Arbeit ist der Einsatz des vorgeschlagenen multistatischen Radarsystems, um die MLT in regionalen oder kontinentalen Maßstäben zu studieren. Mag dies auch ein ambitionierter Plan sein, der den Rahmen dieser Ausarbeitung sprengen würde, so ist doch anzumerken, dass kürzlich ein Vorschlag des MIT Haystack Observatory akzeptiert wurde, ein verteiltes MIMO-Meteorradar-Netzwerk auf der Basis dieser Arbeit in den USA zu bauen.

Appendix A

List of peer-reviewed publications

The work carried out in this thesis led to several peer-reviewed publications, which are listed below:

- **J. M. Urco**, J. L. Chau, M. Milla, J. Vierinen, T. Weber. Coherent MIMO to improve aperture synthesis radar imaging of field-aligned irregularities. *IEEE Transactions on Geoscience and Remote Sensing*, 2018.
- **J. M. Urco**, J. L. Chau, T. Weber, R. Latteck. Enhancing the spatiotemporal features of polar mesosphere summer echoes using coherent MIMO and radar imaging at MAARSY. *Atmospheric Measurement Techniques*, 2018.
- **J. M. Urco**, J. L. Chau, T. Weber, J. Vierinen, R. Volz. Sparse signal recovery in MIMO specular meteor radars with waveform diversity. *IEEE Transactions on Geoscience and Remote Sensing*, 2019.
- J. L. Chau, **J. M. Urco**, J. Vierinen, R. Volz, M. Clahsen, N. Pfeffer, J. Trautner. Novel specular meteor radar systems using coherent MIMO techniques to study the mesosphere and lower thermosphere. *Atmospheric Measurement Techniques*, 2019.

- J. L. Chau, **J. M. Urco**, V. Avsarkisov, J. P. Vierinen, R. Latteck, C. M. Hall, M. Tsutsumi. Four-dimensional quantification of Kelvin-Helmholtz instabilities in the polar summer mesosphere using volumetric radar imaging. *Geophysical Research Letters*, 2019.
- D. Hysell, P. Sharma, **J. M. Urco**, M. Milla. Aperture-synthesis radar imaging with compressive sensing for ionospheric research. *Radio Science*, 2019
- J. Vierinen, J. L. Chau, H. Charuvil Asokan, **J. M. Urco**, M. Clahsen. Observing mesospheric turbulence with specular meteor radars: A novel method for estimating second-order statistics of wind velocity. *Earth and Space Science*, 2019

APPENDIX A. LIST OF PEER-REVIEWED PUBLICATIONS

Symbol notation

Symbol	Name	Description
x	scalar	italic
$\mathbf{x}$	vector	bold lower case
$\mathbf{X}$	matrix	bold upper case
$\mathbf{x}(i, j)$	function	continuous or discrete function
x_i	vector element	element i of a vector $\mathbf{x}$
x_{ij}	matrix element	element i,j of a matrix $\mathbf{X}$
$i = [1, ..., I]$	index	index from 1 to I
x^*	conjugate	the conjugate of a complex number x
$\mathbf{X}^T$	transpose	the transpose of a real matrix $\mathbf{X}$
$\mathbf{X}^\dagger$	Hermitian	the conjugate transpose of a complex matrix $\mathbf{X}$
$\langle x \rangle$	expectation	the expected value of a random variable x
$\mathbf{x} \star \mathbf{y}$	convolution	convolution of vector $\mathbf{x}$ and $\mathbf{y}$
$\mathbf{x} * \mathbf{y}$	cross-correlation	cross-correlation between vector $\mathbf{x}$ and $\mathbf{y}$
$\|\mathbf{X}\|_0$	L0-norm	the number of non-zero elements in $\mathbf{X}$
$\|\mathbf{X}\|_1$	L1-norm	the sum of absolute values of $\mathbf{X}$
$\|\mathbf{X}\|_2$	L2-norm	the sum of squared values of $\mathbf{X}$

Acronyms

AGW	atmospheric gravity waves.
AOA	angle of arrival.
AOD	angle of departure.
Arecibo	Arecibo incoherent scatter radar.
BP	basis pursuit.
CDS	continuous Doppler sounding.
CoSaMP	compressive sampling orthogonal matching pursuit.
CS	compressed sensing.
CW	continuous wave.
DBF	digital beamforming.
DFT	discrete Fourier transform.
EEJ	equatorial electrojet.
EISCAT	european incoherent scatter scientific association.
EM	electromagnetic.
ERC	exact recovery condition.

FaStOMP fast stagewise orthogonal matching pursuit.
FDI frequency domain interferometry.
FFT fast Fourier transform.
FMCW frequency-modulated continuous wave.
foE E-layer critical frequency.
foF2 F2-layer critical frequency.

GOMP generalized orthogonal matching pursuit.
GPS global position system.

HPBW half-power beam width.

IDFT inverse discrete Fourier transform.
IPP inter-pulse period.
ISR incoherent scatter radar.

Jicamarca Jicamarca incoherent scatter radar.

KAIRA Kilpisjärvi atmospheric imaging receiver Array—System.
KHI Kelvin—Helmholtz instability.

LARS least angle regression.
LASSO least absolute shrinkage and selection operator.
LSE least squares estimation.

MAARSY middle atmosphere Alomar radar system.
MAP maximum a posteriori estimator.
MaxEnt maximum entropy.
MF medium frequency.
MFE matched filter estimator.
MIC mutual incoherence condition.
MIMO multiple–input multiple–output.
MISO multiple–input single–output.
MIT Massachusetts Institute of Technology.
MLE maximum likelihood estimator.

MLT mesosphere and lower termosphere.
MMARIA multi–static, multi–frequency agile radar for investigations of the atmosphere.
MMSE minimum mean squares error estimator.
MST mesosphere, stratosphere, and termosphere.
MU middle and up per atmosphere radar.

NLC noctilucent clouds.

OFDM orthogonal frequency-division multiplexing.
OMP orthogonal matching pursuit.

Pansy Pansy.
PMSE polar mesospheric summer echoes.
PMWE polar mesospheric winter echoes.
PRF pulse-repetition frequency.
PRI pulse-repetition interval.
PSLR peak-to-sidelobe ratio.
PW pulse-width.

RCS radar cross–section.
RF radio frequency.
RIM range imaging.
RIP restricted isometry property.
RLSE regularized least squares estimation.
ROMP regularized orthogonal matching pursuit.
RTDI range time Doppler intensity.
RTI range time intensity.

SIC successive interference cancellation.
SIMO single-input multiple-output.
SIMONe spread–spectrum interferometer meteor system observing network.
SMR specular meteor radar.
SNR signal-to-noise ratio.
StOMP stagewise orthogonal matching pursuit.

SVD	singular value decomposition.
TLSE	total least squares estimator.
tSVD	truncated singular value decomposition.
UHF	ultra high frequency.
UPP	uniform uncertainty principle.
VHF	very high frequency.
WLSE	weighted least squares estimator.
WSS	wide–sense stationary.

List of Figures

List of Tables

Bibliography

[AF14] M. L. Ammari and P. Fortier. "Analysis of MIMO receiver using generalized least squares method in colored environments". In: *Journal of Computer Networks and Communications* 2014 (2014), pp. 1–6. ISSN: 2090-7141. DOI: 10.1155/2014/720546. URL: http://www.hindawi.com/journals/jcnc/2014/720546/ (cit. on pp. 72, 115).

[Alt98] D. R. Altschuler. "The national astronomy and ionosphere center's (NAIC) Arecibo observatory in Puerto Rico". In: *AIP Conference Proceedings*. Vol. 444. 1. AIP, 1998, pp. 563–570. DOI: 10.1063/1.56603. URL: https://aip.scitation.org/doi/abs/10.1063/1.56603 (cit. on pp. 14, 17, 87).

[Bar49] E. Barlow. "Doppler radar". In: *Proceedings of the IRE* 37.4 (Apr. 1949), pp. 340–355. ISSN: 0096-8390. DOI: 10.1109/JRPROC.1949.231638. URL: http://ieeexplore.ieee.org/document/1697989/ (cit. on p. 34).

[BD19] R. Bassett and J. Deride. "Maximum a posteriori estimators as a limit of Bayes estimators". In: *Mathematical Programming* 174.1-2 (Mar. 2019), pp. 129–144. ISSN: 14364646. DOI: 10.1007/s10107-018-1241-0 (cit. on p. 72).

[Ber57] F. B. Berger. "The nature of Doppler velocity measurement". In: *IRE Transactions on Aeronautical and Navigational Electronics* ANE-4.3 (Sept. 1957), pp. 103–112. ISSN: 0096-1639. DOI: 10.1109/TANE3.1957.4201534. URL: http://ieeexplore.ieee.org/document/4201534/ (cit. on p. 34).

[BF03] D. W. Bliss and K. W. Forsythe. "Multiple-input multiple-output (MIMO) radar and imaging: degrees of freedom and resolution". In: *The Thrity-Seventh Asilomar Conference on Signals, Systems & Computers, 2003*. Vol. 1. IEEE, 2003, pp. 54–59. ISBN: 0-7803-8104-1. DOI: 10.1109/ACSSC.2003.1291865. URL: http://ieeexplore.ieee.org/document/1291865/ (cit. on pp. 2, 50, 68).

[Bi+16] H. Bi, C. Zhao, H. Bi, Y. Liu, and N. Li. "Performance evaluation of greedy reconstruction algorithms in compressed sensing". In: *2016 9th International Congress on Image and Signal Processing, BioMedical Engineering and Informatics (CISP-BMEI)*. 2016, pp. 1322–1327. DOI: 10.1109/CISP-BMEI.2016.7852921 (cit. on p. 130).

[Bjö96] Å. Björck. *Numerical methods for least squares problems*. Society for Industrial and Applied Mathematics, Jan. 1996. ISBN: 978-0-89871-360-2. DOI: 10.1137/1.9781611971484. URL: http://epubs.siam.org/doi/book/10.1137/1.9781611971484 (cit. on p. 72).

[BM16] S. D. Blunt and E. L. Mokole. "Overview of radar waveform diversity". In: *IEEE Aerospace and Electronic Systems Magazine* 31.11 (Nov. 2016), pp. 2–42. ISSN: 0885-8985. DOI: 10.1109/MAES.2016.160071. URL: http://ieeexplore.ieee.org/document/7771665/ (cit. on p. 136).

[BP00] H. Bölcskei and A. A. J. Paulraj. "Space-frequency coded broadband OFDM systems". In: *2000 IEEE Wireless Communications and Networking Conference*. Vol. 1. IEEE, 2000, pp. 1–6. ISBN: 0-7803-6596-8. DOI: 10.1109/WCNC.2000.904589. URL: http://ieeexplore.ieee.org/document/904589/ (cit. on pp. 55, 63).

[BR84] B. B. Balsley and A. C. Riddle. "Monthly mean values of the mesospheric wind field over Poker Flat, Alaska". In: *Journal of the Atmospheric Sciences* 41.15 (Aug. 1984), pp. 2368–2380. ISSN: 0022-4928. DOI: 10.1175/1520-0469(1984)041<2368:MMVOTM>2.0.CO;2. URL: http://journals.ametsoc.org/doi/abs/10.1175/1520-0469%281984%29041%3C2368%3AMMVOTM%3E2.0.CO%3B2 (cit. on p. 90).

[BSW73] K. A. Browning, J. R. Starr, and A. J. Whyman. "The structure of an inversion above a convective boundary layer as observed using high-power pulsed Doppler radar". In: *Boundary-Layer Meteorology* 4.1-4 (Apr. 1973), pp. 91–111. ISSN: 0006-8314. DOI: 10.1007/BF02265226. URL: http://link.springer.com/10.1007/BF02265226 (cit. on p. 50).

[Cap69] J. Capon. “High-resolution frequency-wavenumber spectrum analysis”. In: *Proceedings of the IEEE* 57.8 (1969), pp. 1408–1418. ISSN: 0018-9219. DOI: 10.1109/PROC.1969.7278. URL: http://ieeexplore.ieee.org/document/1449208/ (cit. on p. 44).

[CDS98] S. S. Chen, D. L. Donoho, and M. A. Saunders. “Atomic decomposition by basis pursuit”. In: *SIAM Journal on Scientific Computing* 20.1 (Jan. 1998), pp. 33–61. ISSN: 1064-8275. DOI: 10.1137/S1064827596304010. URL: http://epubs.siam.org/doi/10.1137/S1064827596304010 (cit. on p. 130).

[Cha+08] J. L. Chau, D. L. Hysell, K. M. Kuyeng, and F. R. Galindo. “Phase calibration approaches for radar interferometry and imaging configurations: Equatorial Spread F results”. In: *Annales Geophysicae* 26 (2008), pp. 2333–2343 (cit. on p. 76).

[Cha+14] J. L. Chau, T. Renkwitz, G. Stober, and R. Latteck. “MAARSY multiple receiver phase calibration using radio sources”. In: *Journal of Atmospheric and Solar-Terrestrial Physics* 118 (2014), pp. 55–63 (cit. on p. 102).

[Cha+17] J. L. Chau, G. Stober, C. M. Hall, M. Tsutsumi, F. I. Laskar, and P. Hoffmann. “Polar mesospheric horizontal divergence and relative vorticity measurements using multiple specular meteor radars”. In: *Radio Science* (2017). ISSN: 1944-799X. DOI: 10.1002/2016RS006225. URL: http://dx.doi.org/10.1002/2016RS006225 (cit. on pp. 109, 113, 119).

[Cha+18] J. L. Chau, D. McKay, J. Vierinen, C. La Hoz, T. Ulich, M. S. Lehtinen, and R. Latteck. “Multi-static spatial and angular studies of polar mesospheric summer echoes combining MAARSY and KAIRA”. In: *Atmospheric Chemistry and Physics* 18.13 (2018), pp. 9547–9560. DOI: 10.5194/acp-18-9547-2018. URL: https://www.atmos-chem-phys.net/18/9547/2018/ (cit. on p. 137).

[Cha+19] J. L. Chau, J. M. Urco, J. Vierinen, R. Volz, M. Clahsen, N. Pfeffer, and J. Trautner. “Novel specular meteor radar systems using coherent MIMO techniques to study the mesosphere and lower thermosphere”. In: *Atmospheric Measurement Techniques* 12.4 (Apr. 2019), pp. 2113–2127. ISSN: 1867-8548. DOI: 10.5194/amt-12-2113-2019. URL: https://www.atmos-meas-tech.net/12/2113/2019/ (cit. on p. 6).

[Cha+20] J. L. Chau, J. M. Urco, V. Avsarkisov, J. Vierinen, R. Latteck, C. M. Hall, and M. Tsutsumi. “Four-dimensional quantification of Kelvin-Helmholtz instabili-

ties in the polar summer mesosphere using volumetric radar imaging". In: *Geophysical Research Letters* 47.1 (Jan. 2020). ISSN: 0094-8276. DOI: 10.1029/2019GL086081. URL: https://agupubs.onlinelibrary.wiley.com/doi/abs/10.1029/2019GL086081 (cit. on pp. 109, 124, 144, 152).

[Che+16] J. Chen, Y. Chu, C. Su, H. Hashiguchi, and Y. Li. "Range imaging of E-region field-aligned irregularities by using a multifrequency technique: validation and initial results". In: *IEEE Transactions on Geoscience and Remote Sensing* 54.7 (2016), pp. 3739–3749 (cit. on p. 31).

[Che+20] G. Chen, Y. Li, S. Zhang, B. Ning, W. Gong, A. Yoshikawa, K. Hozumi, T. Tsugawa, and Z. Wang. "Multi-instrument observations of the atmospheric and ionospheric response to the 2013 sudden stratospheric warming over eastern Asia region". In: *IEEE Transactions on Geoscience and Remote Sensing* 58.2 (Feb. 2020), pp. 1232–1243. ISSN: 0196-2892. DOI: 10.1109/TGRS.2019.2944677. URL: https://ieeexplore.ieee.org/document/8880604/ (cit. on p. 1).

[Che15] H. Cheng. "Efficient sparse representation and modeling". In: *Advances in Computer Vision and Pattern Recognition*. Vol. 59. Springer-Verlag London Ltd, 2015, pp. 117–151. DOI: 10.1007/978-1-4471-6714-3{_}5. URL: http://link.springer.com/10.1007/978-1-4471-6714-3_5 (cit. on p. 130).

[Che18] V. S. Chernyak. *Fundamentals of multisite radar systems*. 15th editi. Amsterdam: Routledge, May 2018. ISBN: 9780203755228. DOI: 10.1201/9780203755228. URL: https://www.taylorfrancis.com/books/9781351446426 (cit. on p. 51).

[CHM09] R. Calderbank, S. D. Howard, and B. Moran. "Waveform diversity in radar signal processing: A focus on the use and control of degrees of freedom". In: *IEEE Signal Processing Magazine* 26.1 (2009), pp. 32–41. ISSN: 10535888. DOI: 10.1109/MSP.2008.930414 (cit. on p. 71).

[Chu72] D. Chu. "Polyphase codes with good periodic correlation properties". In: *IEEE Transactions on Information Theory* 18.4 (July 1972), pp. 531–532. ISSN: 0018-9448. DOI: 10.1109/TIT.1972.1054840. URL: http://ieeexplore.ieee.org/document/1054840/ (cit. on p. 59).

[CL69] S. Chapman and R. S. Lindzen. *Atmospheric tides*. Dordrecht: Springer Netherlands, 1969. ISBN: 978-94-010-3401-2. DOI: 10.1007/978-94-010-3399-2.

URL: http://link.springer.com/10.1007/978-94-010-3399-2 (cit. on p. 118).

[Cre+19] E. Crespo Marques, N. Maciel, L. Naviner, H. Cai, and J. Yang. "A review of sparse recovery algorithms". In: *IEEE Access* 7 (2019), pp. 1300–1322. ISSN: 2169-3536. DOI: 10.1109/ACCESS.2018.2886471. URL: https://ieeexplore.ieee.org/document/8577023/ (cit. on p. 130).

[CRT06a] E. J. Candès, J. K. Romberg, and T. Tao. "Robust uncertainty principles: exact signal reconstruction from highly incomplete frequency information". In: *IEEE Transactions on Information Theory* 52.2 (Feb. 2006), pp. 489–509. ISSN: 0018-9448. DOI: 10.1109/TIT.2005.862083 (cit. on pp. 45, 129).

[CRT06b] E. J. Candès, J. K. Romberg, and T. Tao. "Stable signal recovery from incomplete and inaccurate measurements". In: *Communications on Pure and Applied Mathematics* 59.8 (Aug. 2006), pp. 1207–1223. ISSN: 00103640. DOI: 10.1002/cpa.20124. URL: https://onlinelibrary.wiley.com/doi/abs/10.1002/cpa.20124 (cit. on pp. 45, 46, 130).

[CT05] E. J. Candès and T. Tao. "Decoding by linear programming". In: *IEEE Transactions on Information Theory* 51.12 (2005), pp. 4203–4215. ISSN: 0018-9448. DOI: 10.1109/TIT.2005.858979 (cit. on pp. 45, 46, 129, 135).

[CT06] E. J. Candès and T. Tao. "Near-optimal signal recovery from random projections: universal encoding strategies?" In: *IEEE Transactions on Information Theory* 52.12 (Dec. 2006), pp. 5406–5425. ISSN: 0018-9448. DOI: 10.1109/TIT.2006.885507 (cit. on p. 135).

[CV08a] C.-Y. Chen and P. P. Vaidyanathan. "MIMO radar spacetime adaptive processing and signal design". In: *MIMO Radar Signal Processing*. Hoboken, NJ, USA: John Wiley & Sons, Inc., Mar. 2008, pp. 235–281. ISBN: 9780470178980. DOI: 10.1002/9780470391488.ch6. URL: http://doi.wiley.com/10.1002/9780470391488.ch6 (cit. on p. 3).

[CV08b] C.-Y. Chen and P. P. Vaidyanathan. "Properties of the MIMO radar ambiguity function". In: *ICASSP, IEEE International Conference on Acoustics, Speech and Signal Processing - Proceedings*. 2008, pp. 2309–2312. ISBN: 1424414849. DOI: 10.1109/ICASSP.2008.4518108 (cit. on p. 71).

[CW11] T. T. Cai and L. Wang. "Orthogonal matching pursuit for sparse signal recovery with noise". In: *IEEE Transactions on Information Theory* 57.7 (July 2011), pp. 4680–4688. ISSN: 0018-9448. DOI: 10.1109/TIT.2011.2146090. URL:

http://ieeexplore.ieee.org/document/5895106/ (cit. on pp. 129, 130).

[Dek+05] F. M. Dekking, C. Kraaikamp, H. P. Lopuhaä, and L. E. Meester. *A modern introduction to probability and statistics*. Springer Texts in Statistics. London: Springer London, 2005. ISBN: 978-1-85233-896-1. DOI: 10.1007/1-84628-168-7. URL: http://link.springer.com/10.1007/1-84628-168-7 (cit. on pp. 47, 103).

[Dem+14] T. D. Demissie, P. J. Espy, N. H. Kleinknecht, M. Hatlen, N. Kaifler, and G. Baumgarten. "Characteristics and sources of gravity waves observed in noctilucent cloud over Norway". In: *Atmospheric Chemistry and Physics* 14.22 (Nov. 2014), pp. 12133–12142. ISSN: 1680-7324. DOI: 10.5194/acp-14-12133-2014. URL: https://www.atmos-chem-phys.net/14/12133/2014/ (cit. on p. 85).

[DH06] D. L. Donoho and X. Huo. "Uncertainty principles and ideal atomic decomposition". In: *IEEE Transactions on Information Theory* 47.7 (Sept. 2006), pp. 2845–2862. ISSN: 0018-9448. DOI: 10.1109/18.959265. URL: http://dx.doi.org/10.1109/18.959265 (cit. on p. 135).

[DLH96] R. J. Doviak, R. J. Lataitis, and C. L. Holloway. "Cross correlations and cross spectra for spaced antenna wind profilers: 1. Theoretical analysis". In: *Radio Science* 31.1 (Jan. 1996), pp. 157–180. ISSN: 00486604. DOI: 10.1029/95RS02318. URL: http://doi.wiley.com/10.1029/96RS01790%20http://doi.wiley.com/10.1029/95RS02318 (cit. on p. 90).

[Don+12] D. L. Donoho, Y. Tsaig, I. Drori, and J.-L. Starck. "Sparse solution of underdetermined systems of linear equations by stagewise orthogonal matching pursuit". In: *IEEE Transactions on Information Theory* 58.2 (Feb. 2012), pp. 1094–1121. ISSN: 0018-9448. DOI: 10.1109/TIT.2011.2173241. URL: http://ieeexplore.ieee.org/document/6145475/ (cit. on pp. 130, 131).

[Don06a] D. L. Donoho. "Compressed sensing". In: *IEEE Transactions on Information Theory* 52.4 (Apr. 2006), pp. 1289–1306. ISSN: 0018-9448. DOI: 10.1109/TIT.2006.871582 (cit. on pp. 129, 130).

[Don06b] D. L. Donoho. "For most large underdetermined systems of linear equations the minimal L1-norm solution is also the sparsest solution". In: *Communications on Pure and Applied Mathematics* 59.6 (June 2006), pp. 797–829. ISSN: 00103640. DOI: 10.1002/cpa.20132 (cit. on pp. 46, 130).

[DRV15] C. Dahl, I. Rolfes, and M. Vogt. “Comparison of virtual arrays for MIMO radar applications based on hexagonal configurations”. In: *European Microwave Week 2015: "Freedom Through Microwaves", EuMW 2015 - Conference Proceedings; 2015 45th European Microwave Conference Proceedings, EuMC*. Institute of Electrical and Electronics Engineers Inc., Dec. 2015, pp. 1439–1442. ISBN: 9782874870392. DOI: 10.1109/EuMC.2015.7346044 (cit. on pp. 68, 81).

[DW14] W. Dan and R. Wang. “Robustness of orthogonal matching pursuit under restricted isometry property”. In: *Science China Mathematics* 57.3 (Mar. 2014), pp. 627–634. ISSN: 1674-7283. DOI: 10.1007/s11425-013-4655-4. URL: https://doi.org/10.1007/s11425-013-4655-4%20http://link.springer.com/10.1007/s11425-013-4655-4 (cit. on p. 45).

[Efr+04] B. Efron, T. Hastie, I. M. Johnstone, R. Tibshirani, H. Ishwaran, K. Knight, J. M. Loubes, P. Massart, D. Madigan, G. Ridgeway, S. Rosset, J. I. Zhu, R. A. Stine, B. A. Turlach, and S. Weisberg. “Least angle regression”. In: *Annals of Statistics* 32.2 (Apr. 2004), pp. 407–499. ISSN: 00905364. DOI: 10.1214/009053604000000067 (cit. on p. 72).

[EKB10] Y. C. Eldar, P. Kuppinger, and H. Bolcskei. “Block-sparse signals: Uncertainty relations and efficient recovery”. In: *IEEE Transactions on Signal Processing* 58.6 (2010), pp. 3042–3054. ISSN: 1053-587X. DOI: 10.1109/TSP.2010.2044837 (cit. on p. 133).

[EL97] L. El Ghaoui and H. Lebret. “Robust solutions to least-squares problems with uncertain data”. In: *SIAM Journal on Matrix Analysis and Applications* 18.4 (1997), pp. 1035–1064. ISSN: 08954798. DOI: 10.1137/S0895479896298130 (cit. on p. 72).

[Ern+11] M. Ern, P. Preusse, J. C. Gille, C. L. Hepplewhite, M. G. Mlynczak, J. M. Russell, and M. Riese. “Implications for atmospheric dynamics derived from global observations of gravity wave momentum flux in stratosphere and mesosphere”. In: *Journal of Geophysical Research* 116.D19 (Oct. 2011), p. D19107. ISSN: 0148-0227. DOI: 10.1029/2011JD015821. URL: http://doi.wiley.com/10.1029/2011JD015821 (cit. on p. 85).

[Ern04] M. Ern. “Absolute values of gravity wave momentum flux derived from satellite data”. In: *Journal of Geophysical Research* 109.D20 (2004), p. D20103. ISSN: 0148-0227. DOI: 10.1029/2004JD004752. URL: http://doi.wiley.com/10.1029/2004JD004752 (cit. on p. 85).

[FB08] K. W. Forsythe and D. W. Bliss. “MIMO radar: concepts, performance enhancements, and applications”. In: *MIMO Radar Signal Processing*. John Wiley and Sons, Ltd, Mar. 2008. Chap. 2, pp. 65–121. ISBN: 9780470391488. DOI: 10.1002/9780470391488.ch2. URL: https://onlinelibrary.wiley.com/doi/abs/10.1002/9780470391488.ch2 (cit. on p. 52).

[FG98] G. Foschini and M. J. Gans. “On limits of wireless communications in a fading environment when using multiple antennas”. In: *Wireless Personal Communications* 6 (1998), pp. 311–335 (cit. on pp. 8, 49).

[FH05] D. T. Farley and T. Hagfors. *Incoherent scatter theory …* 2005 (cit. on p. 19).

[FHW83] K. Folkestad, T. Hagfors, and S. Westerlund. “EISCAT: An updated description of technical characteristics and operational capabilities”. In: *Radio Science* 18.6 (Nov. 1983), pp. 867–879. ISSN: 00486604. DOI: 10.1029/RS018i006p00867. URL: https://agupubs.onlinelibrary.wiley.com/doi/abs/10.1029/RS018i006p00867%20http://doi.wiley.com/10.1029/RS018i006p00867 (cit. on pp. 14, 17).

[Fis+06] E. Fishler, A. Haimovich, R. S. Blum, L. Cimini, D. Chizhik, and R. Valenzuela. “Spatial diversity in radars - models and detection performance”. In: *IEEE Transactions on Signal Processing* 54.3 (Mar. 2006), pp. 823–838. ISSN: 1053587X. DOI: 10.1109/TSP.2005.862813. URL: http://ieeexplore.ieee.org/document/1597550/ (cit. on pp. 2, 50, 51, 55).

[FL92] A. Fredriksen and N. B. J. Lilensten. “Incoherent scatter plasma lines at angles with the magnetic field”. In: *Journal of Geophysical Research* 97 (1992), pp. 16921–16933 (cit. on p. 19).

[Fra06] R. Frank. “Polyphase codes with good nonperiodic correlation properties”. In: *IEEE Transactions on Information Theory* 9.1 (Sept. 2006), pp. 43–45. ISSN: 0018-9448. DOI: 10.1109/TIT.1963.1057798. URL: http://dx.doi.org/10.1109/TIT.1963.1057798 (cit. on pp. 59, 136).

[Fri07] B. Friedlander. “Waveform design for MIMO radars”. In: *IEEE Transactions on Aerospace and Electronic Systems* 43.3 (July 2007), pp. 1227–1238. ISSN: 00189251. DOI: 10.1109/TAES.2007.4383615 (cit. on pp. 33, 71).

[Fri11] B. Friedlander. “On the role of waveform diversity in MIMO radar”. In: *2011 Conference Record of the Forty Fifth Asilomar Conference on Signals, Systems and Computers (ASILOMAR)*. IEEE, Nov. 2011, pp. 1501–1505. ISBN: 978-1-4673-

0323-1. DOI: 10.1109/ACSSC.2011.6190268. URL: http://ieeexplore.ieee.org/document/6190268/ (cit. on p. 71).

[GBG81] K. S. Gage, B. B. Balsley, and J. L. Green. "Fresnel scattering model for the specular echoes observed by VHF radar". In: *Radio Science* 16.6 (Nov. 1981), pp. 1447–1453. ISSN: 00486604. DOI: 10.1029/RS016i006p01447. URL: http://doi.wiley.com/10.1029/RS016i006p01447 (cit. on p. 17).

[GDP12] F. Gini, A. De Maio, and L. Patton. *Waveform design and diversity for advanced radar systems*. Ed. by F. Gini, A. De Maio, and L. Patton. The Institution of Engineering and Technology, Michael Faraday House, Six Hills Way, Stevenage SG1 2AY, UK: IET, Jan. 2012, pp. 1–553. ISBN: 9781849192651. DOI: 10.1049/PBRA022E. URL: https://digital-library.theiet.org/content/books/ra/pbra022e (cit. on pp. 3, 71).

[GHB09] H. Godrich, A. Haimovich, and R. S. Blum. "A MIMO radar system approach to target tracking". In: *Conference Record - Asilomar Conference on Signals, Systems and Computers*. 2009, pp. 1186–1190. ISBN: 9781424458271. DOI: 10.1109/ACSSC.2009.5470001 (cit. on p. 3).

[GHB10] H. Godrich, A. Haimovich, and R. S. Blum. "Target localization accuracy gain in MIMO radar-based systems". In: *IEEE Transactions on Information Theory* 56.6 (June 2010), pp. 2783–2803. ISSN: 00189448. DOI: 10.1109/TIT.2010.2046246 (cit. on p. 3).

[GL80] G. H. Golub and C. F. van Loan. "An analysis of the total least squares problem". In: *SIAM Journal on Numerical Analysis* 17.6 (Dec. 1980), pp. 883–893. ISSN: 0036-1429. DOI: 10.1137/0717073. URL: https://doi.org/10.1137/0717073 (cit. on p. 150).

[God+10] H. Godrich, V. M. Chiriac, A. Haimovich, and R. S. Blum. "Target tracking in MIMO radar systems: Techniques and performance analysis". In: *IEEE National Radar Conference - Proceedings*. 2010, pp. 1111–1116. ISBN: 9781424458127. DOI: 10.1109/RADAR.2010.5494453 (cit. on p. 3).

[Gol61] M. Golay. "Complementary series". In: *IEEE Transactions on Information Theory* 7.2 (Apr. 1961), pp. 82–87. ISSN: 0018-9448. DOI: 10.1109/TIT.1961.1057620. URL: http://ieeexplore.ieee.org/document/1057620/ (cit. on p. 101).

[Gol67] R. Gold. "Optimal binary sequences for spread spectrum multiplexing". In: *IEEE Transactions on Information Theory* 13.4 (Oct. 1967), pp. 619–621. ISSN: 0018-9448. DOI: 10.1109/TIT.1967.1054048. URL: http://ieeexplore.ieee.org/document/1054048/ (cit. on pp. 59, 136).

[Gom14] O. Gomez. "MIMO radar with colocated antennas: Theoretical investigation, simulations and development of an experimental platform". PhD thesis. 2014. DOI: 10.13140/RG.2.1.2082.8322 (cit. on p. 3).

[Gre59] T. N. E. Greville. "The Pseudoinverse of a Rectangular or Singular Matrix and Its Application to the Solution of Systems of Linear Equations". In: *SIAM Review* 1.1 (Jan. 1959), pp. 38–43. ISSN: 0036-1445. DOI: 10.1137/1001003. URL: http://epubs.siam.org/doi/10.1137/1001003 (cit. on p. 72).

[GSC19] N. Gudadze, G. Stober, and J. L. Chau. "Can VHF radars at polar latitudes measure mean vertical winds in the presence of PMSE?" In: *Atmospheric Chemistry and Physics* 19.7 (Apr. 2019), pp. 4485–4497. ISSN: 1680-7324. DOI: 10.5194/acp-19-4485-2019. URL: https://www.atmos-chem-phys.net/19/4485/2019/ (cit. on pp. 88, 90).

[Hal+05] C. M. Hall, T. Aso, M. Tsutsumi, S. Nozawa, A. H. Manson, and C. E. Meek. "A comparison of mesosphere and lower thermosphere neutral winds as determined by meteor and medium-frequency radar at 70°N". In: *Radio Science* 40 (2005) (cit. on p. 109).

[Han87] P. C. Hansen. "The truncated SVD as a method for regularization". In: *BIT* 27.4 (Dec. 1987), pp. 534–553. ISSN: 0006-3835. DOI: 10.1007/BF01937276. URL: https://doi.org/10.1007/BF01937276%20http://link.springer.com/10.1007/BF01937276 (cit. on pp. 72, 127).

[Har72] H. F. Harmuth. *Transmission of information by orthogonal functions*. 2nd editio. Springer-Verlag Berlin Heidelberg, 1972, p. 394. ISBN: 978-3-642-61974-8. DOI: 10.1007/978-3-642-61974-8 (cit. on p. 59).

[Hau94] R. Haupt. "Thinned arrays using genetic algorithms". In: *IEEE Transactions on Antennas and Propagation* 42.7 (July 1994), pp. 993–999. ISSN: 0018-926X. DOI: 10.1109/8.299602. URL: http://ieeexplore.ieee.org/document/299602/ (cit. on pp. 68, 81, 93).

[HBC08] A. Haimovich, R. S. Blum, and L. Cimini. "MIMO radar with widely separated antennas". In: *IEEE Signal Processing Magazine* 25.1 (2008), pp. 116–

129. ISSN: 1053-5888. DOI: 10.1109/MSP.2008.4408448. URL: http://ieeexplore.ieee.org/document/4408448/ (cit. on p. 114).

[HC06] D. L. Hysell and J. L. Chau. "Optimal aperture synthesis radar imaging". In: *Radio Science* 41.2 (Apr. 2006), n/a–n/a. ISSN: 00486604. DOI: 10.1029/2005RS003383. URL: http://doi.wiley.com/10.1029/2005RS003383 (cit. on pp. 43, 45, 47, 97, 103, 104).

[HCM13] D. L. Hysell, J. L. Chau, and M. A. Milla. "The Jicamarca phased-array radar". In: *2013 IEEE International Symposium on Phased Array Systems and Technology*. IEEE, Oct. 2013, pp. 669–675. ISBN: 978-1-4673-1127-4. DOI: 10.1109/ARRAY.2013.6731910. URL: http://ieeexplore.ieee.org/document/6731910/ (cit. on pp. 14, 87).

[Hec+07] J. H. Hecht, A. Z. Liu, R. L. Walterscheid, S. J. Franke, R. J. Rudy, M. J. Taylor, and P. D. Pautet. "Characteristics of short- period wavelike features near 87 km altitude from airglow and lidar observations over Maui". In: *Geophys. Res. Atmos.* 112 (2007) (cit. on p. 109).

[Hec03] J. H. Hecht. "Instability layers and airglow imaging". In: *Reviews of Geophysics* 42.1 (2003). DOI: 10.1029/2003RG000131. URL: https://agupubs.onlinelibrary.wiley.com/doi/abs/10.1029/2003RG000131 (cit. on pp. 84, 109).

[HF95] U.-P. Hoppe and D. C. Fritts. "High-resolution measurements of vertical velocity with the European incoherent scatter VHF radar: 1. Motion field characteristics and measurement biases". In: *Journal of Geophysical Research* 100.D8 (1995), p. 16813. ISSN: 0148-0227. DOI: 10.1029/95JD01466. URL: http://doi.wiley.com/10.1029/95JD01466 (cit. on p. 90).

[HFV01] W. K. Hocking, B. Fuller, and B. Vandepeer. "Real-time determination of meteor-related parameters utilizing modern digital technology". In: *Journal of Atmospheric and Solar-Terrestrial Physics* 63.2-3 (Jan. 2001), pp. 155–169. ISSN: 13646826. DOI: 10.1016/S1364-6826(00)00138-3. URL: https://linkinghub.elsevier.com/retrieve/pii/S1364682600001383 (cit. on pp. 52, 109, 113, 118, 120).

[Hin+93] C. O. Hines, G. W. Adams, J. W. Brosnahan, F. T. Djuth, M. P. Sulzer, C. A. Tepley, and J. S. Van Baelen. "Multi-instrument observations of mesospheric motions over Arecibo: comparisons and interpretations". In: *Journal of Atmospheric and Terrestrial Physics* 55.3 (Mar. 1993), pp. 241–287. ISSN: 00219169.

DOI: 10.1016/0021-9169(93)90069-B. URL: https://linkinghub.elsevier.com/retrieve/pii/002191699390069B (cit. on p. 1).

[HK70] A. E. Hoerl and R. W. Kennard. "Ridge regression: biased estimation for nonorthogonal problems". In: *Technometrics* 12.1 (1970), pp. 55–67. DOI: 10.1080/00401706.1970.10488634 (cit. on p. 128).

[HK90] R. T. Hoctor and S. A. Kassam. "The unifying role of the coarray in aperture synthesis for coherent and incoherent imaging". In: *Proceedings of the IEEE* 78.4 (1990), pp. 735–752. ISSN: 15582256. DOI: 10.1109/5.54811 (cit. on p. 64).

[HL07] J. Höffner and F. J. Lübken. "Potassium lidar temperatures and densities in the mesopause region at Spitsbergen (78°N)". In: *Journal of Geophysical Research* 112.D20 (Oct. 2007), p. D20114. ISSN: 0148-0227. DOI: 10.1029/2007JD008612. URL: http://doi.wiley.com/10.1029/2007JD008612 (cit. on p. 84).

[HL15] Y. Huang and G. Liao. "MIMO SAR GMTI with RPCA based method". In: *Proceedings of the 2015 IEEE 5th Asia-Pacific Conference on Synthetic Aperture Radar, APSAR 2015*. Institute of Electrical and Electronics Engineers Inc., Oct. 2015, pp. 827–830. ISBN: 9781467372961. DOI: 10.1109/APSAR.2015.7306331 (cit. on p. 3).

[HM13] B. J. Harding and M. A. Milla. "Radar imaging with compressed sensing". In: *Radio Science* 48.5 (Sept. 2013), pp. 582–588. ISSN: 00486604. DOI: 10.1002/rds.20063. URL: http://doi.wiley.com/10.1002/rds.20063 (cit. on pp. 43, 45, 46, 96, 98).

[HMM15] B. J. Harding, J. J. Makela, and J. W. Meriwether. "Estimation of mesoscale thermospheric wind structure using a network of interferometers". In: *Journal of Geophysical Research-Space Physics* 120.5 (May 2015), pp. 3928–3940. ISSN: 21699402. DOI: 10.1002/2015JA021025 (cit. on p. 147).

[Hoc05] W. K. Hocking. "A new approach to momentum flux determinations using SKiYMET meteor radars". In: *Annales Geophysicae* 23.7 (Oct. 2005), pp. 2433–2439. ISSN: 1432-0576. DOI: 10.5194/angeo-23-2433-2005. URL: http://www.ann-geophys.net/23/2433/2005/ (cit. on pp. 84, 88).

[Hoc83] W. K. Hocking. "On the extraction of atmospheric turbulence parameters from radar backscatter Doppler spectra—I. Theory". In: *Journal of Atmospheric and Terrestrial Physics* 45.2-3 (Feb. 1983), pp. 89–102. ISSN: 00219169. DOI: 10.

1016/S0021-9169(83)80013-0. URL: https://linkinghub.elsevier.com/retrieve/pii/S0021916983800130 (cit. on pp. 20, 52).

[Hoc85] W. K. Hocking. "Measurement of turbulent energy dissipation rates in the middle atmosphere by radar techniques: A review". In: *Radio Science* 20.6 (1985), pp. 1403–1422. DOI: 10.1029/RS020i006p01403. URL: https://agupubs.onlinelibrary.wiley.com/doi/abs/10.1029/RS020i006p01403 (cit. on pp. 6, 20, 52).

[Hof+10] P. Hoffmann, E. Becker, W. Singer, and M. Placke. "Seasonal variation of mesospheric waves at northern middle and high latitudes". In: *Journal of Atmospheric and Solar-Terrestrial Physics* 72.14-15 (Sept. 2010), pp. 1068–1079. ISSN: 13646826. DOI: 10.1016/j.jastp.2010.07.002 (cit. on p. 84).

[Höf18] J. Höffner. *VAHCOLI - Leibniz-Institut für Atmosphärenphysik, Kühlungsborn*. 2018. URL: https://www.iap-kborn.de/aktuelles/nachrichten/archiv/2018/20180118vahcoli/ (cit. on p. 2).

[Hög74] J. A. Högbom. "Aperture synthesis with a non-regular distribution of interferometer baselines". In: *Astronomy and Astrophysics Supplement* 15 (June 1974), p. 417 (cit. on p. 128).

[Hol+97] C. L. Holloway, R. J. Doviak, S. A. Cohn, R. J. Lataitis, and J. S. Van Baelen. "Cross correlations and cross spectra for spaced antenna wind profilers: 2. Algorithms to estimate wind and turbulence". In: *European Journal of Radiology* 32.3 (May 1997), pp. 967–982. ISSN: 0720048X (cit. on p. 90).

[HRC04] D. A. Holdsworth, I. M. Reid, and M. A. Cervera. "Buckland Park all-sky interferometric meteor radar". In: *Radio Science* 39.5 (Sept. 2004). ISSN: 00486604. DOI: 10.1029/2003RS003014. URL: https://agupubs.onlinelibrary.wiley.com/doi/abs/10.1029/2003RS003014 (cit. on pp. 113, 120).

[HRC86] W. K. Hocking, R. Rüster, and P. Czechowsky. "Absolute reflectivities and aspect sensitivities of VHF radio wave scatterers measured with the SOUSY radar". In: *Journal of Atmospheric and Terrestrial Physics* 48.2 (Feb. 1986), pp. 131–144. ISSN: 00219169. DOI: 10.1016/0021-9169(86)90077-2. URL: https://linkinghub.elsevier.com/retrieve/pii/0021916986900772 (cit. on p. 89).

[HT97] W. K. Hocking and T. Thayaparan. "Simultaneous and colocated observation of winds and tides by MF and meteor radars over London, Canada (43°N, 81°W), during 1994-1996". In: *Radio Science* 32.2 (Mar. 1997), pp. 833–865. ISSN:

00486604. DOI: 10.1029/96RS03467. URL: http://doi.wiley.com/10.1029/96RS03467 (cit. on p. 118).

[HTJ97] W. K. Hocking, T. Thayaparan, and J. Jones. "Meteor decay times and their use in determining a diagnostic mesospheric temperature-pressure parameter: Methodology and one year of data". In: *Geophysical Research Letters* 24 (1997), pp. 2977–2980 (cit. on p. 52).

[Hua+11] Y. Huang, P. V. Brennan, D. Patrick, I. Weller, P. Roberts, and K. Hughes. "FMCW based MIMO imaging radar for maritime navigation". In: *Progress In Electromagnetics Research* 115 (2011), pp. 327–342. ISSN: 1559-8985. DOI: 10.2528/PIER11021509. URL: http://www.jpier.org/PIER/pier.php?paper=11021509 (cit. on p. 52).

[Hys96] D. L. Hysell. "Radar imaging of equatorial F region irregularities with maximum entropy interferometry". In: *Radio Science* 31 (1996), pp. 1567–1578 (cit. on p. 44).

[Int] Intel. *Intel distribution for Python*. URL: https://software.intel.com/en-us/distribution-for-python (cit. on p. 149).

[Jam+09] G. James, D. Witten, T. Hastie, and R. Tibshirani. *An introduction to statistical learning*. Vol. 7. Springer, 2009 (cit. on p. 128).

[Jef09] Jeffrey. *Phased-array radar design: application of radar fundamentals*. Radar, Sonar and; Navigation. Institution of Engineering and Technology, Jan. 2009. ISBN: 9781891121692. DOI: 10.1049/SBRA018E. URL: https://digital-library.theiet.org/content/books/ra/sbra018e (cit. on p. 39).

[JH03] G. O. Jones and U.-P. Hoppe. "High-resolution vertical velocity studies within PMSE using EISCAT". In: *European Rocket and Balloon Programmes and Related Research*. Ed. by B. Warmbein. 530. 2003, pp. 309–314. ISBN: 92-9092-840-9. URL: https://ui.adsabs.harvard.edu/abs/2003ESASP.530..309J (cit. on p. 88).

[JLZ12] T. Jin, J. Lou, and Z. Zhou. "Extraction of landmine features using a forward-looking ground-penetrating radar with MIMO array". In: *IEEE Geoscience and Remote Sensing Society* (2012) (cit. on pp. 3, 52).

[JWH98] J. Jones, A. R. Webster, and W. K. Hocking. "An improved interferometer design for use with meteor radars". In: *Radio Science* 33.1 (Jan. 1998), pp. 55–65. ISSN: 00486604. DOI: 10.1029/97RS03050. URL: https://agupubs.

onlinelibrary.wiley.com/doi/abs/10.1029/97RS03050 (cit. on p. 116).

[Kal60] R. E. Kalman. "A new approach to linear filtering and prediction problems". In: *Journal of Basic Engineering* 82.1 (Mar. 1960), pp. 35–45. ISSN: 0021-9223. DOI: 10.1115/1.3662552. URL: https://asmedigitalcollection.asme.org/fluidsengineering/article/82/1/35/397706/A-New-Approach-to-Linear-Filtering-and-Prediction (cit. on p. 104).

[Kat+19] Z. T. Katamzi-Joseph, A. L. Aruliah, K. Oksavik, J. B. Habarulema, K. Kauristie, and M. J. Kosch. "Multi-instrument observations of large-scale atmospheric gravity waves/traveling ionospheric disturbances associated with enhanced auroral activity over Svalbard". In: *Advances in Space Research* 63.1 (Jan. 2019), pp. 270–281. ISSN: 02731177. DOI: 10.1016/j.asr.2018.08.042. URL: https://linkinghub.elsevier.com/retrieve/pii/S0273117718306707 (cit. on p. 1).

[Kay09] S. M. Kay. "Waveform design for multistatic radar detection". In: *IEEE Transactions on Aerospace and Electronic Systems* 45.3 (July 2009), pp. 1153–1166. ISSN: 00189251. DOI: 10.1109/TAES.2009.5259190 (cit. on p. 71).

[Kay93] S. M. Kay. *Fundamentals of statistical signal processing: estimation theory*. Upper Saddle River, NJ, USA: Prentice-Hall, Inc., 1993. ISBN: 0-13-345711-7 (cit. on p. 128).

[KC18] D. Kouba and J. Chum. "Ground-based measurements of ionospheric dynamics". In: *Journal of Space Weather and Space Climate* 8.2017 (May 2018), A29. ISSN: 2115-7251. DOI: 10.1051/swsc/2018018. URL: https://www.swsc-journal.org/10.1051/swsc/2018018 (cit. on p. 19).

[KD10] J. Kantor and S. K. Davis. "Airborne GMTI using MIMO techniques". In: *IEEE National Radar Conference - Proceedings*. 2010, pp. 1344–1349. ISBN: 9781424458127. DOI: 10.1109/RADAR.2010.5494407 (cit. on p. 3).

[Ker+19] J. Kero, D. Kastinen, J. Vierinen, T. Grydeland, C. Heinselman, J. Markkanen, and A. Tjulin. "EISCAT 3D: The next generation international atmosphere and geospace research radar". In: *1st NEO and Debris Detection Conference*. Ed. by T. Flohrer, R. Jehn, and F. Schmitz. ESA Space Safety Programme Office, 2019. URL: www.space-track.org (cit. on p. 2).

[Kir+10] S. Kirkwood, E. Belova, K. Satheesan, T. Narayana Rao, T. Rajendra Prasad, and K. S. Satheesh. "Fresnel scatter revisited – comparison of 50 MHz radar and radiosondes in the Arctic, the Tropics and Antarctica". In: *Annales Geophysicae* 28.10 (Oct. 2010), pp. 1993–2005. ISSN: 1432-0576. DOI: 10.5194/angeo-28-1993-2010. URL: https://www.ann-geophys.net/28/1993/2010/%20https://angeo.copernicus.org/articles/28/1993/2010/ (cit. on p. 17).

[Kop+15] M. Kopp, M. Gerding, J. Höffner, and F. J. Lübken. "Tidal signatures in temperatures derived from daylight lidar soundings above Kühlungsborn (54°N, 12°E)". In: *Journal of Atmospheric and Solar-Terrestrial Physics* 127 (May 2015), pp. 37–50. ISSN: 13646826. DOI: 10.1016/j.jastp.2014.09.002. URL: https://linkinghub.elsevier.com/retrieve/pii/S1364682614002077 (cit. on p. 118).

[KS91] E. Kudeki and F. Sürücü. "Radar interferometric imaging of field-aligned plasma irregularities in the equatorial electrojet". In: *Geophysical Research Letters* 18 (1991), pp. 41–44 (cit. on p. 43).

[KV96] H. Krim and M. Viberg. "Two decades of array signal processing research: the parametric approach". In: *IEEE Signal Processing Magazine* 13.4 (1996), pp. 67–94 (cit. on p. 38).

[Lat+12a] R. Latteck, W. Singer, M. Rapp, T. Renkwitz, and G. Stober. "Horizontally resolved structures of radar backscatter from polar mesospheric layers". In: *Advances in Radio Science* 10 (Sept. 2012), pp. 285–290. ISSN: 1684-9973. DOI: 10.5194/ars-10-285-2012. URL: https://www.adv-radio-sci.net/10/285/2012/ (cit. on p. 2).

[Lat+12b] R. Latteck, W. Singer, M. Rapp, B. Vandepeer, T. Renkwitz, M. Zecha, and G. Stober. "MAARSY: The new MST radar on Andøya-system description and first results". In: *Radio Science* 47.1 (Feb. 2012), n/a–n/a. ISSN: 00486604. DOI: 10.1029/2011RS004775. URL: http://doi.wiley.com/10.1029/2011RS004775 (cit. on pp. 7, 14, 38, 91).

[LB17] R. Latteck and J. Bremer. "Long-term variations of polar mesospheric summer echoes observed at Andøya (69°N)". In: *Journal of Atmospheric and Solar-Terrestrial Physics* 163 (2017), pp. 31–37. ISSN: 1364-6826. DOI: https://doi.org/10.1016/j.jastp.2017.07.005. URL: http://www.sciencedirect.com/science/article/pii/S1364682617300846 (cit. on p. 91).

[Leh+07] N. H. Lehmann, E. Fishler, A. Haimovich, R. S. Blum, D. Chizhik, L. Cimini, and R. Valenzuela. "Evaluation of transmit diversity in MIMO-radar direction finding". In: *IEEE Transactions on Signal Processing* 55.5 (May 2007), pp. 2215–2225. ISSN: 1053-587X. DOI: 10.1109/TSP.2007.893220. URL: https://ieeexplore.ieee.org/document/4156404/ (cit. on pp. 51, 55).

[Li+08] J. Li, L. Xu, P. Stoica, K. W. Forsythe, and D. W. Bliss. "Range compression and waveform optimization for MIMO Radar: A Cramer–Rao bound based study". In: *IEEE Transactions on Signal Processing* 56.1 (Jan. 2008), pp. 218–232. ISSN: 1053-587X. DOI: 10.1109/TSP.2007.901653. URL: http://ieeexplore.ieee.org/document/4359542/ (cit. on pp. 64, 71).

[Li+16] Q. Li, M. Rapp, A. Schrön, A. Schneider, and G. Stober. "Derivation of turbulent energy dissipation rate with the middle atmosphere Alomar radar system (MAARSY) and radiosondes at Andoya, Norway". In: *Annales Geophysicae* 34.12 (2016), pp. 1209–1229. ISSN: 0992-7689. URL: http://nbn-resolving.de/urn/resolver.pl?urn=nbn:de:bvb:19-epub-37387-9 (cit. on p. 52).

[LK81] B. Lewis and F. Kretschmer. "A new class of polyphase pulse compression codes and techniques". In: *IEEE Transactions on Aerospace and Electronic Systems* AES-17.3 (May 1981), pp. 364–372. ISSN: 0018-9251. DOI: 10.1109/TAES.1981.309063. URL: http://ieeexplore.ieee.org/document/4102505/ (cit. on p. 30).

[LM05] E. Le Pennec and S. Mallat. "Bandelet image approximation and compression". In: *Multiscale Modeling & Simulation* 4.3 (Jan. 2005), pp. 992–1039. ISSN: 1540-3459. DOI: 10.1137/040619454. URL: https://doi.org/10.1137/040619454%20http://epubs.siam.org/doi/10.1137/040619454 (cit. on p. 45).

[LS07] J. Li and P. Stoica. "MIMO radar with colocated antennas". In: *IEEE Signal Processing Magazine* 24.5 (Sept. 2007), pp. 106–114. ISSN: 1053-5888. DOI: 10.1109/MSP.2007.904812. URL: http://ieeexplore.ieee.org/document/4350230/ (cit. on pp. 2, 3, 50, 51).

[LS15] R. Latteck and I. Strelnikova. "Extended observations of polar mesosphere winter echoes over Andøya (69°N) using MAARSY". In: *Journal of Geophysical Research: Atmospheres* 120.16 (Aug. 2015), pp. 8216–8226. ISSN: 2169-897X.

DOI: 10.1002/2015JD023291. URL: http://dx.doi.org/10.1002/2015JD023291 (cit. on p. 88).

[LT03] Lizhong Zheng and D. Tse. "Diversity and multiplexing: a fundamental tradeoff in multiple-antenna channels". In: *IEEE Transactions on Information Theory* 49.5 (May 2003), pp. 1073–1096. ISSN: 0018-9448. DOI: 10.1109/TIT.2003.810646. URL: http://ieeexplore.ieee.org/document/1197843/ (cit. on pp. 8, 49).

[Lüb+87] F. J. Lübken, U. von Zahn, E. V. Thrane, T. A. Blix, G. A. Kokin, and S. V. Pachomov. "In situ measurements of turbulent energy dissipation rates and eddy diffusion coefficients during MAP/WINE". In: *Journal of Atmospheric and Terrestrial Physics* 49.7 (1987), pp. 763–775. ISSN: 0021-9169. DOI: https://doi.org/10.1016/0021-9169(87)90018-3. URL: http://www.sciencedirect.com/science/article/pii/0021916987900183 (cit. on p. 6).

[Lüb99] F. J. Lübken. "Thermal structure of the Arctic summer mesosphere". In: *Journal of Geophysical Research Atmospheres* (1999). ISSN: 01480227. DOI: 10.1029/1999JD900076 (cit. on p. 90).

[Luc+06] H. Luce, G. Hassenpflug, M. Yamamoto, and S. Fukao. "High-resolution vertical imaging of the troposphere and lower stratosphere using the new MU radar system". In: *Annales Geophysicae* 24.3 (May 2006), pp. 791–805. ISSN: 1432-0576. DOI: 10.5194/angeo-24-791-2006. URL: http://www.ann-geophys.net/24/791/2006/ (cit. on p. 14).

[Mal47] L. R. Malling. "Radio Doppler effect for aircraft speed measurements". In: *Proceedings of the IRE* 35.11 (1947), pp. 1357–1360. ISSN: 2162-6634. DOI: 10.1109/JRPROC.1947.233900 (cit. on p. 34).

[Mao+17] X. Mao, D. J. Love, J. V. Rispoli, and T. M. Talavage. "Multiple-input multiple-output (MIMO) MRI: An efficient pulse design algorithm to combine parallel excitation and parallel imaging". In: *ICASSP, IEEE International Conference on Acoustics, Speech and Signal Processing - Proceedings*. Institute of Electrical and Electronics Engineers Inc., June 2017, pp. 909–913. ISBN: 9781509041176. DOI: 10.1109/ICASSP.2017.7952288 (cit. on p. 3).

[Mas+10] X. P. Masbernat, M. G. Amin, F. Ahmad, and C. Ioana. "An MIMO-MTI approach for through-the-wall radar imaging applications". In: *2010 International Waveform Diversity and Design Conference*. IEEE, Aug. 2010, pp. 000188–

000192. ISBN: 978-1-4244-8202-3. DOI: 10.1109/WDD.2010.5592466. URL: http://ieeexplore.ieee.org/document/5592466/ (cit. on pp. 3, 52).

[MBL11] B. Matuz, F. L. Blasco, and G. Liva. "On the application of the Baum-Welch algorithm for modeling the land mobile satellite channel". In: *2011 IEEE Global Telecommunications Conference - GLOBECOM 2011*. IEEE, Dec. 2011, pp. 1–5. ISBN: 978-1-4244-9268-8. DOI: 10.1109/GLOCOM.2011.6133807. URL: http://ieeexplore.ieee.org/document/6133807/ (cit. on p. 104).

[McK+15] D. McKay, J. Vierinen, I. I. Virtanen, R. Fallows, M. Postila, T. Ulich, O. Wucknitz, M. Brentjens, N. Ebbendorf, C. Enell, M. Gerbers, T. Grit, P. Gruppen, A. Kero, T. Iinatti, M. S. Lehtinen, H. Meulman, M. Norden, M. Orispää, T. Raita, J. P. de Reijer, L. Roininen, A. Schoenmakers, K. Stuurwold, and E. Turunen. "KAIRA: The Kilpisjärvi atmospheric imaging receiver array-system overview and first results". In: *IEEE Transactions on Geoscience and Remote Sensing* 53.3 (2015), pp. 1440–1451. ISSN: 1558-0644 (cit. on p. 38).

[MCK96] A. Mudukutore, V. Chandrasekar, and R. J. Keeler. "Weather radars with pulse compression using complementary codes: simulation and evaluation". In: *International Geoscience and Remote Sensing Symposium (IGARSS)*. Vol. 1. IEEE, 1996, pp. 574–576. DOI: 10.1109/igarss.1996.516407 (cit. on p. 101).

[MHL07] A. Meta, P. Hoogeboom, and L. P. Ligthart. "Signal processing for FMCW SAR". In: *IEEE Transactions on Geoscience and Remote Sensing* 45.11 (2007), pp. 3519–3532 (cit. on p. 31).

[Moo96] T. Moon. "The expectation-maximization algorithm". In: *IEEE Signal Processing Magazine* 13.6 (1996), pp. 47–60. ISSN: 10535888. DOI: 10.1109/79.543975. URL: http://ieeexplore.ieee.org/document/543975/ (cit. on p. 104).

[Mor+13] A. Moreira, P. Prats-Iraola, M. Younis, G. Krieger, I. Hajnsek, and K. P. Papathanassiou. "A tutorial on synthetic aperture radar". In: *IEEE Geoscience and Remote Sensing Magazine* 1.1 (Mar. 2013), pp. 6–43. ISSN: 2168-6831. DOI: 10.1109/MGRS.2013.2248301. URL: http://ieeexplore.ieee.org/document/6504845/ (cit. on pp. 52, 73).

[MS76] F. J. MacWilliams and N. J. A. Sloane. "Pseudo-random sequences and arrays". In: *Proceedings of the IEEE* 64.12 (1976), pp. 1715–1729. ISSN: 1558-2256. DOI: 10.1109/PROC.1976.10411 (cit. on p. 59).

[MVP50] L. Manning, O. Villard, and A. Peterson. “Meteoric echo study of upper atmosphere winds”. In: *Proceedings of the IRE* 38.8 (Aug. 1950), pp. 877–883. ISSN: 0096-8390. DOI: 10.1109/JRPROC.1950.234124. URL: http://ieeexplore.ieee.org/document/1701348/ (cit. on p. 113).

[New+10] G. E. Newstadt, E. Zelnio, L. Gorham, and A. O. Hero. “Detection/tracking of moving targets with synthetic aperture radars”. In: *SPIE Proceedings, Algorithms for Synthetic Aperture Radar Imagery XVII* 7699 (2010). URL: http://spie.org/Publications/Proceedings/Paper/10.1117/12.850345 (cit. on p. 73).

[NT09] D. Needell and J. A. Tropp. “CoSaMP: Iterative signal recovery from incomplete and inaccurate samples”. In: *Applied and Computational Harmonic Analysis* 26.3 (May 2009), pp. 301–321. ISSN: 10635203. DOI: 10.1016/j.acha.2008.07.002. URL: https://linkinghub.elsevier.com/retrieve/pii/S1063520308000638 (cit. on p. 130).

[NTW99] A. Narula, M. D. Trott, and G. W. Wornell. “Performance limits of coded diversity methods for transmitter antenna arrays”. In: *IEEE Transactions on Information Theory* 45 (1999), pp. 2418–2433. URL: http://citeseerx.ist.psu.edu/viewdoc/summary?doi=10.1.1.32.2610 (cit. on p. 55).

[NV09] D. Needell and R. Vershynin. “Uniform uncertainty principle and signal recovery via regularized orthogonal matching pursuit”. In: *Foundations of Computational Mathematics* 9.3 (June 2009), pp. 317–334. ISSN: 16153375. DOI: 10.1007/s10208-008-9031-3 (cit. on p. 130).

[Pal+98] R. D. Palmer, S. Gopalam, T.-Y. Yu, and S. Fukao. “Coherent radar imaging using Capon’s method”. In: *Radio Science* 33 (1998), pp. 1585–1598 (cit. on pp. 41, 43, 44, 97).

[Pau+11] P. D. Pautet, J. Stegman, C. Wrasse, K. Nielsen, H. Takahashi, M. J. Taylor, K. W. Hoppel, and S. Eckermann. “Analysis of gravity waves structures visible in noctilucent cloud images”. In: *Journal of Atmospheric and Solar-Terrestrial Physics* 73.14-15 (Sept. 2011), pp. 2082–2090. ISSN: 13646826. DOI: 10.1016/j.jastp.2010.06.001. URL: https://linkinghub.elsevier.com/retrieve/pii/S136468261000177X (cit. on p. 85).

[PC08] T. Park and G. Casella. “The Bayesian Lasso”. In: *Journal of the American Statistical Association* 103.482 (June 2008), pp. 681–686. ISSN: 01621459. DOI: 10.1198/016214508000000337 (cit. on p. 72).

[Pey10] G. Peyre. “Best basis compressed sensing”. In: *IEEE Transactions on Signal Processing* 58.5 (2010), pp. 2613–2622 (cit. on p. 45).

[Pla+15] M. Placke, P. Hoffmann, R. Latteck, and M. Rapp. “Gravity wave momentum fluxes from MF and meteor radar measurements in the polar MLT region”. In: *Journal of Geophysical Research-Space Physics* 120 (2015), pp. 736–750 (cit. on pp. 6, 84).

[Poo85] A. W. V. Poole. “Advanced sounding: 1. The FMCW alternative”. In: *Radio Science* 20.6 (1985), pp. 1609–1616 (cit. on p. 31).

[Pow70] M. J. D. Powell. “A hybrid method for nonlinear equations”. In: *Numerical Methods for Nonlinear Algebraic Equations*. Ed. by P. Rabinowitz. Gordon and Breach, 1970 (cit. on p. 45).

[PYC99] R. D. Palmer, T.-Y. Yu, and P. Chilson. “Range imaging using frequency diversity”. In: *Radio Science* 34.6 (1999), pp. 1485–1496 (cit. on p. 31).

[Qin+17] W. Qin, F. Zhao, Y. Li, and S. Gu. “A multitarget tracking before detecting algorithm with MIMO radar”. In: *Proceedings of 2017 IEEE 2nd Advanced Information Technology, Electronic and Automation Control Conference, IAEAC 2017*. Institute of Electrical and Electronics Engineers Inc., Sept. 2017, pp. 825–829. ISBN: 9781467389778. DOI: 10.1109/IAEAC.2017.8054130 (cit. on p. 3).

[Rap+11] M. Rapp, R. Latteck, G. Stober, P. Hoffmann, W. Singer, and M. Zecha. “First three-dimensional observations of polar mesosphere winter echoes: Resolving space-time ambiguity”. In: *Journal of Geophysical Research: Space Physics* 116.A11 (Nov. 2011), n/a–n/a. ISSN: 01480227. DOI: 10.1029/2011JA016858. URL: http://doi.wiley.com/10.1029/2011JA016858 (cit. on p. 2).

[Rap03] M. Rapp. “On the nature of PMSE: Electron diffusion in the vicinity of charged particles revisited”. In: *Journal of Geophysical Research* 108.D8 (Apr. 2003), p. 8437. ISSN: 0148-0227. DOI: 10.1029/2002JD002857. URL: http://doi.wiley.com/10.1029/2002JD002857 (cit. on p. 89).

[Rei87] I. M. Reid. “Some aspects of Doppler radar measurements of the mean and fluctuating components of the wind field in the upper middle atmosphere”. In: *Journal of Atmospheric and Terrestrial Physics* 49.5 (1987), pp. 467–484. ISSN: 0021-9169. DOI: 10.1016/0021-9169(87)90041-9 (cit. on p. 50).

[RGL08] M. Rauthe, M. Gerding, and F. J. Lübken. "Seasonal changes in gravity wave activity measured by lidars at mid-latitudes". In: *Atmospheric Chemistry and Physics* 8.22 (Nov. 2008), pp. 6775–6787. ISSN: 1680-7324. DOI: 10.5194/acp-8-6775-2008. URL: https://www.atmos-chem-phys.net/8/6775/2008/ (cit. on p. 84).

[RGV09] R. Radzokota, E. Golovins, and N. Ventura. "Linear detector performance in ill-conditioned MIMO OFDM channel". In: *2009 International Conference on Ultra Modern Telecommunications & Workshops*. IEEE, Oct. 2009, pp. 1–7. ISBN: 978-1-4244-3942-3. DOI: 10.1109/ICUMT.2009.5345387. URL: http://ieeexplore.ieee.org/document/5345387/ (cit. on pp. 115, 128).

[RL04] M. Rapp and F. J. Lübken. "Polar mesosphere summer echoes (PMSE): Review of observations and current understanding". In: *Atmospheric Chemistry and Physics* 4 (2004), p. 2601 (cit. on pp. 88, 89).

[RL14] B. C. Roberts and M. F. Larsen. "Structure function analysis of chemical tracer trails in the mesosphere-lower thermosphere region". In: *Journal of Geophysical Research* 119 (2014), pp. 6368–6375 (cit. on p. 6).

[RLB03] M. Rapp, F. J. Lübken, and T. A. Blix. "The role of charged ice particles for the creation of PMSE: A review of recent developments". In: *Advances in Space Research* 31.9 (May 2003), pp. 2033–2043. ISSN: 02731177. DOI: 10.1016/S0273-1177(03)00226-6 (cit. on p. 89).

[RLE53] D. Robertson, D. Liddy, and W. G. Elford. "Measurements of winds in the upper atmosphere by means of drifting meteor trails I". In: *Journal of Atmospheric and Terrestrial Physics* 4.4-5 (Dec. 1953), pp. 255–270. ISSN: 00219169. DOI: 10.1016/0021-9169(53)90059-2. URL: https://linkinghub.elsevier.com/retrieve/pii/0021916953900592 (cit. on pp. 88, 113).

[Sal01] D. Salmond. "Target tracking: introduction and Kalman tracking filters". In: *IEE International Seminar Target Tracking: Algorithms and Applications*. Vol. 2001. 174 PART II. IEE, 2001, pp. 2–1. DOI: 10.1049/ic:20010245. URL: https://digital-library.theiet.org/content/conferences/10.1049/ic_20010245 (cit. on p. 104).

[Sat+14] K. Sato, M. Tsutsumi, T. Sato, T. Nakamura, A. Sato, Y. Tomikawa, K. Nishimura, M. Kohma, H. Yamagishi, and T. Yamanouchi. "Program of the Antarctic Syowa MST/IS radar (PANSY)". In: *journal of Atmospheric and Solar-Terrestrial Physics* 118 (2014), pp. 2–15 (cit. on p. 14).

[SBL14] H. Sun, F. Brigui, and M. Lesturgie. “Analysis and comparison of MIMO radar waveforms”. In: *2014 International Radar Conference*. IEEE, Oct. 2014, pp. 1–6. ISBN: 978-1-4799-4195-7. DOI: 10.1109/RADAR.2014.7060251. URL: http://ieeexplore.ieee.org/document/7060251/ (cit. on p. 71).

[SC15] G. Stober and J. L. Chau. “A multistatic and multifrequency novel approach for specular meteor radars to improve wind measurements in the MLT region”. In: *Radio Science* 50.5 (May 2015), pp. 431–442. ISSN: 00486604. DOI: 10.1002/2014RS005591. URL: http://dx.doi.org/10.1002/2014RS005591%20http://doi.wiley.com/10.1002/2014RS005591 (cit. on pp. 2, 6, 52, 86, 113, 118, 119, 124, 144, 147).

[SC16] S. Sommer and J. L. Chau. “Patches of polar mesospheric summer echoes characterized from radar imaging observations with MAARSY”. In: *Annales Geophysicae* 34.12 (Dec. 2016), pp. 1231–1241. ISSN: 1432-0576. DOI: 10.5194/angeo-34-1231-2016. URL: https://www.ann-geophys.net/34/1231/2016/ (cit. on pp. 88, 90, 93).

[SFR08] G. San Antonio, D. R. Fuhrmann, and F. C. Robey. “Generalized MIMO radar ambiguity functions”. In: *MIMO Radar Signal Processing*. Vol. 1. 1. Hoboken, NJ, USA: John Wiley & Sons, Inc., Mar. 2008, pp. 123–152. ISBN: 9780470178980. DOI: 10.1002/9780470391488.ch3. URL: http://doi.wiley.com/10.1002/9780470391488.ch3 (cit. on p. 71).

[SG96] E. Spano and O. Ghebrebrhan. “Sequences of complementary codes for the optimum decoding of truncated ranges and high sidelobe suppression factors for ST/MST radar systems”. In: *IEEE Transactions on Geoscience and Remote Sensing* 34.2 (Mar. 1996), pp. 330–345. ISSN: 01962892. DOI: 10.1109/36.485111. URL: http://ieeexplore.ieee.org/document/485111/ (cit. on p. 101).

[SL15] Y. Shen and S. Li. “Sparse signals recovery from noisy measurements by orthogonal matching pursuit”. In: *Inverse Problems & Imaging* 9 (2015), p. 231. ISSN: 1930-8337. DOI: 10.3934/ipi.2015.9.231 (cit. on p. 45).

[Smi+13] D. S. Smith, L. R. Arlinghaus, T. E. Yankeelov, and E. B. Welch. “Curvelets as a sparse basis for compressed sensing magnetic resonance imaging”. In: *Medical Imaging 2013: Image Processing*. Ed. by S. Ourselin and D. R. Haynor. Vol. 8669. International Society for Optics and Photonics. SPIE, 2013, pp. 621–

627. DOI: 10.1117/12.2007032. URL: https://doi.org/10.1117/12.2007032 (cit. on p. 45).

[Som+13] S. Sommer, G. Stober, C. Schult, M. Zecha, and R. Latteck. "Investigation of horizontal structures at mesospheric altitudes using coherent radar imaging". In: *Advances in Radio Science* 11 (July 2013), pp. 319–325. ISSN: 1684-9973. DOI: 10.5194/ars-11-319-2013. URL: https://www.adv-radio-sci.net/11/319/2013/ (cit. on p. 2).

[Sté09] M. Stéphane. "Sparse representations". In: *A Wavelet Tour of Signal Processing*. Ed. by M. Stéphane. Third Edit. Boston: Elsevier, 2009, pp. 1–31. ISBN: 978-0-12-374370-1. DOI: 10.1016/B978-0-12-374370-1.00005-7. URL: https://linkinghub.elsevier.com/retrieve/pii/B9780123743701000057 (cit. on p. 45).

[Ste77] G. W. Stewart. "On the perturbation of pseudo-inverses, projections and linear least squares problems". In: *SIAM Review* 19.4 (Oct. 1977), pp. 634–662. ISSN: 0036-1445. DOI: 10.1137/1019104. URL: http://epubs.siam.org/doi/10.1137/1019104 (cit. on p. 72).

[Sto+12] G. Stober, R. Latteck, M. Rapp, W. Singer, and M. Zecha. "MAARSY - the new MST radar on Andøya: First results of spaced antenna and Doppler measurements of atmospheric winds in the troposphere and mesosphere using a partial array". In: *Adv. Radio Sci.* (2012), pp. 291–298 (cit. on p. 88).

[Sto+13] G. Stober, S. Sommer, M. Rapp, and R. Latteck. "Investigation of gravity waves using horizontally resolved radial velocity measurements". In: *Atmospheric Measurement Techniques* 6.10 (Oct. 2013), pp. 2893–2905. ISSN: 1867-8548. DOI: 10.5194/amt-6-2893-2013. URL: https://www.atmos-meas-tech.net/6/2893/2013/ (cit. on pp. 2, 88, 90).

[Sto+18] G. Stober, S. Sommer, C. Schult, R. Latteck, and J. L. Chau. "Observation of Kelvin–Helmholtz instabilities and gravity waves in the summer mesopause above Andenes in Northern Norway". In: *Atmospheric Chemistry and Physics* 18.9 (May 2018), pp. 6721–6732. ISSN: 1680-7324. DOI: 10.5194/acp-18-6721-2018. URL: https://www.atmos-chem-phys.net/18/6721/2018/ (cit. on p. 4).

[Sto92] A. G. Stove. "Linear FMCW radar techniques". In: *IEE Proceedings F - Radar and Signal Processing* 139.5 (1992), pp. 343–350 (cit. on p. 31).

[Sul15] M. Sulzer. "Radar — Incoherent scatter radar". In: *Encyclopedia of Atmospheric Sciences*. Ed. by G. R. North, J. Pyle, and F. Zhang. 2nd editio. Oxford: Elsevier, 2015, pp. 422–428. ISBN: 978-0-12-382225-3. DOI: 10.1016/B978-0-12-382225-3.00330-3. URL: http://www.sciencedirect.com/science/article/pii/B9780123822253003303%20https://linkinghub.elsevier.com/retrieve/pii/B9780123822253003303 (cit. on p. 52).

[SV01] M. N. Sasi and L. Vijayan. "Turbulence characteristics in the tropical mesosphere as obtained by MST radar at Gadanki (13.5° N, 79.2° E)". In: *Annales Geophysicae* 19.8 (2001), pp. 1019–1025. DOI: 10.5194/angeo-19-1019-2001. URL: https://www.ann-geophys.net/19/1019/2001/ (cit. on p. 85).

[SZW10] X. Song, S. Zhou, and P. Willett. "Reducing the waveform cross correlation of MIMO radar with space-time coding". In: *IEEE Transactions on Signal Processing* 58.8 (Aug. 2010), pp. 4213–4224. ISSN: 1053587X. DOI: 10.1109/TSP.2010.2048207 (cit. on p. 71).

[Tag+17] O. Taghizadeh, V. Radhakrishnan, G. Alirezaei, E. Zandi, and R. Mathar. "Optimal linear MMSE design for passive distributed radar sensor network systems". In: *2017 IEEE International Conference on Wireless for Space and Extreme Environments, WiSEE 2017*. Institute of Electrical and Electronics Engineers Inc., Nov. 2017, pp. 81–85. ISBN: 9781538633182. DOI: 10.1109/WiSEE.2017.8124897 (cit. on p. 72).

[Tal+16] S. H. Talisa, K. W. O'Haver, T. M. Comberiate, M. D. Sharp, and O. F. Somerlock. "Benefits of digital phased array radars". In: *Proceedings of the IEEE* 104.3 (2016), pp. 530–543. ISSN: 1558-2256. DOI: 10.1109/JPROC.2016.2515842 (cit. on p. 52).

[Tan+18] L. Tang, H. Meng, X. Chen, J. Zhang, L. Lv, and K. Liu. "A novel 3D imaging method of FMCW MIMO-SAR". In: *2018 China International SAR Symposium, CISS 2018 - Proceedings*. Institute of Electrical and Electronics Engineers Inc., Nov. 2018. ISBN: 9781538671931. DOI: 10.1109/SARS.2018.8551995 (cit. on p. 3).

[Tel99] E. Telatar. "Capacity of multi-antenna Gaussian channels". In: *European Transactions on Telecommunications* 10 (1999), pp. 585–595. DOI: 10.1002/ett.4460100604. URL: http://dx.doi.org/10.1002/ett.4460100604 (cit. on pp. 8, 49, 52).

[TG07] J. A. Tropp and A. C. Gilbert. “Signal recovery from random measurements via orthogonal matching pursuit”. In: *IEEE Transactions on Information Theory* 53.12 (Dec. 2007), pp. 4655–4666. ISSN: 0018-9448. DOI: 10.1109/TIT.2007.909108. URL: https://doi.org/10.1109/TIT.2007.909108%20http://ieeexplore.ieee.org/document/4385788/ (cit. on p. 130).

[Tib96] R. Tibshirani. “Regression shriknage and selection via the Lasso”. In: *Journal of the Royal Statistical Society. Series B (Methodological)* 58.1 (1996), pp. 267–288. ISSN: 00359246. DOI: 10.2307/2346178 (cit. on p. 72).

[Tik+95] A. N. Tikhonov, A. V. Goncharsky, V. V. Stepanov, A. G. Yagola, A. N. Tikhonov, A. V. Goncharsky, V. V. Stepanov, and A. G. Yagola. “Regularization methods”. In: *Numerical Methods for the Solution of Ill-Posed Problems*. Springer Netherlands, 1995, pp. 7–63. DOI: 10.1007/978-94-015-8480-7{_}2 (cit. on p. 72).

[TM02] D. S. Taubman and M. W. Marcellin. “Image transforms”. In: *JPEG2000 Image compression fundamentals, standards and practice*. Boston, MA: Springer US, 2002, pp. 143–207. ISBN: 978-1-4615-0799-4. DOI: 10.1007/978-1-4615-0799-4{_}4. URL: https://doi.org/10.1007/978-1-4615-0799-4_4 (cit. on p. 45).

[Tri+12] A. Trimeche, N. Boukid, A. Sakly, and A. Mtibaa. “Performance analysis of ZF and MMSE equalizers for MIMO systems”. In: *7th International Conference on Design and Technology of Integrated Systems in Nanoscale Era, DTIS 2012*. 2012. ISBN: 9781467319287. DOI: 10.1109/DTIS.2012.6232979 (cit. on p. 72).

[Tro04] J. A. Tropp. “Greed is good: algorithmic results for sparse approximation”. In: *IEEE Transactions on Information Theory* 50.10 (2004), pp. 2231–2242. ISSN: 0018-9448. DOI: 10.1109/TIT.2004.834793 (cit. on pp. 130, 135).

[TT09] R. J. Tibshirani and R. Tibshirani. “A bias correction for the minimum error rate in cross-validation”. In: *The Annals of Applied Statistics* 3.2 (June 2009), pp. 822–829. ISSN: 1932-6157. DOI: 10.1214/08-AOAS224. URL: https://doi.org/10.1214/08-AOAS224 (cit. on p. 128).

[Tur60] G. L. Turin. “An introduction to matched filters”. In: *IEEE Transactions on Information Theory* 6.3 (June 1960), pp. 311–329. ISSN: 0018-9448. DOI: 10.1109/TIT.1960.1057571. URL: http://ieeexplore.ieee.org/document/1057571/ (cit. on pp. 72, 115, 126).

[UCA15] UCAR - Center for science and education. *Earth's atmosphere*. 2015. URL: https://scied.ucar.edu/shortcontent/earths-atmosphere (cit. on p. 4).

[Urc+18] J. M. Urco, J. L. Chau, M. A. Milla, J. Vierinen, and T. Weber. "Coherent MIMO to improve aperture synthesis radar imaging of field-aligned irregularities: First results at Jicamarca". In: *IEEE Transactions on Geoscience and Remote Sensing* 56.5 (May 2018), pp. 2980–2990. ISSN: 0196-2892. DOI: 10.1109/TGRS.2017.2788425. URL: http://ieeexplore.ieee.org/document/8267289/ (cit. on pp. 58, 75, 87, 102).

[Urc+19a] J. M. Urco, J. L. Chau, T. Weber, and R. Latteck. "Enhancing the spatiotemporal features of polar mesosphere summer echoes using coherent MIMO and radar imaging at MAARSY". In: *Atmospheric Measurement Techniques* 12.2 (Feb. 2019), pp. 955–969. ISSN: 18678548. DOI: 10.5194/amt-12-955-2019. URL: https://www.atmos-meas-tech.net/12/955/2019/ (cit. on pp. 58, 109).

[Urc+19b] J. M. Urco, J. L. Chau, T. Weber, J. P. Vierinen, and R. Volz. "Sparse signal recovery in MIMO specular meteor radars with waveform diversity". In: *IEEE Transactions on Geoscience and Remote Sensing* 57.12 (Dec. 2019), pp. 10088–10098. ISSN: 0196-2892. DOI: 10.1109/TGRS.2019.2931375. URL: https://ieeexplore.ieee.org/document/8802292/ (cit. on p. 124).

[Van+07] S. Van Huffel, I. Markovsky, R. J. Vaccaro, and T. Söderström. "Total least squares and errors-in-variables modeling". In: *Signal Processing* 87.10 (Oct. 2007), pp. 2281–2282. ISSN: 01651684. DOI: 10.1016/j.sigpro.2007.04.008. URL: https://linkinghub.elsevier.com/retrieve/pii/S0165168407001557 (cit. on p. 72).

[VB88] B. D. Van Veen and K. M. Buckley. "Beamforming: a versatile approach to spatial filtering". In: *IEEE ASSP Magazine* 5.2 (1988), pp. 4–24 (cit. on pp. 38, 73).

[Vie+16] J. Vierinen, J. L. Chau, N. Pfeffer, M. Clahsen, and G. Stober. "Coded continuous wave meteor radar". In: *Atmospheric Measurement Techniques* 9.2 (Mar. 2016), pp. 829–839. ISSN: 1867-8548. DOI: 10.5194/amt-9-829-2016. URL: https://www.atmos-meas-tech.net/9/829/2016/ (cit. on pp. 2, 6, 32, 33, 59, 72, 113–115, 121, 122, 124, 127, 136).

[Vie+19] J. Vierinen, J. L. Chau, H. Charuvil, J. M. Urco, M. Clahsen, V. Avsarkisov, R. Marino, and R. Volz. "Observing mesospheric turbulence with specular me-

teor radars: A novel method for estimating second-order statistics of wind velocity". In: *Earth and Space Science* 6.7 (July 2019), pp. 1171–1195. ISSN: 2333-5084. DOI: 10.1029/2019EA000570. URL: https://onlinelibrary.wiley.com/doi/abs/10.1029/2019EA000570%20https://agupubs.onlinelibrary.wiley.com/doi/abs/10.1029/2019EA000570 (cit. on pp. 4, 6, 7, 85, 147, 153).

[Vin15] R. A. Vincent. "The dynamics of the mesosphere and lower thermosphere: a brief review." In: *Progress in Earth and Planetary Science* 2.4 (Dec. 2015), p. 4. ISSN: 21974284. DOI: 10.1186/s40645-015-0035-8. URL: http://www.progearthplanetsci.com/content/2/1/4 (cit. on pp. 4, 85).

[VV91] S. Van Huffel and J. Vandewalle. *The total least squares problem*. Society for Industrial and Applied Mathematics, Jan. 1991. ISBN: 978-0-89871-275-9. DOI: 10.1137/1.9781611971002. URL: http://epubs.siam.org/doi/book/10.1137/1.9781611971002 (cit. on p. 72).

[Wan+07] C. Wang, E. Au, R. Murch, W. Mow, R. Cheng, and V. Lau. "On the performance of the MIMO Zero-Forcing receiver in the presence of channel estimation error". In: *IEEE Transactions on Wireless Communications* 6.3 (Mar. 2007), pp. 805–810. ISSN: 1536-1276. DOI: 10.1109/TWC.2007.05384. URL: http://ieeexplore.ieee.org/document/4133864/ (cit. on p. 115).

[Wan12] W.-Q. Wang. "Virtual antenna array analysis for MIMO synthetic aperture radars". In: *International Journal of Antennas and Propagation* 2012 (2012), pp. 1–10. ISSN: 1687-5869. DOI: 10.1155/2012/587276. URL: http://www.hindawi.com/journals/ijap/2012/587276/ (cit. on p. 51).

[Wee93] V. Weerackody. "Diversity for the direct-sequence spread spectrum system using multiple transmit antennas". In: *IEEE International Conference on Communications*. Publ by IEEE, 1993, pp. 1775–1779. ISBN: 0780309510. DOI: 10.1109/icc.1993.397586 (cit. on p. 55).

[Wel74] L. Welch. "Lower bounds on the maximum cross correlation of signals (Corresp.)" In: *IEEE Transactions on Information Theory* 20.3 (1974), pp. 397–399 (cit. on p. 33).

[WEV13] T. Wimalajeewa, Y. C. Eldar, and P. K. Varshney. "Recovery of sparse matrices via matrix sketching". In: *CoRR* abs/1311.2 (Nov. 2013). URL: http://arxiv.org/abs/1311.2448 (cit. on p. 130).

[WH06] J. M. Wallace and P. V. Hobbs. *Atmospheric science*. Second. Elsevier, 2006, pp. 1–488. ISBN: 9780127329512. DOI: 10.1016/C2009-0-00034-8. URL: https://linkinghub.elsevier.com/retrieve/pii/C20090000348 (cit. on p. 1).

[Wid+67] B. Widrow, P. Mantey, L. Griffiths, and B. Goode. "Adaptive antenna systems". In: *Proceedings of the IEEE* 55.12 (1967), pp. 2143–2159. ISSN: 0018-9219. DOI: 10.1109/PROC.1967.6092. URL: http://ieeexplore.ieee.org/document/1448022/ (cit. on pp. 50, 52).

[Wie30] N. Wiener. "Generalized harmonic analysis". In: *Acta Mathematica* 55.1 (Dec. 1930), pp. 117–258. ISSN: 0001-5962. DOI: 10.1007/BF02546511. URL: http://projecteuclid.org/euclid.acta/1485887877 (cit. on p. 147).

[Wil09] M. Wilson. "Meteor trails track upper atmospheric winds". In: *Physics Today* 62 (2009), p. 16 (cit. on p. 88).

[WKS12] J. Wang, S. Kwon, and B. Shim. "Generalized orthogonal matching pursuit". In: *IEEE Transactions on Signal Processing* 60.12 (Dec. 2012), pp. 6202–6216. ISSN: 1053-587X. DOI: 10.1109/TSP.2012.2218810. URL: http://ieeexplore.ieee.org/document/6302206/ (cit. on pp. 130, 131).

[Wol+98] P. Wolniansky, G. Foschini, G. Golden, and R. Valenzuela. "V-BLAST: an architecture for realizing very high data rates over the rich-scattering wireless channel". In: *1998 URSI International Symposium on Signals, Systems, and Electronics. Conference Proceedings (Cat. No.98EX167)*. IEEE, 1998, pp. 295–300. ISBN: 0-7803-4900-8. DOI: 10.1109/ISSSE.1998.738086. URL: http://ieeexplore.ieee.org/document/738086/ (cit. on p. 128).

[Woo+19] R. F. Woodman, D. T. Farley, B. B. Balsley, and M. A. Milla. "The early history of the Jicamarca Radio Observatory and the incoherent scatter technique". In: *History of Geo- and Space Sciences* 10.2 (2019), pp. 245–266. DOI: 10.5194/hgss-10-245-2019. URL: https://www.hist-geo-space-sci.net/10/245/2019/ (cit. on pp. 17, 38).

[Woo72] R. F. Woodman. "East-west ionospheric drifts at the magnetic equator". In: *Space Res.* 12 (1972), pp. 969–974 (cit. on p. 50).

[Woo97] R. F. Woodman. "Coherent radar imaging: signal processing and statistical properties". In: *Radio Science* 32.6 (Nov. 1997), pp. 2373–2391. ISSN: 00486604. DOI: 10.1029/97RS02017. URL: http://doi.wiley.com/10.1029/97RS02017 (cit. on p. 43).

[WSC13] W.-Q. Wang, H. Shao, and J. Cai. "MIMO antenna array design with polynomial factorization". In: *International Journal of Antennas and Propagation* 2013 (2013). Ed. by Y. Yao, p. 358413. ISSN: 1687-5869. DOI: 10.1155/2013/358413. URL: https://doi.org/10.1155/2013/358413 (cit. on pp. 68, 81).

[WSG94] J. H. Winters, J. Salz, and R. D. Gitlin. "The impact of antenna diversity on the capacity of wireless communication systems". In: *IEEE Transactions on Communications* 42.234 (1994), pp. 1740–1751. ISSN: 00906778. DOI: 10.1109/TCOMM.1994.582882 (cit. on p. 55).

[WWL03] G. Wang, D. Wang, and D. Li. "An efficient ZF-SIC detection algorithm in MIMO CDMA system". In: *14th IEEE Proceedings on Personal, Indoor and Mobile Radio Communications, 2003. PIMRC 2003.* Vol. 2. IEEE, 2003, pp. 1708–1711. ISBN: 0-7803-7822-9. DOI: 10.1109/PIMRC.2003.1260406. URL: http://ieeexplore.ieee.org/document/1260406/ (cit. on p. 128).

[XLS06] L. Xu, J. Li, and P. Stoica. "Radar imaging via adaptive MIMO techniques". In: *European Signal Processing Conference*. Vol. 1. 2006, pp. 1–5 (cit. on p. 3).

[Xua+17] V. N. Xuan, K. Hartmann, W. Weihs, and O. Loffeld. "Modified orthogonal matching pursuit for multiple measurement vector with joint sparsity in super-resolution compressed sensing". In: *2017 51st Asilomar Conference on Signals, Systems, and Computers*. 2017, pp. 840–844. DOI: 10.1109/ACSSC.2017.8335466 (cit. on p. 133).

[YH17] X. Yuan and R. Haimi-Cohen. "Image compression based on compressive sensing: end-to-end comparison with JPEG". In: (June 2017). URL: http://arxiv.org/abs/1706.01000 (cit. on p. 45).

[Yiğ+09] E. Yiğit, A. S. Medvedev, A. D. Aylward, P. Hartogh, and M. J. Harris. "Modeling the effects of gravity wave momentum deposition on the general circulation above the turbopause". In: *Journal of Geophysical Research: Atmospheres* 114.D7 (2009). DOI: 10.1029/2008JD011132. URL: https://agupubs.onlinelibrary.wiley.com/doi/abs/10.1029/2008JD011132 (cit. on p. 6).

[YP68] K. O. Yngvesson and F. W. Perkins. "Radar Thomson scatter studies of photoelectrons in the ionosphere and Landau damping". In: *Journal of Geophysical Research* 73 (1968), pp. 97–110 (cit. on p. 17).

[YPH00] T.-Y. Yu, R. D. Palmer, and D. L. Hysell. "A simulation study of coherent radar imaging". In: *Radio Science* 35.5 (Sept. 2000), pp. 1129–1141. ISSN: 00486604. DOI: 10.1029/1999RS002236. URL: http://doi.wiley.com/10.1029/1999RS002236 (cit. on pp. 96, 98).

[Zec+01] M. Zecha, J. Röttger, W. Singer, P. Hoffmann, and D. Keuer. "Scattering properties of PMSE irregularities and refinement of velocity estimates". In: *Journal of Atmospheric and Solar-Terrestrial Physics* 63 (2001), pp. 201–214 (cit. on p. 89).

JUAN M. E. URCO CORDERO

Ph.D. in Electrical Engineering

@ mcordero@illinois.edu (+1) 217 7218562 302 South First St., 61820 Champaign, IL, USA

EDUCATION

Ph.D. in Electrical Engineering
University of Rostock
April 2016 – March 2021 Rostock, Germany

MS in Information Technology and Telematics
Universidad Nacional Mayor de San Marcos
Aug 2010 – Jul 2012 Lima, Peru

BA in Electrical Engineering
Universidad Nacional Mayor de San Marcos
March 2001 – Dec 2005 Lima, Peru

RESEARCH EXPERIENCE

Postdoctoral Research Associate
University of Illinois at Urbana-Champaign
June 2021 – present Champaign, IL, USA

Ph.D. candidate
Institute for Atmospheric Physics
2016 – 2021 Kühlungsborn, Germnany

R&D department
Jicamarca Radio Observatory
2009 – 2016 Lima, Peru

Summer Research Experience Program
MIT Haystack Observatory
Summer 2014 MA, USA

Summer Undergraduate Research Program
Pontificia Universidad Catolica del Peru
Summer 2016 Lima, Peru

REASEARCH INTEREST

- Statistic analysis, inverse problems
- Model reduction, sparse sensing
- Machine learning and data science for modeling high-dimensional complex systems.
- Fluid dynamics, transport phenomena

PROGRAMMING SKILLS

Python
C/C++
Matlab
IDL
Assembler
Java
Others

STRENGTHS

Highly motivated and eager to learn
Self-learning
Problem solving
Dot connecting skill

AWARDS AND HONORS

2019	**CEDAR poster competition award - Honorable mention** Santa Fe, USA
2010-2012	**Fully funded scholarship for Master's studies** CONCYTEC, Peru
2009	**Best employee of the year award** Jicarmarca Radio Observatory.
2006	**Graduate student award - Second place** XIII INTERCON, IEEE, Peru
2005	**Undergraduate student award - First place** XII INTERCON, IEEE, Peru

PEAR-REVIEWED PUBLICATIONS

1. **Urco, J. M.**, Kamalabadi, F., Kamaci, U., Harding, B. J., Frey, H. U., Mende, S. B., Huba, J., England, S. L., Immel, T. J. (2021). Conjugate photoelectron energy spectra derived from coincident FUV and radio measurements. Geophys. Res. Lett [under review].

2. Asokan, H. C., Chau, J. L., Marino, R., Vierinen, J., Vargas, F., **Urco, J. M.**, Clahsen, M., Jacobi, C. (2021). Study of second-order wind statistics in the mesosphere and lower thermosphere region from multistatic specular meteor radar observations during the SIMONe 2018 campaign. Atmos. Chem. [under review].

3. Volz, R., Chau, J., Erickson, P., Vierinen, **Urco, J. M.**, J. M., Clahsen, M. (2021). Four-dimensional mesospheric and lower thermospheric wind fields using Gaussian process regression on multistatic specular meteor radar observations. Atmospheric Measurement Techniques Discussions, 1–29.

4. Chau, J. L., **Urco, J. M.**, Vierinen, J., Harding, B. J., Clahsen, M., Pfeffer, N., Kuyeng, K. M., Milla, M. A., Erickson, P. J. (2021). Multistatic Specular Meteor Radar Network in Peru: System Description and Initial Results. Earth and Space Science, 8(1), e2020EA001293.

5. Conte, J. F., Chau, J. L., **Urco, J. M.**, Latteck, R., Vierinen, J., Salvador, J. O. (2021). First Studies of Mesosphere and Lower Thermosphere Dynamics Using a Multistatic Specular Meteor Radar Network Over Southern Patagonia. Earth and Space Science, 8(2).

6. Stamm, J., Vierinen, J., **Urco, J. M.**, Gustavsson, B., Chau, J. L. (2021). Radar imaging with EISCAT 3D. Annales Geophysicae, 39(1), 119–134.

7. Chau, J. L., **Urco, J. M.**, Avsarkisov, V., Vierinen, J. P., Latteck, R., Hall, C. M., Tsutsumi, M. (2020). Four-Dimensional Quantification of Kelvin-Helmholtz Instabilities in the Polar Summer Mesosphere Using Volumetric Radar Imaging. Geophysical Research Letters, 47(1).

8. **Urco, J. M.**, Chau, J. L., Weber, T., Latteck, R. (2019). Enhancing the spatiotemporal features of polar mesosphere summer echoes using coherent MIMO and radar imaging at MAARSY. Atmospheric Measurement Techniques, 12(2), 955–969.

9. Chau, J. L., **Urco, J. M.**, Vierinen, J., Volz, R., Clahsen, M., Pfeffer, N., Trautner, J. (2019). Novel specular meteor radar systems using coherent MIMO techniques to study the mesosphere and lower thermosphere. Atmospheric Measurement Techniques, 12(4), 2113–2127.

10. Vierinen, J., Chau, J. L., Charuvil, H., **Urco, J. M.**, Clahsen, M., Avsarkisov, V., Marino, R., Volz, R. (2019). Observing Mesospheric Turbulence With Specular Meteor Radars: A Novel Method for Estimating Second-Order Statistics of Wind Velocity. Earth and Space Science, 6(7), 1171–1195.
11. **Urco, J. M.**, Chau, J. L., Weber, T., Vierinen, J. P., Volz, R. (2019). Sparse signal recovery in MIMO specular meteor radars with waveform diversity. IEEE Transactions on Geoscience and Remote Sensing, 57(12), 10088–10098.
12. Hysell, D. L., Sharma, P., **Urco, J. M.**, Milla, M. A. (2019). Aperture-synthesis radar imaging with compressive sensing for ionospheric research. Radio Science, 54(6), 503–516.
13. **Urco, J. M.**, Chau, J. L., Milla, M. A., Vierinen, J., Weber, T. (2018). Coherent MIMO to improve aperture synthesis radar imaging of field-aligned irregularities: First results at Jicamarca. IEEE Transactions on Geoscience and Remote Sensing, 56(5), 2980–2990.

POSTERS AND PRESENTATIONS

Conjugate photoelectrons on the nightime ionosphere derived from coincident ICON and COSMIC2 measurements

CEDAR Workshop, June 2021

Virtual

Observation and characterization of small and large-scale mesospheric structures through MIMO and inverse problem technique

RWTH Aachen University, February 2020

Aachen, Germany

Observation and characterization of kilometer and meso-scales structures: MIMO and inverse problem techniques

Institute for Atmospheric Physics, January 2020

Kühlungsborn, Germany

A novel meteor radar network based on MIMO to study the MLT dynamics

CEDAR Workshop, June 2019

Sanfa Fe, NM, USA

Enhancing spatio-temporal PMSE features using coherent MIMO and radar imaging

LPMR Workshop, March 2018

Kborn, Germany

Coherent MIMO to improve aperture synthesis radar imaging

MST15 Workshop, May 2017

Tokyo, Japan

A modular and powerful radar signal processing software for atmospheric data

CEDAR workshop, June 2014

Seattle, WA, USA

Estimation of 2D vector velocity of ionospheric irregularities over Jicamarca using Particle Image Velocimetry

CEDAR Workshop, June 2012

Santa Fe, NM, USA

Radar Signal Processing

Signal Processing Workshop, July 2011

JRO, Lima, Peru

Parallel processing for imaging equatorial Spread F irregularities

Winter International Scientific Meeting, July 2010

Lima, Peru

Madrigal database at Jicamarca: A scientific database

Summer International Scientific Meeting, January 2010

Lima, Peru

Open radar workshop on software radar

MIT Haystack Observatory & JRO, October 2010

Lima, Peru

Real-time parallel processing software for radar imaging

National Meeting of Radio Scientists, URSI, August 2010

Lima, Perú

A distributed atmospheric database, Madrigal at Jicamarca

CEDAR Workshop, June 2009

Santa Fe, NM, USA

REFERENCES

Juha Vierinen Ph.D., Associate Professor

Department of Physics and Technology, The Artic University of Norway

+47 77645163, juha-pekka.vierinen@uit.no

Marco Milla Ph. D., JRO Director

Jicamarca Radio Observatory

+51 317 - 2313, marco.milla@jro.igp.gob.pe

Philip Erickson Ph. D., Group Leader and Principal Research Scientist

Atmospheric Sciences Group, MIT Haystack Observatory

+1 781 981 5769, pje@haystack.mit.edu